UNIVERSIDADE DA BEIRA INTERIOR
Engenharia

Structural Design of a Variable Span Morphing Wing: Analysis, Optimisation and Study of the Effect of Design Parameters on its Mass

Diogo Bento Sousa

Dissertação para a obtenção do Grau de Mestre em
Engenharia Aeronáutica
(Ciclo de estudos integrado)

Orientador: Prof. Doutor Pedro Vieira Gamboa

Covilhã, Junho de 2017

Dedication

Is my deep wish to dedicate this work to my family and closest friends, for giving me the strength to be always the best person I can, to overcome all the obstacles I found throughout my academic life and go beyond what everyone expected from me. Thank you for sharing with me the joy of leaving this life.

To my sister, Barbara, that with only the age of sixteen lost the company of a brother that used to be so close. Thanks for understanding my absence on all the time spent away doing this course. I wish only the best for your future.

To Catarina, whose affection and encouragement were my source of inspiration. For your tireless support and comprehension throughout my academic life, for your invaluable advice in so many moments and finally for walking this path with me. You will always have a special place in my heart.

Para a minha mãe, Alexandra, pelo seu amor incondicional em todas as fases da minha vida. Sei que sou um felizardo por saber que posso contar sempre contigo. Sem ti, nunca teria atingido todas os desafios que superei até hoje.

To my father, Carlos, for his support, friendship and for all surf sessions we could not share while I was studying far away. Thanks for being the role model I have tried to follow since a young age. A big part of what I am and achieved today I owe it to you.

"The secret of change is to focus all of your energy, not on fighting the old, but on building the new."

— Dan Millman, *Way of the Peaceful Warrior*

Acknowledgements

The realisation of this thesis would not have been possible without the invaluable contribution of two people to whom I wish to express my sincere gratitude.

I would like to take this opportunity to express my sincere gratitude to my supervisor, Professor Pedro Gamboa, whom was always there to ensure that I was following the right path. This work would not have been possible without your valuable knowledge, guidance and encouragement. There are not enough words to thank you for the enlightenment provided along the course, your abiding readiness and support, for giving me the necessary means to the development of this work and for giving me the unique opportunity to enter the world of aircraft design. Finally, I am aware that I still have much to learn with you and hope to find the opportunity for it.

I am also deeply indebted to Pedro Santos, for mentoring me in a variety of aspects throughout the project, for his availability and willingness to help and for developing an essential part of the current work, namely co-developing and solving several persistent problems that arose during the implementation of the structural analysis and APDL optimisation procedure for the parametric model and FEM sizing of the VSW. A big part of what it was accomplished in this work I owe it to you. Moreover, thank you for integrating me in your team, for your careful advices and for providing me so much valuable information that was undoubtedly crucial along the entire research. Thank you for first introducing me to APDL, ANSYS and for giving me some hints on LaTeX, which proved really useful in this work. I wish to thank you for all this, but above all, for being a good friend.

Further acknowledgements should be addressed to Professor Miguel Ângelo, who has been my first professor in this university, who guided me along several interesting aeronautic projects and international competitions and inspired me to enroll in some ecological and local projects that undoubtedly contributed, not necessarily to my professional education, but for my personal growth as a citizen. After concluding this phase of teacher-student relationship, I would be grateful if we could keep a good friendship relation in the future.

Additionally, I would like to acknowledge the valuable contribution of João Gomes, whom have first introduced me to carbon-fibre hand layup process and helped me day and night to manufacture a proof-of-concept continuous flap during early stages of the project. Moreover, to Pedro Albuquerque, whom has performed along his work the MDO sizing of the VSW.

This work has been partially funded by the European Community's Seventh Framework Programme (FP7) under the Grant Agreement 314139. The CHANGE project (Combined morphing assessment software using flight envelope data and mission based morphing prototype wing development) is a Level 1 project funded under the topic AAT.2012.1.1-2. The project, involving 9 partners, started on August 1st 2012.

Abstract

A continuing search for design methods pointing towards optimising flight overall efficiency renewed interests in unconventional design solutions for aircraft future demands. In line with several other unconventional designs, the development of morphing wing technologies for in-flight shape adaptation is one of the richest and most challenging interdisciplinary fields researchers have focused in recent years. A detailed guide on a telescopic wing design and sizing is presented, effects of design parameters on wing structural mass are investigated and a full mass predicting function is developed to be applied on future telescopic wing designs.

A telescopic wing is designed for the new Olharapo III RPAS operating in the range of speeds from about the stall speed of 11 m/s to 40 m/s. This wing is a high mounted, straight telescopic wing, without ailerons. The current version has a wingspan of 3.554 m for a RPAS of 150 N. Its design makes use of aerodynamically optimised aerofoils and winglets, a minimum-mass optimised structure and actuation system and also, comprises morphing high-lift surfaces. The established actuation system has a mass of 0.325 kg. Proper aerofoil design to ensure geometric compatibility and good aerodynamic performance is performed. Trends on geometric and aerodynamic characteristics of resulting inward and outward offset aerofoils are discussed. Further wing characteristics are defined and CAD technical drawings are performed. Physics-based structural analysis and minimum mass optimisation, constrained by strength and stiffness limits, are built in APDL and solved in ANSYS. FEM associated errors are analysed and a mesh convergence study is carried. The resulting VSW is sized to 1.0 kg. Wing skin converged for a thickness of 2.24 mm. IFW and OMW spar caps are sized to a width of 21.7 mm and 0.8 mm, respectively.

Morphing concepts typically present mass penalties due to their inherent complexity both in the load carrying structure and in systems that perform morphing. Simple yet suitably accurate mass predicting methods to aid design telescopic wings at early design phases, as well as to assess their benefits over conventional wings, are non-existent in the scientific community. A parametric study, which encloses an optimisation loop performing FEA, is implemented to obtain wing structural mass databases. The considered design parameters are maximum wingspan, wing chord, span variation ratio, aircraft take-off weight and flap's chord ratio. Mass functions are created by fitting multivariable high order polynomials to the obtained data. A MATLAB® script is developed to compute the regression models, obtain the polynomial coefficients and perform post-processing calculations. From the latter, a screening to the significant terms and a goodness-of-fit assessment are conducted. A nonlinear ERR-Causality regression method is employed and a high fitting accuracy is accomplished. Conclusions on the effects of design parameters on wing structural mass are taken from ensuing partial derivatives and 3D plots. Moreover, a preliminary VSW full mass predicting function is developed from adding mass contributions of secondary structural components, actuation system and non-optimum effects to the structural mass function.

Keywords

Aircraft design; Morphing technologies; Variable-span wing (VSW); RPAS; Parametric study; FEM-based structural optimization; Data fitting; Wing mass function; Aerodynamic analysis; Aerofoil offset; *CATIA V5*; *APDL-ANSYS*; *Matlab*; *XFOIL*.

Resumo

A conjuntura da indústria aeronáutica sustenta a futura necessidade de desenvolver projetos com foco na eficiência em voo, renovando-se assim o interesse em soluções não convencionais. A investigação de asas com tecnologias morphing para adaptação da geometria em voo é uma das áreas interdisciplinares mais ricas e desafiantes da atualidade. Os principais objectivos alcançados no decorrer desta dissertação foram: elaborar o projeto e dimensionamento de uma asa telescópica, analisar os impactos dos parâmetros de projeto na massa estrutural destas asas e desenvolver uma função para estimar a massa total de asas telescópicas em projetos futuros.

Uma asa é projetada para o novo Olharapo III RPAS, o qual opera entre uma velocidade de perda de 11 m/s e 40 m/s. A VSW é uma asa alta telescópica, sem enflexamento, sem ailerons e com uma envergadura de 3.554 m para um RPAS de 150 N. O seu projeto inclui perfis e pontas de asa otimizados, estrutura e sistema de atuação dimensionados e ainda, superfícies de alta sustentação morphing. Os perfis foram desenhados de modo a garantir compatibilidade e desempenho. As tendências das alterações geométricas e características aerodinâmicas dos perfis modificados por offsets para dentro ou para fora são discutidas. As características da VSW são definidas e os seus desenhos técnicos são elaborados em CAD. Uma análise e otimização em elementos finitos para minimizar a massa, condicionada por limites de rigidez e resistência estrutural, é implementada no APDL e resolvida no ANSYS. Um estudo de convergência de malha e erros associados ao modelo são ponderados. A massa resultante do dimensionamento da VSW é 1.0 kg e do sistema de atuação é 0.325 kg. A espessura da casca da asa convergiu para 2.24 mm e a largura das mesas das longarinas da IFW e OMW para 21.7 mm e 0.8 mm, respetivamente.

Os conceitos morphing usualmente apresentam um acréscimo de massa devido à inerente complexidade da estrutura carregada e do sistema que permite a variação de forma. Métodos simples, porém precisos, para estimar a massa de asas telescópicas em fases iniciais de projeto e para avaliar as suas mais valias em relação a asas convencionais, são atualmente inexistentes na comunidade científica. Um estudo paramétrico, que inclui um ciclo de otimização empregando uma FEA, é implementado no cálculo da massa estrutural de uma base de dados de asas. Os parâmetros de projeto considerados são envergadura máxima, corda, fração de variação de envergadura, peso máximo à descolagem e fração de corda do flap. As funções de massa são criadas através da modelação dos dados a funções polinomiais multivariáveis de ordem superior. Um código escrito em MATLAB® corre os métodos de regressão, define os coeficientes polinomiais e calcula o pós-processamento. A significância dos termos e a precisão da aproximação são analisadas. O método de regressão não linear ERR-Causality é aplicado e uma elevada precisão é obtida. Os efeitos dos parâmetros de projeto na massa estrutural das asas são analisados através de derivadas parciais e gráficos 3D. Uma função preliminar de aproximação da massa total de asas VSW ▫ definida com base nas contribuições de massa da estrutura primária, secundária, sistema de atuação e efeitos não ótimos de projeto.

Palavras-chave

Projecto de aeronaves; Tecnologias morphing; Asa de envergadura variável; RPAS; Estudo paramétrico; Optimização estrutural com elementos finitos; Modelação de dados; Função de massa; Análise aerodinâmica; Offset de perfis; *CATIA V5*; *APDL-ANSYS*; *Matlab*; *XFOIL*.

Contents

List of Figures

List of Tables

List of Acronyms

ANSYS®	ANalysis SYStems, Inc - computer-aided engineering software
APDL	ANSYS Parametric Design Language
App.	Appendix
ARA	Aircraft Research Association
ASTM	American Society of Testing and Materials
bl	Boundary layer
CAD	Computer-aided design
CHANGE	Combined morphing assessment software using flight envelope data and mission based morphing prototype wing development
CCD	Central composite design
CFD	Computational fluid dynamics
CFRP	Carbon fibre reinforced polymer
CG	Center of gravity
CS	Certification specifications
DARPA	Defence advanced research projects agency
DC	Direct current
DCA	Departamento de Ciências Aeroespaciais (Aerospace Sciences Department, UBI)
DLR	Deutsches Zentrum f□r Luft und Raumfahrt e.V.
DoE	Design of experiments
DPP	vDijk Pultrusion Products
EASA	European Aviation Safety Agency
ECO	Enhanced collaborative optimization
EDA	Effective dihedral angle
ERR	Error reduction ratio
ESC	Electronic speed controller
EU	European Union
FEA	Finite element analysis
FEM	Finite element method
FLYRT	Flying radar target
FPV	First-person view
FS	Factor of safety
GPS	Global positioning system
HALE	High altitude long endurance
HP	High power
ICAO	International Civil Aviation Organization
IFW	Inboard fixed wing
INVENT	Innovative Verbundwerkstofferealisation und Vermarktung Neuertechnologien
IPCC	International Panel on Climate Change
ISA	International Standard Atmosphere
ISO	International Organization for Standardization
ITWSR	Inverse of Tsai-Wu strength ratio index

LE	Leading edge
MADCAT	Mission Adaptive Digital Composite Aerostructure Technologies (NASA's team)
MALE	Medium altitude long endurance
MAS	Morphing aircraft structures program
MATLAB®	MATrix LABoratory programming language
MDO	Multidisciplinary design optimisation
MIT	Massachusetts Institute of Technology
MP	Medium power
MPC	Multi-point constrain
MSL	Mean sea level
MTOW	Maximum take-off weight
MTOM	Maximum take-off mass
NASA	National Aeronautics and Space Administration
NATO	North Atlantic Treaty Organization
OMW	Outboard moving wing
PAN	Polyacrylonitrile
PTFE	Polytetrafluoroethylene
PVC	Polyvinyl chloride
PWM	Pulse width modulation
RPAS	Remotely piloted aircraft system
RPM	Rotations per minute
RTO	Research and Technology Organization of NATO
SMA	Shape memory alloys
SU	Swansea University
SVD	Singular value decomposition
TE	Trailing edge
TRL	Technology readiness level
TUDelft	Technische Universiteit Delft
TWSI	Tsai-Wu strength index
UAS	Unmanned aerial system
UAV	Unmanned aerial vehicle
US	United States (of America)
UBI	Universidade da Beira Interior
UNFCCC	United Nations Framework Convention on Climate Change
VLA	Very light aeroplanes
VLM	Vortex lattice method
VSW	Variable-span wing

Nomenclature

$2D$	Two-dimensional	[$-$]
$3D$	Three-dimensional	[$-$]
a	Ellipse's semi-major axis or acceleration	[m or m/s^2]
a'	Aeroplane/wing normal force coefficient curve slope per radian (CS-VLA)	[rad^{-1}]
A_p	Horizontally projected panel area	[m^2]
AR	Wing aspect ratio	[$-$]
b	Wing span or Ellipse's semi-minor axis	[m]
c	Aerofoil chord	[m]
$\bar{c}$	Mean geometric chord	[m]
c_a	Aerodynamic chord	[m]
$\overline{c}_{flap}$	Flap's chord to wing chord ratio	[m]
C_l	Aerofoil lift coefficient	[$-$]
$C_{l'}$	Rolling moment coefficient	[$-$]
C_L	Wing lift coefficient	[$-$]
C_{l0}	Aerofoil lift coefficient at zero-angle of attack	[$-$]
$C_{l_{op}}$	Design operation C_l	[$-$]
C_{l_β}	Dihedral effect, stability derivative in $C_{l'}$ per degree of change in β	[$-$]
C_d	Aerofoil drag coefficient	[$-$]
C_{di}	Induced drag coefficient	[$-$]
C_D	Wing drag coefficient	[$-$]
C_m	Aerofoil pitching moment coefficient	[$-$]
C_M	Wing pitching moment coefficient	[$-$]
$coef$	Regression polynomial coefficients	[$-$]
C_p	Pressure coefficient	[$-$]
d_{Cent}	Distance between the OMW panel centroid and the centre of the wing	[m]
d_{TO}	Take-off distance	[m]
D	Drag force or Component's diameter	[N or m]
e	Oswald's efficiency factor	[$-$]
E	Young's modulus	[Pa]
F	Force	[N]
$\overline{FE}_{ITWSR}$	Failed elements ratio (using ITWSR criterion)	[$-$]
g	Acceleration due to gravity	[m/s^2]
G	Shear Modulus	[Pa]
h	True altitude (above MSL)	[m]
H	Horizontal force	[N]
i	Wing incidence angle	[$degree$]
I	Regression $indepvar$ design matrix	[$-$]
$indepvar$	Regression independent variables vector	[$-$]
k	Constant coefficient or correction factor	[$-$]

k_{flap}	Flap's mass correcting factor	$[-]$
K_g	Gust alleviation factor	$[-]$
k_{tip}	Multiplying factor that correlates the wing tip span with the average wingspan	$[-]$
l_{ext}	VSW semi-span length when fully extended	$[m]$
l_{flap}	Flap semi-span length	$[m]$
l_{fus}	Fuselage semi-width	$[m]$
l_{IFW}	IFW semi-span length	$[m]$
l_{OMW}	OMW semi-span length	$[m]$
l_{over1}	Overlapping area at OMW root	$[m]$
l_{over2}	Overlapping area at IFW-OMW limits	$[m]$
l_{retr}	VSW semi-span length when fully retracted	$[m]$
l_{tip}	Horizontal projection of tip semi-span length	$[m]$
l_{var}	Variable-span section length	$[m]$
$\bar{l}_{var}$	Variable-span ratio	$[m]$
L	Wing lift force	$[N]$
L/D	Aerofoil lift-to-drag	$[-]$
m	Component mass or aircraft MTOM or regression model matrix	$[kg$ or $-]$
M	Pitching moment	$[Nm]$
$\overline{m}_{flap}$	Flaps' predicted mass	$[kg]$
m_{FW}	Structural mass of a fixed conventional wing	$[kg]$
m_{VSW}	Structural mass of a telescopic wing	$[kg]$
$\overline{m}_{VSW}$	Structural estimated mass of a telescopic wing	$[kg]$
$\overline{m}_{sys}$	Telescopic actuation system's estimated mass	$[kg]$
m_w	Wing mass results (from FEM-based optimisation)	$[kg]$
$\overline{m}_w$	Wing estimated mass values (from regression polynomials)	$[kg]$
m/S	Wing loading	$[kg/m^2]$
n	Polynomial degree or limit manoeuvring load factor or independent variables number	$[-]$
N	Number of spanwise sections or number of DoE	$[-]$
$No.$	Number	$[-]$
q_L	Distributed lift	$[N/m]$
$q_L{}'$	Non-dimensional distributed lift	$[-]$
q_D	Distributed drag	$[N/m]$
$q_D{}'$	Non-dimensional distributed drag	$[-]$
q_M	Distributed pitching moment	$[N]$
$q_M{}'$	Non-dimensional distributed pitching moment	$[-]$
R	Flight range	$[m]$

Re	Reynolds number	[$-$]
RoC	Rate of climb	[m/s]
S	Wing planform area	[m^2]
S_{flap}	Flap planform area	[m^2]
S_{wetted}	Wing wetted area	[m^2]
t	Thickness of component	[m]
t_{lam}	Skin's laminate CRFP thickness	[m]
$(t/c)_{max}$	Aerofoil maximum thickness-to-chord ratio	[$-$]
U_{de}	Derived gust velocities	[m/s]
V	Air speed or actuation velocity or vertical force	[m/s or N]
V_A	Design manoeuvring speed for maximum turn ratio	[m/s]
V_c	Design cruising speed, fast cruise	[m/s]
V_D	Design dive speed or maximum operating velocity	[m/s]
V_l	Design loiter speed, slow cruise	[m/s]
V_{stall}	Stall velocity	[m/s]
V_{s+}	Positive stall velocity	[m/s]
V_{s-}	Negative stall velocity	[m/s]
V_{TO}	Take-off velocity	[m/s]
V_∞	Air flow velocity in the free-stream region	[m/s]
$vars$	Regression polynomial variables	[$-$]
VSW_{II}	VSW version of Olharapo II	[$-$]
$VSW_{II_{mod}}$	VSW modified version of Olharapo II	[$-$]
VSW_{III}	VSW version of Olharapo III	[$-$]
W	Aircraft MTOW	[N]
W'	Equivalent MTOW for regression model ($W \times 10^{-2}$)	[hN]
w_{cap}	Spar cap's width	[m]
w_{tip}	Tip deflection	[m]
x	Longitudinal axis	[$-$]
x_1	Non-dimensional position of front spar	[$-$]
x_2	Non-dimensional position of aft spar	[$-$]
x_{LE}	Aerofoil leading edge longitudinal position to chord ratio	[$-$]
y	Transversal axis	[$-$]
y_i	Wing spanwise length at each i^{th} section	[m]
y'	Semi-span distance from wing root to $b/2$ ratio	[$-$]
z	Vertical axis	[$-$]

Greek letters

α	Angle of attack	[$degree$]
β	Aircraft sideslip angle	[$degree$]
Δt	Timespan	[s]
ε	Wing twist angle or Normal strain	[$degree$ or $-$]
ε	Absolute error	[$-$]
η	Percent relative error	[$-$]
θ_i	Angle between the aerofoil offset direction and the vertical axis	[$degree$]
$\theta_{y,tip}$	Tip rotation angle	[$degree$]
γ	Shear strain	[$-$]
Γ	Wing dihedral angle	[$degree$]
Λ	Wing sweep angle	[$degree$]
μ	Absolute viscosity or Friction coefficient	[$Pa.s$ or $-$]
μ_g	Aircraft mass ratio	[$-$]
ν	Poisson's ratio	[$-$]
ϕ	Mass per area	[kg/m^2]
π	Ratio of a circle's circumference to its diameter	[$-$]
ρ	Density	[kg/m^3]
ρ_0	Air density at sea level	[kg/m^3]
ρ_∞	Air flow density in the free-stream region	[kg/m^3]
σ	Normal stress	[Pa]
τ	Stall torque or Shear stress	[Nm or Pa]
ω	Angular velocity	[rad/s]

Subscripts

0	Centre point
1,2	Force components
ave	Average, arithmetic mean
c	Compression (stress)
f	Final
i	Initial or Iteration number or Spanwise section number
lam	Laminated composite
L	Lower surface tangent point
max	Maximum
min	Minimum
misc	Miscellaneous
ref	Reference data
struct	Structure
sys	Wing actuation system
t	Tensile (stress)
U	Upper surface tangent point
x,y,z	Cartesian system coordinates

Chapter 1

Introduction

1.1 Motivation

The aeronautical industry, as many other worldwide sectors, is experiencing a restructuring process being increasing efficiency and productivity levels, the goals required to meet the challenges of the twenty-first century market demands. Advances in propulsion systems, aerodynamic surfaces as well as in aircraft's structures have been held in order to decrease fuel consumption, operation noise and manufacturing and maintenance requirements. A continuing search for design methods pointing towards optimizing flight overall efficiency, together with progress in material and manufacturing technologies, renewed interests in unconventional design solutions for aircraft future demands. In line with several other unconventional designs, the development of morphing wing technologies for in-flight adaptation is one of the richest and challenging interdisciplinary fields researchers have focused in recent years.

Morphing is a concept in the field of aircraft design that has born from the word "morphology" and characterizes the ability of an aircraft to acquire in-flight adaptability at different flight regimes/conditions, by modifying the geometry and/or size of one or more aircraft components. The ability to perform aircraft shape change is highly desirable as advances in these technologies enable new design approaches that can potentially benefit an aircraft on achieving:

- Increased aircraft overall energy efficiency in a multi-task mission;
- Better aerodynamic performance (range and endurance, for example);
- Extended manoeuvrability (flight envelope stretches); and
- Mission flexibility, i.e. to perform different missions with same platform.

From an aerodynamics perspective, the overall shape of wing and aerofoil(s) is of paramount importance in aircraft design. There is usually a single ideal geometrical configuration suitable for each specific type of mission or operation condition [8]. Therefore, a non-morphing aircraft is highly efficient at some design flight conditions while it becomes less fitted in others. For aircraft such as airliners, this is not necessarily a problem, since the cruise condition so heavily dominates a typical mission. However, other aircraft such as UAVs, may be expected to perform well at a wide range of flight conditions. Morphing wing technologies may be a solution to this problem as they allow wings to be high performing during distinct missions and enable new multi-role mission that are not possible with a conventional fixed wing concept, as demonstrated by Tidwell et al. [9].

Although many interesting concepts have been synthesized, few have progressed to wing tunnel testing, and even fewer have ever flown. The first motivation behind the present work lies in the desire to design a variable-span wing of the telescopic type, as an improvement of previous versions for a new remotely piloted aircraft system (RPAS), called Olharapo III, under development

at the Aerospace Sciences Department (DCA) of University of Beira Interior (UBI). Wing loading distribution and wing-root bending moments can vary considerably due to span variation, thus aerodynamic, structural and control characteristics of the vehicle should be investigated in the design of such telescopic concept. Accordingly, Olharapo III wing design is to be performed with a focus on aerodynamic and structural analysis and optimisation.

Morphing wing technologies for flight regime adaptation may become important for aircraft's operations in near-optimal overall flight efficiency point. However, as these technologies are still recent and lack adequate maturity, morphing concepts typically present actuation challenges and an undesired mass increase due to their inherent complexity both in the load carrying structure and in the systems that perform morphing. Mass growth is also interrelated with current control systems, where distributed approaches would be more suited for morphing than the actual centralized approach [10]. Apart from the increased complexity of compliant morphing structures, increases in aircraft's mass can significantly reduce or eliminate the benefits of the morphing aircraft.

Efforts that are currently in progress to optimally size morphing aircraft and investigate its benefits upon conventional concepts are critically dependent on a prediction of the aircraft's empty weight. Since no prior experimental or empirical data exists for morphing components, simple estimates based on conventional data are used to predict morphing components' empty weight. Although these estimates are based on seemingly reasonable assumptions, there is no guarantee that the prediction is accurate and any sizing results must be approached with some scepticism. Clearly, a credible mass equation for morphing structures would more rigorously substantiate morphing aircraft structure studies – particularly the impact of new morphing technologies on the aircraft as a system.

Wing weight estimative methods are indispensable in the design process due to the intrinsic implications of its weight in aircraft performance. Accurate estimates for wing weight at the conceptual design phase are crucial for early compliance verification of requirements and performance trends as well as, due to its effect on the maximum take-off weight and operational empty weight, in production and operation costs [11]. Therefore, morphing wings progress, as any other ground-breaking concept, is an iterative process between design and experiment, for which weight estimates for upcoming designs are a research gap to be addressed.

Moreover, unmanned aerial systems (UAS) have great potential for testing morphing technologies due to, between other unique characteristics, the absence of direct risk to a crew, increased flexibility, decreased complexity, smaller and cheaper support infrastructures, lower safety and certification requirements, lower production and operation costs and simpler operation procedures relatively to manned aircraft. In addition, RPAS (a subset of UAS) present the advantages of UAS and include a simple remote radio-control system. All in all, due to their characteristics, RPAS concepts usually minimize the disadvantages and maximize the advantages of several research assignments which makes them highly fitted as test platforms for novel and risky concepts, as morphing approaches are. This also offers a great opportunity to showcase and test successful designs at an early stage, and to attract industry attention to develop new technologies for large-scale vehicles.

Simple yet suitably accurate mass prediction methods to aid design RPAS morphing wings at

the conceptual or preliminary design phases are seldom available in the scientific community or non-existent at all. The benefits that one morphing concept can offer over another or even over a fixed wing are thus quite difficult to assess without resorting to complicated and time consuming finite-element models (FEM) computational fluid dynamics (CFD) studies. This fact is even more evident for the more particular case of variable-span morphing wings' concepts, which have a technology readiness level (TRL) that is still very low with very few in-flight proven prototypes.

Some works have been aimed on verifying if, in a wing performance point of view, such concepts could completely substitute conventional designs. Currently, a morphing assessment software under the objectives of the European CHANGE project is under development. CHANGE project is further discussed in Section 1.2 and pretends to achieve the highest possible performance at each flight condition by continuously providing the most suited wing shape. CHANGE telescopic wing is here used as an inspiration base and proof-of-concept for the development of the current wing design. Both, this wing design and CHANGE software, would benefit with the development of an analytic function that would accurately model the increment in the wing's mass due to its telescopic morphing design.

The second motivation behind the present work is therefore, to develop a structural wing mass function and a telescopic actuation system mass function (both based on Olharapo III wing design) that summed will form an overall wing mass predicting function for upcoming designs. Moreover, the structural mass increment of a telescopic wing may be predicted by the developed structural wing mass function, when divided by a conventional wing mass function. The effects of various wing design parameters on the structural mass of a such concept may then be addressed.

1.2 CHANGE Project

CHANGE (Combined morphing assessment software using flight envelope data and mission based morphing prototype wing development) is a Collaborative Project financed under the Transport (including Aeronautics) theme of the Cooperation Programme of the 7th Framework Programme of the European Comission.[1]. The CHANGE project (Contract Number 314139) started on the 1^{st} of August 2012, with an expected duration of three years and was postponed for one extra year in 2015. The main objective of this project was to study and develop a novel morphing system which would integrate up to four different morphing mechanisms into in a single wing and to validate its in-flight performance. The preliminary selected morphing mechanisms were: camber variation, sweep variation, twist variation and span variation of the telescopic type.

The wing system, fitted in a RPAS, would take advantage of all the performance improvements achieved by adopting a wing shape configuration according to the mission requirements of each flight phase. Therefore, this project envisions to mitigate the required energy to perform a selected flight mission. Moreover, the necessary flight manoeuvres should be accomplished by the system's capacity to adapt the aircraft geometry to a better planform to perform each required manoeuvre. Such adaptation is expected to lessen the required energy and enhance flight characteristics, such as lift over drag ratio, efficiency in aerodynamic control or lower stall velocity (V_{stall}). Besides developing a RPAS prototype, it was also aimed the creation of

a software capable of rendering the most efficient morphed wing based on the information of each current flight phase. Such software focused on the basis of an eventual cognitive morphing on-board controller with autonomous control capabilities of all morphing system of the wing [1].

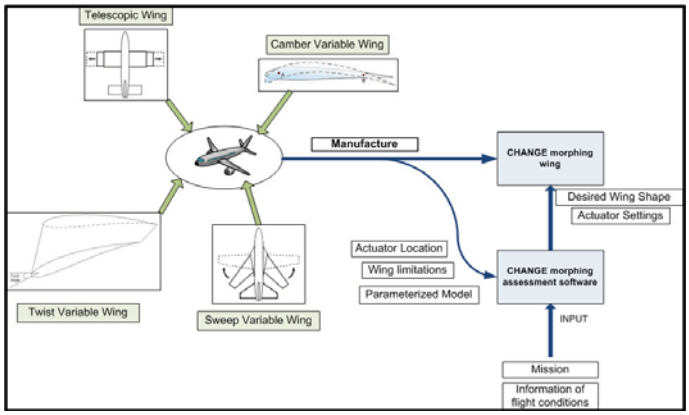

Figure 1.1: CHANGE project schematic [1].

A total of 9 partners participate in this project: TEKEVER ASDS, Deutsches Zentrum für Luft und Raumfahrt e.V. (DLR), Aircraft Research Association limited, UBI, Cranfield University, Swansea University, Innovative Verbundwerkstofferealisation und Vermarktung Neuertechnologien (INVENT), Middle East Technical University and Technische Universiteit Delft (TUDelft). The role of UBI was focused in the telescopic wing concept, its design, manufacture and validation.

In UBI, a proof-of-concept prototype, presented in Fig. 1.2, was built and on-ground tested for structural requirements compliance and actuation performance. Both leading and trailing edges were not integrated in this design as further morphing capabilities were to be added to these wing components and only after assembled to the main structure. Such morphing capabilities were investigated by project partners. Bench tests, performed to evaluate wing under load, showed that the system was capable of performing the required extension/retraction cycles and was suitable to be installed on a small RPAS prototype.

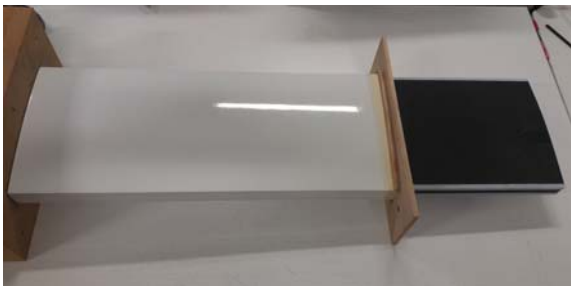

Figure 1.2: On-ground proof-of-concept of the telescopic functionality.

Figure 1.3: Olharapo II fitted with the VSW concept from CHANGE technology proceedings.

Soon after, a telescopic wing prototype, presented in Figure 1.3, was also developed in UBI for in-flight tests. This variable-span wing was intended to provide high lift flight efficiency in an extended operational speed range by modifying the wing span to the flight speed, symmetrically for lift adaptability and asymmetrically for rolling control. In-house developments of such a concept have already proven successful, with some published references as in Gamboa et al. [12], Mestrinho et al. [13], Felício et al. [14] and in Gamboa and Santos [15].

To perform such tests on the employed technology, the telescopic wing was based on an in-house developed RPAS, called Olharapo. This experimental RPAS was previously developed in the Aerospace Sciences Department of UBI and its airframe was modified and instrumented to serve as a suitable test bed aimed to investigate the operation performance enhancements on using a telescopic wing rather than a conventional fixed wing. Accordingly, it was purposely designed to enable both conventional fixed wings and telescopic wings. In addiction, along with these developments, an in-house implemented optimisation software employing a multidisciplinary and multilevel aircraft design methodology was used to optimally design the Olharapo RPAS as well as the telescopic morphing wing. Further details on the CHANGE project and resulting publications may be found on the project page [1].

1.2.1 Olharapo III RPAS

Olharapo III system is under design by a team of students with the support of the PhD student, Pedro Santos, and the supervision of the professor, Dr. Pedro Gamboa. The PhD student, Pedro Albuquerque is in charge of the multidisciplinary optimisation software for the aircraft and wings sizing as a function of the required mission, Ricardo Sousa is in charge of the RPAS airframe design fitted with a conventional, fixed wing (FW) and the author of the current thesis is in charge of the telescopic type morphing wing design. Such telescopic wing is hereinafter referred as to variable-span wing (VSW).

1.2.1.1 Design Background

Olharapo III RPAS is the third version of an in-house design with some modifications and a geometrical resize of previous versions which are detailed in [16]. Olharapo I was the first RPAS version of such concept and was capable of operating from about the stall speed of 11 m/s to 40 m/s. It was a high-wing pusher aircraft and the propulsion system uses an electric brushless motor with 750W. The motor was integrated between the end of the fuselage body and the beginning of the tailcone. The propeller was located in the in the end of a V-tail, connected to the motor by a transmission shaft. The maximum take-off weight of the aircraft (MTOW) was 60 N.The RPAS length was 1.54 m and the original (non-morphing) wing had a 2.5 m wingspan (b), a constant chord (c) of 0.25 m across the span and a wing planform area (S) of 0.625 m^2.

Olharapo II is the successor of Olharapo I. It was in all similar to the first version, although the V-tail shape was replaced by a H-tail design, as it was understood that such shape would benefit the aircraft controllability. In a V-tail concept, the yaw control is connected to the pitch control. In a H-tail design these are disconnected hence enabling a more reliable and efficient control as a failure by mixing both controls is avoided. Moreover, design parameters are easier to size for control effectiveness in a H-tail concept. This RPAS version was fitted with flight data acquisition, telemetry and first-person view (FPV) capabilities. Amongst other airborne systems, two electric motor's batteries (LiPo 3S 10Ah), a control systems battery (LiPo 3S 5Ah), NiMh backup batteries, a long range receiver, a Pixhawk autopilot, a real-time video transmitter, a motor electronic speed controller (ESC), a telemetry transceiver, a FPV video camera with pan and tilt motion, a microphone and circular polarised antennas are used. The ground control station integrates a video receiver, a LCD screen, a digital video recorder, two battery voltage checkers, a power module and two LiPo batteries that sustain more than 12 hours of operation. A long range radio control system, a heliaxial high directivity antenna and

an additional laptop for the GPS signal and RPAS position recording are used.

Figure 1.4: Olharapo II fitted with the FW.

Figure 1.5: RPAS ground control systems.

Olharapo I and II performed multiple successful flights either with the VSW and the FW. By using the same platform and switching between either the VSW and the FW when performing a typical mission, these prototypes were able to measure under identical conditions the performance advantages of the morphing to the conventional concept. In-flight performance data was generated and comparatively analysed. Although aerodynamic and structural analysis were performed during the development of these wings, the VSW design was mission-optimised whereas the design of the conventional fixed wing was not. Alternatively, it was designed to have same geometric characteristics as the VSW for an even comparison, as shown in Figure 1.4. Figure 1.5 shows the RPAS complete ground system which integrates (from left to right on the image): FPV control station, GPS positioning and telemetry station. Olharapo III is fitted with the VSW on the background of this image. For a more realistic concepts comparison, it was later considered that the telescopic concept would only proof its advantages if both wings were mission-optimised, taking in consideration its inherent constraints only. Such methodology is to be now implemented in the third version of these wings design.

The necessity of the current third version of Olharapo RPAS came to broad the applications range of the telescopic technology. Olharapo III shares the same design features that were important to the success of the previous test flight campaigns, namely high wing positioning and H-tail configuration. One differentiating key aspect is that Olharapo III is to be designed heavier than its predecessor, in order to allow higher payload. Accordingly, the design MTOW has increased to 150 N. The higher payload is important to allow more and better instrumentation and also to allow more batteries to extend the flight time. The propulsion system is a pusher type, but the electric motor is now to be installed in the end of the tail cone, i.e. no transmission shaft. This is expected to increases propulsion system efficiency, as well as, reducing weight and complexity. The center of gravity (CG) is surely affected but locating the high wing a little further back should not be a problem to balance it.

1.2.1.2 Mission Profile

Olharapo III RPAS should be capable of operating in the same range of speeds as with the original wing, from about the stall speed of 14m/s to 30m/s. Figure 1.6 shows the mission profile to take into account in the design of Olharapo III.

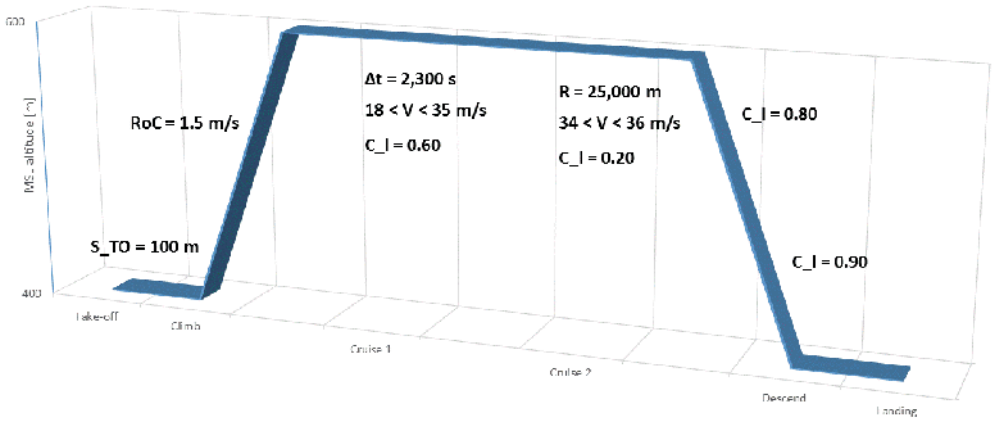

Figure 1.6: Olharapo III mission profile.

As illustrated in Figure 1.6 and considering ISA conditions, the mission profile encloses the following requirements at each flight phase:

1. Take-off at an altitude of h=400m, with a take-off distance of d_{TO}=100m and a safety speed to stall speed ratio of V_2/V_{stall}=1.150;
2. Climb from h_i=400m to h_f=600m, with a rate of climb of RoC=1.5m/s;
3. Cruise 1 during a timespan of Δt=2,300s, with C_l=0.60, h=600m and cruise velocity (V_c) comprised between V_{min}=18.0m/s and V_{max}=35.0m/s;
4. Cruise 2 for a range of R=25,000m, with C_l=0.20, h=600m and loiter velocity V_l comprised between V_{min}=34.0m/s and V_{max}=36.0m/s; and
5. Descent from h_i=600m to h_f=400m, with C_l values from C_{l_i}=0.80 to C_{l_f}=0.90, respectively.

Cruise 1 may be seen as a loiter cruise and cruise 2 is a high-speed cruise. One may notice that the difference between V_{min} in cruise 1 and V_{min} in cruise 2 is considerably high. Such mission requires an enlarged flight envelope that would be easier to obtain using an in-flight adaptable wing geometry. Compared to conventional aircraft, morphing aircraft become more competitive as how different missions are and as more mission tasks are added to their requirements. It is assumed in Figure 1.6 that V_2 is equal to the lift-off speed (V_{LO}.

1.2.1.3 Technical Specifications

Olharapo III main specifications are identified in Table 1.1.

Table 1.1: Main specifications of Olharapo III RPAS.

FW Parameters	Values	Platform and Systems	Values
b	3.1 m	MTOW	150 N
x_{kink}	0.6 m	Fuselage length	2.07 m
Γ_{LE}	0°	Fuselage width	0.225 m
$\Gamma_{LE,kink}$	9°	Electric motor	Scorpion SII-4025-520 KV
c_a	0.284 m	Propeller	Aeronaut CAM Carbon 15x10”
c_{root}	0.33 m	Batteries	LiPo 6s2p 24 Ah
c_{tip}	0.18 m	Autopilot	Pixhawk

Wing geometrical parameters presented in Table 1.1 were obtained from a optimisation procedure further detailed in Chapter 3. x_{kink} is the spanwise kink location and $\Gamma_{LE,kink}$ the leading edge dihedral after the kink. c_a, c_{root} and c_{tip} are the aerodynamic, root and tip chords, respectively. Fig 1.7 shows a preliminary CAD design of the RPAS fitted with the FW.

Figure 1.7: Preliminary CAD design of Olharapo III RPAS.

The H-tail has a horizontal stabilizer of 0.597 m span and 0.149 m chord, and two vertical stabilizers of 0.229 m span and 0.152 m chord each. Olharapo III undercarriage is a non-retractable landing gear in a tricycle arrangement. Landing gear main strut is made of laminated carbon-epoxy composite and wheels use rubber tires. The nose gear has an integrated damper whereas the main gear has an inverted V-shape and supports landing impacts by deflection of the carbon material.

The FW is composed by a rectangular centre portion and tapered wing tip sections. It was optimized separately to the morphing wing so that it could take advantage of its design space without the morphing wing design inherent constraints, thus enabling a ensuing fair comparison between concepts' performance. The optimisation goal was to minimize drag in a range of velocities between 18m/s and 30m/s, for a MTOW of 140 N, guaranteeing a V_{stall} below 13.5 m/s and keeping the trailing edge (TE) straight. The MTOW here is 10 N below Olharapo III design MTOW to account for the expected decreased weight of the FW in relation to the VSW concept. Whereas design requirements for the VSW will be described later on Chapter 3, FW's design requirements are:

1. High $C_{l_{max}}$, between 1.6 and 1.8;
2. High L/D, not smaller than 80;
3. Low C_d during cruise; and
4. Aerofoil thickness to chord ratio t/c with values between 10% and 13%.

The FW geometry, defined for each semi-span section, is presented in Table 1.2. It includes the wing's c, sweep angle (Λ), twist angle (ε) and dihedral angle ($Gamma$). Each wing position is the distance measured from the wing root (y'). The FW has a wingspan of 2.84 m, a mean chord ($\bar{c}$) of 0.284 m and a wing wetted area (S_{wetted}) of 0.8804 m^2. Its optimum wing incidence angle (θ) is 0.83°. FW's V_{stall}, take-off speed (V_{TO}) and take-off distance (d_{TO}) are 13.4 m/s, 16.4 m/s and 99.2 m, respectively. The aerofoil used in the FW is UBI_O3_16, an in-house optimised

aerofoil for its specific flight condition. Moreover, the aerofoil used in the aircraft's H-tail is NACA 0010.

Table 1.2: Olharapo III FW geometry.

y' [m]	Chord [m]	Λ [degrees]	ε [degrees]	Γ [degrees]
0.00	0.332	0.0	0.0	0.0
0.60	0.332	0.0	0.0	0.0/3.2
1.55	0.180	-1.6	-0.53	3.2

1.3 Scope of the Current Study

1.3.1 Object and Main Objectives

The object of the current dissertation is a variable-span morphing wing of the telescopic type. The main objectives are two and may be summed up as to firstly, design such a wing and secondly, derive a mass function for this morphing concept and evaluate the effect of design parameters on wing structural mass. Each of these two main goals may be divided into some sub-objectives.

The morphing wing design may be divided into eight sub-objectives, which together complete the wing conceptual and preliminary design phases. The first is to define the wing layout, by understanding the technology constraints and geometric correlations. The second is to define an adequate structural concept and the materials to be employed. Here, the challenge is to design a structure that is capable of withstanding the prescribed loads while it is also able to change its shape. The third sub-objective is to perform an aerofoil design and performance analysis. The fourth is to design and size an actuation system which should enable wing shape change. The fifth sub-objective is to evaluate the wing loading and the sixth is to perform a wing structural analysis and optimisation to size key components of the wing structure. The seventh sub-objective is to document wing overall characteristics and the eighth and final sub-objective is to draw a Computer Assisted Design (CAD) of the developed wing and document the respective technical drawing.

The second main objective is to derive a wing mass predicting function for wings employing telescopic technology. Its corresponding first sub-objective is to use the previously designed wing as a baseline wing to develop a parametric study. The second is to integrate a FEM analysis and optimisation methodology into the parametric study and obtain a mass value for each dataset of the parametric study. The third is to to obtain empirical, multi-parameter structural mass functions by performing data fitting with the resulting parametric study databases. The fourth is to investigate the effects of several design parameters on the structural mass of a variable-span morphing wing. The fifth is similar to the fourth but focused in the wing mass penalty of such concept, i.e. to non-dimensional wing mass results that are scaled relatively to a conventional wing concept. The sixth, last sub-objective is to define a new full wing mass function by adding mass contributions for secondary structural components and non-structural components as the actuation system.

Beyond to aid the design of the telescopic wing, this final overall mass predicting function has the goal of extending morphing wings design literature in the conceptual and preliminary phases by generating a mathematical equation that would explain the trade-off between the effects of each design parameter on the final overall wing mass. In sum, the goals of this study is to present a detailed guide on a morphing wing design as well as to develop a mass predicting function that any student or engineer could easily and in a short period of time, employ in future telescopic wing designs.

1.3.2 Interests and Applicability

The preliminary interest of this work is to qualify an aircraft in performing a range of missions with different speeds and altitudes, levels of agility and manoeuvrability. Wings with large spans have good range and fuel efficiency, but lack manoeuvrability and have relatively low cruise speeds. By contrast, aircraft with low aspect ratio wings can fly faster and become more manoeuvrable, but show poor aerodynamic efficiency. Shape adaptable wings have the potential to integrate into a single aircraft the advantages of both designs by increasing the aircraft flight envelope [17]. In fact, an aircraft with the capability to adapt itself to each given situation present is prone to achieve greater efficiency, versatility and performance in multi-mission operation instead of requiring a specific aircraft to conduct one specific mission [18]. Therefore, the study applicability rests in morphing wing technology for multi-role missions, in particular the design of a variable-span wing, a type of wing morphing.

In order to demonstrate the profitability of morphing wing concepts among many morphing wing concepts developed at present time, the choice has been to assess the advantages of using a variable span wing compared to a fixed wing. This choice has been based on two fundamental reasons. Firstly, this is clearly one of the morphing wing solutions that produces most significant performance impacts as the lifting surface area and aspect ratio are design parameters of paramount relevance. Increasing the wing span increases the aspect ratio and wing area and decreases the spanwise lift distribution for the same lift. Thus, the drag of the wing can be decreased, and consequently, the range or endurance of the vehicle increases. Secondly, the fact that previous in-house developments of such a concept have already proven successful, further supported this choice.

However, the sensitivity of the performance benefits to a range of mass penalties associated with span morphing should be considered. For a specific wing layout and size, to know wing's mass with an acceptable accurateness in early design phases is essential to guarantee improved overall variable-span wing performance over a lighter conventional fixed wing. A purposely developed mass predicting function for morphing wing structures would more rigorously substantiate morphing aircraft studies, particularly the impact of such morphing technologies on the aircraft as a system. Therefore, another interest of this work is to understand mass penalties in a morphing wing design and provide the CHANGE software as well as future telescopic wing designs, with analytical functions that would more accurately model the wing's mass of a particular morphing design under development.

1.4 Dissertation Outline

This thesis is structured in six chapters, all of which essentially address to the objectives detailed in Section 1.3. In the current chapter, the author expresses his motivation behind the development of this thesis. Here, the benefits of a morphing technology and its technological application challenges are presented. The European project in which this topic of study is inspired is briefly presented and RPAS in-house developed and with morphing capability are introduced. Finally, the objectives proposed for this dissertation are presented, corresponding interests and applicability.

A bibliographic review is summarised in Chapter 2, with a historical background on morphing wings in order to understand the challenges and concerns that appeared throughout the time on their development. More recent developed breakthroughs are also investigated, with a focus on span morphing. Types of mass models, both for conventional and morphing wings, are researched with higher incidence on methods which are applicable for early design phases. Moreover, parametric study methodologies and types of data-fitting regression are presented.

The third chapter addresses the conceptual and preliminary design phases of a telescopic wing suited for a RPAS. Design requirements and the selected morphing concept is detailed. Wing geometry, aerodynamic and structural concepts are detailed. Aerofoils and wing panels are characterised for performance and layout, considering the restrictions inherent to telescopic concepts. Wing is sized based on an in-house developed multidisciplinary design optimisation. Materials are selected based on its properties for the wing structure and the actuation system. CAD technical drawings are performed. Finally, a wing loading analysis is conducted and results analysed.

The fourth chapter presents all numerical results obtained in the course of a finite-element analysis (FEA) and optimisation procedure to size the VSW to a minimum-mass design point. A mesh convergence study is presented. Wing structural characteristics and resulting structural mass achieved after the optimisation procedure are detailed. Moreover, numerical model errors are discussed.

Chapter five details the work done regarding the methodology employed and the results achieved during the development of a wing mass function for morphing wings design, in particular of the telescopic type. Design of experiment (DoE) simulations are performed where several parameters are varied to investigate the sensitivity of the mass solution to the design parameters. A grid of design parameters is created, an objective function is defined and the DoE simulation is run using a FEM-based optimisation procedure. A regression model is used to generate mass polynomials and data fitting accuracy is analysed. A discussion on the effects of design parameters in the wing structural mass is presented. Moreover, a preliminary full VSW mass predicting function is developed.

The sixth and last chapter contemplates the dissertation synthesis, final considerations and the prospects for future work in this matter.

Chapter 2

Literature Review

The current chapter is aimed to investigate past and state of the art solutions for morphing wings, predicting mass models for early design phases and regression analysis.

2.1 Historical Background on Morphing Wings Design

Morphing is short for metamorphose and in the aeronautical field various definitions coexist for morphing aircraft. Generically, morphing aircraft or polymorphous aircraft is the terminology adopted for air-vehicles that allow shape variation. Weisshaar [5] defines it as ”a set of technologies that increase a vehicle’s performance by manipulating certain characteristics to better match the vehicle state to the environment and task at hand”. On the other hand, NATO *RTO Technical Team on Morphing Vehicles* suggested that ”morphing is the real-time adaptation to enable multi-point optimized performance” [19].

A more detailed definition was provided by *DARPA Morphing Aircraft Structures* (MAS) program. According to Seigler [20], the MAS program defines the morphing aircraft as ”a multirole platform that changes its state substantially to adapt to changing mission environments, provides superior system capability not possible without reconfiguration, and uses a design that integrates innovative combinations of advanced materials, actuators, flow controllers, and mechanisms to achieve the state change”. Such definitions consider conventional mechanisms as flaps, slats and retractable landing gears as being morphing. However, many researchers believe that the morphing concept carries a connotation for radical shape changes or shape changes only possible with near-term or futuristic technologies [21]. In fact, a consensual general definition or even the extent of geometrical changes necessary to qualify an aircraft as a morphing vehicle, have not reached an agreement between researchers.

Morphing may be useful in several components of an aircraft, such as the fuselage (variable incidence noses, for instance), wings, stabilizers, control surfaces, various fairings, landing gear, propulsion system, etc. However, much of the emphasis has been on morphing wings, since these are the primary lift source of an aircraft and hence morphing has the most effect. Moreover, concepts developed for wings maybe readily utilized for similarly shaped profiles as for example horizontal and vertical stabilizers, rotary wing aircraft blades or wind turbine blades.

Historically, the morphing wing concept is as old as the wing itself [22]. The Wright brothers’ Flyer launched in 1903 was controlled partially through the use of a morphing concept called wing warping. They used Inspired by nature, they observed the flight of turkey buzzard and designed a series of pulleys and cables that twisted the wing to change directions [23]. In fact, even before the official beginning of controlled human flight in 1903, radical shape changing aircraft appeared and then disappeared, contributing little to aviation [5]. The reason for

the disappearance of morphing was the increased need for larger structural rigidity as higher airspeeds were achieved. Clement Ader conducted flight experiments in France as early as 1873 and proposed a wing morphing design as early as 1890. [24]. The first experiments with in-flight variable geometry were allegedly conducted in 1911 in France, although no record survives. In April 1914 Edson F. Gallaudet of Norwich, Connecticut applied for a patent for a “variable skewed” wing and was granted the patent in October 1916 [25]. This configuration was intended to improve controllability and variable sweep as an alternative to ailerons.

Aircraft morphing concepts, which initially have been only applied for aircraft control purposes, were only later extended to perform aircraft shape changes when it was recognized that geometry and size modifications could benefit aircraft aerodynamic performance and extend its flight envelope for off-design flight conditions. Many recent developments have focused on design methods pointing towards optimising flight overall efficiency together with progress in materials, smart structures and manufacturing technologies. The potential of enhancing aircraft performance and increasing energy efficiency with morphing led to a resurgence of interest in unconventional design solutions, with more substantial shape changes, for aircraft future demands [26].

In line with several other unconventional designs, the development of morphing wing technologies for inflight adaptation is one of the richest and challenging interdisciplinary fields researchers have focused in recent years. Joshi et al. [2] demonstrated the impact of a morphing wing on aircraft performance and provided a method to compare various morphing strategies using a ”spider plot”.

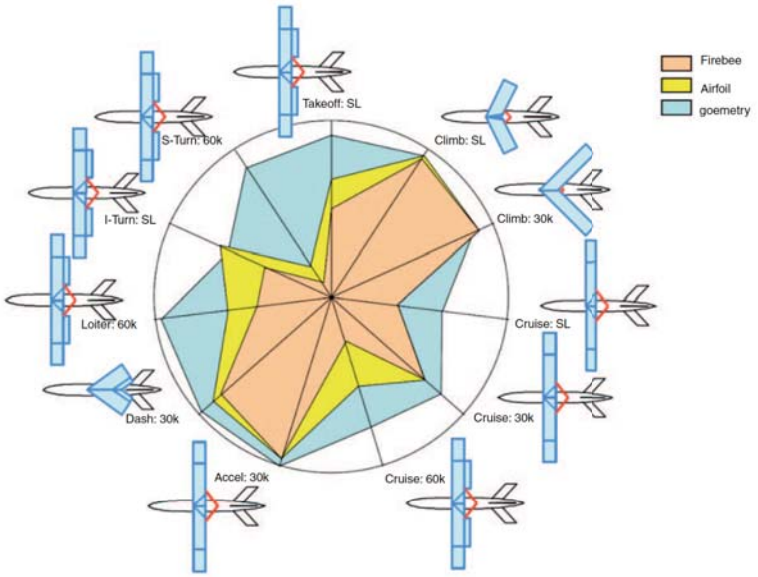

Figure 2.1: Spider plot comparing predicted performance of the baseline Firebee, a morphing aerofoil Firebee and a morphing planform Firebee [2].

In Figure 2.1, a spider plot was proposed for Firebee, a morphing-capable system. The performance of the conventional fixed geometry Firebee is represented in the plot inner most area, followed by an aircraft suited with Firebee’s aerofoil morphing capabilities and the outermost shaded area represents the performance of a Firebee sized aircraft with a wing capable of telescoping, chord extension and variable sweep. The aircraft performance is significantly improved

moving outward from the center. The aerofoil morphing provides some notable improvements in performance, particularly in the phases of flight for which the original Firebee is not well suited as for high altitude flight. Moreover, the best performing wing configuration for each flight phase is illustrated around the spider plot limits. By resorting to this plot, it is possible to conclude that advances in morphing technologies, by considering shape modifications, enable new design approaches and improvements in multi-task flexibility.

Figure 2.2: NASA's Active Aeroelastic Wing F/A-18 [3].

In the 1980s, NASA launched two research programs dedicated to morphing structures with the Active Flexible Wing program [27] and its Mission Adaptive Wing program [28]. This research effort was followed by several research programs in the 1990s and 2000s in the USA [19]: the Smart Materials and Structures Demonstration program, the Aircraft Morphing program, the Active Aeroelastic Wing program (see Figure 2.2) and the Morphing Aircraft Structures program. This was followed by the Smart Wing Program, a joint DARPA, AFRL and NASA venture to use smart materials and structures [3]. More recently, a bio-inspired aircraft concept, illustrated in Figure 2.3, with adaptive skins and structures was designed in NASA Dryden Flight Research Center. With a bone-and-muscle-like wing structure beneath flexible skin, this concept for a morphing aircraft mimics bird flight behavior though not flapping. An Institute for Biologically Inspired Materials was established to investigate and design materials that mimic the extraordinary structural and self-repairing properties of biological substances such as bone or sea shells. NASA predicts that such concept will fly by 2030.

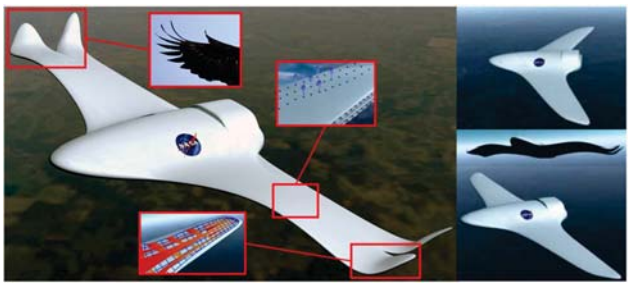

Figure 2.3: NASA's Bio-inspired morphing aircraft concept.

Figure 2.4: Ultra-light composite cellular material morphing wing prototype [4].

In 2016, the Mission Adaptive Digital Composite Aerostructure Technologies (MADCAT) team at

NASA's Ames Research Center, in collaboration with students from the Massachusetts Institute of Technology (MIT) and several other universities, used emerging composite materials and manufacturing methods to build and demonstrate an ultra-light wing that actively changes shape. The wing is constructed from building-block units made of advanced carbon fibre composite materials so that wings twist and move independently of each other, as seen in Figure 2.4, eliminating the need for wing flaps and ailerons.

DARPA's Morphing Aircraft Structures (MAS) Program, currently managed by Dr. Terry Weisshaar, "will provide and integrate enabling technologies required to design, build, and demonstrate aerodynamically efficient, shape-changing, morphing wings to provide optimal, uncompromised performance during complex military missions" [29]. DARPA's MAS program has been funding proof-of-concept projects with three contractors from 2012: Lockheed-Martin, Raytheon Missile Systems and Hypercomp/NextGen Aeronautics. All three MAS contractors adopted a systems approach and conducted a functional analysis that concluded that changing wing planform area (to allow a wide range of wing loadings in flight) and wing span were the primary enablers of a new class of morphing air vehicles [30].

Fig 2.5 shows the Lockheed-Martin design in its morphed and unmorphed configurations. Additionally, Fig 2.6 presents an interesting detail on the folding actuation mechanism and how the bottom smart material bends in compliance with the hinge geometry. This innovative design "hides" a substantial portion of the wing area during the low altitude, transonic dash portion of its mission. It requires substantial use of advanced skin materials to maintain surface smoothness for aerodynamic efficiency when the wing folds in flight [31].

Figure 2.5: Lockheed-Martin Agile Hunter morphing design [5].

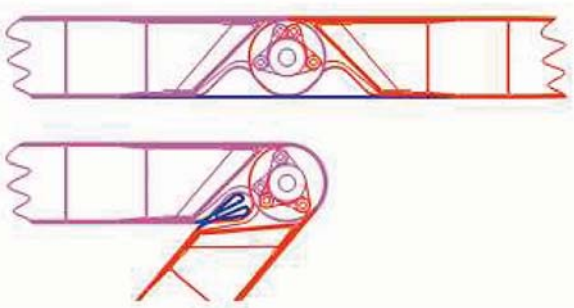

Figure 2.6: Lockheed-Martin elastomeric skin and joint design [6].

Figure 2.7 shows the Raytheon telescoping wing design in its morphed and unmorphed configurations. This design addresses a unique challenge since the wing loading is high and the available volume for actuators and support structure is small. An interview by Marks [23] to Dr. Terry Weisshaar, reveals that Raytheon is currently looking at telescopic wings and that full-capability telescopic wings may be in the skies by 2020-2030.

The Hypercomp/NextGen design, shown in Figures 2.8 and 2.9, used substantial in-plane shape

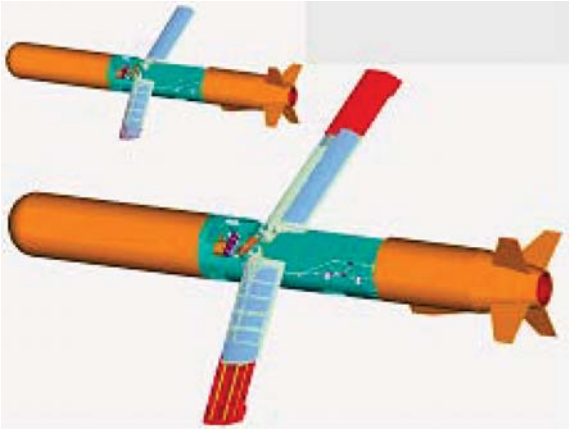

Figure 2.7: Raytheon morphing wing design [5].

changes and surface area reduction to transform the wing from an efficient, high-aspect-ratio loiter shape to an efficient, swept, reduced-wing-area transonic, low altitude dash shape. Inspired in previous industry-leading projects, further studies are continuasly being employed by researchers. One such example is presented in Johnson et al. [32] where a nonlinear analysis and two-stage design optimization of a diamond cell morphing wing, similar to NextGen's batwing concept, is developed. Results from a finite element model that considered elastic skin, actuator and aerodynamic loads, showed that placement and position optimization produce small gains in energy efficiency. In this line, researchers are committing a huge effort to develop efficient and reliable morphing aircraft systems.

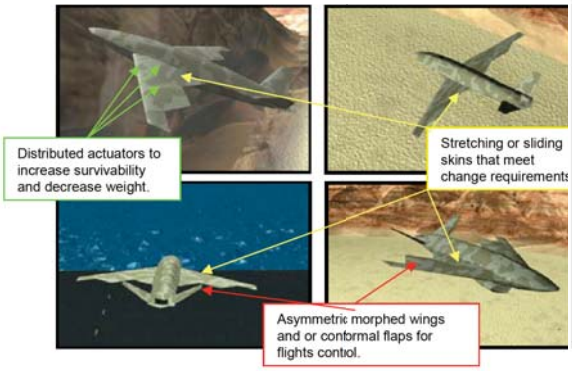

Figure 2.8: NextGen morphing design [5].

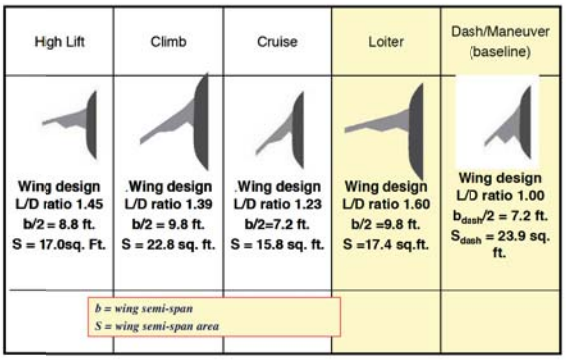

Figure 2.9: NextGen morphing wing planform configurations [6].

The European Union has also funded several research programs since 2002, including the Active Aeroelastic Aircraft Structures (3AS) project, the Aircraft Wing Advanced Technology Operations (AWIATOR) project, the New Aircraft Concepts Research (NACRE) project, the Smart Fixed Wing Aircraft (SFWA) project, the Smart Intelligent Aircraft Structures (SARISTU) project, the Novel Air Vehicle Configurations (NOVEMOR) project and the CHANGE project.

In 2004, Jha and Kudva [33] tried to summaryse morphing aircraft concepts, classifications and challenges. Moreover, a survey has been conducted in 2007 by Rodriguez [3] to organize the many contrasting projects, concepts and technologies of morphing aircraft. Although many interesting concepts have been synthesized, few have progressed to wing tunnel testing, and even fewer have flown. A more extensive review on concepts which thrived to be functional in flight, for both fixed-wing and rotary-wing aircraft, is given in Barbarino et al. [34]. Current challenges

upon morphing vehicle design are the additional weight and complexity, the power consumption of the required actuation concepts and the development of structural mechanization concepts covered by flexible skins. Additionally, there is a strong need to understand the scalability of morphing wing concepts to achieve sufficient structural stiffness, robust aero-elastic designs, and an adequate flight control law to handle the changing aerodynamic and inertia characteristics of morphing vehicles [35].

2.1.1 Out-of-plane Shape Morphing

Methods of wing morphing can be classified as planform shape morphing, out-of-plane shape morphing or aerofoil adjustment. Out-of-plane shape morphing is mainly affected by three wing parameters, either individually or combined: wing twist, dihedral and span-wise bending. Out-of-plane shape morphing has been highly dependent on the materials applied and respective properties. Continuing developments on smart materials are increasing the potential of morphing these parameters. Varying the twist distribution of the wing enhances flight performance and control authority of the aeroplane. Wing twist morphing has been historically targeted of a more extensive research.

As reference, some works may be cited from literature. Wright Brothers employed the wing warping technique to change the twist of a flexible wing and provide roll control for their first flying machine [36]. Rodrigue et al. [37] developed a cross-shaped twisting structure using smart soft composite based on shape memory alloys (SMA). Mistry et al. [38] examined a warp-induced twist concept to obtain quasi-static large amplitude twist changes of helicopter or tiltrotor blades. Smart structures were used for a active twist prototype. Experimental measurements correlated well with a FEM implemented to access actuation requirements and the effect of structural parameters on the system behaviour.

One of the first applications of variable dihedral wings was the IS-1 fighter, designed by Nikitin-Shevchenko in 1932, morphed out-of-plane from a bi-plane to a monoplane that was to operate at high speed. Most of the lower wing folded into the fuselage to reduce the wetted area to create a design that resembled a monoplane with a small canard surface [34]. By varying the dihedral, one may control the aerodynamic span, replace conventional control surfaces, enhance the flight characteristics of high-performance aircraft; reduce the induced drag (by changing the vorticity distribution) and improve stall characteristics. However, it was only recently due to innovative material research, that variable dihedral wings have aroused more interest to enhance aircraft performance and flight control.

Span-wise bending morphing is also a biologically inspired out-of-plane shape morphing solution. Manzo [39] investigated two approaches to allow shape morphing of a furled continuous hyper elliptic cambered span wing, a concept developed by NASA researchers. A similar approach, documented in Galantai et al. [40], used a morphing wing concept where the wing could continuously flex laterally.

2.1.2 Planform Shape Morphing

Planform shape morphing include shape modification mainly in three wing parameters: span, chord and sweep. These parameters can affect the wing aspect ratio, which modifies the lift-

to-drag ratio. Thus, an increase in wing aspect ratio would result in an increase in both range and endurance [41]. Modifications in chord and span also produce differences in aerodynamic forces due to wing area change. Planform shape morphing has been the morphing type with highest research investment. The reason lies in the fact that this is clearly one of the morphing wing solutions that produces most significant performance impacts as the lifting surface area and aspect ratio are design parameters of paramount relevance.

Sweep changes has been implememted since 1931, when first flew the Pterodactyl IV tailless monoplane. Its design, from G.T.R. Hill's, drew attentions to variable sweep tailless aircraft. The aeroplane had a variable sweep range between 4°and 75°, enabled by a mechanical worm and wheel arrangement driving hinged wings in-plane to change sweep angle [42]. Today's most successful military morphing wing aircraft, use variable sweep wing design. A favourable trade between increased mission effectiveness and the high weight central pivot mechanisms required to sweep the wing in-plane make it attractive from a performance perspective. MiG-23, F-14, B-1 bomber, Tupolev-22, Bell- X-5 are only some examples of modern variable geometry aircraft.

The chord length of a conventional aircraft wing is altered using leading and trailing edge flaps, usually actuated by screw systems. The added weight and complexity of the a chord morphing design are considerable disadvantages. The application of smart materials to achieve chord change has received little attention. The Cornerstone Research Group experimented to alter chord length with a lightweight dynamic modulus foam. A shape-memory polymer was proposed for the skin, to accommodate large strains, and temperature activation was realised using thin nichrome wires embedded in the skin. Although the prototype wing section was able to extend the chord upon heating, it could not return to its original shape upon cooling [43].

Span morphing is the main subject of this work. Thereby, this morphing solution is not presented in the current section, as it is going to be further discussed in Section 2.2.

2.1.3 Aerofoil Adjustment

Aerofoil adjustment is also a type of morphing. In fact, due to its pioneering implementations, aerofoil adjustment morphing has been mistakenly considered as the morphing definition itself. This morphing type is mainly affected by camber variation and thickness change. Control on wing camber, the effective curvature of an aerofoil, has been more deeply investigated rather than thickness change. The wing camber can change either on specific parts (leading or trailing edges) or in a global manner, letting the entire wing act as a unique control surface.

Airfoil morphing, and more specifically camber morphing, is the dominant research topic in subsonic aerodynamic applications when compared to the planform and out-of-plane morphing methods. An early example of camber morphing aerofoils is the 1920 design by Parker [44]. Research activity in this area elucidate that camber changes are being trendily towards compliance rather than mechanism-driven morphing. Even single mission aircraft must operate at a wide range of altitudes, weights and flight speeds. Variable camber has been shown to improve performance of several aircraft at different flight conditions. The already mentioned Mission Adaptive Wing (MAW) project from NASA, produced supercritical aerofoil camber change concepts to create optimum camber by discrete surfaces over a range of airspeeds for low subsonic to supersonic. This control was achieved by continuously smooth and deformable leading and

trailing edge deflection, using internal mechanisms to bend the chordwise shape.

Tests conducted in the 1980's used the AFTI/F-111 flight demonstrator [3]. Also, F-16 and F-18 aircraft use discrete leading edge and trailing edge flap deflections to control camber. In this line, in Gaspari and Ricci [45], the design of leading and trailing edges in optimal aerofoil-morphing design was implemented based on a compact approach to describe the aerofoil geometry coupled to a two-level optimization procedure. Many other projects used camber morphing. Marques et al. [46] design and tested a variable camber flap for improved efficiency. Strelec et al. [47] designed and implemented a shape memory alloy actuated reconfigurable aerofoil. A wind tunnel model reconfigurable wing was fabricated and the predicted structural and aerodynamic response was experimentally verified. Fincham and Friswell [48] performed an aerodynamic optimisation of a camber morphing aerofoil.

2.2 State of Art on Span Morphing Technologies

Most span morphing concepts are based on a telescopic mechanism, following Ivan Makhonine ideas of a wing with an outer panel that telescoped inside an inner panel. He began to produce several variable geometry wing designs in the 1930's. On August 1931 MAK-10 flew for the first time, hence being considered the first operative design with a telescopic wing. Makhonine's telescoping wing had three major parts that slid over each other to change the wing span and area: in operation, this aeroplane changed wing span 162% (from 13 meters to 21 meters) while the wing area changed 157% (from 21 to 33 square meters). Pneumatic actuators provided the energy for extension and contraction. [29]. A second successful variable-geometry aircraft design by Makhonine was the MAK-123, which first flown in 1947 in France and demonstrated extension retraction of telescoping wings with no adverse effects.

Bakshaev LIG-7, illustrated in Figure 2.10, is an unusual and innovative morphing aircraft with two-dimensional in-plane operation, was developed in the Soviet Union in 1937 [25]. This aircraft had a high aspect-ratio and thin wing designed for cruising flight. For take-off and landing, six broad-chord wing sections were extended from the fuselage to 2/3 of the wingspan. The telescoping wing sections were retracted and extended by tensioned steel wires, operated manually from the cockpit. All retractable sections were completely hidden inside the fuselage when retracted.

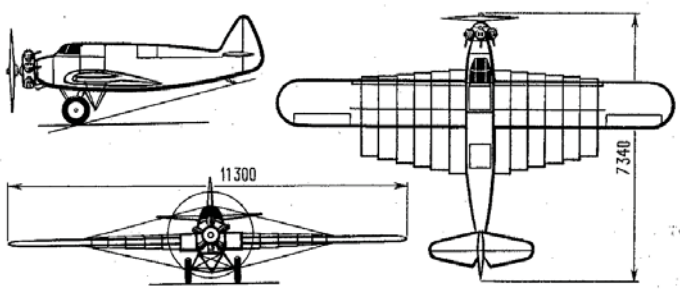

Figure 2.10: Bakshaev LIG-7 technical drawings.

As it is possible to observe from Figure 2.10, Bakshaev LIG-7 ailerons were located on the outer one-third of the wing span. During 1937, flight tests showed that wing retraction (requiring from 20 to 30 seconds) and extension (requiring from 30 to 40 seconds) was easier to perform

in-flight than it was on the ground. According to observers, the effect of morphing on take-off and landing characteristics was impressive and reliable. On the other hand, the morphing impact on performance was not as significant as for this small and slow aircraft the wing contributed only 20% of total drag.

Developments in variable-span wings have been conducted primarly for rotary wings from 1969 to 1994 [34]. A variable-span concept for non-rotary wings has been documented in 1994 by Bovais and Davidson [49], from the US Naval Research Laboratory. They built an experimental non-recoverable ship-launched expendable radar decoy named FLYRT (Flying Radar Target) that had a fully expanded rigid wing. FLYRT was first flown in September 1993, launched with rigid folded wings and tail surfaces from an MK 36 launcher.

In sailplane competitions, the quest for any measure of aeroplane superiority is highly competitive. This granted sailplained wing morphing designs to reach an early relatively high level of maturity [50]. The German, Akaflieg Stuttgart fs-29 glider, shown in Figures 2.11 and 2.12 was designed in 1976 with a telescoping wing to improve soaring performance at two different speeds, depending on whether it is in the cruise or climb mode [51]. Designers used a long circumferential belt to extend and retract outer wing panels over the inner panels. Also, camber changing flaps and water ballast were used to improve performance between flight modes.

Figure 2.11: fs-29 glider at the Deutsches Museum Flugwerft Schleißheim.

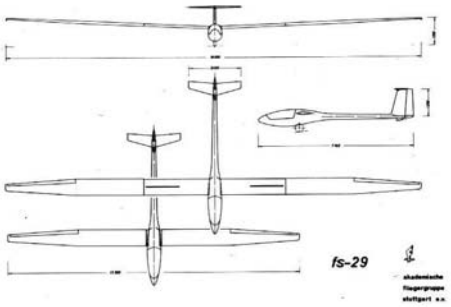

Figure 2.12: Akaflieg Stuttgart fs-29 glider technical drawings.

An detailed discussion of sailplane design and performance was presented by Thomas [52]. He believed that the key to telescopic wings success is a structure that can be contained inside a host structure and then deployed when needed. This structure, he added, ”must resist binding under load, particularly under the action of wing deflections that are relatively large for highly loaded, efficient, light-weight structures. A second requirement is power and actuators to drive the system”. The fs-29 uses pilot cranking to extend or retract the wing outer surfaces [52].

In 1997, Gevers Aircraft Inc. [53] investigated a telescopic wing to use on a six-seat amphibious aircraft. The wing was composed by a fixed center section and two extendable outer sections, using an overlapping extension spar system. In Arrison et al. [54], a performance study was conducted for a modified Delta Vortex RC aircraft suited with a telescopic wing. This wing had a sliding skin actuated by a rack and pinion system. Implemented in 2003 by Virginia Tech, this system was the first design to be operative in an UAV. The new vehicle, renamed BetaMax, could increase wingspan by 254 mm. A range increase of 19% over the conventional aircraft was predicted, allowing for the increased weight. The RC vehicle was successfully flown. In the following year, Neal et al. [55] also designed and demonstrated a variable planform UAV capable

of large wing planform changes, both in sweep and span. It was used a telescopic pneumatic actuator. The aspect ratio could change up to 131% through combined span and sweep, while wing area could change by 31%. Later on, in Neal et al. [56] redesigned the vehicle to implement a variable-geometry tail and increase the strength of structure and mechanisms.

Also in 2003/2004, Blondeau et al. [57] and Blondeau and Pines [58] discussed the design, development and testing of an inflatable lightweight telescopic wing for an UAV that could undergo a 114% change in the aspect ratio while simultaneously, supporting structural wing loads. The key element was a pressurized three segmented telescopic spar that could undergo large-scale spanwise changes. Hollow fibreglass shells were used to preserve the spanwise aerofoil geometry and ensure compact storage and deployment of the telescopic wing. Later on, Blondeau and Pines [59] developed a new prototype that could undergo a 230% change in aspect ratio. It used a concept with two telescopic spars, mechanically coupled coupled by the ribs, to prevent wing twist and fluttering. In its fully deployed condition the telescopic wing could achieve lift-to-drag ratios as high as 16, which was similar to its solid foam-core wing counterpart.

Seigler [20] investigated asymmetrical span extension for increased manoeuvrability of bank-to-turn cruise missiles. By formulating a full nonlinear model of the missile, they showed that the control authority can be significantly larger when compared to conventional tail surface control. However, it was found that improved manoeuvrability is highly dependent on angle of attack, linear actuation speed and span extension length. Also, Ajaj et al. (2012) investigated the use of asymmetric span morphing to replace conventional ailerons and provide roll control for a medium altitude long endurance (MALE) UAV. In addition, they optimised the rolling strategy to minimise drag for a steady roll manoeuvre. In the same line, Bae et al. [60] performed both static aerodynamic and aeroelastic studies on the wing of a long-range cruise missile and highlighted some of the benefits and challenges associated with span change. The total drag of the morphing wing decreased by approximately 25%, and the range increased by approximately 30%. The aeroelastic analysis showed that the flexibility of the morphing wing structure increased as the wingspan increased. At a given flight condition, the deformation from the aerodynamic loads was much larger than that of the conventional wing. Static aeroelastic considerations showed that a variable-span wing requires increased bending stiffness because the bending deformation is more significant than twist.

In 2005, the first variable-span micro-aerial vehicle (MAV) was documented by Heryawan et al. [61]. The design made use of an expandable morphing wing based on a typical bird wing. The wing was divided into two rigid parts and the outer wing was driven by a small direct current (DC) motor through reinforced composite linkages. The actuation of two lightweight piezo-composite actuators produced an additional 16% lift. In 2006, similar developments and flight testings of a batwing morphing concept with span variation were performed in the NextGen MFX-1, [26]. Later improvements, led to the design in 2007 of MFX-2, which also included sweep change.

In his master thesis, Supekar [62] evaluated the structural and aerodynamic performance of a two-segment telescopic wing for a UAV that could also undergo variable dihedral of the outer wing. Although a crude prototype was manufactured, no successful actuation of the mechanism was reported due to fabrication problems. Also in 2007 but with higher success, Han et al. [63] documented a model using telescopic wings actuated by two separate servomotors. It was

performed wind tunnel tests to study the effect of variable aspect ratio on wing-in-ground effect vehicles operating inside a channel.

The use of the telescopic concept was further investigated by Vale et al. [64], [65] and Gamboa et al. [66]. The design had a wing section capable of independent changes of span and aerofoil chord and shape by the use of extendable ribs and spars. The mechanism could expand in the span-wise direction, keeping the ribs evenly distributed, and in the cross-section direction, increasing the ribs chord.The performance achievable with such a morphing wing was compared to a conventional wing by a minimum drag analyse at different flight velocities (15 to 50 m/s). An aero-structural analysis was performed. At 30 m/s, the accomplished reduction in drag was 22.5% when compared to the non-morphing wing. The final design was too heavy due to servomotors, transmission components, and other equipments. Torque actuation requirements for the chord expansion mechanism were prohibitive. Gamboa et al. [12] proposed new structural designs for chord and span extension. In 2011, prototype results became available in the variable-span wing evaluation study detailed in Felício et al. [14] and the design optimisation presented in Mestrinho et al. [13]. Later improvements and upgraded aircraft versions have been documented in Santos et al. [16] and in Gamboa and Santos [15], including structural a analysis of the telescopic wing-box concept.

Furthermore, a large number articles were published with extensive investigation on aerodynamic shape optimization and multidisciplinary design optimization for such telescopic design concepts. In 2005 and 2006, Secanel et al. [67] used high-fidelity optimisation models. Vale et al. [68] presented in 2011 an aero-structural optimization and performance evaluation and in 2013 [69], compared energy efficiency between a fixed wing and a telescopic wing equipped with variable camber aerofoil stations. An analytical model for the development of optimal longitudinal controls was employed and static results showed that the telescopic wing presented an extended operational range whereas dynamic results were considered satisfactory in optimal control calculation for trajectory tracking. Furthermore, actuation energy estimates were found to be two orders of magnitude below the engine output. In 2014 Vicente et al. [70] documented parameterization formulations for aerofoil shape optimization and in Albuquerque et al. [71], a parametric aircraft design optimisation using span and mean chord was developed, followed by a multidisciplinary and multilevel aircraft design methodology using enhanced collaborative optimization, published in 2015 [72].

Similar projects have been cureently developed. Leite et al. [73] further investigated morphing strategies for telescopic wing concepts with aerofoil shape change capability, although their prototype only performed span change. In Ajaj et al. [74], [75], [76], [76], abiding conceptual design studies were performed to assess the potential benefits of a variable-span wing-box technology and to determine its feasibility when incorporated on medium altitude long endurance (MALE) UAVs. To replace conventional ailerons, stability and control benefits were investigated by operating the morphing span asymmetrically. On the other hand, using symmetrical actuation, operational performance benefits were found for 22% of actuated span, which reduced the total drag by 13%, enhanced the endurance by 6.5% and reduced the take-off and landing distance by 28% and 10%, respectively. It is shown that even if current morphing technologies are heavier and more complex than conventional technologies, their multiple functionalities and capabilities keep them potential candidates in terms of overall benefits. The Agile Hunter UAV, a wind tunnel prototype developed by Lockheed Martin, has been considered one of the

biggest successes in span morphing ([31], [77] and [78]). The prototype was capable of folding the inner sections of the wing near the fuselage to reduce the surface area and drag during transonic flight at low altitude. The US Air Force Research Laboratory also developed in 2011 an UAV called ALICE (Air Launched Integrated Counter-measure, Expendable). ALICE outer rigid wing panels deployed for loiter and several advanced morphing concepts were also implemented in other fields as the propulsion system.

All morphing concepts available in literature can be categorized as usign either compliant, mechanical, or hybrid structures, the latter being a mixture of compliant and mechanisms [21]. Compliant structures usually employ flexible skins to maintain a smooth aerodynamic shape of the wing during all stages of morphing. Such structures are promising solutions due their low weight and maintenance costs (no rigid body motion), which seem to work well for small UAVs. However, as the size and weight of the vehicle increase and hence aerodynamic loads increase, it becomes prohibitive to employ compliant structures due to their relatively low stiffness and strength. There is a wide range of flexible skins ranging from corrugated skins to fiber reinforced elastomer. Wereley and Gandhi [79] assembled a journal special topical issue at the forefront of flexible skins technology that brought together a group of ongoing projects seeking to achieve physical realisations of flexible skins for practical applications in morphing aircraft. Broad-scale area change of a non-porous surface while maintaining resistance to aerodynamic loading was demonstrated by Bubert et al. [80] through the development of a passive elastomeric matrix composite morphing skin, which included an elastomer-fibre-composite surface layer that is supported by a flexible honeycomb structure. A morphing skin prototype demonstrated 100% uniaxial extension accompanied by a 100% increase in surface area. Applications to wing span morphing UAVs were slightly discussed. Similarly, Vocke et al. [81] designed, manufactured and tested a feasible conformal 100% span-extending prototype for an UAV aimed for shape change without discrete moving parts or abrupt changes in the aerofoil profile. A wind tunnel test highlighted the resulting viable aerodynamic surface in a wind tunnel test up to 130 km/h wind speeds. A refined elastomer matrix composite skin fabrication technique was also devised and experimentally validated on skins of various thicknesses and overall dimensions.

The diverse design requirements that need to be met are the challenges for a morphing skin structure as outlined by Kikuta [82] while evaluating the mechanical properties of candidate materials for morphing wings. Thill et al. [83] provided an extensive review of the state-of-the-art morphing skins and believed that concepts, materials or structures found in the literature do not fulfil all morphing-required skin characteristics. It is suggested that the level of maturity for morphing skins is low and the existing concepts are very early in their development. However, there are quite a few principles available, especially in nature, that can be used as a starting point. For example, to achieve large area increases a deployable structure such as a ‘roller blind’ concept is revealed promising. For shape changes or small area increases, anisotropic or variable stiffness structures offer the potential to combine compliance and stiffness [83]. The drawback of the state-of-the-art flexible skins is that they cannot work as main load carrier members.

The actual state of knowledge framework on telescopic wings is therefore dictated by several ongoing projects that are being published around the world. Such very recent research on planform variable-span wing concepts, include flexible skins, telescopic and folding concepts ([84], [85], [86], [87], [88], [89], [90], [91], [92], [93], [94], [95], [96], [97], [98]). With

the use of lightweight innovative materials as composite or smart materials, state-of-the-art actuators and sensors and also, pioneering wing designs with increasingly less limited shape and size changes, are being gradually conceivable and may see industry applications in the following years.

2.3 Mass Models for Aircraft Wing Design

2.3.1 For Conventional Wings

Along all design phases, mass studies are of paramount importance as mass highly affects overall performance of an aircraft. The need for thin wings of high torsional stiffness led to the use of wing-box concepts, in which both bending strength and torsional stiffness are provided by a single structural box. Existing wing-box weight estimation models are either semi-empirical or finite element-based. Semi-empirical models are based on data from similar existing aircraft hence its robustness depend on aircraft similarity. Therefore, semi-empirical models are limited to early design stages where detailed geometric, structural, and aerodynamic knowledge are typically unavailable [99]. Furthermore, semi-empirical models are incapable of handling complex wing geometries as it is common for morphing concepts. In addition, early mass models were mainly applied for commercial and transport aircraft hence this models were usually limited to conventional aerospace materials such as light alloys. Further material properties were only later added to semi-empirical models in York and Labell [100] and still today model adaptations are required due to the frequent developments on materials. On the other hand, time consuming finite-element method (FEM) analysis are frequently not suitable. In 1992, a design-sensitive weight prediction method for wing structures of transport category aircraft was developed by Torenbeek [101]. Torenbeek demonstrated the limitations of semi-empirical methods by comparing its results with his linear beam theory method for different scales of aircraft.

Nevertheless, it was soon in 1985 that Dr. Jan Roskam published the fifth part of this book aimed at component weight estimation for the preliminary design of aeroplanes [102]. This game-changing book classified the mass estimation models available in literature into two main categories: class I and class II methods. Later on, also a class III method was adopted. These different types of weight model were classified proportionally to the volume of required aircraft design data. The taxonomy of such models is detailed in [103]. Class I and class II methods are low accuracy methods mostly based on statistics, while higher class methods feature a predominant use of physics based calculations. Examples of class I methods, to predicted the maximum take-off weight (MTOW) with little design information, are presented by Raymer [104], Torenbeek [105] and Roskam [102]. Class II methods are used when the designer already has the aircraft baseline geometry and uses semi-empirical relations together with load factors and parameters data to estimate the mass of the main aircraft components. Some examples of class II models are presented by Raymer [104], Torenbeek [101], Roskam [102] and Howe [106].

There are more advanced class II methods, termed class II-1/2 methods. These methods are quasi-analytical methods that make use of elementary strength/stiffness analysis of wing box structures, in combination with empirical factors and statistics based methods. In particular, the amount of required material to resist the loads applying on the wing is estimated using

elementary, physics based structural analysis, while statistics and semi-empirical data is used to estimate weight contributions of secondary structure components. The quality of class II-1/2 wing mass predictions may vary considerable, as shown by Elham et al. [107]. Relative error measurements in this article, shown that predictions could range from very accurate (in the order of 1%) to quite less accurate predictions (exceeding 25%). The first class II-1/2 wing mass prediction methods were introduced in a RAE technical report, aimed for ”wings of box construction” weight prediction, in 1955 by Burt [108]. This report gave a method by which the wing weight for four types of box construction could be predicted from data available in the project stage of a new design. The equations were not entirely derived on a theoretical basis, but were supported as far as possible by analysis of existing aluminium-alloy structures at ambient temperature. In 1992 Torenbeek presented a class II-1/2 method for commercial aircraft [101]. In 1995, a semi-analytical method to predicted wing mass was documented in Macci et al. [109], where the aim was the wing structure. In the same year, Kelm et al. [110] presented a wing primary structure weight estimation of transport aircraft in the pre-development phase. In 1996, Ardema et al. [99] performed an analytical fuselage and wing weight estimation model for transport aircraft. More recent examples of class II-1/2 methods for wing mass estimation were developed [111], [112], [113], [107], [114].

Class III methods are more complex and make use of high-fidelity CFD, integrated with a FEM analysis software to study the flow over the wing and stresses acting in its structure, respectively. Such mass methods provide huge information that can be integrated in multidisciplinary design optimisation (MDO) solutions. Nevertheless, they require much more computational resources and its application range is narrowed for few aircraft configurations at a time. In 1992, a class III method using finite element model weight estimation was documented by Droegkamp [115]. State of the art examples for class III methods are presented in Sensmeier [116], Bindolino [117], Kenway and Martins [118] and Liem et al. [119]. Also, class IV mass estimation methods exist, but lie outside the conceptual and preliminary design phases.

2.3.2 For Adaptative Wings

Many challenges currently exist for developing simple yet suitably accurate physics-based conceptual aircraft design tools. Often engineers struggle with determining the appropriate levels of fidelity in models or techniques to be used in the conceptual design phase [120]. One challenge of particular relevance to the current effort is the desire to accurately and efficiently predict weights and loadings for unconventional designs such as blended and hybrid wing body, wing-box or morphing concepts, which are expected to break through the conventional designs’ limitations.

While many of previously presented authors investigated wing mass estimation models for commercial and transport aircraft [121], few others focused in more unconventional configurations and even fewer in morphing applications. In 1986, structural optimization capabilities, obtained by integrating a finite element structural analysis program and a numerical optimization script, were developed by Miura and Shyu [122] and applied to a joined wing structures. Hajela et al. [123] documented in 1988 a preliminary weight estimation of both conventional and joined wings using equivalent beam models. In turn, Kaufman et al. [124] worked with high speed aircraft. More recently, Andrews et al. [125] researched in 2015 nonplanar configurations and Ghiringhelli [126] developed in 2016 a weight prediction of the lifting system for an uncon-

ventional aircraft configuration, more precisely a swept wing-box concept. The link amongst stiffness properties and structural weight was made by means of simplified models of the box cross-sections. Gundlach [127] documented some analytical mass estimative equations for Unmanned Aircraft Systems (UAS), which consisted on adapted glider predicting mass functions.

Wing mass prediction models, specifically developed for morphing wing concepts at the conceptual or preliminary design phases, are seldom available in the scientific community or nonexistent at all. Historically, the added complexity and weight required for morphing have not paid for themselves in terms of system performance [34]. The ability to assess, in a rapid manner, the feasibility of morphing innovative designs is crucial to progress on sustainable proof-of-concept applications. Furthermore, to understand the performance impact for each morphed parameter is paramount. In 2005, Campanile [128] documented in the German aerospace center (DLR), some initial thoughts on weight penalty effects in shape-adaptable systems. In this article it was compare the lightweight suitability of different solutions (conventional or not) by defining weight penalty measure criteria which are independent of the particular system under consideration and just characterize a given design option, like using pin-jointed hinges, ball bearings or flexural pivots. Only the application to a conventional hinge technique was described and penalty measure criterion proposed, with substantial weight penalty effects. Moreover, it was concluded that the hinge-induced additional weight increased with the smoothness requirements to the hinge's motion. No references to rack and pinion mechanisms were given.

In Skillen and Crossley [129], parametric morphing wing weight equations were found using response surface methods. The geometric adaptation employed is a two-degrees of freedom planform shape morphing, in which the root chord and the wing sweep angle are the variable parameters. A DoE based on the wing's geometry and two FEM-based optimisation methods were implemented. A set of empirical structural weight data of such wing concept, and including the various (DoE) wing geometries, was developed. From the acquired data, a new weight equation for the conceptual design was fitted using a conventional weight equation and a quadratic polynomial. Adequate wing weight predictions were reached, the trends were based on a single small sample of results though. In 2013, Ajaj et al. [76] developed an integrated conceptual design study focused in span morphing technology. However, limited considerations were made regarding wing mass predicting methods for such concepts.

An in-house study was performed in 2014, by Cunha [130] under the CHANGE project to access the mass penalties of a the telescopic wing technology. It was used CHANGE requirements for a structural analysis of the variable-span wing-box, followed by a parametric study for a limited range of wingspan values as modelled. Predicting expressions were modelled for the wing-box mass and tip displacement. Such mass and tip displacement predicting equations were fitted using a second-order polynomial and the study was limited to two wing parameters (variable-span and span) hence undervaluing further wing parameters. A trend was found for the three wingspan values evaluated. With increasing moving fractions and wingspan, wing mass increased. Wing tip deflection increased with span and its minimum value was 0.033 m for a 2 m semi-span and a 0.16 m moving fraction. It was not presented a fitting error analysis for the developed polynomial. This study is an antecedent of the current work as a more detailed analysis is required and further conclusions may be taken.

2.4 Data Fitting Regression Models

Parametric mass equations that predict wing mass as a function of main aircraft parameters provide rapid estimations suitable for sizing and trade studies during early design phases. Because a morphing wing performs significant shape changes, with a different sets of design flight loads for each planform geometry, an analytical approach to build a wing mass function would require multiple approximate models that would had undesirable complexity. Alternatively, an approach based on empirical data from a FEM-based parametric study may be modelled by regression algorithms with reasonable accuracy [104]. No mass database for existing span morphing aircraft is available for modelling a wing mass equation. Therefore, one approach is "to collect data from a finite set of computational experiments and build the mass equation from this data", as proposed by Skillen [129]. These "computational experiments" would be based on a limited sample of variable-span wings, with a morphing concept in common but differently sized geometries, i.e. each wing design (computational experiment) requires a FEM analysis for a given set of wing parameters, followed by a structural optimisation of the wing's components subjected to the respective design loads of such wing configuration. Such approach has been already used in past works on aircraft concepts that deviate significantly from common designs. One example of such is the work on high speed civil transport aircraft documented in Balabanov et al. [131].

Frequently, in research methodologies that evaluate a greate number of design experiments, a DOE approach is implemented. In DOE all factors are considered in a minimal number of experiments, and the results are modelled with recognized statistical methods [132]. A design of experiments is described by both the number of factors (or design variables) and the number of levels to evaluate each of these factors. The factors are the parameters that describe the wing's geometry and loading conditions; the weight equation will predict the wing's weight as a function of these parameters. In each experiment, factors are set to predetermined values or levels. Often, two or three levels are used for each factor; using two levels would appropriately model a linear response while three levels appropriately model a quadratic response.

Table 2.1: Some quadratic approximation DoE types and its characteristics.

DoE type	No. of levels per variable	No. of data points (for n variables)
Central Composite Design (CCD)	3	$2^n + (2n + 1)$
Face-Centered CCD	3	$2^n + (2n + 1)$
Saturated D-Optimal Design	3	$(n + 1)(n + 2)/2$

Several types of DoE types exist. The types presented in 2.1 are the ones which best suit a DoE with a two to four levels and a response surface objective. Also, different regression methods using DoE may be selected. The response surface method is also known as the least squares quadratic polynomial fitting. This method minimizes the deviation of measured data to the best-fitted function [133] or similarly, it is the method where "the overall solution minimizes the sum of the squares of the errors made in the results of every single equation" [134]. Equally to some other regression methods (Kriging interpolation, radial basis function interpolation, etc.), the response surface is used for approximation of functions $f(x)$ with more than three variables, where x is an input vector of n independent variables. For a set of given input vectors $x1, x2, ..., x_N$ and corresponding function values $f(x1), f(x2), ..., f(xN)$ (with N the number of DoE evaluated), an approximation of $f(x)$ is found [135]. Further information regarding response

surface methodologies may be found in Myers et al. [136].

The DoE dependent variable is commonly expected not to have constant variance hence the least-square method, used to find the best-fit curve for each regression method, is in fact an iterative weighted least squares, which minimizes the sum of weighted squared residuals and recalculating weights on each iteration [137]. The residual would be the difference between the data provided by the parametric study (measured data) and the corresponding approximation calculated from the fitted polynomial (predicted data). In a least-square method approach, both linear and nonlinear regressions may be employed. Linear regression relates observational data to one or more independent variables, as a linear combination of unknown model parameters [138]. Although linear regression models are easier to fit and the statistical properties of the resulting estimators are easier to determine, also a nonlinear regression that uses successive approximations to fit the data was used in the present work. Its applicability relies in the possibility of the wing mass estimate relate non-linearly to the polynomial coefficients [139].

When computing a best fit solution to a system of linear equations with a non-invertible matrix where the system lacks a unique solution, alternative but still linear methods may be applied. From two examples of such methods, one makes use of a left matrix divide operation and the other, a Moore-Penrose pseudo-inverse. The left matrix divide operation consists in an orthogonal-triangular decomposition (also called a QR decomposition) [140], [141]. The Moore-Penrose pseudo-inverse is the most widely known type of matrix pseudo-inverse, a generalization of the inverse matrix operation. Both methods thrive on finding a solution for DoE with a singular matrix, but potentially present numerical instabilities [142]. Each method uses a different approach to fit the data, so they may return very different results and proper evaluation of whether the results are acceptable for each specific dataset should be accessed [143].

In, turn, nonlinear methods are effectively implemented in the $C++$ [144]. Where a search for computational simplicity is essential, traditional nonlinear methods implemented in $C++$ are far complex, whereas the Granger causality test complies with simplicity requirements and is a common method suited for both linear and nonlinear regression that detects causality [145]. Further details on the Granger causality method are presented by Granger et al. [146], [147]. An overview of statistical causality is presented by Carlos et al. [148]. However, several authors have suggested that the result is very sensitive to the value of the norm tolerance once Granger causality test "does not account for latent confounding effects and does not capture instantaneous and nonlinear causal relationships", as demonstrated by Eichler et al. [149]. Therefore, extensions to this method were proposed to address some of the Granger causality test issues.

A proposed extension method that could better describe wing parameters relationships in a mass function is a causality nonparametric detection method that comprises an orthogonal least squares algorithm, uses a nonlinear system identification and procedures an error reduction ratio-causality (ERR-causality) test for what it is called. ERR-causality test, developed by Dr. Y. Zhao, can be used to "detect and track causal relationships between two signals" and is fully explained in Zhao et al. [150] and [151]. The author explains that a major advantage of the ERR-causality test, is that it effectively detects the time-varying direction of linear or nonlinear causality between two signals. Furthermore, one of the main benefits it presents to the traditional Granger method is that it detect the direction of signals' interactions and splits the term set and calculates the ERR values for some terms without requiring the remaining terms

hence it does not need to fit a complete model to provide a correct order of significant terms, making it ”a more powerful and robust causality detection method” [150].

Chapter 3

Telescopic Wing Design

3.1 VSW Conceptual Design

3.1.1 Design Requirements

In the development of a new high performing two-panel telescopic wing, the design requirements are first and foremost, such that its design, when integrated in the RPAS, would enable Olharapo III to accomplish its mission requirements detailed in Section 1.2. Olharapo III RPAS fitted with the VSW should therefore be capable of operating in the same range of speeds as with the original wing, from about the stall speed of 11m/s to 40m/s. Moreover, when fitted with the VSW, it is required to comply with the mission profile with equal or even enhanced flight performance relative to the obtained with the FW. A similar performance at low speed is expected, better performance at high speed is required though.

From the mission profile that is illustrated in Figure 1.6, one understands that the mission profile has multiple operating conditions with no single flight condition prevailing over all others. An adaptive design is desirable for such mission profile hence attaining an enlarged flight envelope for which, a morphing wing concept would potentially feature a better aerodynamic performance. Accordingly, VSW aerodynamic characteristics should be such that the VSW would highly perform simultaneously for loiter and fast cruise. Overall, it should achieve high $C_{L_{max}}$ and L/D and low C_d during both fast and slow cruise conditions.

VSW's structural design requirements are in conformity with EASA certification specifications for Very Light Aeroplanes (CS-VLA) [152]. The structure's main goal is to be safe, light and functional, resorting to the highest possible variable-span range for morphing capabilities. VSW structure should be analysed on stiffness and strength, whereas the structural constraints for the wing sizing include not exceeding the materials' ultimate stress with a specified safety factor, as well as not overcoming a defined limit of wing tip torsion and wing tip deflection.

Likewise older versions, the new VSW must be a straight telescopic wing, high mounted in the aircraft fuselage and without ailerons, allowing for structural simplicity and improved aerodynamic performance. Rolling moments should be effectively controlled by asymmetrical wing deployment. The differentiating factors of the VSW third version in relation to the previous ones is that, besides the increased dimensions to enable higher payloads, its design makes use of aerodynamically optimised aerofoils and winglets, as detailed in Sections 3.2.1 and 3.2.1.4, respectively; a minimum-mass optimised structure and actuation system and also, it comprises the possibility of adding morphing high-lift surfaces, as detailed in Section 3.1.5.

3.1.2 Span Variation Concept

The VSW concept relies on the particularities of telescopic wings. Span variation allows the wing to be fully extended for take-off and landing, in a configuration of high lift where the lift-to-drag ratio is improved, and provide reduced take-off and landing distances. The fully extended span configuration is also suitable for low speed loiters. On the other hand, with the outboard panel retracted, while in cruise or at high speeds, the wing planform area and AR are reduced, decreasing parasite drag for improved range and cruise efficiency [16]. In this manner, the layout of the VSW concept is based on a hollow inboard fixed wing (IFW) that is fixed to the fuselage inside of which an outboard moving wing (OMW) slides actuated by an electromechanical mechanism. This concept is illustrated in Figure 3.1 with the IFW, the light grey root panel and the OMW, the tip panel in three different positions: one coloured in dark grey, which is fully retracted and completely located inside the IFW panel; a second drawn with positive 30 deg-oriented lines, which is half extracted and a third drawn with negative 30 deg-oriented lines, which is fully extracted and keeping a panel intersection fraction for its support.

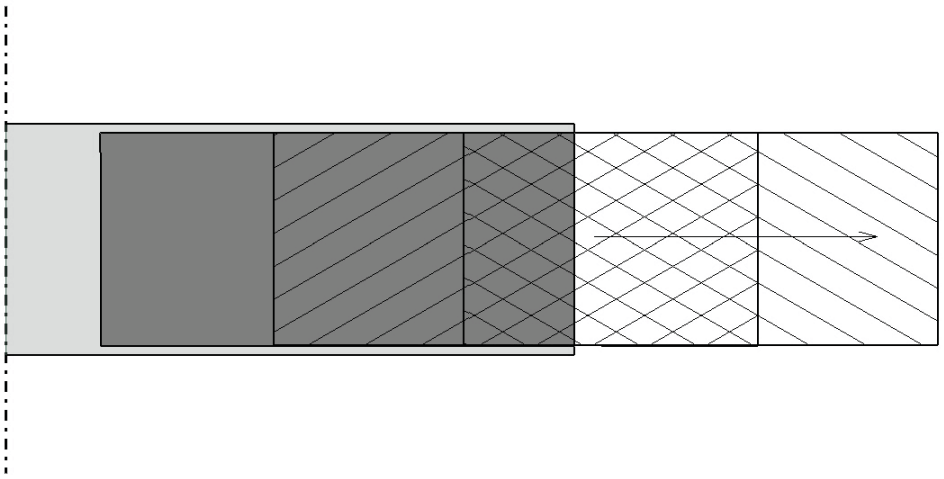

Figure 3.1: Concept for a variable-span wing of the telescopic type.

Both IFW and OMW wing panels keep chord and aerofoil geometry constant along the span. IFW spar web do not extend throughout the entire wing span to allow OMW retraction into the IFW inner section. Along these characteristics, the VSW concept seeks manufacturing simplicity, proper fitting and support of the OMW by the IFW structure. Also, one of the wing panels must have a higher chord to allow the other panel to fit and slide inside it. In Figure 3.1, the IFW is the larger panel, while the OMW slides inside it. Notwithstanding, the opposite is possible and one should selected the most promising concept. On one hand, further investigation is required to decide between which concept, in terms of aerodynamic efficiency. On the other hand, the presented concept is highly beneficial in terms of structural performance and actuation system's simplicity, the reason why it is selected for the current design. Moreover, instead of employing only two panels, extra panels are possible to add for smoother and more flexible adaptability, compromising maximum variable-span fraction to a lower value though. As the current wing is being designed for a small RPAS, adding extra panels to such relatively short wing is not worthwhile.

3.1.3 Wing Geometry

The VSW geometry is based on the previously presented telescopic wing concept and its respective geometrical relations and constraints. Figure 3.2 exhibits the VSW main geometrical details.

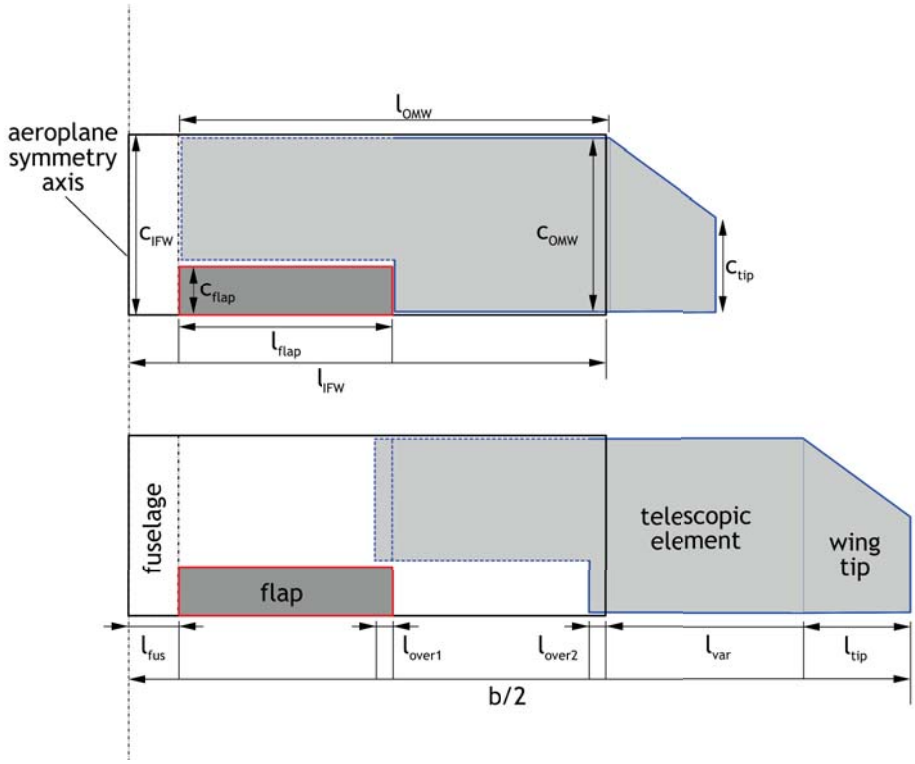

Figure 3.2: VSW planform view: full retracted configuration above and full extended configuration below. Geometrical wing parameters are identified. (Courtesy of Pedro Santos)

It may be perceived from Figure 3.2 that the VSW is composed by the IFW and OMW panels. The IFW panel's semi-span is defined by l_{IFW} and the OMW panel's semi-span is defined by l_{OMW}. Both IFW and OMW wing panels have constant chord along each panel's span, whereas the OMW panel incorporates a tapered wing tip. l_{var} is defined by the length of the wing panel that performs span variation, which results in the movement of the entire OMW panel. Both $l_{over1}$and l_{over2} sections are overlapping areas that are included as safe geometrical extensions to keep proper fitting of the OMW in the beginning of the IFW flap section and the IFW tip section, respectively. Also, for the structurally critical wing configuration, which corresponds to the maximum span in a fully extended (l_{ext}) configuration, both l_{over1} and l_{over2} sections highly contribute in the loads transference from the OMW panel to the IFW panel.

l_{fus} is given as a constant wing parameter that defines the IFW span fraction from the wing root to the beginning of the flap. l_{fus} has been sized to account with the required wing length to fix the high mounted wing to the fuselage as well as keeping an additional slot of free space to grant a safe flaps' actuation. l_{flap}, on the other hand, is the span of the IFW panel occupied by the flap. In order to make use of full retracting capabilities of the OMW section, l_{flap} is geometrically constrained to a maximum value that is a function of l_{var} and l_{over1}.

$$l_{flap} \leq l_{var} + l_{over1} \tag{3.1}$$

The wing tip has a horizontal projected span (l_{tip}) defined as

$$l_{tip} = k_{tip} l_{ave} \tag{3.2}$$

with l_{ave}, the VSW average semi-span and k_{tip}, a multiplying correlation factor that relates the tip span with the average wingspan. It may also be deduced from Figure 3.2 the wing semi-span for fully extended (l_{ext}) and fully retracted (l_{retr}) wing configurations, defined in the following form

$$l_{ext} = b/2 = l_{fus} + l_{flap} + l_{over2} + 2 * l_{var} + l_{tip} \tag{3.3}$$

$$l_{retr} = l_{ext} - l_{var} \tag{3.4}$$

The wing average span will consequently be defined as the arithmetic mean of l_{ext} and l_{retr}.

$$l_{ave} = \frac{1}{2}(l_{ext} + l_{retr}) \tag{3.5}$$

By considering l_{ave}, k_{tip}, l_{var}, l_{fus}, l_{over1} and l_{over2} given parameters, further geometric relations between wing parameters may be derived from Figure 3.2.

Replacing in Eq. 3.5, both Eqs. 3.3 and 3.5 and assuming the maximum flap's span

$$l_{flap_{max}} = l_{var_{max}} + l_{over1}$$

l_{ext} is therefore redefined as a function of the given parameters as

$$\begin{aligned} 2L_{ave} &= 2l_{ext} - \left[\frac{1}{3}l_{ext} - \frac{1}{3}(l_{fus} + l_{over1} + l_{over2} + l_{tip})\right] \\ l_{ext} &= \frac{6}{5}l_{ave} - \frac{1}{5}(l_{fus} + l_{over1} + l_{over2} + l_{tip}) \end{aligned} \tag{3.6}$$

By means of Eq. 3.4, l_{retr} is also redefined as function of the given parameters as

$$l_{retr} = \frac{6}{5}l_{ave} - \frac{1}{5}(l_{fus} + l_{over1} + l_{over2} + l_{tip}) - l_{var} \tag{3.7}$$

Moreover, l_{OMW} and l_{IFW} are defined as

$$l_{OMW} = l_{over1} + l_{over2} + 2l_{var} + l_{tip} \tag{3.8}$$

$$\begin{aligned} l_{IFW} &= l_{ext} - l_{var} - l_{tip} \\ &= l_{fus} + l_{over1} + l_{over2} + 2l_{var} \end{aligned} \tag{3.9}$$

l_{flap} should not be given, but resulting from a function of other main wing parameters. Contrariwise, l_{var} is a major parameter that quantifies the variable-span capability and must be given from an optimisation study. Notwithstanding, from Eq. 3.9, l_{var} may additionally be defined as function of l_{ext} and given wing parameters, as follows

$$l_{var} = \frac{1}{3}(l_{ext} - l_{fus} - l_{over1} - l_{over2} - l_{tip}) \tag{3.10}$$

3.1.4 Structural Concept

While morphing wings present mass penalties due to the inherent increased complexity, its structural design and materials' selection should give preference to lightweight solutions, while maintaining enough strength and rigidity to carry the required flight loads, to allow system integration into realistic aircraft applications. The devised solution for the VSW structural concept comprises parts with a semi-monocoque structure and parts with a monocoque structure by either using an internal structure of spars and ribs or a hollow wing-box with a sandwich load-carrying skin, respectively. Such wing structural concept generally consists in a stressed thin skin construction that carries shear loads, reinforced by a single, dual or multiple spar configuration to carry bending and torsion moments and also, spanwise distributed ribs to preserve skin shape and transmit skin shear loads to spars [153].

The skin is made-up of a sandwich structure composed by a foam core and two external carbon fibre reinforced polymers (CFRP). The foam core increases the skin stiffness and by being located between the fibre layers enable embedding four spar caps in the skin sandwich. In the locations of each embedded spar cap, the foam layer is replaced with rectangular cross-section rods that are integrated into the skin along the complete wing length. Two spar caps are located into the upper surface and the other two are into the lower surface. It is structurally advantageous that the main spars are located in the aerofoils' thicker section. The two front spar caps compose the IFW main spar and are located in the aerofoil maximum thickness position, while the two rear spar caps are located in a given chord fraction in relation to the trailing edge (c_{flap}), following which the flap is attached. Two front spar caps together with a sandwich spar web compose the OMW main spar and two rear spar caps located at the IFW's c_{flap} plus a given clearance for the OMW panel sliding.

Integral ribs are used along the OMW, as illustrated in Fig 3.4. However, being the l_{fus} section an exception, it is not possible to use full ribs in the IFW due to the required IFW open segment inside of which the OMW slides. Without resorting to ribs, loads transmitted from the OMW into the IFW structure would easily deform the IFW skin. Therefore, transversal CFRP enforcements are applied in critical wing sections. The previous described structural details are illustrated in Figs 3.3 and 3.4.

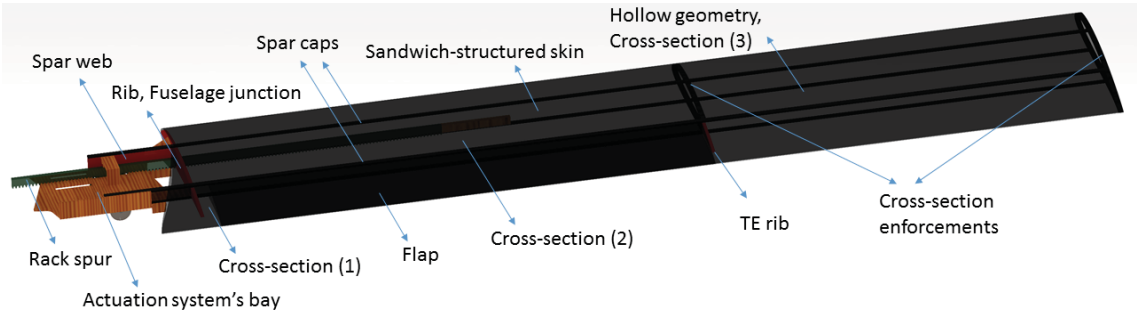

Figure 3.3: Olharapo III VSW structural details: IFW view.

In the case of the VSW, skin and spar webs compose a wing-box that provides bending and torsion stiffness to the wing structure. Figure 3.3 shows full CAD model of the IFW panel with the skin in a transparent view to exhibit its internal structure. Spar caps and skin are illustrated. The full inner rib and a small LE rib in the end of the flap span are presented. Also, it is highlighted

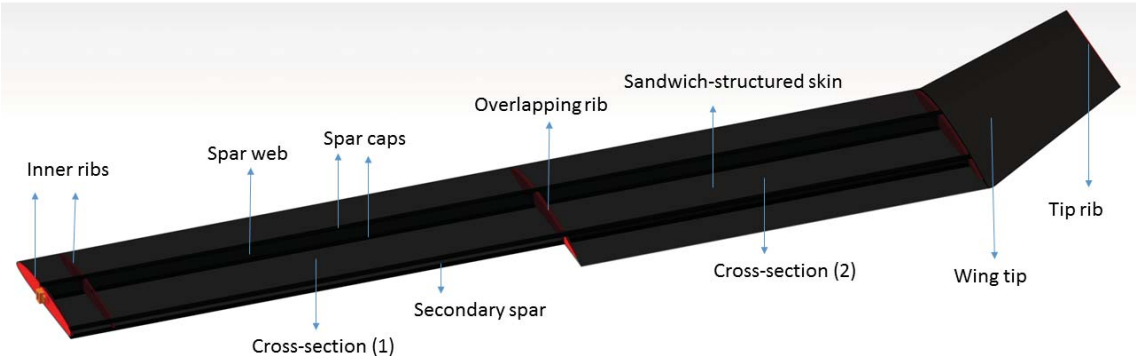

Figure 3.4: Olharapo III VSW structural details: OMW view.

where the use of transversal CFRP enforcements (in black) is required in the IFW panel. Two transversal enforcements are located along the span, one at the end of the flap and a second in the tip of the IFW panel. Naturally, the OMW does not require transversal enforcements because unlike the IFW, it has a conventional semi-monocoque structure with ribs and spars composing the OMW internal structure. From the total length of the OMW, the stroke and the tip are only a fraction of the wingspan, being the remaining length the overlap with the IFW, so that bending and torsion moments may be effectively transmitted from the OMW wetted surface to the IFW structure. Furthermore, Figure 3.4 illustrates the OMW internal structure with a transparent view of the OMW skin. It is possible to see the distribution of ribs, spar cabs and spar webs. Cross-sections are numbered in both IFW and OMW panels for latter analysis.

Each wing cross-section numbered in Figs 3.4 and 3.3 has different geometrical constrains and loading conditions. Therefore, different structural concepts have been implemented in each of them, as it may be observed in the following figures that are ordered from each panel's root to the tip.

Figure 3.5: IFW cross-section (1), near the wing root.

Figure 3.6: IFW cross-section (2), throughout the flap's length.

Figure 3.7: IFW cross-section (3), between the flap's end and the IFW tip.

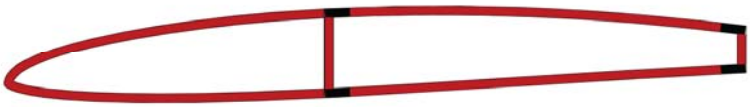

Figure 3.8: OMW cross-section (1), between the OMW root and the overlapping area.

Figure 3.9: OMW cross-section (2), between the overlapping area and the wing tip.

Figures 3.5 to 3.9 illustrate the cross-sections of the IFW and OMW internal wing structures, without ribs for interpretation easiness. It may be perceived from the first three figures that the IFW wing-box extends from the leading edge (LE) to the TE to enable an open box inside of which will slide the OMW structure. An exception applies in the flap location, where the IFW wing-box is naturally reduced, starting from the LE and finishing in the secondary spar where the flap, formed by an identical composite sandwich skin, is attached. On the other hand, it may be perceived from Figures 3.8 and 3.9 that, as the OMW does not need to have an hollow structure, it has two spanwise spar webs, which define the boundaries between the LE wing-box, the centre wing-box and the TE fraction. The latter is only existent in the second half wing section though. The wing tip presents a hollow structure, with a rib in its root and another in its tip. Its skin is made of only the extension of the sandwich outer CRFP face from the OMW. Both in the IFW and OMW panels, most inner ribs are perforated to serve as rack-guide and keep enough free space around for racks proper motion, even when vibration occurs.

Based upon this structural concept, an optimal wing sizing is achieved by a structural analysis and optimisation model which resorts to the finite element method (FEM), as detailed in Chapter 4.

3.1.5 Morphing Flap Application

The implemented telescopic wing concept is intended to integrate an adaptive high-lift surface to extend its wing morphing capabilities. The application of a continuous flap is selected and briefly analysed. This flap adds further morphing capabilities to the VSW design, enabling chord and aerofoil camber changes for wing aerodynamic enhancement in off-design flight conditions. In this concept, the skin is compliant with the aerofoil geometry and its lower surface is actuated by small servomotors. Similar concepts have been gradually implemented, in particular with successful accomplishments obtained in Politecnico de Torino, by Ricci [45] and in DLR, by Monner [154], [155]. In-house previous studies on this concept were developed by Marques et al. [46], which designed and tested a variable camber flap for improved efficiency.

Challenges on the application of this design in the VSW are to arrange space to servomotors in the small volume that is available in the inner structure of the flap. Such small servomotors may not have the power to perform shape change of the flap's skin. Moreover, another concerning aspect in the implementation of continuous flaps, is the ability to perform shape change without loosing completely the aerofoil aerodynamic shape in the flap's chord fraction. On one hand, the skin must be stiff to prevent this to happen. On the other hand, a too stiff material requires

huge actuation power. Trade studies on this subject aimed to morphing flap devices, were presented by Ai et al. [156].

These two challenges that are inherent to continuous flap's technology, are further investigated by implementing a proof-of-concept continuous flap. It is located at 70% of the wing chord and is made of CFRP with two bidirectional $\pm 45^{\circ}$ fabric layers. After the hand layup process, it has a thickness 0.35 mm, corresponding to a laminate of 540 g/m^2 plain weave carbon-epoxy. Figure 3.10 shows the experimental apparatus, with a flap prototype installed in a supporting frame which also supports a dynamometer. The dynamometer is used to measure the required force to apply in order to obtain a desired TE deflection. To obtain reasonable flap actuation effectiveness, deflections of $+30^{\circ}$(down) and -10°(up) are considered.

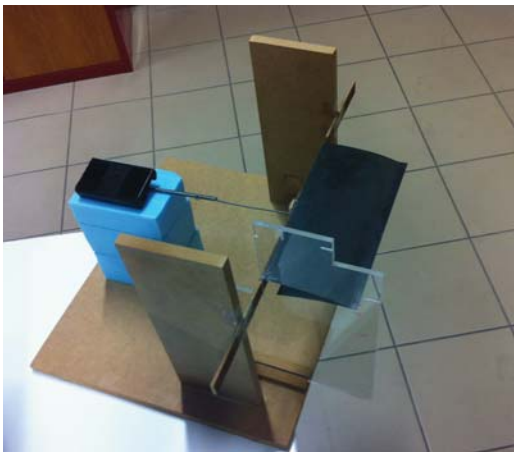

(a) Flap installed in the supporting frame.

(b) Flap's shape with no applied loading.

(c) Flap's shape change - 30°down.

(d) Flap's shape change - 10°up.

Figure 3.10: Continuous flap proof-of-concept.

Table 3.1 shows experimental results of the actuation required force (F_1 and F_2) to obtain a flap's displacement of +30°and -10°, respectively.

Table 3.1: Experimental deflection measurements on the flap's prototype.

Trial	1	2	3	4	5	6	7	8	Average
F_1 [N]	4.37	4.76	4.51	4.61	4.76	4.66	4.41	4.86	4.62
F_2 [N]	2.31	2.45	2.16	2.47	2.29	2.57	2.48	2.60	2.42

Average results for material deflection in Table 3.1 present a maximum required force of 4.6

N for F_1, which shows that the concept has a viable application, as small lightweight and commercially available servomotors can deliver forces up to 25 N, approximately. Two examples of servomotors with such characteristics are *BMS-210DMH Metal Gear Coreless Digital Nano Servo 3.9kg.cm / 0.13sec / 16 g* [157] and *D-MG16 Metal Gear Digital Servo 2.9 kg.cm / 0.08sec / 18.8 g* [158]. Assuming an approximate length of the servomotor lever arm of 10 mm and servomotors' torque from specifications, the available forces of the former and latter servomotors are 38.3 N and 28.5 N, respectively. Both servomotors are thus suitable to apply in the current design. Nevertheless, the presented measurements do not consider the aerodynamic loading on the flap's skin, which would further increase F_1 and decrease or increase F_2 depending on skin thickness and flap loading. Moreover and as seen in Figure 3.10, it is concluded that for a positive deflection, the flap does not present high distortions of the aerofoil aerodynamic shape, not being the case of the negative deflection though, as it presents an 'S' shaped curve near the TE.

Although a static analysis does not account with the loading dynamic response when the flap deflects, an ANSYS static analysis is performed to understand in which form would the servomotors required force vary by the application of the aerodynamic loading. For a zero flap deflection of its geometry and respective chord distributed aerodynamic loading obtained in XFOIL, the analysis results showed that the required force to keep zero flap deflection is 15.8 N and 16.1 N, presenting a maximum tensile stress of 37.6 MPa and 97.6 MPa and a maximum shear stress of 19.3 MPa and 49.8 MPa, for a flap's skin thickness of 0.4 mm and 0.3 mm, respectively. When applying these forces, flaps original shape is kept within a deflection absolute error below 10^{-5} m. For the analysed skin thickness range, a flap's deflection condition of -10° is achieved mainly by the aerodynamic loading, with little servomotors actuation requirements. The condition of +30° flap's deflection is the most critical in servomotors strength requirements, for which the lift increases due to the increase in the aerofoil curvature. To prove that the force application requirements for a +30° flap's deflection are under the strength limits of commercially available servomotors that would fit inside the wing's geometry, further studies should consider a dynamic load response when deflecting the flap. A distributed approach by using a group of servomotors at each flap would decrease its strength requirements and therefore decrease its size to fit inside the wing, with a probable mass penalty though.

3.2 VSW Preliminary Design

3.2.1 Aerofoils Geometric Offset and Aerodynamic Performance

In a variable-span wing of the telescopic type, the cross-sections of the sliding panels, whether be two, three or more, must be made geometrically compatible among them. This requirement serves two purposes: to minimize the aerofoils geometric discontinuity, which negatively affects wing drag and lift; and to provide proper fitting and structural support between any two panels. As outlined in Mestrinho et al. [13], a convenient way to match the IFW aerofoil to the OMW aerofoil of a two-panel telescopic wing is to create an aerofoil for the IFW from a positive (outward) offset of the aerofoil selected for the OMW so that the smallest possible discontinuity between wing sections is obtained. However, it is not clear weather this procedure is the most appropriate for any given general situation where maximum aerodynamic performance is mandatory. Therefore, the need to validate the decision of selecting a more adequate combina-

tion between keeping an original aerofoil for the OMW and the corresponding modified aerofoil with an outward offset for the IFW or, alternatively, setting the original aerofoil for the IFW and modifying it with an inward offset for the OMW, has emerged. Moreover, after assessing each set of aerofoils for their resulting shape and aerodynamic characteristics, two aerofoils' data points must be provided as inputs to an overall VSW aerodynamic optimisation procedure to be performed afterwards.

The method employed is divided into two parts. Firstly, two new aerofoils are mathematically created based on the modification of a given aerofoil selected for a specific application, with inward and outward offsets, where the size of the offset is usually selected based on geometrical and structural considerations; and simultaneously, the LE and the TE geometries are adjusted with some specified methods inserted in the main mathematical implementation. Secondly, a comparison of the aerodynamic performance of those two modified aerofoils relative to their respective initial aerofoil is performed. The algorithm to create the offset aerofoils is implemented in a spreadsheet. To build each offset aerofoil some previous information is required, as follows:

1. Original aerofoil data points (unit chord);
2. Aerofoil's chord length, c;
3. Offset value, d;
4. TE thickness, t_{TE} (only applicable for the outward offset); and
5. Starting point for the aerofoil's LE, $(x, z)_{LE}$ (only applicable for the inward offset).

The output results are the inward and outward offsets of the original aerofoil, using different order polynomial interpolations for expanding the outward offset aerofoil's TE and different types of curves for rebuilding the inward offset aerofoil's LE.

3.2.1.1 Offset Creation

The spreadsheet used to create the desired offset aerofoils introduces firstly the original aerofoil data points. Inward or outward offset aerofoil's points are created using a normal vector that has a predefined length (the offset length) chosen by the user, which is perpendicular to the original aerofoil's surface at any given point. It is worth pointing out that from this point forward till the end of Chapter 3.2.1, all positions and dimensions are relative to the aerofoil's chord length unless otherwise specified.
As illustrated in Figure 3.11, a normal vector to each aerofoil data point gives the position of the respective offset point. The normal vector is defined by inverting the slope of the respective vector tangent to the original aerofoil (computed by central finite differences in the present case). Knowing the position of each point of the original aerofoil, the slope of the normal vector and the desired offset length (negative for the inward offset and positive for the outward offset), the offset aerofoil points' position can then be obtained from trigonometry.

To obtain the modified aerofoil coordinates $(x_i\prime, z_i\prime)$ from the original aerofoil coordinates (x_i, z_i), by defining an offset value, one must compute the following system of simplified equations

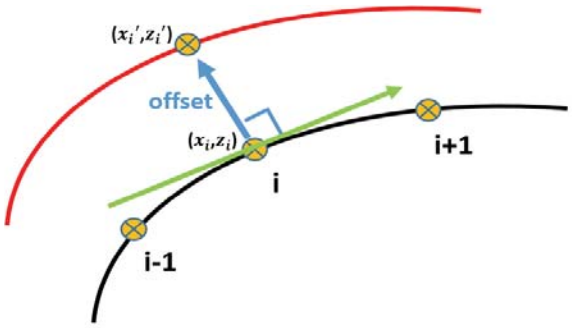

Figure 3.11: Conceptual method applied to obtain a modified aerofoil (lighter curve) from a geometric offset applied to a given initial aerofoil (darker curve).

$$\begin{cases} x_i\prime = x_i - \sin(\theta_i)\,\frac{offset}{c} \\ z_i\prime = z_i + \cos(\theta_i)\,\frac{offset}{c} \end{cases} \tag{3.11}$$

with θ_i, the angle defined between the offset direction and the vertical axis, as

$$\theta_i = \tan^{-1}\left(\frac{z_{i+1} - z_{i-1}}{x_{i+1} - x_{i-1}}\right) \tag{3.12}$$

Due to the geometric modifications obtained by offsetting the original aerofoil shapes, small geometric conflicts or imperfections need to be corrected in the aerofoil regions near the LE and TE. Different mathematical representations are applied in order to improve the geometry of the LE and TE regions of the offset aerofoils and attain good aerodynamic performance. In the case of the outward offset, the critical situation lies in the creation of the TE, whereas for the inward offset it lies in the creation of the LE. The outward offset TE has to be extended so that the desired gap thickness is respected and the aerofoil's surface is smoothly closed. Polynomial functions are used for this purpose, using at least two interpolated points at the TE of the outward offset modified aerofoil. In small sized aerofoils it is often convenient to have a non-zero thickness TE to facilitate manufacturing and avoid damage during normal handling of the wings. This thickness is defined by the designer as a percentage of the chord according to specific requirements.

If required, the original aerofoil is converted to unit chord and thus the offset value must be divided by the chord length before the desired offset geometry is calculated. The TE is created with different degree polynomial interpolations, using the last points of the upper and lower surfaces of the aerofoil (starting from around 95% to 100% of the offset aerofoil's chord). Polynomial interpolations applied are of different order: first, second and third order. Figure 3.12 shows one example where a second order polynomial interpolation is applied to the TE.

As illustrated in Figure 3.13, the inward offset of an aerofoil creates a sharp LE due to the intersection of the normal offset of the upper and lower surfaces of the aerofoil. This critical situation imposes the creation of a new LE segment. As mentioned previously, a distance from the original aerofoil LE must be provided indicating the new offset aerofoil's LE position. Three different curves are used to create the desired smooth LE, defined by elliptic, parabolic or cubic functions. The previous definitions are simplified as each methodology is actually defined by a double function (e.g. double-elliptic). The methodology consists on the use of two functions

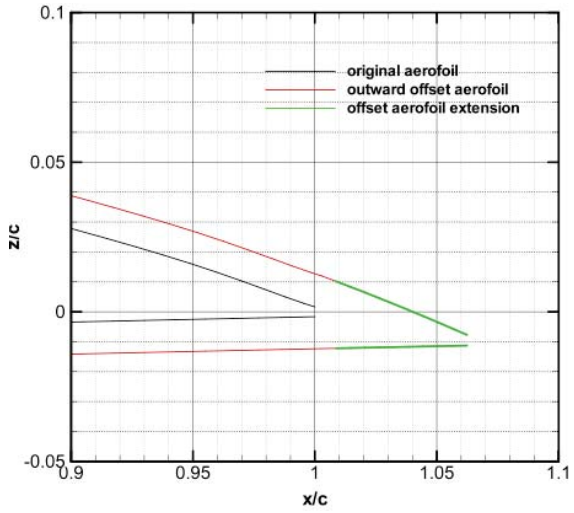

Figure 3.12: TE extension for an outward offset aerofoil.

describing the selected type of curve, one for the upper surface and another for the lower surface of the aerofoil. The LE curves defined by parabolic and cubic functions are simple polynomials, whereas the elliptic uses ellipses. An example of this method is illustrated in Figure 3.14 for the elliptic curve that is detailed hereinafter.

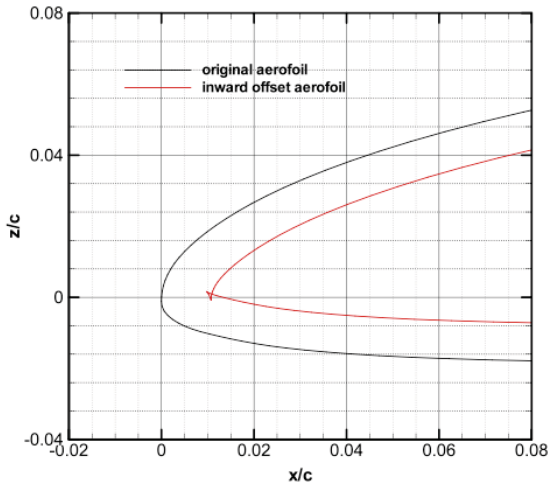

Figure 3.13: LE curve for an inward offset aerofoil.

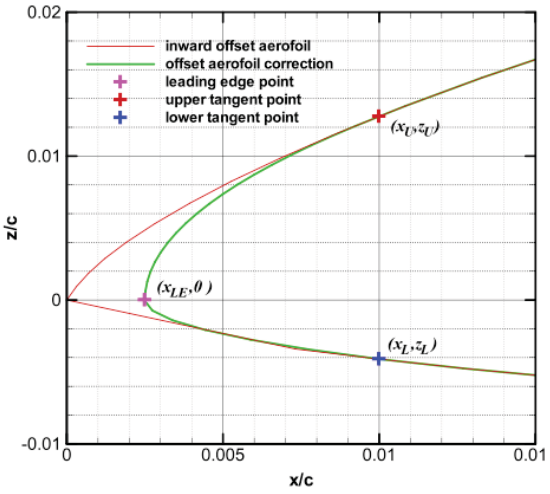

Figure 3.14: Double-elliptical LE correction.

With this ellipse definition, three boundary conditions can be imposed, i.e., each ellipse function should:

1. Pass through a new LE point of the offset modified aerofoil, to be defined by the user;
2. Be tangent to the offset modified aerofoil; and
3. Be perpendicular to the horizontal axis at the new LE point.

The aerofoil is defined in the zx plane. The z-coordinate of each point of the new smooth LE is fixed to create a constant height panel size (in the z-direction) between the upper and lower limits of the new LE, so that the only parameters to be defined are x-coordinates of the points. The ellipse function is as follows

$$\frac{(x-x_0)^2}{a^2} + \frac{(z-z_0)^2}{b^2} = 1 \tag{3.13}$$

where x_0 and z_0 are the ellipse's centre point coordinates and a and b are half the width (semi-major axis) and half the height (semi-minor axis) of the ellipse, respectively. In the present case, it is used $x_0 = x_{LE} + a$ and z_0, where x_{LE} is the x-coordinate of the LE point and z_0 is the z-coordinate, both being user specified. From Equation 3.13, for any given value of z, the corresponding value of x is given by

$$x = x_{LE} + a\left(1 + \sqrt{1 - \left(\frac{z - z_0}{b}\right)^2}\right) \tag{3.14}$$

In order to guarantee the tangency of the new LE curve with the aerofoil's surface, the derivative of Equation 3.14 with respect to z is required as follows

$$\frac{\mathrm{d}x}{\mathrm{d}z} = -\frac{a(z - z_0)}{b\sqrt{b^2 - (z - z_0)^2}} \tag{3.15}$$

Solving Equations 3.14 and 3.15 simultaneously with boundary conditions specified at a given point on the surface of the original aerofoil (x and z in the former, $\mathrm{d}x/\mathrm{d}z$ and z in the latter), the only unknown variables, a and b, can be computed. This is performed in turn for the upper and lower ellipses. In order to define the upper ellipse, a point on the upper surface of the aerofoil is selected and the boundary conditions $x = x_U$ at $z = z_U$ and $\mathrm{d}x/\mathrm{d}z_U$ at $z = z_U$ are applied. The lower ellipse is obtained by selecting a point on the lower surface and applying the boundary conditions $x = x_L$ at $z = z_L$ and $\mathrm{d}x/\mathrm{d}z_L$ at $z = z_L$. Functions $z = z(x)$ or $x = x(z)$ of both upper and lower surfaces are either known or interpolated from aerofoil data points.

Parameters a and b of the ellipses are obtained by iteratively changing x_{LE} and x_U(or x_L) to solve the system of equations in order to produce a few leading edge geometries which are then aerodynamically analysed. The best aerodynamic results, obtained from the different leading edges, reveal the best leading edge geometry, i.e. the best combination of x_{LE}, a and b for the given modified aerofoil. Consequently, both elliptic functions defining the new LE can be iteratively created by using Equation 3.14 and 3.15 for each modified aerofoil. A similar formulation is employed for the polynomial curves by applying the same boundary conditions.

3.2.1.2 Aerodynamic Analysis of Resulting Aerofoils

Given an initial aerofoil geometry and its respective modified aerofoils with a constant offset applied to its contour, the effect of such modifications on the resulting aerodynamic performance is measured, namely the effect on aerodynamic coefficients, lift-to-drag ratio, camber, twist, relative thickness and aerofoil stall behaviour. The 2-dimentional (2D) aerodynamic coefficients as functions of the angle of attack α and Reynolds number (Re) are obtained using the open source XFOIL software [159], which is a widely used aerofoil design and subsonic analysis program written in FORTRAN by Drela in MIT, in collaboration with Youngren.

XFOIL uses a panel method in which the steady Euler equations in integral form are used to represent the inviscid flow, and a compressible lag-dissipation integral method is used to rep-

resent the boundary layers (bl) and wake. The entire viscous solution (bl and wake) is strongly interacted with the incompressible potential flow via the surface transpiration model, which permits proper calculation of limited separation regions. Data for the aerofoils' lift coefficient, C_l, curves and aerofoils' parasite drag coefficient, C_d, curves, including the non-linear regime, are obtained from this aerofoil aerodynamic analysis software. The aerofoils' lift-to-drag, (L/D), versus C_l curves are also obtained. XFOIL has been shown to adequately predict the shape of the aerodynamic curves $C_l \times \alpha$ and $C_d \times C_l$ at low Re and also their trends with varying Re for a variety of aerofoil geometries [160], [161].

In the study of the new high performing VSW, three aerofoils are initially considered as suitable candidates: modified MH115, modified SG6042 and UBI-03-012. These aerofoils are medium camber, low speed aerofoils with a good compromise between maximum lift coefficient, C_{lmax}, maximum lift-to-drag ratio, $(L/D)_{max}$, and low C_d in the speed range from about 14 m/s to 30 m/s. Accordingly, the analysis is conducted for Mach numbers between 0.041 and 0.088. The maximum thickness-to-chord ratio, $(t/c)_{max}$, of the modified MH115 is 11.3% whilst that of the other two aerofoils is 10%. Moreover, the concept applied to this study is based on the characteristics and flight conditions of an aerofoil with a c of 280 mm and a 3 mm offset for the inward and outward modified aerofoils. Commonly, aerofoil analysis are conducted for constant design Re value (Re_d), notwithstanding the current study employs a condition of constant $Re\sqrt{C_l}$.

$$\begin{cases} Re = \frac{\rho V c}{\mu} \\ V = \sqrt{\frac{2W}{\rho S C_l}} \end{cases} \quad \Leftrightarrow \; Re\sqrt{C_l} = \frac{c}{\mu}\sqrt{\frac{2\rho W}{S}} \tag{3.16}$$

From Re and V equations, the resulting Eq. 3.16 shows that the aerodynamic analysis condition of constant $Re\sqrt{C_L}$ is only function of constant parameters for a fixed aircraft and flight condition, hence this analysis condition is more interesting to evaluate for the design than merely the constant Re condition. With a Re_d of 686,000 ($\frac{1.225*30*0.28}{1.5\times10^{-5}}$) and a cruise C_L value of 0.225, $Re\sqrt{C_L}$ value to be used hereinafter equals to 325,000, approximately.

The modified MH115 and modified SG6042 aerofoils are MH115 and SG6042 aerofoils, respectively with their TE cut-off so that their thicknesses are 1 mm with the chord length mentioned above and are referred to as MH115 and SG6042 hereinafter. The MH115 aerofoil exhibits the highest camber, a C_{lmax} greater than 1.6 and has a $(L/D)_{max}$ of 107 for a C_l of around 1.17. The SG6042 aerofoil exhibits a C_{lmax} just over 1.5 and has a $(L/D)_{max}$ of 108 for a C_l of around 0.93. UBI-O3-012 aerofoil was in-house developed through an optimisation procedure applied to the SG6042 aerofoil to increase its C_{lmax} and reduce its C_d over a wider range of C_l values. This aerofoil exhibits a C_{lmax} just under 1.6 and has a $(L/D)_{max}$ of 111 for a C_l of around 0.92.

The methodology described previously is applied, entering the original/non-modified aerofoil coordinates and input data defined by the user. Some studies to find the most adequate LE and TE representations are performed using XFOIL. After computing the respective LE or TE geometrical modifications, also a local refinement on the aerofoil segments with highest curvature is performed. As aerofoil geometries are approximated by line segments in XFOIL, these local refinements that increase the number of points in the LE and TE most curved segments are intended to grant a smooth and almost continuous geometry to enhance aerofoils aerodynamic

behaviour. The aerodynamic effect of the TE extension formulation is studied using the outward offset aerofoil obtained from the MH115 aerofoil.

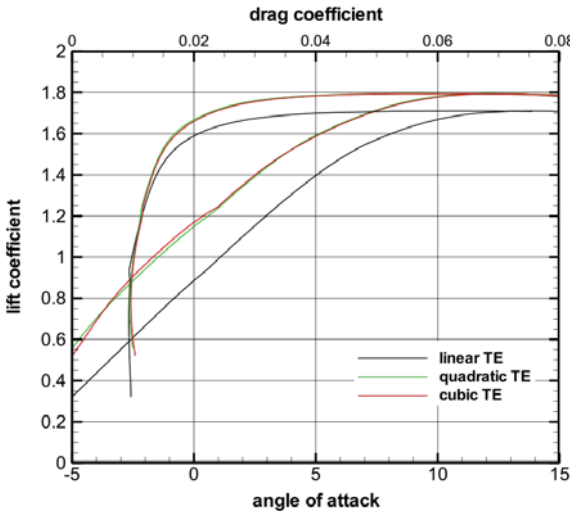

Figure 3.15: Lift curves and drag polars for the outward offset MH115 aerofoil with different TE extensions.

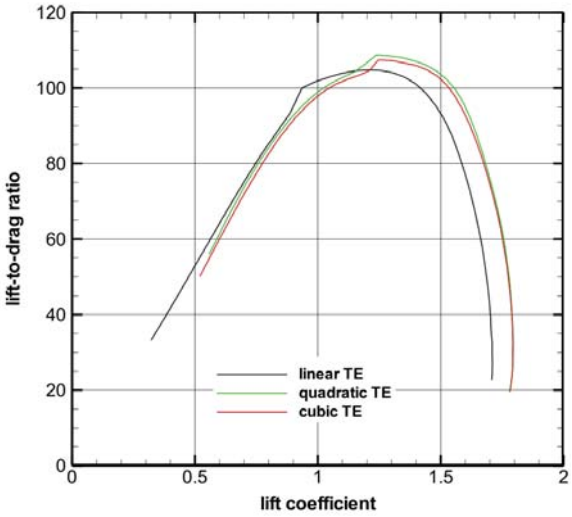

Figure 3.16: Lift-to-drag ratio curves for the outward offset MH115 aerofoil with different TE extensions.

In terms of geometry impact, from the three types of TE extension implemented, the third degree polynomial is the one that increases the aerofoil's camber the most whilst the linear extension is the one with the smallest effect closely followed by the second degree polynomial extension. Those shape changes have an impact on the aerodynamic performance of the outward offset aerofoil as shown in Figures 3.15 and 3.16 for different trailing edge extensions and with α in degrees. These data is obtained from MH115 for a flow condition corresponding to a constant $Re\sqrt{C_L}$=325,000. For the linear extension aerofoil, C_{lmax}=1.71 and $(L/D)_{max}$=104.9 are lower than the values observed for the other two TE extensions. Better overall performance is obtained with the second degree polynomial extension, though marginally better than the third degree polynomial extension, with values of C_{lmax}=1.79 and $(L/D)_{max}$=108.5.

The inward offset aerofoil obtained from the MH115 aerofoil is also used to analyse the effect of different LE corrections on the aerofoil's aerodynamic performance. Three mathematical formulations are used to perform the LE correction as described above: elliptic, parabolic or cubic functions. Each of these formulations is applied to the inward offset aerofoil and varying the values of leading edge longitudinal position to chord ratio (x_{LE}).
Figure 3.17 summarizes the main aerodynamic effects due to the LE geometrical modifications. These results show that, for all LE corrections in general, an increase in leading edge x-position will increase $C_{l_{max}}$ but will reduce $(L/D)_{max}$. The cubic LE correction produces higher $(L/D)_{max}$ for values of x_{LE} above 0.11 and higher values of $C_{l_{max}}$ for values of x_{LE} below 0.005. Nevertheless, in the middle range of x_{LE}, it produces the lowest values of $(L/D)_{max}$ and $C_{l_{max}}$. The other two formulations present very similar performance regarding $(L/D)_{max}$ being the elliptic LE correction slightly better for higher x_{LE} values. Higher $C_{l_{max}}$ is achieved with the cubic polynomial LE, slightly better than the elliptic LE though.

Novel aerofoils are created with the outward or inward offsets and the most adequate LE and TE formulations. Based on the LE correction and TE extension studies, one concluded that the double-elliptic LE for the inward offset aerofoils and the second degree polynomial TE for the

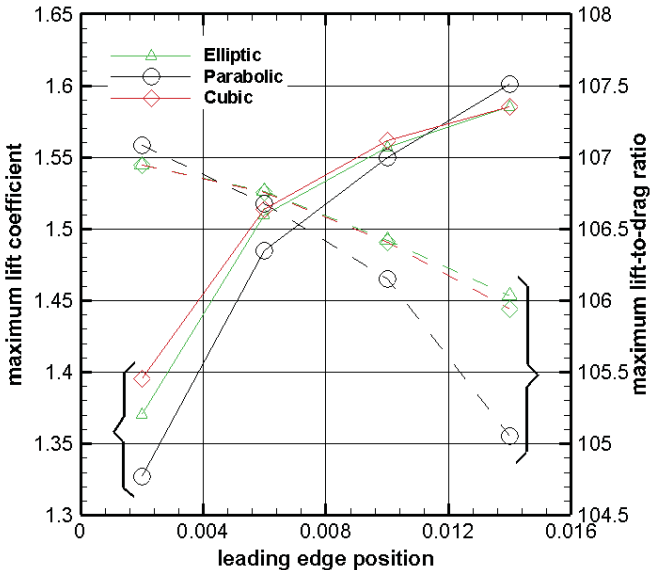

Figure 3.17: Aerodynamic effect of LE correction and LE position on C_{lmax} and $(L/D)_{max}$ of the inward offset aerofoil.

outward offsets best suit the aerofoils design, i.e. the gap between the original aerofoil and the modified aerofoil is not excessively large, the modified section is smooth and continuum with the rest of the aerofoil and the resulting aerodynamic data and stall characteristics are enhanced, producing a better aerodynamic performance. Furthermore, a leading edge position of 0.006 is used.

Figure 3.18 shows the aerofoil geometries. Using the original aerofoil with unit chord (represented in black), the inward offset aerofoil is obtained (represented in green) together with the outward offset aerofoil (represented in red). On the left hand column the aerofoils are represented to scale relative to the original aerofoil whilst on the right hand column they are all illustrated with unit chord for better geometry comparison. For all three original aerofoils, the offsets present identical trends. The inward offset produces an aerofoil with reduced maximum camber and maximum thickness ratio, whose positions move aft, and with decreased incidence. On the other hand, the outward offset produces an aerofoil with increased maximum camber and maximum thickness ratio, whose positions move forward, and with increased incidence. Other important aspects of the aerofoil geometry are the TE thickness and TE angle. It is observed that, the smaller the original TE angle, the greater will the variation in chord of the offset aerofoils be, provided the curvature of the upper and lower surfaces at the TE are not highly different as is the case with the UBI-03-012 aerofoil. In general, and from a structural point of view, thicker aerofoils are preferred for the inboard panels due to the higher structural depth, and higher TE angles result in stiffer offset TE's and smaller variations in chord lengths.

The geometric modifications also have strong effects on the aerodynamic characteristics of the resulting aerofoils and must be investigated. Figure 3.19 illustrates the main aerodynamic characteristics of the studied aerofoils at $Re\sqrt{C_L}$=325,000. On the left hand column lift curves ($C_l \times \alpha$ curves) and drag polars ($C_l x C_d$ curves) are shown whilst on the right hand column lift-to-drag ratio curves ($L/D \times C_l$ curves) are represented. From the lift curves, it is observed that the outward offset aerofoil produces an increase in C_{lmax} and in the zero-angle of attack lift coefficient, C_{l0}. Its drag polar is moved to larger C_l values, resulting that $(L/D)_{max}$ occurs

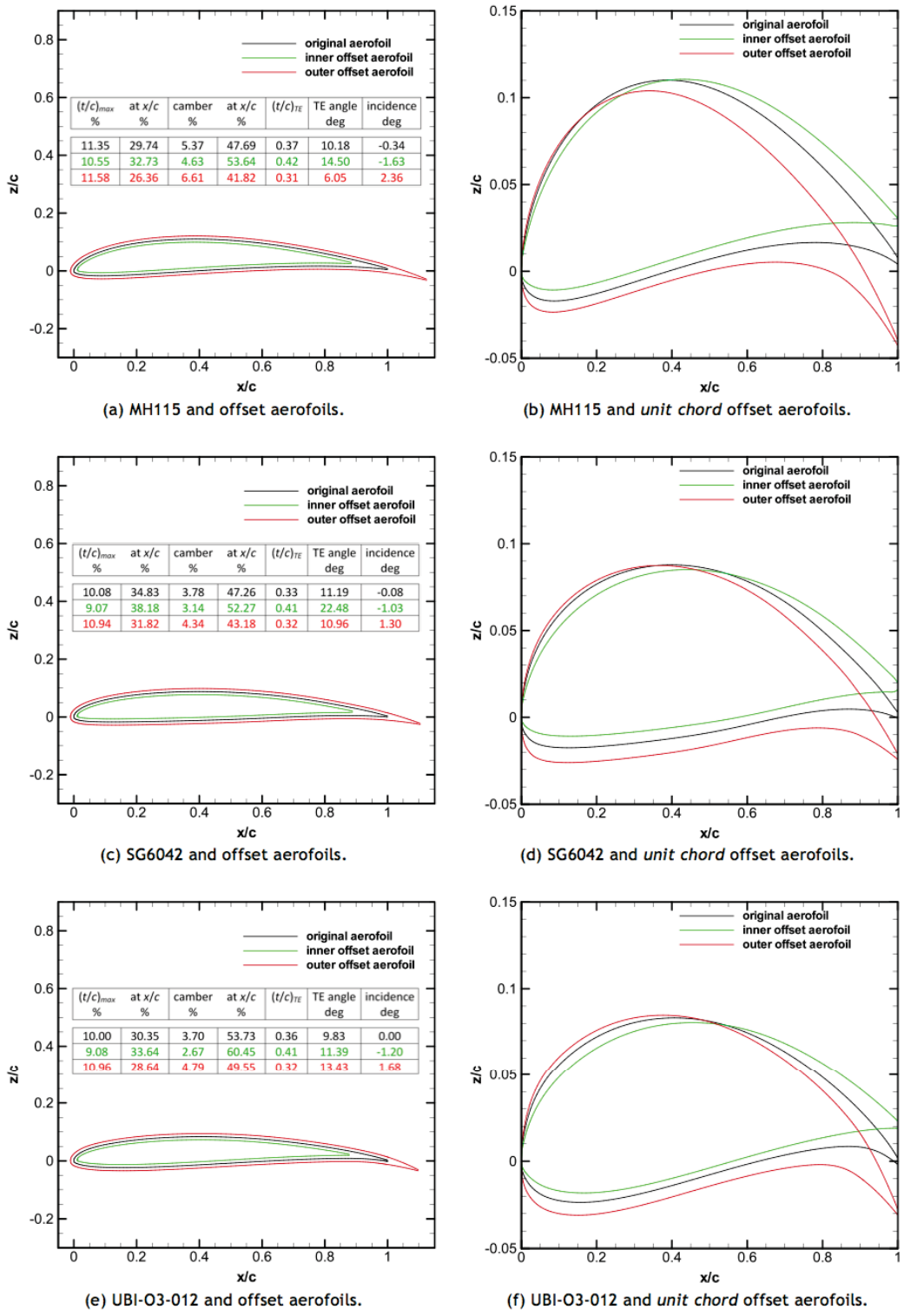

$(t/c)_{max}$ %	at x/c %	camber %	at x/c %	$(t/c)_{TE}$	TE angle deg	incidence deg
11.35	29.74	5.37	47.69	0.37	10.18	-0.34
10.55	32.73	4.63	53.64	0.42	14.50	-1.63
11.58	26.36	6.61	41.82	0.31	6.05	2.36

$(t/c)_{max}$ %	at x/c %	camber %	at x/c %	$(t/c)_{TE}$	TE angle deg	incidence deg
10.08	34.83	3.78	47.26	0.33	11.19	-0.08
9.07	38.18	3.14	52.27	0.41	22.48	-1.03
10.94	31.82	4.34	43.18	0.32	10.96	1.30

$(t/c)_{max}$ %	at x/c %	camber %	at x/c %	$(t/c)_{TE}$	TE angle deg	incidence deg
10.00	30.35	3.70	53.73	0.36	9.83	0.00
9.08	33.64	2.67	60.45	0.41	11.39	-1.20
10.96	28.64	4.79	49.55	0.32	13.43	1.68

Figure 3.18: Original aerofoils and aerofoils obtained by inward and outward offsets: on the left hand column aerofoils are shown to scale; and on the right hand column aerofoils are scaled to unit chord.

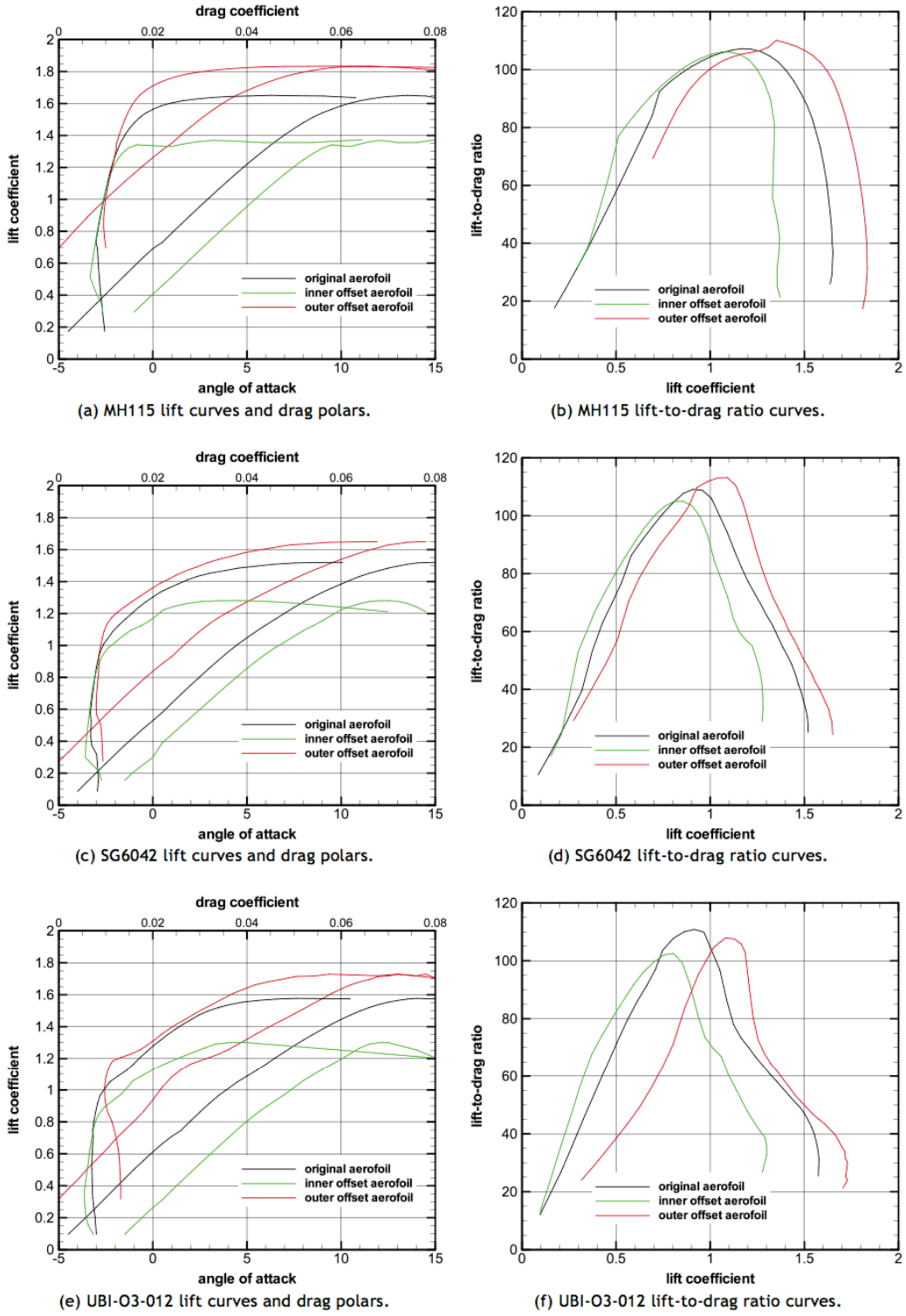

(a) MH115 lift curves and drag polars.

(b) MH115 lift-to-drag ratio curves.

(c) SG6042 lift curves and drag polars.

(d) SG6042 lift-to-drag ratio curves.

(e) UBI-O3-012 lift curves and drag polars.

(f) UBI-O3-012 lift-to-drag ratio curves.

Figure 3.19: Aerodynamic data obtained for the original aerofoils and the aerofoils obtained by inward and outward offsets at $Re\sqrt{C_L}$=325,000: on the left hand column lift curves and drag polars are shown; and on the right hand column lift-to-drag ratio curves are shown.

at a higher C_l value, and the minimum C_d value is slightly increased. Not shown in Figure 3.19, but also an important result, the pitching moment coefficient (C_m) becomes more intense in the outward offset aerofoil. The opposite is true for the inward offset aerofoil. These results were expected since the outward offset aerofoils' mean camber and incidence were positively incremented and the inward offset aerofoils' mean camber and incidence were decremented.

It is interesting to point out that $(L/D)_{max}$ increases with the outward offset and decreases with the inward offset for the MH115 and SG6042 aerofoils. The same is not seen with the UBI-O3-012 aerofoil, where the highest value of $(L/D)_{max}$ occurs for the original aerofoil and not for the outward offset aerofoil, but its lowest value is still exhibited by the inward offset aerofoil. The reduced $(L/D)_{max}$ in the outward UBI-O3-012 offset aerofoil may be explained by the narrower laminar flow region observed in the drag polar curve, indicating that the laminar boundary layer in this case cannot extend so further aft at higher C_l values as with the other two aerofoils. Stall characteristics do not seem to be affected since the shape of the lift curves in the stall region do not present any significant differences among them.

3.2.1.3 Aerofoil and Offset Type Selection

A methodology for developing offset aerofoils given any existing aerofoil, including corrections for the leading edge and trailing edge geometries of the resulting aerofoils, was presented. The analysis of the offset aerofoils obtained from three initial known aerofoils enabled a better understanding of the geometric changes suffered by the offset aerofoils and the effect on their aerodynamic characteristics. From the three aerofoils studied the following trends could be observed. In terms of the geometric characteristics one may conclude that:

1. The inward offset aerofoils have: reduced maximum camber at a further aft chord position; reduced $(t/c)_{max}$ at a further aft chord position; decreased incidence;
2. The outward offset aerofoils have: increased maximum camber at a further fore chord position; increased $(t/c)_{max}$ at a further fore chord position; increased incidence; and
3. The smaller the trailing edge angle of the original aerofoil, the shorter and the longer will the inward and the outward aerofoils, respectively, be.

The above geometric characteristics produce the following aerodynamic properties trends:

1. The inward offset aerofoils have: reduced $C_{l_{max}}$; reduced C_{l0}; reduced C_l for $(L/D)_{max}$; less intense C_m; reduced $C_{d_{min}}$ and corresponding C_l;
2. The outward offset aerofoils have: increased $C_{l_{max}}$; increased C_{l0}; increased C_l for $(L/D)_{max}$, more intense C_m; increased $C_{d_{min}}$ and corresponding C_l; and
3. The effect of the inward or outward offsets on $(L/D)_{max}$ does not present a consistent trend: $(L/D)_{max}$ depends greatly on the capability of the laminar boundary to still extend over a long distance on the upper surface and this is greatly affected by aerofoil LE and TE curvatures and also by thickness and camber distributions.

These outcomes may help design a set of compatible aerofoils suitable for finite wings of aircraft employing the telescopic concept. Nevertheless, each design case must be analysed to

select and/or develop an adequate set of aerofoils specifically for its constraints and operating conditions. In what concerns the current VSW concept that is being designed, the aerofoil that best suits the operating conditions of Olharapo III must be selected. First and foremost, before comparing each aerofoil's performance, one must decide between two possible concepts: to use an original aerofoil in the IFW whereas its respective inward offset would suit the OMW or alternatively, to use an aerofoil with outward offset in the IFW whereas its respective original aerofoil would suit the OMW. Different concepts using a smaller chord in the IFW would result in a more complex actuation system and would attain a structural penalty in the support and sliding of the OMW as well as due to the reduced aerofoil's $(t/c)_{max}$ in the root panel.

As the original aerofoils are designed for conditions similar to the current analysis, it would be naturally expected that the original, non-modified version of each aerofoil exhibit an overall enhanced aerodynamic performance for this specific operating condition, when compared with its respective offset modified versions. This aerodynamic behaviour was indeed verified for the design C_l of operation ($C_{l_{op}}$) in the range of [0.3, 0.83]. Adding the last to the fact that the IFW is constantly exposed to the airflow while the OMW is retracted or extended depending on the flight condition, IFW's aerofoil is considered to have more influence in the overall wing performance than OMW's aerofoil, thus the concept selected is the one employing the original aerofoil in the IFW and its respective inward offset in the OMW.

Besides, outward offset aerofoils benefit from an increase in $C_{l_{max}}$, with the consequence of increasing $C_{d_{min}}$, whereas inward offset present a much lower $C_{d_{min}}$ and a $C_{l_{max}}$ lower, but high enough to grant the design requirement of $C_{l_{max}} \geq 1.44 C_{l_{op}}$. Moreover, another aerodynamic advantage of selecting the inward offset aerofoil to the OMW is decreasing both maximum curvature and θ without the need to add a negative twist angle (ε) in this panel. By decreasing both maximum curvature and θ in the OMW, the aerodynamic loading decreases which is desirable for an outer wing panel hence it becomes more consistent with a finite wing ideal lift distribution that decreases along the span, from a maximum value in the root to near zero in the tip.

The set of aerofoils to suit the VSW are selected between the MH115 set, UBI-OG-010 set, SG6042 set and UBI-03-012 set, all with the previously selected LE and TE corrections, i.e. an elliptic LE and a TE extension defined by a second degree polynomial. Accordingly, an aerodynamic analysis was performed for each aerofoil set (original and inward offset) coupled for different percentages of IFW-OMW airflow exposition (100%-0%, 80%-20% and 70%-30%) and compared against each other. Furthermore, for the VSW extended configuration (100%-0%) that is intended for the fast cruise at 30 m/s, it was used $Re_d = Re_{max}$=750,000 and C_l=0.3/0.5, while for the remaining configurations, intended for slow cruise at 18 m/s, it was used $Re_d = Re_{min}$=456,000 and C_l=0.83.

For Re_{max}, UBI-03-012 is the aerofoils' set (100%-0%) with lower $C_{d_{min}}$. It has by far the lowest C_d for C_l=0.3 and the second lowest C_d for C_l=0.5, closely after SG6042. Moreover, MH115 aerofoil, followed by UBI-03-012, has the highest $C_{l_{max}}$, although MH115 has the backlash of much higher $C_{d_{min}}$. For Re_{min}, both wing configurations (80%-20% and 70%-30%) present a similar trend in regard to $C_{d_{min}}$ with exception to the 80%-20% configuration for UBI-03-012 that presents lower $C_{d_{min}}$. For the slow cruise a high $C_{l_{max}}$ is paramount and again, MH115 and UBI-03-012 present a smaller difference, the highest $C_{l_{max}}$ values. UBI-03-012 aerofoils' set presents the highest $(L/D)_{max}$ value for the the current design C_l range, which makes sense

as this aerofoil was designed purposely for the VSW operating conditions. Overall performance measured, UBI-03-012 was selected rather than MH115 and SG6042.

An additional conclusion may be attained on the aerodynamic effect due the offset value. A small inward offset value is favourable to suit the OMW, as it decreases θ although also decreases $C_l(\alpha)$. Notwithstanding, high inward offset values result in completely modified aerofoil geometries, with too low $(t/c)_{max}$ values and C_l values highly below $C_{l_{op}}$, therefore deteriorating both structural and aerodynamic performance.

Summing up, results from the aerodynamic study enabled the selection of a design that suits the IFW with the original UBI-03-012 and the OMW with the inward offset version of UBI-03-012, with a elliptic LE and x_{LE} =0.64%. UBI-03-012 $(t/c)_{max}$ is 10% at 30.35% of the chord whereas its inward offset version has a $(t/c)_{max}$ of 9.08% at 33.64% of the aerofoil chord. By knowing this, main spars may now be located in the aerofoils' thicker section. Accordingly, the beginning of the IFW main spar caps are aligned at 30.35% of the IFW chord and the outward skin of the OMW main spar web is located at 33.64% of the chord. The wing tip uses the same aerofoil as the OMW, with a decreased tip chord though.

3.2.1.4 Winglets

A preliminary wing geometry without wing tip was considered. Results from a multidisciplinary optimisation software led to the conclusion that the VSW aerodynamic performance was being highly penalised by the VSW straight geometry that was leading to a low Oswald's efficiency factor e of 0.95, an induced drag correction factor to compare 3D wings with an ideal wing with same AR and an elliptical lift distribution. So that the VSW would potentially reach a better performance than the FW, besides the essential minimisation of its structural mass, an aerodynamically efficient wing tip should be used. The wing tip device selected is a winglet. Although the inclusion of a wing tip would represent a OMW panel outer extension, causing a decrease on $l_{var_{max}}$ value for a fixed b value, it enables an increase on e hence reducing tip induced drag by decreasing the size of vortices shed by the wing tip. A larger l_{tip} leads to a higher e but with the cost of also leading to a smaller $l_{var_{max}}$. Considering these opposite trends, the design point that benefits VSW performance for different velocities is reached by using an optimisation procedure on the wing tip geometry.

Furthermore, the aircraft lateral stability analysis revealed that the dihedral effect for a straight wing design was below the admissible value for this stability derivative (C_{l_β}), hence results from the multidisciplinary optimisation software exhibited the need to add a dihedral angle (Γ) in the VSW design. Near the envelope minimum velocity, in which the wing is fully extended, the resulting Γ required for the VSW design is near 6.8°. Under other conditions, slow cruise (V_l=18 m/s and b=b_{max}=3.55 m) and fast cruise (V_c=34 m/s and b=b_{min}=2.65 m), the resulting Γ required for the VSW design is 4.4° and 2.6°, respectively. Although the critical stability design point takes place near the envelope minimum velocity, the aircraft is intended to fly below V_l values only during landing and take-off, thus Γ for the slow cruise condition is selected for the VSW design, since this flight condition is more predominant than the the minimum velocity cruise condition and more critical to lateral stability than the fast cruise condition.

The settlement of a positive Γ in the wing root has the consequence of increasing VSW inherent

complexity on structure, manufacturing and systems integration. Hence it is applied an equivalent value of Γ in the wing tip. This equivalent Γ value is found by equalling the overall wing's effective dihedral angle (EDA) to the Γ selected in the VSW design. The advantages of including twist in the wing tip are also investigated. As observed in a wing performance study, adding ε in the wing tip does not enhance performance in the current design. This comes from the fact that the OMW aerofoil has already an adequate negative θ resulting from its inward offset geometrical modification detailed in Section 3.2.1.

An EDA calculator tool [162] especially suited for determining the EDA for multi-panel polyhedral wings is used. EDA is a function of the horizontally projected area of each panel (A_p), each panel's dihedral (Γ_p) and the distance between the panel centroid and the centre of the wing (d_p) as

$$EDA = \sum A_p \Gamma_p d_p \tag{3.17}$$

Firstly, chord and panel lengths (L_p) are entered for each wing panel as well as keeping all panels' Γ null except the tip's Γ_p that is entered with an arbitrary preliminary value in radians. Secondly, A_p and d_p are computed for a 4-panel wing by

$$A_p = \cos(\Gamma_p) L_p \left(\frac{c_{p_i} + c_{p_f}}{2} \right) \tag{3.18}$$

$$d_p = \cos(\Gamma_p) L_p \left(\frac{c_{p_i}/6 + c_{p_f}/3}{c_{p_i}/2 + c_{p_f}/2} \right) + \sum \cos(\Gamma\prime_p) \tag{3.19}$$

with c_{p_i} and c_{p_f}, the panels root (initial) and tip (final) chords, respectively. $\Gamma\prime_p$ refers to the dihedral angle of all panels that are located nearer the wing root than the panel under analysis.

Thirdly, Γ_{tip} is iteratively modified until the equivalent dihedral angle reaches the design value of 4.4° previously defined. Considering the VSW average configuration, i.e. with span b_{ave} =3.10 m, the resulting Γ_{tip} is equal to 31.6°. Moreover, considering l_{tip} =0.155 m and using simple trigonometric calculations, the tip's rise at the tip panel is approximately 0.0953 m. Both b_{ave} and l_{tip} values considered in the present analysis, are further detailed in the following Section 3.2.2. Also, from these results, regarding the wing chord distribution, an optimal negative sweep angle (Λ) of 19.1° is set to the winglet.

With the tip panel geometry clearly defined, two different concepts are compared for performance. Version 1 has a constant taper ratio in the tip panel keeping the TE straight and version 2 has a near semi-elliptic taper, also with a straight TE. The aerofoil is the same as for the OMW, UBI-03-012 inward offset, with a tip chord of c_{tip} =0.18 m. In Figure 3.20, tip's version 1 has a LE discontinuity, which may be adverse in a 3D flow analysis. It is undoubtedly simpler on manufacturing though, as it could be produced as an independent straight panel and later attached to the OMW panel. Tip's version 2, on the other hand, has a smooth LE that is tangent to the OMW's LE with a vector tuner with norm equal to 1 mm that sets the LE curvature to near elliptic.

A 3D wing analysis is performed in XFLR5 v6.30, an aerodynamic tool that incorporates a XFOIL version translated to the $C++$ language and extends its application for 3D wings. Both tools

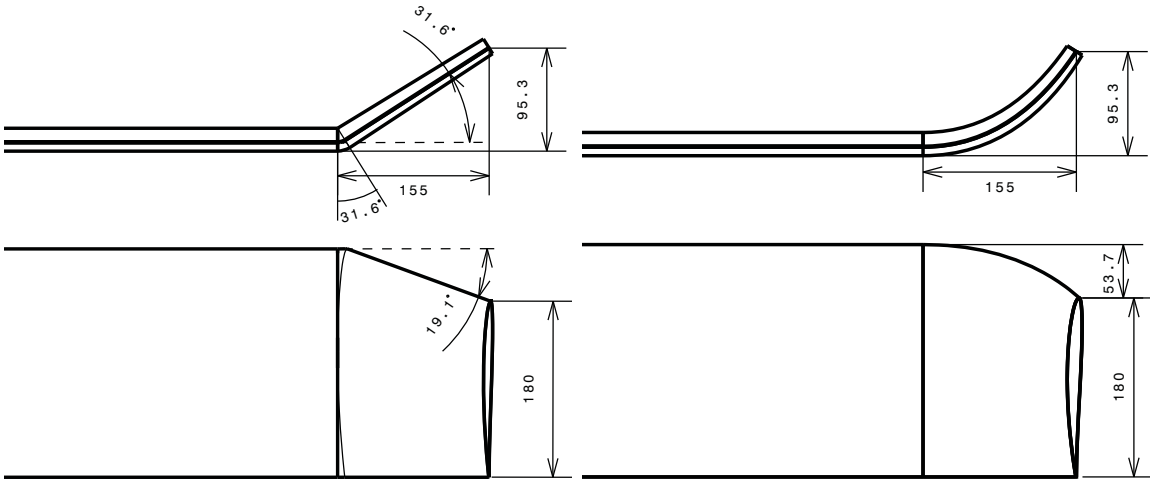

(a) Version 1 - Linear tapered tip. (b) Version 2 - Semi-elliptic tapered tip.

Figure 3.20: Wing tip technical drawings.

are only valid for low Re numbers. XFLR5 includes 3D wing design and analysis by means of three different methods. Deperrois [163] clarifies the performance capabilities of XFLR5 between model predictions and experiments. An analysis on XFLR5 may be computed from one of three methods: LLT (Non-linear Lifting Line Theory), VLM (Vortex Lattice Method) and 3D Panel Method [164]. LLT is derived from Prandtl's wing theory and only applies for very low Re numbers. It assumes implicitly that all the surfaces lie in the $z-x$ plane and also, does not use Γ and Λ in the calculation of the lift distribution. Accordingly, to properly investigate winglet performance, the LLT is not applicable.

VLM and Panel methods are essentially inviscid potential methods, assuming irrotational fluid, i.e. their calculations are independent of the wing's speed and of the air's viscous characteristics. Nevertheless, a coupling with XFOIL calculation results enables the estimation of the viscous drag associated with the wing. The author mentioned that the use of XFOIL transition results to wings with finite AR is probably the most questionable assumption of XFLR5 algorithm, although this approximation should be reasonable for wings with moderate to high AR [164]. VLM models the perturbation generated by the wing by a sum of vortices distributed over the wing's planform and its limitations are for $(t/c)_{max}$values higher than 10%, as it only considers the wing mean camber line and for high α values, as viscous variables are interpolated from C_l on the previously XFOIL-generated polars. The 3D panel method is based on Euler equations and is the method of VSAero described in NASA contractor report 4023a [165]. It is a refined full 3D method, providing insight in the C_p distributions over the wing top and bottom surfaces and taking into account the wing's thickness. Furthermore, this method is applicable to most common wing geometries, including those with non-zero Λ values, low AR, high Γ and winglets [164]. To an accurate use of the vortex lattice method (VLM), a 10% limit of aerofoils' $(t/c)_{max}$ is established. As the current wing geometry includes winglets and a $(t/c)_{max}$ slightly higher than 10%, the 3D panel method is adopted.

Aerodynamic results in Table 3.2 are obtained for a type 2 fixed lift analysis (L =150 N), using the 3D Panel Method with 3102 panel elements, Dirichlet boundary conditions and adding viscous interpolation from XFOIL results. Each tip version is analysed for two flight conditions:

Table 3.2: Aerodynamic main results for a 3D wing analysis using two different wing tips.

	Extended configuration		Retracted configuration	
	Tip version 1	Tip version 2	Tip version 1	Tip version 2
V	18	18	30	30
α	6.0	6.0	1.5	0.5
C_L	0.817	0.811	0.407	0.397
C_D	0.025	0.025	0.012	0.011
e	1.01	0.991	0.999	0.995
L/D	32.680	32.440	33.917	36.091
C_m	-0.538	-0.528	-0.318	-0.319

loiter (V =18 m/s) and fast cruise (V =30 m/s) respectively for retracted and extended VSW configurations. It may be observed that C_L is higher for the loiter condition whereas for each velocity, it is higher for tip version 1. C_D apparently is not much affected by the type of tip, but only by V. L/D values are higher for the fast cruise condition and for tip version 2. Nevertheless, for the loiter condition L/D value is higher for tip version 1. C_m values are approximately constant for each V value. The Oswald's factor (e) is an efficiency factor which is a measure of the deviations of the wing's induced drag from that of an optimal elliptic loading, and is defined as

$$e = \frac{C_L^2}{\pi\, AR C_{di}} \tag{3.20}$$

with C_{d_i}, the induced drag coefficient. For numerical reasons in 3D Panel calculations [164], e may be overestimated, whereas a refinement of the panel density in the streamwise direction is required to reduce it for values below unity. As expected, values achieved and presented in Table 3.2 for e are higher than 0,95, the e value for VSW preliminary version without tip. Moreover, e values are slightly higher for the linear tip (version 1). Whereas the semi-elliptic tip (version 2) presents an increased aerodynamic performance for the fast cruise relative to tip version 1, the increment in L/D is merely 6.4% and for loiter, it even slightly decreases. Accordingly, tip version 2 presents slight aerodynamic enhancement for fast cruise when compared to tip version 1. The opposite happens for loiter. Tip version 2 manufacturing complexity would be higher to tip version 1 though. Therefore, an option for manufacturing simplicity is made and tip version 1 is selected.

Summing up, a wing tip is added to increase aerodynamic efficiency as well as to meet the wing's stability requirements. Winglets provide all effective dihedral angle hence they enable the telescopic sections of the wing to be flat and so, decreasing the actuation system complexity that would result from a non-flat telescopic wing. Accordingly, winglets with a Γ of 31.6°, a Λ of 19.1° and no ε is added to the OMW geometry. Between the two different concepts, a tip with linear taper is selected for manufacturing simplicity.

3.2.2 Multidisciplinary Wing Sizing

All work described in previous sections of the preliminary design is a decisive intermediate step to characterize the aerofoils and wing tips to suit the VSW intended to be installed on Olharapo III UAV. Its results fed a multidisciplinary design optimisation (MDO) algorithm in order to obtain wing's final mission-optimised dimensions. The multidisciplinary and multilevel design

methodology is fully explained in Albuquerque et al [72] and has the aim of implementing a multilevel optimisation architecture as well as the physical models for a generic UAV with morphing technologies at the preliminary design stage, with the implementation of a slightly modified Enhanced Collaborative optimisation (ECO) multilevel architecture with a gradient-based optimisation algorithm.

The overall optimum aircraft layout, and, more specifically, the wing sizing for Olharapo III's mission profile is assessed to both, validate the implemented optimisation methodology and also, obtain the design optimal wing size that would match a fixed wing performance. For such, a routine that computes the aircraft performance for the user defined mission profile and vehicle's performance requirements has been implemented with the main goal of minimizing the mission-required overall energy.

First and foremost, one should acknowledge that the level of optimisation of a morphing wing as the VSW, is not possibly compared with the high level of optimisation achieved for a conventional fixed wing. The inherent characteristics of such wings, as geometrical adaptability, enable the designer to optimise wing and aerofoil only for a flight condition and configuration design point, normally an intermediate configuration or the one more frequently used during operation. Accordingly, the VSW sizing is performed for mean chord ($\bar{c}$) and average wingspan (b_{ave}) for an intermediate extension of OMW.

The case study presented in [72] clearly shows that albeit the overall structural and systems weight increase due to the use of the variable-span mechanism, it is advantageous to use the VSW rather than the FW for improving the overall aircraft performance as long as the appropriate wingspan is in use at each different mission stage. It is worthwhile to mention that these VSW's energy savings are highly dependent on the intended mission profile hence impossible to quantify the general gain of using such concept without prompting to a specific mission. Accordingly, in some cases the use of the VSW might proof of little or even negative effectiveness on decreasing overall energy, whereas in other cases, namely the ones with at least two different mission stages with a significant energy consumption, the performance impact shall be highly positive which validates the profitability of such concept. In our case, two different mission stages with a significant energy consumption are considered, as it may be acknowledged from the mission profile presented in Figure 1.6.

From the different ways of optimising a wing layout, a monolithic optimisation is generally used for conventional fixed wings in which the wingspan and wing chord are optimised for the cruise condition with possible performance limitations in all other mission stages. Alternatively, a distributed optimisation may be employed which globally optimises the wingspan and wing chord so that these will be compatible in all flight stages. The VSW concept duly employs a distributed optimisation albeit it keeps $\bar{c}$ fixed in all flight stages and optimises the b_{ave} for each mission stage. The last methodology is employed to obtain the VSW layout and performance indicators. Olharapo III mission profile parameters is used as design constraints for optimisation purposes. Moreover, the considered manoeuvre load factors (n) are +3 and -1.5. VSW's concept and mission results are presented in Table 3.3.

Results from Table 3.3 are obtained for ISA conditions and aircraft's W =150 N, integrating 28.35 N of payload, 11.46 N of flight systems, 39.49 N of energy (batteries) and assuming 70.70 N of

Table 3.3: VSW-related results of the multidisciplinary and multilevel design optimisation.

Geometrical Parameter	Value	Unit	
$\bar{c}$	0.257	m	
c_{tip}	0.180	m	
b_{ave}	3.100	m	
$l_{var_{ave}}$	0.225	m	
k_{tip}	0.1	-	
Γ	4.651	deg	
θ	2.396	deg	
Performance Parameter	**Value**	**Unit**	
RoC	3.3	m/s	
V_{stall}	14.644	m/s	
V_{TO}	15.491	m/s	
d_{TO}	56.968	m	
Mission phase	**Energy required [J]**	**Thrust setting**	**Time [s]**
Take-off	9019.6 (0.5%)	1.000	6.1
Climb_1	105058.6 (5.6%)	0.905	90.9
Loiter	965834.9 (51.2%)	0.508	3600.0
Descend_1	2248.4 (0.1%)	0.000	112.4
Climb_2	175008.5 (9.3%)	0.910	151.5
Fast cruise	623726.3 (33.0%)	0.825	833.3
Descend_2	6673.8 (0.35%)	0.000	333.7
Total	1887570.1 (100%)	-	5128.0

structural weight. In comparison with the previous VSW version, which had a wingspan of 2.5 m, the current design wingspan has increased to 3.1 m. One should acknowledge that performance parameters are found for b_{ave} hence such results are merely design indicative as better results may be found for differently extended wing configurations; for instance the actual V_{stall} is 13.6 m/s which is found for b_{max} rather than the value presented for b_{ave} wing configuration. l_{over1}, l_{over2} and l_{fus} are fixed as constant parameters. l_{over1} and l_{over2} are equal to 0.125 m and 0.025 m, respectively, and are selected based on previous experience so that bending and torsion moments can be effectively transmitted from the OMW to the IFW. l_{fus} is equal to 0.120 m and is calculated as the sum of half the width of the fuselage and a selected slot of free space to grant a safe flap's actuation.

With $l_{var_{ave}}$=0.225 m and considering $l_{var_{min}}$ =0 m, then $l_{var_{max}}$ turns to be twice the $l_{var_{ave}}$ value hence $l_{var_{max}}$ =0.45 m beeing the maximum range of operation for the variable-span mechanism. Further calculations with formulas from Section 3.1.3 are employed to find the remaining wing parameters' size as function of the settled geometrical parameters. From Eq. 3.1 and considering $l_{var} = l_{var_{max}}$, $l_{flap} \leq$0.575 m $= l_{flap_{max}}$. From Eq. 3.2, l_{tip} =0.155 m; from Eqs. 3.6 and 3.7, and with $l_{var_{ave}} = \frac{1}{2} b_{ave}$, the values of l_{ext} and l_{retr} are equal to 1.775 m (thus, b_{max} =3.550 m) and 1.55 m, respectively; from Eqs. 3.8 and 3.9, l_{OMW} and l_{IFW} are equal to 1.205 m and 1.170 m, respectively. VSW's specifications are summarised in Appendix A.

IFW and OMW final aerofoil geometries were exported from XFOIL previously to knowing the wing's $\bar{c}$ from the MDO sizing and the chord distribution was not yet established by then. Calculations for proper chord values are now required for each wing panel. An iterative study is implemented to determine c_{IFW}, c_{OMW} and c_{tip} by means of the spanwise integration of wing

chords in the form of

$$\bar{c} = \left[\int_0^{y'_{\text{IFW}}} c_{IFW} \, \mathrm{d}y + \int_{y'_{\text{IFW}}}^{y'_{\text{OMW}}} c_{OMW} \, \mathrm{d}y + \int_{y'_{\text{OMW}}}^{y'_{\text{tip}}} \frac{c_{OMW} + c_{tip}}{2} \, \mathrm{d}y \right] \frac{1}{b/2} \tag{3.21}$$

ith y'_{IFW}, y'_{OMW} and y'_{tip}, the root distance of IFW, OMW or wing-tip panels' tip position. The integral Equation 3.21 presented is applied to investigate such wing chord distribution for a VSW intermediate span configuration, i.e. using $l_{var_{ave}}$=0.225 m ($l_{var_{max}}$/2). Additionally, this formulation considers all previously computed wing parameters' results, such as c_{tip}=0.18 m, l_{tip}=0.155 m, l_{IFW}=1.170 m and so on; and comes to light as

$$c_{IFW} = \frac{0.3844 - 0.3025 c_{OMW}}{1.170} \tag{3.22}$$

To be consistent with the aerodynamic study, a 3 mm offset is again assumed between the IFW and OMW panels. From the implementation of the inward offset, detailed in Section 3.2.1, at UBI-O3-012 aerofoil and taking into account the selected LE and TE corrections, the following Equation 3.23 is drawn from the geometric modifications as

$$c_{OMW} = k_{offset} k_{LE} c_{IFW} \tag{3.23}$$

with k_{offset} and k_{LE}, the chord correction factors that account for the decrease of the modified aerofoil's chord respectively due to the inward offset and elliptic LE creation. While k_{LE} is constant and equal to 0.99361 for the established elliptic LE with x_{LE}=0.0064 (unit chord dimensions), k_{offset} is otherwise dependent on a reference chord (c_{ref}) that is the baseline wing chord as it defines the aerofoil geometric offset. Once the IFW is fitted with the original aerofoil from which the offset is performed, c_{ref} is settled as c_{IFW}. Accordingly, each calculation of c_{IFW} and c_{OMW} is directly dependent on c_{ref}, which in turn is dependent on c_{IFW}. The aerofoils offset is kept equal to 3 mm, but c_{ref} is variable though and therefore, the system of Eqs. 3.22 and 3.23 needs to be computed iteratively to perform successive approximations of c_{ref} equal to c_{IFW} from the last iteration ($c_{IFW_{i-1}}$). The iterative process is supported by a set of Microsoft Excel® workbooks. For each iteration, one workbook creates a new aerofoil by performing the offset, LE and TE corrections for c_{ref} of the current iteration and generates its respective coordinates. A second workbook extracts k_{offset} and computes the system of equations to obtain a new VSW chord distribution for the previously obtained offset aerofoil. A new set of c_{IFW} and c_{OMW} values is obtained and if convergence is not reached, a new set of workbooks is created and a new aerofoil is generated for the next iteration. As presented in Table 3.4, these workbooks together with the system of equations (see Eqs. 3.22 and 3.23) enabled the iterative calculation of c_{IFW} and c_{OMW} with a stopping criteria below 0.1% measured by the percent relative error ($\delta = \left| \frac{c_{ref} - c_{IFW}}{c_{ref}} \right| \times 100$).

Table 3.4: VSW chord distribution iterative study.

i	c_{ref} [mm]	k_{offset}	k_{LE}	c_{IFW} [mm]	c_{OMW} [mm]	δ [%]
1	280.0	0.8670	0.9936	267.84	234.81	4.34
2	267.84	0.8768	0.9936	268.15	233.61	-0.11
3	268.15	0.8770	0.9936	268.14	233.64	0.003

As presented in Table 3.4, the iterative process quickly converged for c_{IFW} and c_{OMW} values of 268.1 mm and 233.6 mm, respectively. Re values are directly proportional to c values, as one may observe in Eq. 3.16. Therefore, as the chord distribution is now defined, IFW, OMW and tip's aerofoils' aerodynamic characteristics need to be redetermined for its respective Re. Instead of the Re_d value considered in the preliminary aerofoil study for the fast cruise, Re values may now be computed, for the same flight condition, in the form of

$$Re_{IFW} = Re_d \frac{c_{IFW}}{c}$$

$$Re_{OMW} = Re_d \frac{c_{OMW}}{c}$$

$$Re_{tip} = Re_d \frac{c_{tip}}{c}$$

With c =280 mm, the design chord previously used in the preliminary aerofoil study to determine Re_d =686,000. Using c_{IFW} =269.03 mm, c_{OMW} =230.20 mm and c_{tip} =180.0 mm, one obtains Re_{IFW} =659123.5, Re_{OMW} =563,990 and Re_{tip} =441,000 for the fast cruise. For the loiter condition, Re values are found by multiplying the previous results by (18/30). Finally, with the aerofoils and type of offset selected and also, the chord distribution defined, an iterative aerodynamic study using XFOIL is performed to select the highest performing inward offset aerofoil between different elliptic geometries defining the LE. For this purpose, the aerofoil's x_{LE} is iteratively changed and all remaining geometric constraints are kept constant. This simple geometric modification resulted in different elliptic geometries that are afterwards aerodynamically compared amongst each other for respective Re values, due to chord variations in the OMW aerofoil.

Three preliminary x_{LE} values are selected (0.10, 0.13, 0.16) followed by other three (0.0, 0.32, 0.64). The step between values in each group is maintained constant for easier comparison and application of the bisection method. The LE modifications displayed minor effect on both $C_{d_{min}}$ and $(l/d)_{max}$, with the last varying between 118 and 122 (3.4% variation), for the highest and lowest x_{LE} values, respectively. On the other hand, its effect on $C_{l_{max}}$ is substantial, varying between 1.25 and 1.55 (24% variation), with the highest x_{LE} value, i.e. lowest chord and highest LE radius, the best performing geometry for both groups. Consequently, a third study is performed for higher x_{LE} values (0.64, 0.8, 0.96) that led for a fourth group using the bisection method (0.64, 0.72, 0.8). Concerning the last case, $C_{l_{max}}$ is slightly higher for higher x_{LE}, whereas $(l/d)_{max}$ is considerably higher for the lowest x_{LE} and therefore, x_{LE} =0.64% is finally selected.

Summing up, the IFW panel is fitted with the original UBI-03-012 aerofoil with a 268.1 mm chord and the OMW with the inward offset version of UBI-03-012 with an elliptic LE, x_{LE} =0.64% and a 233.6 mm chord. The wing tip makes use of the same aerofoil as the OMW, but with a decreased chord of 180.0 mm. VSW final aerofoil data is documented in Appendix B.

3.2.3 Selection of Applicable Materials

The VSW structure is made of a combination of five main materials which provide proper strength and stiffness. Such materials are: a laminated bidirectional CFRP, for the external faces of the skin sandwich structure; a polymeric foam, for the core of the skin sandwich; a pultruded

unidirectional carbon-epoxy profile, for the spar caps; a laminated unidirectional CFRP, for the transversal reinforcements and plywood, for the wing ribs. The actuation system is composed by different components with different materials, being the most relevant: aluminium and zinc alloys, plywood, oil-filled cast nylon, PTFE Extruded film tape and hardened stainless steel (e.g. gearbox output shaft). Altogether, the VSW design makes use of several materials with different properties that together fulfil its functionality and structural requirements.

The current design makes extensive use of composites of carbon fibre. In the late 60's, carbon fiber became a serious material for lightweight applications. The several advantages composites have to offer in aircraft applications is well documented in the literature [166]. Carbon fibre properties, such as high stiffness, high tensile strength, low weight, high chemical resistance, high temperature tolerance and low thermal expansion, make it one of the most desirable materials by the industry. Moreover, the specific strength and elastic modulus of fibre composites are higher than other comparable metallic alloys. For the industry it means greater weight savings resulting in improved aircraft's performance, greater payloads, longer range and fuel savings.

There are two types of carbon fibers in species, one is polyacrylonitrile (PAN)-based carbon fiber made of acrylic fibers and the other is pitch-type made of coal tar or petroleum. PAN-based carbon fibers are more widely used. In Figure 3.21 it may be observed the great advantage of composites on its multiplicity of applications from low to high modulus and low to high strength. Moreover, the plot uses specific tensile strength and specific modulus that are strength and modulus parameters divided by the materials' density. Such figures of merit are highly useful for applications in which both mechanical properties and low weight are important [167].

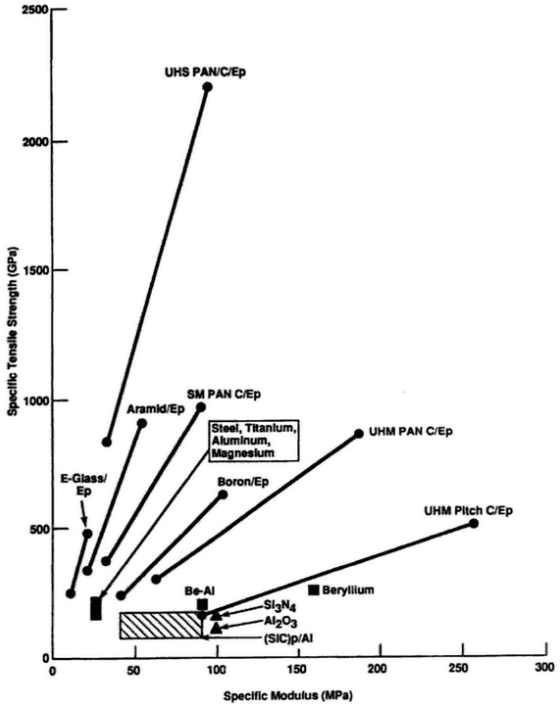

Figure 3.21: Specific tensile strength vs specific modulus of composite materials compared with metals and ceramics [167].

Several classifications are given to different types of carbon fibre fabrics in mechanical proper-

ties: ultra high elastic modulus (UHM), high elastic modulus (HM), intermediate elastic modulus type (IM), standard elastic modulus (SM) which is also known as hight tensile strength (HS); low elastic modulus (LM) and ultra high tensile strength (UHS). In the VSW design, a HS carbon fiber fabric, REBELCO® 090P 1000 (95 g/m^2, is selected. It is a plain weave bidirectional fabric with 50% warp and 50% weft. The fabric string is a TORAICA® T300 (1.76 g/cm^3) with a tensile strength of 3,530 MPa, tensile modulus of 230 GPa and strain of 1.5 %. The epoxy resin selected is Biresin® CR122. This is a medium viscosity epoxy resin (1170 kg/m^3) suitable for the production of high performance CFRP composites with a thermal performance up to 120°. Biresin® CH122-3 (940 kg/m^3) is the hardener selected which must be mixed in a weight proportion of 3 to 10 part to the epoxy resin.

The load-carrying skin is a sandwich-structured composite composed by, from inside out, a set of layers of bidirectional ($\pm 45°$) laminated carbon-epoxy composite (1600 kg/m^3), a core of 2 mm polymeric closed-cell, cross-linked rigid foam (100 kg/m^3) and finally, another set of layers of bidirectional ($\pm 45°$) laminated carbon-epoxy composite (1600 kg/m^3). Airex® C70.90 is a red foam with excellent rigidity and a great stiffness to weight ratio. It can be processed with all common resin systems and processes. The manufacturer states that this foam is the ideal core material for many lightweight sandwich structures subject to dynamic or static loads. Moreover, its fine cell structure supports excellent adhesion of face sheets keeping low resin absorption. The properties of the skin sandwich faces are assumed for a hand lay-up procedure with vacuum curing of the carbon fibre fabric impregnated with epoxy resin. Carbon fibre fabrics are plain weave and layers' orientation of $\pm 45°$ is with respect to the wingspan direction.

The four spar caps, which are longitudinally integrated into the skin sandwich, are thin rods with a rectangular cross-section and are made of HS pultruded profiles of unidirectional carbon-epoxy composite. The manufacturer is vDijk Pultrusion Products (DPP) specialised in reliable, high-grade pultrusion products. Such rods combine the unique properties of composite materials within very close tolerances, and the advanced highly-automated pultrusion technologies developed by DPP [168]. Transversal reinforcements applied in critical sections of the IFW are made of unidirectional laminated carbon-epoxy composite. Similarly to the skin faces, they are in-house manufactured by a hand lay-up procedure with vacuum curing. The fabric selected is REBELCO® 125U 1000, an unidimensional carbon fiber fabric with 80% warp and 20% weft.

All ribs were initialy designed with balsa wood. Due to the added complexity of modelling woods' bilinear properties, Airex® PVC is selected. Moreover, foams are linear isotropic materials which clearly is more manageable for structural analysis. Material properties for TORAICA® T300 carbon fabric strings, Biresin® CR122 epoxy resin, DPP^{TM} pultrusion profiles, Airex® polymeric foam, Ertalon® LFX oil-filled cast nylon and 3M^{TM} PTFE extruded film tape are obtained from the manufacturers' datasheet.

The actuation system is made of a mix of metals and polymers, with higher use of: aluminium alloys (2700 kg/m^3), in servomotors and mounting hubs; zinc alloys (7130 kg/m^3), in brackets and in some servomotors' parts; oil-filled cast nylon sheets (1135 kg/m^3), in the rack spurs and spur gears; teflon film (2200 kg/m^3) for surfaces in contact and birch plywood (approximately 600 kg/m^3), in the actuation system supporting board, fixing components and rack curbs. Also hardened stainless steel is slightly present in some highly loaded parts that have propensity for fatigue as for example, the gearbox output shaft.

Ertalon® LFX oil-filled nylon sheets are cast polyamide 6 (or nylon 6). This material is self-lubricating, specifically developed for unlubricated moving parts applications, presenting good sliding properties. It has half the coefficient of friction when compared with common nylon materials and up to ten times the wear resistance. It has high mechanical strength (above 70 MPa) and good fatigue resistance. Another used material for friction reduction is 3M™ PTFE Film Tape. PTFE is polytetrafluoroethylene, more commonly known as teflon. Extruded PTFE film tape is glued to the IFW's upper and lower inner surfaces to drastically reduce friction between moving surfaces. Its backing thickness is 0.13 mm which lies flatter when applied. Birch plywood is used for the supporting board.

3.2.4 Actuation System

The actuation system is an assembly of different components that together are assigned to drive and control the OMW's motion for symmetric or asymmetric wingspan variation. The system is actuated by a electromechanical mechanism that encloses, for each wing moving panel, a set of components: a gearmotor, a controller, a feedback, a rack spur, two spur gears (pinions), a mounting hub and two brackets. To use a DC gearmotor in the place of a servomotor, the position sensing as well as a feedback to the controller needs to be externally added. Still, a major benefit on using DC gearmotors is that they offer more power than servomotors with same size or same price. Moreover, they provide direct control over the given pulse width modulation (PWM) signal, hence torque is user-adjustable. So being, for each wing moving panel a rack spur and a servomotor set are used. The latter comprises a gearmotor, an external controller, a feedback and a mounting hub. Additionally, on each gearmotor and feedback, an aluminium bracket secure mounting, a properly sized spur gear for the feedback-gearmotor link and a gearmotor-rack link are used. The gearmotor-rack link is intended to transfer the mechanical motion for the OMW panel, when actuated by the servomotor.

Two different actuation concepts are analysed for functionality. On one hand, the rack spur is fixed to the IFW panel and the servomotor's position is variable depending on l_{var}, with the servomotor being attached to the OMW root rib. On the other hand, the servomotor is fixed to the IFW and the rack spur moves according to the OMW motion. While the former concept is lighter as it requires a shorter rack spur, the last is adopted for geometrical reasons as the actuation system does not fit inside both VSW panels. Here, the aerofoils' low $(t/c)_{max}$ is a concerning aspect for the servomotor-rack integration and proper motion inside the wing. Moreover, the impossibility of embodying the overall actuation system inside the center wing panel, led to the design option of occupying some fuselage volume. This option granted that all actuation components fit inside the aircraft without further parasite drag and are accessible for maintenance when the wing is disassembled from the fuselage. Buckling is critical for the structural integrity of rack spurs. Accordingly, a plywood stringer with higher relative stiffness than the oil-filled cast nylon is selected and applied to the rack spur fraction that is not in contact with the spur gear.

Three design constraints are considered for designing such actuation system:

1. The force generated by the gearmotor should be above the force required for the OMW actuation and motion inside the desired speeds range;

2. The selected gearmotor must have a 12 V rated voltage; and

3. All spur gears must have a diameter between 0.03 m (not too small for handling) and twice the IFW's maximum thickness.

By applying these constraints to the following methodology, gearmotors are selected and respective spur gears sized. Both VSW extended and retracted configurations are employed for comparison. The force required for the system actuation (F_{sys}) is calculated as

$$F_{sys} = F_{friction} + F_{inertia} = \mu F_{normal} + m_{OMW} a \tag{3.24}$$

with $F_{friction}$, the actuation force for static friction between wing panels; $F_{inertia}$, the inertial force that resists to OMW motion's changes in velocity; μ, the static friction coefficient between panels' materials; m_{OMW}, the OMW mass; a, the acceleration imposed to the OMW and F_{normal}, the normal (vertical) force due to lift applied to the OMW (including tip), which comes as follows

$$F_{normal} = L \frac{S_{OMW}}{S} \tag{3.25}$$

with S_{OMW}, the air-exposed OMW planform area (including tip); S, the wing air-exposed planform area and L, the wing lift, given by the product of the aeroplane $MTOW$ with n. A design n equal to three is considered.

Friction between panels is reduced by using PTFE tape as previously explained. μ values for teflon vary between 0.02 and 0.1. Because a precise μ value for PTFE-carbon friction, the highest value (0.1) is used in the current design for a conservative approach. Furthermore, as the contact area between panels is smaller for the extended configuration, the compression force can not be kept negligible, hence a conservative 20% increment on μ is assumed for this configuration. Considering Olharapo III specifications and VSW geometry, it is found that the extended configuration requires a higher $F_{friction}$ value (16.17 N), due to higher S_{OMW} and μ, than the retracted configuration (3.86 N), being the extended configuration the critical one to be used on the actuation system sizing.

To obtain $F_{inertia}$, two operating conditions need to be considered: OMW motion for performance (1) or OMW motion for performance and control (2). Whereas the former requires lower actuation velocities only for lift variation, the latter requires increased velocities on asymmetric actuation for controlling roll. The top velocity of the rack, in a linear motion, is defined to be not lower than 0.025 m/s and 0.25 m/s for the condition 1 and 2, respectively. So that the time to reach actuation top velocity from stationary condition is 1 s and 1/4 s, the required acceleration to the OMW is 0.025 m/s^2 and 1 m/s^2 for the condition 1 and 2, respectively. The distance of the acceleration course is 0.005 m and 0.03125 m and finally, the full l_{var} motion is actuated in a total time, including the acceleration course followed by linear motion at top velocity, of 18.5 s and 1.925 s, respectively. Such values are employed for the current actuation system sizing. Considering a values presented and assuming m_{OMW} equal to 0.5 kg, $F_{inertia}$ is 0.0125 N or 0.50 N, and F_{sys} is approximately 16.18 N or 16.67 N, depending if the operation is for performance only (1) or also control (2), respectively.

It is perceived that F_{sys} highly depends on $F_{friction}$ but only slightly on $F_{inertia}$. Moreover, the condition 2 will be considered hereinafter as it is the most critical and the VSW is intended

also for roll control. From the first design constraint, the force generated by the gearmotor ($F_{gearmotor}$) to be selected must be higher than 16.67 N. $F_{gearmotor}$ is a function of parameters commonly given in technical specifications, which are free-run rotation speed, in rotations per minute (RPM) and stall torque (τ), in Nm. The equation considered is

$$F_{gearmotor} = \tau \frac{\omega}{V} \tag{3.26}$$

with V, the actuation top velocity and ω, the angular velocity calculated by

$$\omega = \frac{2\pi}{60} RPM$$

For the gearmotor selection, a factor of safety (FS) of 1.5 is used, hence the minimum acceptable $F_{gearmotor}$ value in the current design is 25 N ($F_{sys} \times FS$). Considering that the IFW maximum thickness is approximately 0.026 m, from the third design constraint, pinions' diameter must be in the interval [0.03, 0.05] m. The diameter of gearmotors' pinions (D_{pinion}) is measured as

$$D_{pinion} = \frac{2V}{\omega} \tag{3.27}$$

Although brushless gearmotors generally have higher efficiency and lifespan, brushless outrunners exhibit low torque at low angular velocities and regarding brushless inrunners, it is harder to find a suitable controller. Accordingly, brushed gearmotors are to be selected from Pololu® catalogue for cylindrical brushed DC metal gearmotors. The selection must address the second design constraint, thus only gearmotors with 12 V of rated voltage are considered. From those, 25D high-power (HP), 25D medium-power (MP) and 27D classes with stall current at 12 V of 5.6 A, 2.1 A and 5.0 A, respectively, are compared to suit the first and third design constraints.

Table 3.5 exhibits the available DC metal gearmotors in Pololu® catalogue with 12 V of rated voltage and excluding the 25D low-power type that do not generate enough actuation force. Considering the third design constraint, the most suitable candidates would be both 100 and 130 RPM from 25D-HP type; the 100 RPM from 25D-MP type and 100 and 150 RPM from 37D type. All of these candidates present higher $F_{gearmotor}$ than the design minimum value from the first design constraint, hence the selection is targeted to a minimum mass and maximum power in excess. Accordingly, 37D gearmotors are eliminated due to presenting more than twice the mass. Otherwise, 25D-HP and 25D-MP gearmotors present similar mass between each other, so the one achieving higher $F_{gearmotor}$ is selected, i.e. the gearmotor with 130 RPM from 25D-HP type: *47:1 Metal Gearmotor 25Dx52L mm HP 12V with 48 CPR Encoder* [169], is selected. This gearmotor consists of a cylindrical, high-power, 12 V brushed DC motor combined with a 46.85:1 metal spur gearbox. It has an integrated encoder on the motor shaft that provides 2248.86 counts per revolution of the gearbox's output shaft. The gearmotor's diameter is slightly under 25 mm and has a D-shaped shaft with 4 mm in diameter. Its key specifications at 12 V are: 210 RPM and 300 mA free-run, 12 kg.cm and 5.6 A stall.

The selected controller is the *Pololu Jrk 12v12 USB Motor Controller with Feedback* [170], as it is the controller with highest power from those including feedback in Pololu® catalogue. It is a highly configurable brushed DC motor controller that supports four interface modes, with a continuous output current of approximately 12 A (30 A max) and the operating range of 6–16 V

Table 3.5: Pololu® DC metal gearmotors with 12 V of rated voltage.

Type	RPM @12V	τ @12V [Nm]	D_{pinion} [m]	$F_{gearmotor}$ [N]	Mass (w/ encoder) [kg]
25D-HP	10200	0.039	0.0005	165.9	0.06
	2250	0.162	0.0021	153.1	0.095
	1030	0.311	0.0046	134.1	0.095
	500	0.600	0.0095	125.7	0.098
	290	0.847	0.0165	102.9	0.101
	210	1.165	0.0227	102.5	0.101
	130	1.695	0.0367	92.3	0.104
	100	2.118	0.0477	88.7	0.104
25D-MP	7800	0.019	0.0006	62.3	0.06
	1700	0.078	0.0028	55.3	0.095
	770	0.155	0.0062	50.1	0.095
	370	0.297	0.0129	46.0	0.098
	220	0.445	0.0217	41.0	0.101
	160	0.600	0.0298	40.2	0.101
	100	0.883	0.0477	37.0	0.104
	76	1.165	0.0628	37.1	0.104
	43	1.765	0.1110	31.8	0.107
	33	2.260	0.1447	31.2	0.107
37D	500	0.593	0.0095	124.2	0.215
	350	0.777	0.0136	113.9	0.215
	200	1.200	0.0239	100.6	0.225
	150	1.412	0.0318	88.7	0.225
	100	1.554	0.0477	65.1	0.23
	80	1.765	0.0597	59.2	0.235

(with transient protection up to 40 V). The feedback is a potentiometer, the *Multi Turn Wire-wound Potentiometer - 534: 10 Turns, 5* $k\Omega$, from Vishay®. It is a rotational potentiometer with 22.2 mm in diameter, mechanical and electrical rotation capability of ten turns and resistance of 5 $k\Omega$.

A CAD representation of the actuation system integration with its components' location and attachments to the IFW structure, is presented in Figure 3.22. In this figure, the upper surface skin cover is hidden for simplicity. A plywood board is added to support the actuation system and small plywood curbs keep the contact distance between racks and spur gears. PTFE film tape is added, to reduce friction between components. It is applied in the inward surface of the IFW to reduce friction between panels' surfaces and also in the bottom of the plywood curbs to reduce friction due to the movement of rack spurs.

Not presented in Figure 3.22 are PTFE film tape, electric cables and links, among others. Although drowned in the CAD, the mounting hubs are not observable due to the selected render view. Table 3.6 details the mass properties of the actuation system main components.

Although components with "*" are not part of the actuation system, the actuation system has an impact on their sizing, hence the mass increment due to the actuation system's loads on such components is given in Table 3.6. To make it perfectly clear, the mass presented for components with "*" is only the mass fraction of such components due to the actuation system loads. Overall, one concludes that the mass of the actuation mechanism is 0.325 kg, which represents 2.3% of the aeroplane design MTOM.

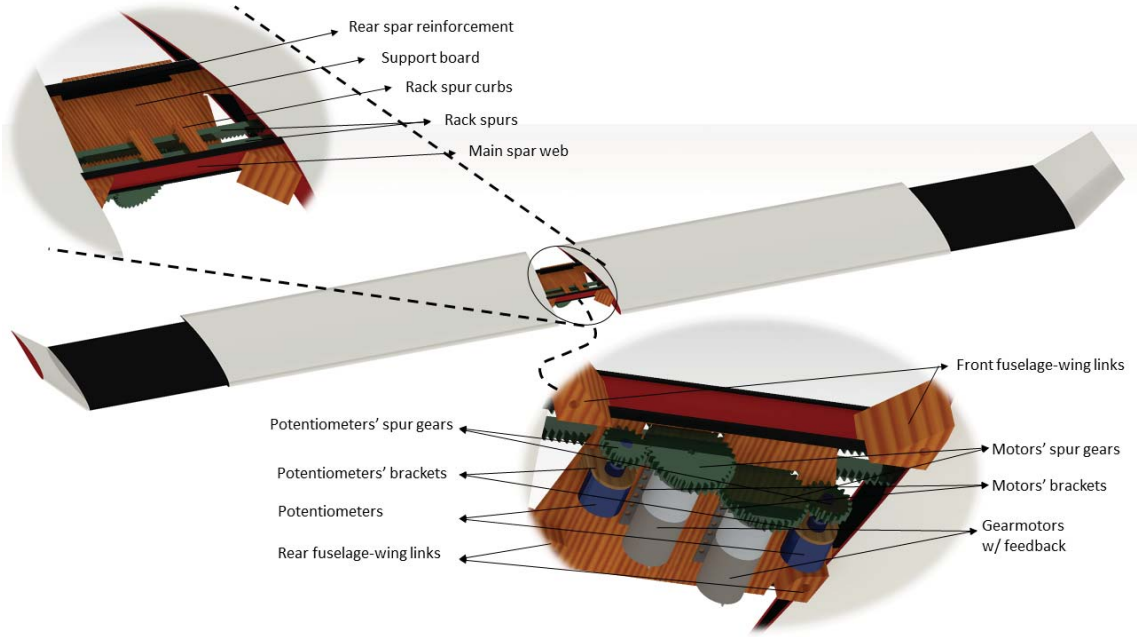

Figure 3.22: Actuation system's components assemble.

Table 3.6: Actuation system's components mass properties

Components	Gearmotors	Controllers	Potentiometers	Rack Spurs
Volume [x10^{-5} m^3]	4.882	1.611	1.504	8.088
Density [kg/m^3]	-	-	-	1135
Mass [kg]	0.110	0.014	0.020	0.092

Components	Motors' Spur Gears	Pot. Spur Gears	Motors' Brackets	Pot. Brackets
Volume [x10^{-5} m^3]	1.872	0.458	0.482	0.04
Density [kg/m^3]	1135	1135	7130	7130
Mass [kg]	0.021	0.005	0.034	0.003

Components	Mounting Hubs	Support Board	Rack Spur Curbs	PTFE Film Tape
Volume [x10^{-5} m^3]	0.232	6.41	0.492	0.211
Density [kg/m^3]	2700	600	600	2200
Mass [kg]	0.006	0.040	0.003	0.005

Components	Spar Web*	Root ribs*	Fuselage-wing link*	Totals
Volume [x10^{-5} m^3]	0.135	0.294	0.976	27.688
Density [kg/m^3]	600	600	600	-
Mass [kg]	0.001	0.002	0.006	0.361

3.2.5 Technical Drawings

With the wing layout defined as in Section 3.1, the wing sized by a FEM optimisation presented in Chapter 4 and with all the dimensions needed extracted from Section 3.2.2, a 3D CAD representation of the VSW is conducted with the commercial software *CATIA V5*.

The methodology employed during the development of the CAD focused on being flexible, so

that the need for a mid-course change at aerofoils, geometry or any wing component sizing, would not compromise the CAD functionality without deep modifications. This was crucial for the conceptual and preliminary design phases characterized by a permanent iterative process. 2D technical drawings are produced from CAD drawings and may be found in Appendix C.

3.3 Wing Loading Analysis

3.3.1 Methodology

So that a precise wing structural analysis may be performed (see Chapter 4), the aerodynamic loading applied to the wing structure should be beforehand investigated. For such, CS-VLA, Book 1 (Airworthiness Code), Subpart C - Structure [152], is extensively used.

The aerodynamic analysis of the VSW concept is employed for three wing configurations assuming symmetrical flight conditions. The configurations selected are: the wing fully extended, the wing with an intermediate span configuration and the wing fully retracted. Manoeuvre and gust diagrams (V-n) that plot air flight speeds versus design load factors, are used to find the critical design points to feed the aerodynamic analysis. Flight load factors represent the ratio of the aerodynamic force component (acting normal to the assumed longitudinal axis of the aeroplane) to the weight of the aeroplane. A positive flight load factor is one in which the aerodynamic force acts upward, with respect to the aeroplane [152].

Considering VSW characteristics, its design air speeds and assuming a steady standard atmosphere (ISA conditions), the operating flight conditions are obtained. C_L values for each mission phase are obtained from the optimisation design software introduced in Section 3.2.2 and corresponding V values for each mission phase and wing configuration resulted from a 3D aerodynamic analysis performed in XFLR5. To account with out-of-mission flight conditions, EASA CS-VLA 335 [152] is applied to determine flight parameters at further design points. Accordingly, positive and negative stall velocities (V_{s+} and V_{s-}), design dive speed or maximum operating velocity (V_D) and manoeuvring speed for minimum turn radius (V_A) are determined. Considering steady level flight, V_D and V_{stall} are determined as follows

$$V_D = 1.25 V_c \tag{3.28}$$

$$V_{stall} = \sqrt{\frac{W}{\frac{1}{2}\rho S C_{l_{max}}}} \tag{3.29}$$

To compute the Eq. 3.29, one must change S for each wing configuration and considering a fixed W, V_{stall} is found for corresponding $C_{L_{max}}$. The positive stall lift coefficient ($C_{L_{max}+}$) is assumed as 90% of the design maximum lift coefficient $C_{L_{max}}$ and the negative stall lift coefficient ($C_{L_{max}-}$) is assumed as 50% of $C_{L_{max}+}$. Although the accuracy of these approximations is difficult to assess, these assumptions are adequately conservative since experience dictates that such values tend to be higher than the ones assumed. Equations from EASA CS-VLA 341 [152], that account for a symmetrical vertical gust in steady level flight, are used to design the gust envelope. Gust load factors may be computed as follows

$$n_{gust} = 1 + \frac{\frac{1}{2}\rho_0 V a' K_g U_{de}}{g m_S^{\S}} \tag{3.30}$$

$$\text{where } K_g = \frac{0.88_g}{5.3 + {}_g}; \tag{3.31}$$

$$\mu_g = \frac{2m/S}{\rho\,\bar{c}\,a'} \text{ and} \tag{3.32}$$

$$U_{de} = \begin{cases} 7.62\text{m/s at} V_D \\ 15.24\text{m/s at} V_c \end{cases} \tag{3.33}$$

with K_g, the gust alleviation factor; U_{de}, the derived gust velocities referred to in CS-VLA 333(c); μ_g, the aeroplane mass ratio; ρ_0, the air density at sea level; ρ, the air density at flight level; m/S, the wing loading; g, the acceleration due to gravity; $\bar{c}$, the mean geometric chord and $a\prime$, the aeroplane/wing normal force coefficient curve slope per radian. For the latter, as CS-VLA 341 [152] explains, "the wing lift curve slope CL per radian may be used when the gust load is applied to the wings only and the horizontal tail gust loads are treated as a separate condition". Therefore, as the current work accounts for the wing design only, a' is assumed equal to $\frac{\mathrm{d}C_L}{\mathrm{d}\alpha}$.

For each wing configuration, three manoeuvre V-n diagrams and three gust V-n diagrams are developed and merged together, to obtain three V-n combined-diagrams. The wing design must comply with strength and stiffness requirements at any combination of velocity and load factor that is within the boundaries of the flight envelope. Nevertheless, in accordance with Niu [171] at an initial and preliminary design stage, a number of load cases may be analysed when designing a wing structure. Accordingly, from each V-n combined-diagram, the critical operating flight conditions must be selected for the loading critical design points for torsion and bending, so that a combination of relevant V-n data is selected for the VSW structural analysis.

A 2D aerodynamic analysis using the selected IFW and OMW aerofoils is established in XFOIL at a suitable interval of Re numbers and subsequently, a full-wing 3D aerodynamic analysis for the three VSW configurations is implemented. This analysis is aimed to find the V design values to be introduced in the V-n diagrams. An iterative study is performed by varying α values with the aim of finding the V values for which the wing presents a C_L equal to the C_L of each mission phase. This study is performed for each of the three considered wing configurations by setting a fixed L and varying V and α values. With wing's α and V values that correspond to each flight operating condition, the lift distributions, viscous drags, induced drags and pitching moments are estimated for each wing configuration using XFLR5.

Thereafter, using this data file, three wing loading polynomials (for lift, drag and pitching moment) are fitted for the selected combination of V, α and wing configuration. Spanwise loading distribution of the VSW is obtained by integrating equations along b. Moreover, these loadings are spanwise unit scaled and are converted into non-dimensional distributed loads ($q_L\prime, q_D\prime, q_M\prime$) to achieve a flexible model that adjusts the loading magnitude relatively to wing size variations. Load factors as well as safety factors are only considered in the following structural analysis. Accordingly, a cruise leveled flight with n equal to unity is considered. Using the span i^{th} section distributed coefficients generated from the wing aerodynamic analysis ($C_L(i)$, $C_D(i)$ and $C_M(i)$), the L, D and M loads may be integrated as follows

$$L = \int_0^b \frac{1}{2}\rho V^2 c(i) C_L(i) dy \tag{3.34}$$

$$D = \int_0^b \frac{1}{2}\rho V^2 c(i) C_D(i) dy \tag{3.35}$$

$$M = \int_0^b \frac{1}{2}\rho V^2 c(i)^2 C_M(i) dy \tag{3.36}$$

with b, the wing span for each wing configuration and $c(i)$, the chord in the i^{th} section at a span position. As $C_L(i)$, $C_D(i)$ and $C_M(i)$ are discretised in i^{th} sections along the span, the formulation is altered from integrals to summations. Spanwise distributed coefficients are therefore calculated by applying algebraic transformations in the previous Eqs. 3.34, 3.35 and 3.36 and resulting in the succeeding equations

$$C_L = \frac{\left[\sum_{i=1}^{N} c(i) C_L(i) \left(y_i - y_{i-1}\right)\right]}{S} \tag{3.37}$$

$$C_D = \frac{\left[\sum_{i=1}^{N} c(i) C_D(i) \left(y_i - y_{i-1}\right)\right]}{S} \tag{3.38}$$

$$C_M = \frac{\left[\sum_{i=1}^{N} c(i)^2 C_L(i) \left(y_i - y_{i-1}\right)\right]}{S} \tag{3.39}$$

with N, the number of spanwise i^{th} sections and y_i, the wing length at each i^{th} section, with values between zero and b from the left to the right wing tips. The IFW chord is selected as the model reference chord ($c = c_{IFW}$). For simplicity of the model, $L = W$, $D = W\left(\frac{C_D}{C_L}\right)$ and C_M are assumed as constant along the span. Thereafter, spanwise distributed loads (q_L, q_D, q_M) result from modifying Eqs. 3.37, 3.38 and 3.29, as follows

$$q_L = \frac{W}{b}\left(\frac{C_L(i)c(i)}{C_L c}\right) \tag{3.40}$$

$$q_D = \frac{W}{b}\left(\frac{C_D}{C_L}\right)\left(\frac{C_D(i)c(i)}{C_L c}\right) \tag{3.41}$$

$$q_M = \frac{1}{2}M\left(\frac{C_D(i)c(i)^2}{C_L c^2}\right), with M = \frac{1}{2}\rho V^2 C_M S c \tag{3.42}$$

These equations model how the wing is spanwise loaded. To enable the application of the previous loads at differently sized wings and different flight conditions, non-dimensional spanwise distributed loads ($q_L\prime, q_D\prime, q_M\prime$) are obtained by scaling each y_i by b, i.e. $y_i\prime = \frac{y_i}{b}$. By implementing these alterations to Eqs. 3.40, 3.41 and 3.42,non-dimensional spanwise distributed loads are defined as

$$q_L\prime = q_L\frac{L}{W} = \frac{C_L(i)c(i)}{C_L c} \tag{3.43}$$

$$q_D\prime = q_D\frac{D}{W\frac{C_D}{C_L}} = \frac{C_D(i)c(i)}{C_D c} \tag{3.44}$$

$$q_M\prime = q_M\frac{M}{\frac{1}{2}\rho V^2 C_M c^2 b} = \frac{C_D(i)c(i)^2}{C_L c^2} \tag{3.45}$$

As it may be observed from Eqs. 3.43, 3.44 and 3.45, the non-dimensional spanwise distributed loads are scaled by wing parameters (b, c, S), aircraft characteristics (W) and flight conditions (V, ρ). Therefore, the resultant loading may be applied in differently sized wings and flight conditions. For such, one needs to multiply the $q_L\prime$, $q_D\prime$ and $q_M\prime$ functions by the actual values of these variables. In the VSW design, Eqs. 3.40, 3.41 and 3.42 are used to describe the wing loading.

3.3.2 Loading Results

By adopting the methodology presented, an aerodynamic analysis is conducted to the wing loading of Olharapo III VSW. Olharapo III MTOW is 150 N and the considered manoeuvre load factor is equal to 3, so the design wing lift is 450 N ($L = Wn$). The morphing wing has a $\bar{c}$ of 0.257 m, a b_{max} of 3.554 m in the full extended configuration and a b_{min} of 3.104 m in the full retracted configuration. The variable-span fraction ($\bar{l}_{var}$) that performs morphing is approximately 0.254 (25.4% of $b/2$) for the full extended configuration, which corresponds to a a l_{var} of 0.45 m. The intermediate span wing configuration is achieved for a l_{var} value of 0.225 m.

Considering the VSW characteristics, its design air speeds and assuming a steady standard atmosphere (ISA conditions), the operating flight conditions are obtained to be plotted in a V-n diagram. C_L values for each mission mission phase are obtained from the optimisation design software introduced in Section 3.2.2. V values for each mission phase and wing configuration are found by an aerodynamic analysis in which α values are iteratively modified until obtaining the V that corresponds to each C_L. Results are presented in Table 3.7.

Table 3.7: Velocities and lift coefficients for each mission phase.

Mission phase	C_L	l_{ext} =1.775 m	l_{ave} =1.550 m	l_{retr} =1.325 m
		V [m/s]		
Take-off	0.8442	17.82	19.07	20.62
Climb	0.8000	18.31	19.59	21.19
Loiter	0.9214	17.06	18.25	19.74
Fast cruise	0.4070	25.67	27.47	29.70
Descent	0.4788	23.66	25.32	27.39

To account for out-of-mission profile flight conditions, EASA CS-VLA 335 [152] is applied to determine flight parameters at further design points. Accordingly, positive and negative stall velocities (V_{stall+} and V_{stall-}), design dive speed or maximum operating velocity (V_D) and manoeuvring speed for maximum turn ratio (V_A) are determined by the previously presented formulation. Also, gust velocities Such equations require the determination of the wing's $dC_l/d\alpha$ values. The 3D aerodynamic analysis in XFLR5 established $dC_l/d\alpha$ values of 5.157, 4.956 and 4.773, respectively for the full extended, mean span and full retracted configurations. Results are presented in Table 3.8.

V-n combined diagrams (in solid lines), illustrated in Figures 3.23, 3.24 and 3.25, are associated by manoeuvre (in dash lines) and gust (in dotted lines) V-n diagrams assuming symmetrical flight conditions. These diagrams show the scope of loading conditions inside of which, for any combinations of V and n, the aircraft loaded structure must comply with the strength

Table 3.8: Velocities and load factors computed for three VSW configurations.

	l_{ext} =1.775 m	l_{ave} =1.550 m	l_{retr} =1.325 m
V_{stall} [m/s]	13.646	14.602	15.792
V_{max} [m/s] (= V_D)	44.177	47.272	51.123
V_A [m/s]	31.555	33.765	36.516
dC_L/d_α	5.157	4.956	4.773
u_{V_C} [m/s]	10.670	11.032	11.389
$n_{gust_{V_C}}$	10.064	7.646	6.918
u_{V_D} [m/s]	5.335	5.516	5.694
$n_{gust_{V_D}}$	5.532	4.323	3.959

requirements referred in CS-VLA, for both manoeuvring and gust criteria. In the manoeuvre envelope, a 3 maximum load factor and a -1.5 minimum load factor values are considered.

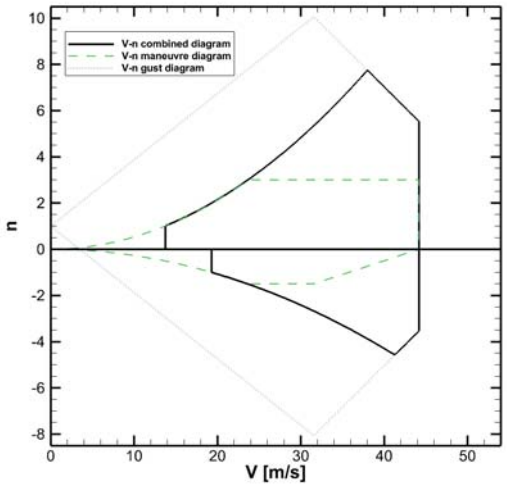

Figure 3.23: Flight envelope for VSW extended span configuration.

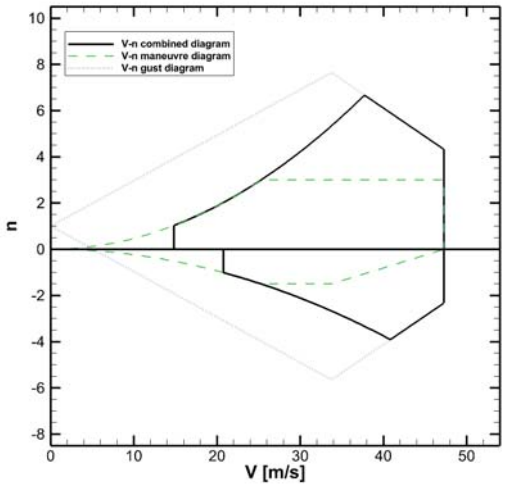

Figure 3.24: Flight envelope for VSW mean span configuration.

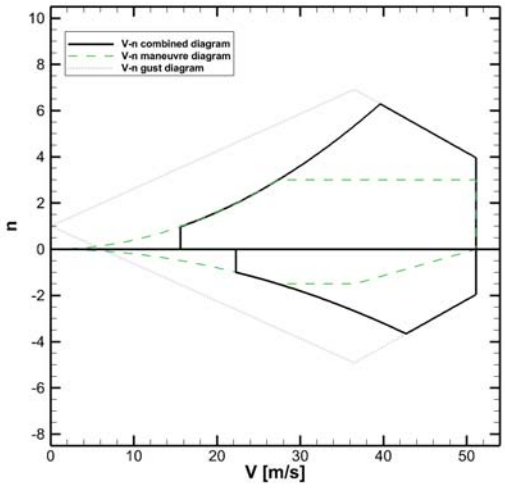

Figure 3.25: Flight envelope for VSW retracted span configuration.

It may be concluded from Figures 3.23, 3.24 and 3.25 that gust diagrams are more critical than manoeuvre diagrams, thus the manoeuvre diagram has negligible influence in the wing

sizing. The three diagrams include equally scaled axis so that an easier comparison between wing configurations may be performed. While b decreases from the extended configuration to the retracted configuration, n also decreases whereas V_D increases. These observed two main trends were expected as the extended configuration is aimed for low velocity cruise, take off and landing, while the retracted configuration is aimed for high-speed cruise.

In a wing design there are frequently two structural critical points in the V-n diagram to be addressed in a wing structural analysis. The critical design points for torsion and bending is the symmetric condition for maximum positive load factor at V_D. The critical design point due to shear (the point with more lift) is the point with highest load factor. In the current case, the maximum positive load factor is defined by stall characteristics and the gust diagram. The V-n diagram for the VSW maximum span configuration presents higher n values for same velocity values hence the wing extended configuration is considered to be the most structurally demanding configuration and is hereinafter assumed as the critical configuration for which the wing must be structurally designed. In fact, for the extended configuration, there is less skin surface in contact between the IFW and the OMW, thus when the OMW is subjected to a specific loading condition, the transference of the load to the IFW will be distributed by a smaller surface, increasing local stress.

The extended wing configuration at V_D is used in the following calculations to define the wing distributed aerodynamic loading (q_L, q_D, q_M) of the VSW. A full-wing 3D aerodynamic analysis that uses a polar type 2 and a fixed L is performed for this flight condition.Loading data is scaled to unit span and converted into non-dimensional distributed loads ($q_L\prime, q_D\prime, q_M\prime$) using the mathematical formulation detailed previously. The resulting approximated coefficients for the critical flight condition at maximum speed (V_D =43.03 m/s), are C_L ≅0.133451, C_D ≅0.008389, with L/D ≅32.5931 and C_m is assumed to be constant at each wing panel and equal to $C_{m_{IFW}}$ ≅-0.14043 and $C_{m_{OMW}}$ ≅-0.09002, for -5° $< \alpha <$5°. It is assumed, for model simplicity, that C_m is constant along the wingspan. Such assumption reflects negligible accuracy losses once C_m spanwise variability is extremely low for low α values in a wing with no dihedral, taper and and twist.

Chapter 4

VSW Structural Sizing

The current chapter presents a FEA model and optimisation procedure to size the VSW to an overall minimum-mass design. Results achieved and model errors are discussed.

4.1 FEM Numerical Model

To complete the preliminary design phase, a wing structural sizing must be fulfilled to validate the designed structural concept, the selected materials as well as obtaining structural components final dimensions. Thereafter, resorting to the structural concept detailed in Section 3.1.4, FEM-based structural analysis and optimisation must be employed to reach an optimal sizing of some key VSW structural components. For such, a minimum mass-objective optimisation constrained by structural strength and stiffness limits is developed.

FEA is a mathematical representation of a physical system comprising a model, material properties and applicable boundary conditions. It also includes the solution of that mathematical representation and results evaluation. The current numerical model is developed using ANSYS® Parametric Design Language (APDL) [172] with shell elements according to the base geometrical variables and design variables. The APDL script is written to handle geometry creation, material definition, section properties, meshing, analysis and post-processing. The developed script allow the computation of a static solution using small deformations and the post-processing of the wing deformations, rotations and stresses. The analysis is performed in compliance with EASA CS-VLA regulation [152].

4.1.1 Geometry, Materials and Boundary Conditions

A surface-based geometry is created using VSW characteristics and dimensions specified in Chapter 3. The analysis is performed uniquely for the VSW fully extended configuration as it is the design most structurally demanding configuration, specially due to its lower overlapping area to transfer loads transference from the OMW to the IFW.

Material properties are defined in accordance with those presented in Section 3.2.3, excluding the materials used in the actuation system though, as only the wing airframe is being structurally analysed. Ultimate tensile and compressive strengths in both longitudinal (x) and transverse (y) directions, as well as ultimate shear strength, are considered in the current analysis. To account with material imperfections, a correction factor is applied in the elastic modulus and shear modulus of each material. A multiplying factor of 0.9 is used in the pultruded carbon-epoxy profiles and factors of 0.75 and 0.65 are applied in the laminated unidirectional and bidirectional carbon-epoxy composites, respectively. Lower factors are considered for the laminated composites because these are in-house manufactured whereas pultruded profiles are from industrial production. A reference temperature is considered for all materials. Tables 4.1 and 4.1 sum-

marise the typical properties [173] for the three types of composite materials employed in the VSW design.

Table 4.1: Elastic properties and density of VSW composite materials.

	E_x [GPa]	E_y [GPa]	E_z [GPa]	G_{xy} [GPa]	G_{yz} [GPa]	G_{xz} [GPa]	ν_{xy}	ν_{yz}	ρ [kg/m^3]
CFRP1	126.0	9.0	9.0	4.5	4.5	4.5	0.3	0.3	1600
CFRP2	105.0	7.5	7.5	3.8	3.8	3.8	0.3	0.3	1600
CFRP3	45.5	45.5	45.5	3.3	3.3	3.3	0.1	0.1	1600

Table 4.2: Mechanical properties of VSW composite materials.

	$\sigma_{t,x}$ [MPa]	$\sigma_{c,x}$ [MPa]	$\sigma_{t,y}$ [MPa]	$\sigma_{c,y}$ [MPa]	τ_{xy} [MPa]
CFRP1	1500	-1200	50	-250	70
CFRP2	1500	-1200	50	-250	70
CFRP3	600	-570	600	-570	90

	$\varepsilon_{t,x}$	$\varepsilon_{c,x}$	$\varepsilon_{t,y}$	$\varepsilon_{t,y}$	γ
CFRP1	0.0105	-0.0085	0.003	-0.025	0.014
CFRP2	0.0105	-0.0085	0.003	-0.025	0.014
CFRP3	0.0085	-0.008	0.0085	-0.008	0.018

With CFRP1, the pultruded carbon-epoxy profiles; CFRP2, the laminated unidirectional carbon-epoxy composite; CFRP3, the laminated bidirectional carbon-epoxy composite; E, the Young's modulus (or elastic modulus); G, the Shear Modulus; ν, the Poisson's ratio; σ, the normal stress (with t for tensile and c for compression), τ, the shear stress; ε, the normal strain and γ, the shear strain. x, y and z coordinates are Cartesian coordinates with the x-axis pointing towards the wingspan and the y-axis aligned with the wing chord.

The foam is otherwise a linear isotropic material hence its properties do not have directional sensitivity. Table 4.3 summarises AIREX C70.90 density, elastic and mechanical properties, based in ISO and ASTM standards.

Table 4.3: Foam Airex® C70.90 mechanical and failure properties.

E [GPa]	G [GPa]	ν	ρ [kg/m^3]	$\sigma_{t,x}$ [MPa]	$\sigma_{c,x}$ [MPa]	τ_{xx} [MPa]
0.084	0.04	0.05	100	2.7	2	1.7

Since a symmetric wing planform is assumed, only half of the wing is modelled. Accordingly, boundary conditions (loads and constrains) are applied with this under consideration. Wing loads are applied in accordance with the characterised spanwise distributed aerodynamic loading. Model constraints are defined at wing root nodes. For such, the designed wood sockets aimed to fix the wing inner ribs to the fuselage, are not considered. Therefore, it is assumed that only the wing skin is root constrained. As only sandwich skin and spar caps are being structurally optimised, to consider that all loads are being transferred by them, is a conservative assumption, thus considered valid. The wing is thereby considered to be constrained as a cantilevered beam. Accordingly, its constraints are as follows:

1. The wing root does not experience any deflection;

2. The wing root is static in xy-plane (horizontal) with no rotation, so that the derivative of the deflection function is zero at that point;
3. Zero bending moment at the wing tip is assumed; and
4. Zero shearing force acting at the wing tip is assumed.

4.1.2 Element and Contact Type

IFW and OMW are both discretised using the same approach. The sandwich skin is modelled with three layers built as offset surfaces from the aerofoil contour according to their own thickness. These three layers are composed by two faces of carbon-epoxy woven composites and a foam core, which is cut off by four embedded spar caps. OMW inner wing-box structure is modelled with the same three layers concept and ribs are modelled with a a single layer of foam. Accordingly, a element type that allows single and multilayer shell definition is preferable to discretise this wing structure. A comparison of beam and shell theory for mass estimation in preliminary wing design by Dorbath [174] clarifies the benefits of this choice.

Due to computational resource optimisation, SHELL281 element is used to discretise the surfaces. The SHELL281 element is an eight-node element suitable for analysing thin to moderately-thick shell structures. The element has a total of six degrees of freedom at each node: translations in x, y and z directions, and rotations about x, y and z-axes. The element is well-suited for linear, large rotation and/or large strain nonlinear applications. For nonlinear analyses, change in shell thickness is accounted. The element formulation is based on logarithmic strain and true stress measures. SHELL281 section commands allow multilayered shell definition and options are available for specifying thickness, material, orientation, and number of integration points through the thickness of the layers. Accordingly, SHELL281 is suited for layered applications for modelling composite shells or sandwich construction [7]. The accuracy in modelling composite shells is governed by the first-order shear-deformation theory. This theory is usually referred to as Mindlin-Reissner shell theory, an extension of Kirchhoff–Love plate theory that takes into account shear deformations through-the-thickness of a plate [175], [176].

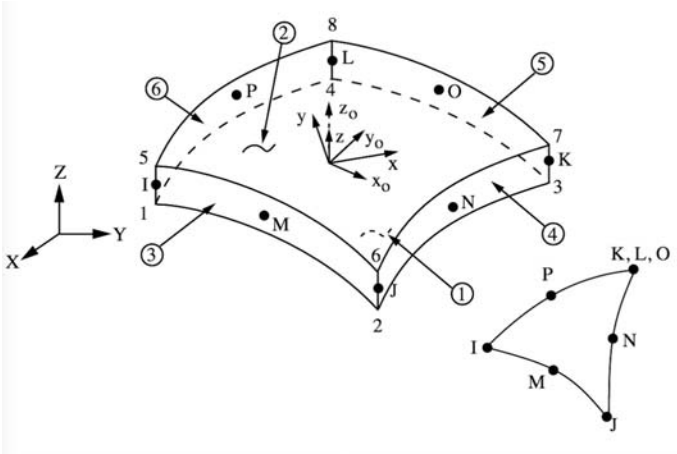

Figure 4.1: SHELL281 element geometry [7].

Figure 4.1 shows geometry, node locations and the element coordinate system for SHELL281 element type. This element is defined by shell section information and by eight nodes (I, J, K, L, M, N, O and P). A triangular-shaped element may be formed by defining the same node

number for nodes K, L and O. Nevertheless, ANSYS, Inc. recommends against using this element in triangular form, except as a filler element.

The peculiar VSW structure required the use of contact elements to correctly model the wing panels' interface. Such contact elements are located in the overlap surface between the IFW and the OMW. In order to reduce computational cost, an asymmetric contact is created. In this type of contact, one surface is designated to be the target and the other a contact surface. Then, one contact pair is created between the contacting surfaces. Contrary, in the symmetric contact both surfaces are designated target and contact, which requires the creation of two contact pairs and reducing penetration between contact surfaces. Although the potential for penetration increase, the asymmetric contact is more efficient than the symmetric contact. The IFW-OMW contact interaction is modelled with a shell to shell contact using TARGE170 and CONTA174. The former defines the target elements and the latter the contact elements. TARGE170 is used to represent various 3D target surfaces for the associated contact elements. Translational or rotational displacements, as well as forces and moments, may be imposed on target elements. For rigid target surfaces, these elements can easily model complex target shapes, whereas for flexible targets, these elements will overlay the shell elements describing the boundary of the deformable target body and are potentially in contact with the target surface.

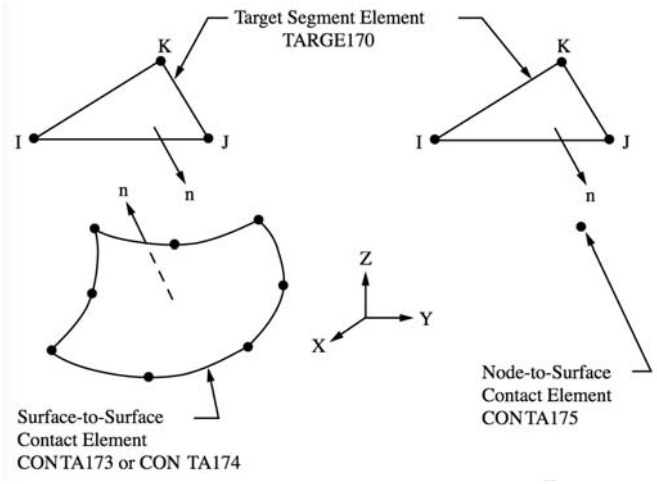

Figure 4.2: TARGE170 target elements geometry [7].

Figure 4.2 shows TARGE170 geometries for CONTA174 and CONTA175. The contact interaction between IFW and OMW panels is a surface-to-surface contact thus CONTA174 elements are selected. CONTA174 is a 8-node surface-to-surface contact element located on the surface of 3D shells with mid side nodes (such as TARGE170). It is applicable to 3D structural and coupled-field contact analyses and may be used to represent contact and sliding between 3D target surfaces and a deformable surface defined by this element.

Figure 4.3 shows that CONTA174 share the same geometric characteristics as the shell element face with which it is connected. Contact occurs when the element surface penetrates an associated target surface. The contact elements' behaviour is chosen to be bonded, in order to reduce the computation cost of each analysis. However, an increase in the local stiffness is to be expected, which has the effect of underestimating wing tip's displacement and rotation. This reaction is due to an expectable cross-section opening of the IFW skin in the overlapping area,

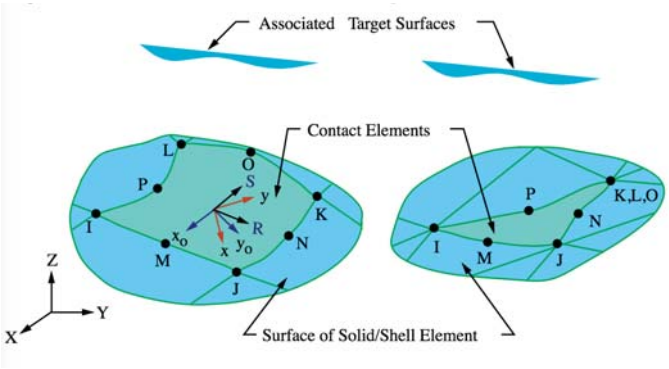

Figure 4.3: CONTA174 contact elements geometry [7].

even though considering the presence of the cross-section reinforcements. Contact interactions are controlled between specific surfaces that could potentially be in contact.

Several different concepts are evaluated to understands which bounding configuration to apply. To bound all overlapping area, results in a very stiff wing that can not predict accurately the IFW and OMW real interaction. Accordingly, the contact between the inner surface of the IFW and the outer surface of the OMW is added uniquely in l_{over1} and l_{over2} panel areas. Nevertheless, l_{over1} panel region should be kept free for a proper sliding. Preliminary tests showed that to bound merely l_{over2} resulted in too high tip deflections as the OMW upper skin is surpassing the IFW upper skin. In the end, it is selected an intermediate approach in which the lower surface of the l_{over1} area and the upper surface of the l_{over2} are bounded.

The bonded contact uses a multi-point constraint (MPC) formulation. MPC connection uses rigid constraint equations between the elements on the contact and target faces to model the bonded connection. Connection locations are determined using the contact element pinball radius (near-field contact depth between two elements). It is used a 'bonded initial' hence soon after the FEA beginning, contact elements are replaced with internal constraint equations. Moreover, only those contact nodes that are initially in contact or have a very small gap are always constrained via internal MPC.

4.1.3 Optimisation Concept

An optimisation loop is carried out with the purpose of reducing wing mass while ensuring that each wing supports the prescribed loading. ANSYS®Mechanical APDL optimisation facilities are used to carry out the optimisation using the APDL internal language. The APDL optimisation method employed is the first order method. It is based on design sensitivities and is more suitable for problems that require high accuracy. The first order method is selected since it is the most accurate and robust method available [172]. This method of optimisation calculates and uses derivative information. The constrained problem statement is transformed into an unconstrained one via penalty functions. Derivatives are formed for the objective function and the state variable penalty functions. This leads to a direction search in the design space. Various steepest descent and conjugate direction searches are performed during each iteration until convergence is reached. Each iteration is composed of sub-iterations, which include search direction and gradient computation [172].

Some VSW structural key components are selected as design variables for the optimisation. Such design variables are sized in each optimisation loop while keeping other structural components' size constant. The design variables adopted in the current study are:

1. IFW and OMW skin's laminate CRFP thicknesses ($t_{lam,IFW}$ and $t_{lam,OMW}$); and
2. IFW and OMW spar cap's pultruded profiles widths ($w_{cap,IFW}$ and $w_{cap,OMW}$).

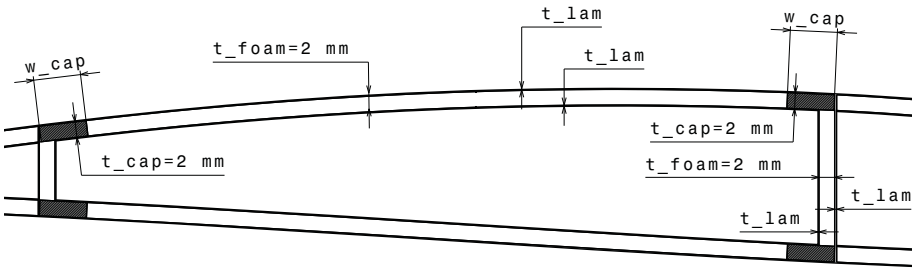

Figure 4.4: FEM optimisation variables - the OMW case.

Figure 4.4 illustrates FEA design variables positioning in the OMW cross-section layout. w_{cap} is used in the main and secondary spars, both upper and lower surfaces. t_{lam} is used in the skin's inner and outer faces as well as in the spars web's surfaces. The IFW case is not presented as the structural design variables are the same and similarly positioned. Figure 4.4 also shows that skin foam core, spar webs foam core and the spar caps thicknesses are kept constant and equal to 2 mm. Moreover, to the current FEA, ribs and wing cross-section reinforcements sizes are also considered constant. Ribs are 3 mm thick and cross-section reinforcements are 6 mm large (in the spanwise direction) and 2 mm height (same as foam thickness, for proper embedding). FEA design variables are subject to geometrical constraints, which are considered in the optimisation loop.

Three constraint functions are considered in the FEA. Maximum tip deflection (w_{tip}) is limited to 2.5% of the wingspan, hence limited to 0.089 m of vertical displacement, and maximum tip rotation ($\theta_{y,tip}$) is confined to the interval [-0.6°, 0.6°]. While in CS-VLA [152] the advised constraint function's limits are wider (e.g. w_{tip} < 10% of wingspan), to select narrower constraints within the current application is necessary to allow an even slide of the two wing components. In fact, if the tip displacement or rotation are too large, the VSW mechanism could eventually jam, compromising system's integrity and functionality. These constraint bounds are derived from past experience, namely in the analyses performed by Gamboa et al. [15].

Additionally, the third constraint variable is a failure criterion constraint that is used to detect structural failure of wing's components. There are several popular approaches to determine failure. Composites are brittle materials which have strong orthotropic properties. Many of the criteria traditionally used for CFRP are quadratic full interactive criteria, in which all stress and strain components are merged in a quadratic polynomial. Possible failure of the material can be evaluated by the Tsai-Wu failure criterion. Tsai-Wu criterion is selected as it is a quadratic full interactive criterion, specially suited for composites [177]. Tsai-Wu criterion is also a non phenomenological material failure criterion, i.e. the mode of failure is not described by it. In APDL there are available two implementation types of the Tsai-Wu failure criterion. The first

form is the 'strength index' (TWSI) and the second form is the inverse of Tsai-Wu 'strength ratio index' (ITWSR). ITWSR failure criterion is selected and is given as

$$I_r = \frac{1}{R} = \left[-\frac{B}{2A} + \sqrt{\left(\frac{B}{2A}\right)^2 + \frac{1}{A}} \right]^{-1} \tag{4.1}$$

with the A term, in the 2D case of plane stress, defined as

$$A = \frac{(\sigma_x)^2}{\varepsilon_{t,x}\varepsilon_{c,x}} + \frac{(\sigma_y)^2}{\varepsilon_{t,y}\varepsilon_{c,y}} + \frac{(\tau_{xy})^2}{\gamma^2} + c_1 \frac{\sigma_x \sigma_y}{\sqrt{\varepsilon_{t,x}\varepsilon_{c,x}\varepsilon_{t,y}\varepsilon_{c,y}}} \tag{4.2}$$

where c_1 is a coupling coefficient of the Tsai-Wu theory which is -1 by default. The B term is defined as

$$B = \left(\frac{1}{\varepsilon_{t,x}^2} - \frac{1}{\varepsilon_{c,x}^2}\right)\sigma_x + \left(\frac{1}{\varepsilon_{t,y}^2} - \frac{1}{\varepsilon_{c,y}^2}\right)\sigma_y \tag{4.3}$$

Generically, when evaluating the strength of a CFRP, if the ITWSR value is less than 1, then the material will not fail. However, if this value is higher than 1, then damage to the material may occur [178]. The number of elements that display failure or alternatively, the ratio of failed elements to the overall number of used elements, may be assessed in the APDL post-processing. In the current FEA implementation, the ratio of failed elements using the ITWSR failure criterion ($\overline{FE}_{ITWSR}$), which varies between 0 (no failure) and 1 (all elements under failure), is analysed. The third constraint is therefore $\overline{FE}_{ITWSR}$, which must be below 0.1% of the total number of elements. Such a value is imposed rather than imposing that all elements does not display failure. This is due to the possibility of existing small areas with failed elements that could be easily solved using local reinforcements. Since the current study is appropriate for the conceptual and preliminary design phases (and not for the detailed design phase), possible load concentration in such small areas should not drive the overall design. Finally, the three constraint functions selected in the current FEA are:

1. Maximum tip deflection: $w_{tip_{max}}$ < 2.5b_{max};
2. Maximum tip rotation: $|\ \theta_{y,tip}\ |$<0.6°; and
3. Failed elements ratio (using ITWSR criterion): $\overline{FE}_{ITWSR}$<0.1%.

4.1.4 Mesh Quality and Convergence

How fine should the element mesh be in order to obtain reasonable results? This question should be properly answered as mesh density is extremely important in FEA. On one hand, if the mesh used is too coarse, FEA results may contain significant errors. Therefore, the mess quality should be modelled till an "acceptable" error level is reached. On the other hand, if it is too refined, it carries an expense of computational resources. Overall, mesh uniformity and elements quality is essential.

In the current model, the type of selected mesh enables a mapped meshing where it is possible and a free meshing in the remaining areas. The element shape used for meshing is an area mesh

(2D model) suitable for elements that support multiple shapes [179]. Figure 4.5 illustrates the mesh applied in the VSW for FEA purposes.

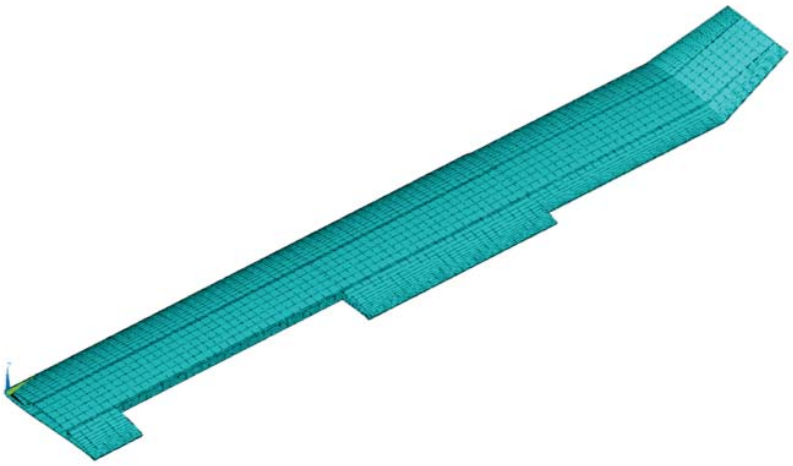

Figure 4.5: Mesh grid implemented in the VSW analysis from the APDL script.

4.1.5 Processing

In the APDL processing environment, the boundary conditions previously defined are applied to the wing, the type of analysis is selected and the type of equation solver is specified. Structural analysis will be either linear static, non-linear static or linear dynamic. Linear model analysis assumes that the material does not plastically deform. Non-linear models consist on cutting apart contact conditions when the loaded materials have surpassed its elastic range into the plastic zone, or alternatively, when loaded materials bend more than 10% of the model's length, from which a large deformation FEA case is considered. Non-linear analysis require higher computational resources. Linear dynamic analysis involve loads and corresponding response states that vary with time.

In the current FEA, no time dependency exists, large deflections are not activated and the contact formulation is MPC based, thus the employed solution is obtained by a linear static structural analysis. This allows a reduced computation time for each static analysis, greatly reducing the optimisation time and increasing the robustness of the analysis. Additionally, it increases the optimisation stability, since it eliminates the possibility of diverged solutions. The 'sparse direct equation solver' from ANSYS is selected. This solver is well suited for shell models and is an alternative to iterative solvers since it combines both speed and robustness. On the other hand, it requires considerably more computational memory [180].

4.1.6 FEM Post-processing

FEM post-process environment is used to interpret the raw data generated in the FEA by sorting the data and enabling graphical representations. Graphical displays are here created to show the relevant aspects of the model, i.e. the design function's results and if the constraint function are kept within the desired boundaries. Interpretation of these post-processed results is the key to identifying structural areas of potential concern (regions with possible failure) and areas of material waste (areas of the model bearing little or no load).

First and foremost, the solution is evaluated for convergence for the lower wing mass value that bear the imposed FEA constraints, whereas if it does, the three constraints are analysed. The wing tip deflection is assessed by evaluating the y-position (vertical) of each node and selecting the highest value. The wing tip rotation is obtained by a trigonometric function of a defined tip deflection vector and tip LE and TE coordinates. Finally, the $\overline{FE}_{ITWSR}$ value is measured by dividing the obtained failed elements by the total number of elements.

4.1.7 FEM Associated Errors

Errors in FEM can compromise the validity of the results. Errors may be generated from the user, which are prevented by being methodical when developing an analysis and applying a comprehensive pre and post processing methodology. Another source of error in the FE solution is the error introduced due to the assumptions and simplifications made in the analysis. A completely accurate representation of a physical model by a mathematical expression, may lead to an extremely complex mathematical model that may be hard to solve with the available hardware and software resources. Simplifications are then mandatory. In the current model, the assumptions made about the calculated results are:

1. To consider a linear structure, i.e. calculated displacements are considered to be directly proportional to the load applied. This assumption states that the materials used in the VSW design have a constant slope of the stress-strain curve in the elastic region;
2. To consider small displacements, in which it is assumed that calculated displacements are small in comparison to the principal dimensions of the wing; and
3. To use thin shell element derivation assumptions, in which finite-elements can not have a radius of curvature to thickness ratio ≤ 0.5.

Loads are often not accurately known or may derive from other software that may themselves be approximate in nature. Boundary conditions may need to be approximated as well to keep the modelling effort and model size simple. In the current case, the wing root constraint do not fully describe the concept in which the wing is attached to the fuselage. Another high error contributor in a FEM model is the characterisation of materials' properties, which may not be accurately known.

Commonly, mean values are assumed for materials' volumetric mass, mechanical properties and failure parameters, without accounting with lot-to-lot variability and even manufacturing inaccuracy. For example, in the present case, CRFP layers are modelled based on assumed empirical properties which will certainly vary depending on the approach and conditions during the VSW hand layup process. If these assumptions and simplifications are excessive, the results obtained from the finite element model may be inaccurate. To account with all these, in the current implementation, correcting factors are considered for material properties. A correcting factor of 0.95 is applied to the foam properties, whereas to the composites correction factors of 0.9, 0.75 and 0.65 are applied depending on if it is a pultruded unidirectional profile, a unidirectional or a bidirectional laminate, respectively.

Finally, one of the major error contributors is frequently the mesh refinement, the reason why a mesh convergence study should be completed before hand to quantify the associated error in each particular application.

4.2 Mesh Convergence Study

A convergence analysis for the finite element model applied to the VSW structure is carried out to assess the sensitivity of the maximum tip displacement and rotation as a function of the element number in the mesh. Several meshes are created and a static analysis is performed with a spanwise distributed loading along wing spars. The refinement of the grid is achieved by changing the global element size and using line size refinements in ANSYS. Figure 4.6 shows the convergence of the maximum wing tip deflection and rotation for several meshes.

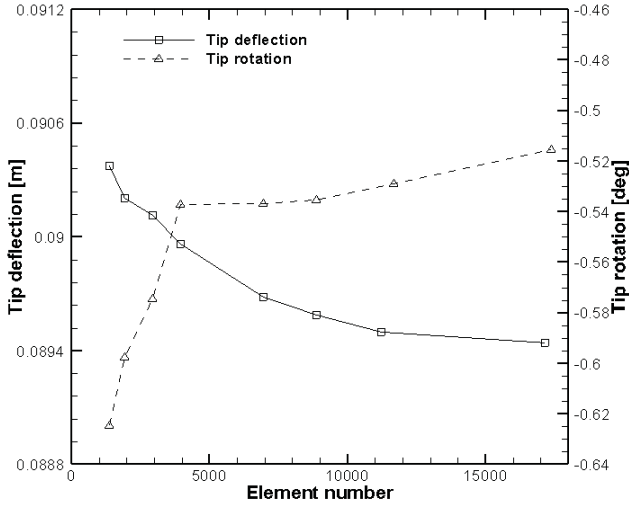

Figure 4.6: Maximum tip deflection and rotation for a different numbers of mesh elements.

The tip rotation presents a larger variation until 4000 elements, after which the variation is small. The tip deflection shows a more gradual convergence, showing, however, a reduction of the slope only for 10000 elements. Accordingly, it is possible to conclude that the solution is stabilized for a grid with about 10000 elements, where both the tip deflection and rotation present variations well below 1%. Therefore, a finite element model with 10000 elements is selected for the current analysis.

Mesh element sizes of 0.024 m are employed in the overall geometry, whereas a refinement is applied in more critical parts. A mesh refinement of 0.0084 is applied in the IFW spar web in the spanwise direction and skin's LE and TE regions in the chordwise direction. A mesh refinement of 0.0042 m is applied in the OMW spars web in the spanwise direction and in the cross-section reinforcements in the chordwise direction. Finally, nodes and area elements are generated within mesh areas.

4.3 VSW Structural Sizing Results and Discussion

4.3.1 Structural Optimisation

The VSW wing underwent structural optimisation with a linear static FEA model. Since the VSW design is not only meant for conceptual studies, but a wing prototype is actually planned to be built and installed in Olharapo III, one should take in consideration design variables minimum bounds due to manufacturing constraints. Regarding the skin faces and considering previous manufacturing experience, laminated CFRP have a minimum thickness of 0.12 mm after the

hand layup process, corresponding to a layer of 95 g/m^2 plain weave carbon-epoxy. Therefore, both $t_{lam,IFW}$ and $t_{lam,OMW}$ minimum optimisation bounds are set to this value. Spar widths minimum bounds are selected based on standard available sections from vDijk high-strength pultrusions [168]. Consulting the list, one concludes that the minimum available section is 2 mm$\times$0.4 mm, being used as limit to $w_{sc,IFW}$ and $w_{sc,OMW}$. From the wing layout parameters that are considered constant, l_{fus} is sized to 0.12 m, l_{over1} to 0.125 m, l_{over2} to 0.025 m and l_{tip} to 0.155 m.

Using the above considerations, a FEM-based optimisation is run with the VSW geometrical dimensions and loading. In Table 4.4, initial and final values of the optimisation design variables are presented.

Table 4.4: Initial and final optimised values for wing design variables.

	$w_{sc,IFW}$ [mm]	$t_{lam,IFW}$ [mm]	$w_{sc,OMW}$ [mm]	$t_{lam,OMW}$ [mm]
Initial	50.0	0.48	40.0	0.13
Final	21.7	0.12	0.8	0.12

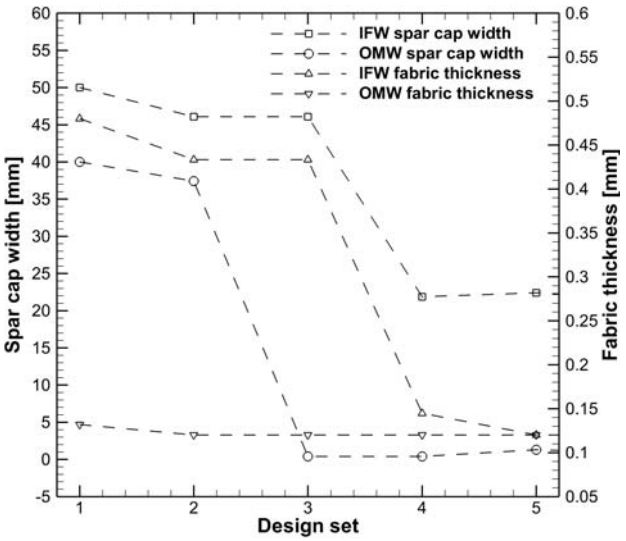

Figure 4.7: Variation of wing parameters along VSW optimisation design sets.

The initial values of the design variables are selected so that the wing has enough stiffness to guarantee a feasible solution. In this lines, the optimisation is initiated with a purposely oversized wing design so that all structural constraints are fulfilled from the start. This is seen in Table 4.4, in which all design variables present considerably lower sizes after the optimisation procedure. The optimisation converged for the minimum optimisation bounds of the IFW and OMW skin laminates, which dominate the optimisation. From these mass-optimised results, and considering that foam thickness is constant and equal to 2 mm, it may be concluded that the final design of the VSW skin has an overall thickness of 2.24 mm. IFW and OMW spar caps are sized to a width if 21.7 mm and 0.8 mm, respectively.

In Figure 4.7, skin fabric thicknesses and spar cap widths are presented throughout the design sets. It is possible to conclude that between the third and the fourth design sets, the design variables converged. In Table 4.5, initial and final values of the optimisation objective and

constraint variables are presented.

Table 4.5: Initial and final optimised values for objective and constraint variables.

	m_{wing} [kg]	w_{tip} [m]	$\theta_{y,tip}$ [deg]	$\overline{FE}_{ITWSR}$ [%]
Initial	2.54	0.028	-0.09	0.0073
Final	1.00	0.088	-0.36	0.0113

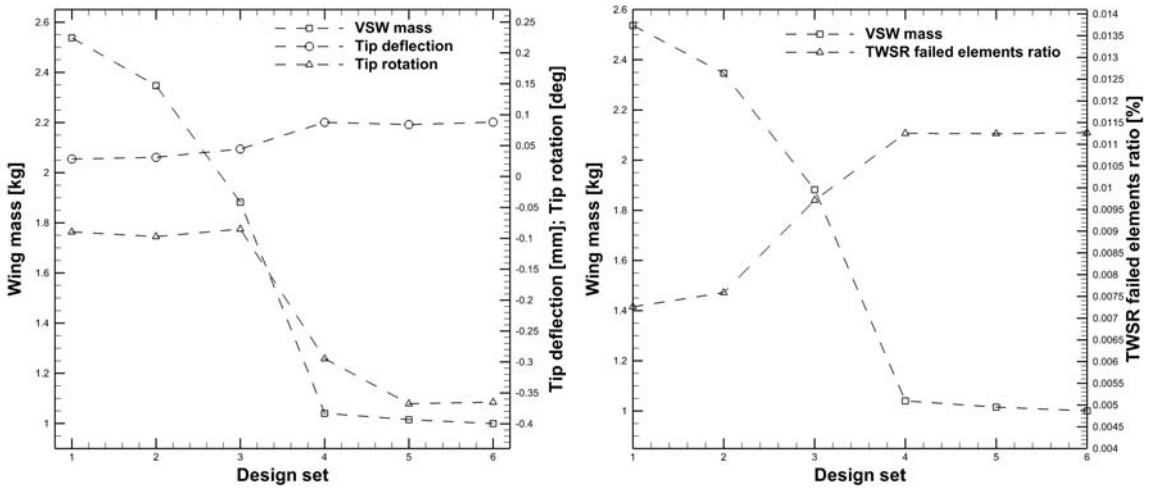

(a) VSW mass and rigidity-related constraints for each design set.

(b) VSW mass and strength-related constraints for each design set.

Figure 4.8: Trade-off study on the mass-physical properties for the VSW optimisation design.

The mass is decreased from the initial given value to the final optimised value of precisely 1 kg, as seen in Table 4.5. From Table 4.5 one concludes that strength is not problematic since the final optimised $\overline{FE}_{ITWSR}$ result is not near the constraint value of 0.1%. It should be noticed that both tip deflection and tip rotation satisfy the imposed optimisation constraints ($< 2.5\%$ of span and between $\pm$ 0.6°, respectively). Tip deflection reaches the optimisation bound limits of 0.088 m, but torsion is far from its maximum values. Torsion is dominated by the skin, which means that the minimum value selected for the skin fabric, due to its market availability is too high. If thinner fabrics were available, the optimisation could converge for a lighter wing.

In Figure 4.8, the variation of the objective and constraints variables along the design sets is presented. Exceeding mass is taken from the structure along an optimisation procedure, therefore it is expected that $\overline{FE}_{ITWSR}$ increases throughout design sets, as seen in the right hand side of Fig 4.8. In left hand side, wing rigidity-related constraints and wing mass are represented along the optimisation design set. Both w_{tip} and $\theta_{y,tip}$ suffer an increase (in absolute value) along the optimisation while mass decreases. In sum, while the obtained results seem reasonable, optimality has not been established as skin laminate is driving the optimisation and has a too high minimum thickness.

By using the optimised results for the design variables (fabric thicknesses and spar cap widths), the wing may now be FEM-based analysed for this particular case. A detailed analysis is performed from interpreting FEM-generated wing surface plots. For such, wing vertical displacement and the ITWSR failure criterion are assessed.

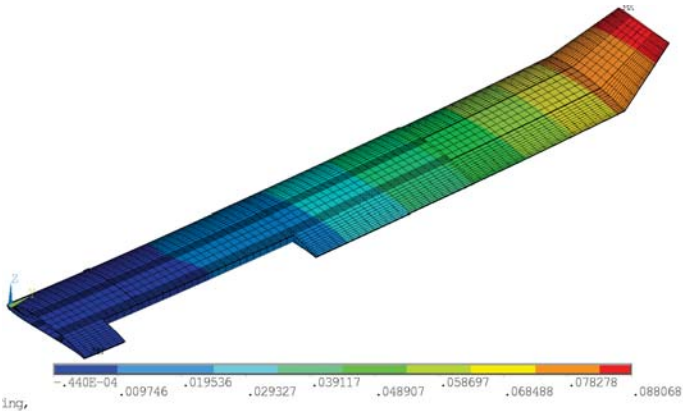

Figure 4.9: Vertical displacement of the optimised VSW design.

In Figure 4.9, wing vertical displacements are exhibited. The displacement distribution smoothly increases from the wing root to the tip. Wing maximum displacement is 0.88 m, in the first quarter chord of the wing tip, being around 2.5% of the span. As expected, the maximum twist also appears at the wing tip and has a value of 0.45°.

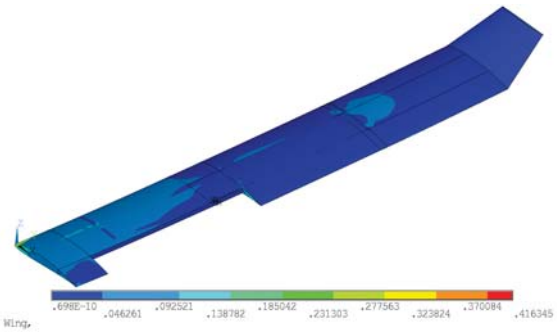

(a) VSW skin outer layer: laminated CRFP.

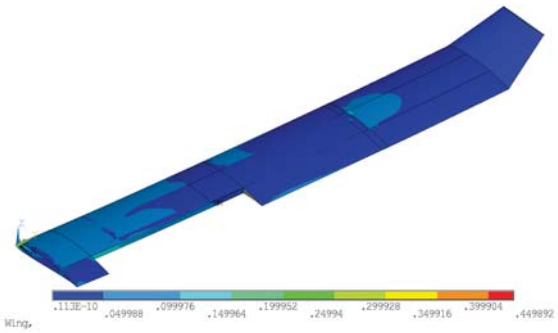

(b) VSW skin inner layer: laminated CRFP.

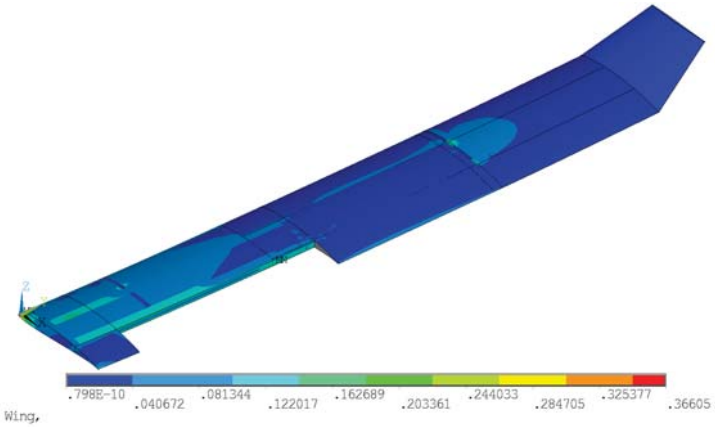

(c) VSW skin core layer: foam and pultruded carbon-epoxy profiles.

Figure 4.10: Inverse of Tsai-Wu strength ratio (ITWSR) of the optimised VSW design.

Figure 4.10 shows ITWSR criteria of the VSW for the three layers of the sandwich-structured skin: the outer CFRP laminate, the core composed by foam and pultruded carbon-epoxy profiles, and the inner CRFP laminate. It may be concluded that most of the wing presents considerably lower values of ITWSR (up to ten times lower) than the maximum felt in a particular point of the structure. Between the three layers, the one that presents higher ITWSR is the inner layer, closely followed by the outer layer. The maximum value of ITWRS is located in the

wing root, near the LE region of the inner and core layers of the VSW skin. This result is expectable as all loading is transferred for the wing root as a bending moment. Transversal reinforcements are not used in the wing root, but have a strong contribution to the structure strength in the overlapping area. This contribution is illustrated by the plot's colour change in the areas where reinforcements are used. The maximum ITWSR value measured in the skin outer layer is otherwise located in the overlapping area, more specifically near the secondary spar of the l_{over1} area. This may be explained by the transference of loads from the OMW to the IFW panel, which is concentrated in the lower surface of l_{over1} and in the upper surface of l_{over2}. In the core layer case, failure is presented for both foam and pultuded composite materials. It is possible to see that a variation on ITWSR occurs in the spar regions, where material changes.

It should be acknowledged that the FEA type of contact used in the current study is still the bounded contact modelled by a MPC formulation. Accordingly, both IFW and OMW must be analysed together as a unique piece. From Figure 4.10, it is possible to see that ITWSR values are locally slightly higher in the OMW panel, soon after the overlapping area. This happens because the contact is bonded and therefore, after the overlapping area a thickness reduction occurs.

As a conclusion, a mass optimisation procedure sized the VSW to a minimum mass of 1 kg. This result is obtained for an optimisation point in which the torsion constraint is not converging to its maximum value. As torsion is dictated by skins' stiffness, one concludes that if a lower skin thickness value is setted as the skin minimum thickness bound to be considered in the script, the mass optimisation procedure could probably reach a lighter wing solution.

Chapter 5

Effect of Design Parameters on Wing Mass

This chapter details the work done regarding the methodology employed and the results achieved during the development of a wing mass function for morphing wings design, in particular of the telescopic type. Results are analysed and a discussion on the effects of design parameters in the wing mass is presented.

5.1 Problem Definition

No wing mass predicting functions for telescopic wings are available in the literature for accessing mass properties of such wings in early design phases. Moreover, a database with morphing wings' masses is also not available hence empirical estimates are difficult to obtain. In addition, it is predicted that in a VSW design, the wing mass is highly dependent on the wingspan and the amount of enabled telescopic retraction. Also, a certain dependence on the wing chord, the aircraft MTOW and the flap's chord fraction is predicted. For the literature gap reason, and in order to provide an insight into the telescopic wing mass dependence on these five parameters, a parametric study is conducted.

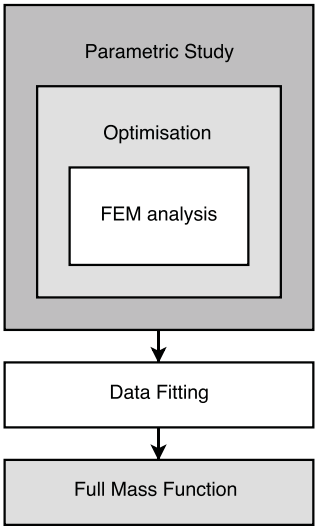

Figure 5.1: Parametric design flowchart.

Figure 5.1 presents the methodology applied to obtain the full morphing wing mass predicting function. The methodology to obtain such a function intends to reach an accuracy level equivalent to class II-1/2 mass models, therefore it similarly follows these models' steps by firstly understanding the critical design points in the aerodynamic loads, followed by a physics-based structural analysis and sizing, and finally adding non-optimum effects in the structure sizing, inertial relief and mass related to secondary components. In the present study, the first three steps are iteratively performed for a set of DoE. Therefore, the implemented approach makes

use of a parametric study, which encloses an optimisation loop performing FEA, to obtain the mass database for the wing structure exclusively. Three DoE databases are created:

1. Structural mass of a fixed conventional wing (m_{FW});
2. Structural mass of a telescopic wing (m_{VSW}); and
3. Structural mass ratio of a telescopic wing over a fixed wing (m_{VSW}/m_{FW}).

These databases feed data fitting regression models to create a wing structural mass predicting function for each DoE case. Soon after, predicting functions for the actuation system's mass ($\overline{m}_{sys}$) and flaps' mass ($\overline{m}_{flap}$) are obtained based on empirical studies and added to the VSW structural mass predicting function ($\overline{m}_{VSW}$) and the most suitable correction increment(s) (k), so that a new full wing mass predicting function ($\overline{m}_{VSW,full}$) suited for morphing wing design, is obtained as

$$\overline{m}_{VSW,full} = \overline{m}_{VSW} + \overline{m}_{sys} + \overline{m}_{flap} + k \tag{5.1}$$

Eq. 5.1 needs to be addressed as a compact function of some limited specified design parameters so that its implementation may be a practicable and feasible solution to access the mass properties of telescopic wings' future designs. It may be seen as a stepping stone into solving the literature gap on mass models for such wing morphing concepts. Moreover, the effect of each specified design parameter on the resulting wing mass may be, with this approach, evaluated. In these lines, a mass ratio function to predict morphing wing structural mass penalties when compared to a conventional fixed wing structural mass predicting function is implemented and investigated.

5.2 Methodology

5.2.1 Parametric Study

In the methodology to derive the mass functions, a separation of the main structure and secondary wing components (flaps and actuation system) is considered. A parametric study methodology is employed to the creation of mass databases for wings' main structure, whereas secondary components' mass functions are further discussed in Section 5.2.8. The development of three DoE databases allows to study and compare multiple conventional and telescopic wing configurations in a short period of time. Two parametric studies, which are conducted by performing a FEM-based mass optimisation study, generate two DoE databases (VSW and FW). A third DoE database (VSW/FW) is created by computing the quotient of the first two databases. In each parametric study, the same concept (FW or VSW) and respective geometry are considered for differently sized wings. The wing sizing is defined by an iterative selection of the magnitude of a set of specified design parameters (or DoE variables). In the current parametric studies, five DoE variables are used, including four geometrical wing parameters and one inertial parameter, which are:

1. Wingspan for VSW fully extended configuration (b_{max}) $- b$;
2. IFW chord (c_{IFW}) $- c$;

3. Wing variable-span fraction ratio with respect to the wing semi-span ($\frac{l_{var}}{b/2}$) $-$ $\bar{l}_{var}$;

4. Flap chord ratio ($\frac{c_{flap}}{c}$) $-$ $\bar{c}_{flap}$; and

5. Aircraft maximum take-off weight (MTOW) $-$ W.

For model simplicity and user-friendly characteristics, b, instead of b_{max}; c as the model's reference chord, instead of c_{IFW}; $\bar{l}_{var}$ as the quotient of the span fraction length that performs morphing (l_{var}) and the wing semi-span ($b/2$), instead of $\frac{l_{var}}{b/2}$; $\bar{c}_{flap}$ as the quotient of the chord occupied by the flap by the reference chord, instead of $\frac{c_{flap}}{c}$ and W, instead of MTOW are used hereinafter. The inclusion of each of these parameters in particular, as parametric design variables, is important for two main reasons. On one hand, the selected geometric parameters are meant to fully define the wing geometry by means of correlating functions and constants previously defined. On the other hand, they are selected with respect to its predicted potential to influence the primary structural mass of the VSW concept. $\bar{l}_{var}$ is the parameter that defines the wing capability to perform morphing, b and c are main parameters that drive the wing layout, W accounts with the aircraft most critical inertial case scenario and finally, $\bar{c}_{flap}$ is selected for characterising the effect on the wing mass due to flaps existence and chord-related positioning. One should mention that other design parameters, directly or indirectly affecting the wing structural mass, may certainly exist; it is assumed that the ones currently selected have higher preponderance in the wing mass though.

A DoE methodology enables the creation of databases with all possible combinations for a selected range of wing parameters magnitudes and respective FEM-based structural mass for each of these combinations. DoE quadratic methods are the methods available that best suit a DoE with two to four levels and a response surface objective. A DoE of the CCD type is adopted for simplicity and suitability to our dataset. CCD is a quadratic DoE with three levels per variable and $2^n + (2n + 1)$ number of data points for n variables, as seen in Table 2.1. In the current study, five DoE variables are used, therefore 43 data points would be required if three values were selected for each parameter. Notwithstanding, not all design variables have three values, being $\bar{c}_{flap}$ and $\bar{l}_{var}$ the exceptions. The DoE is still mainly CCD-based, but with modifications due to some sustained options that should benefit the model.

Only two levels of $\bar{c}_{flap}$ are employed to reduce computational time/cost, with the disadvantage though of decreasing the ensuing predicting function response from quadratic to linear relative to mass impact due to the chord of the flap. Regarding $\bar{l}_{var}$, which is only applicable in the second and third DoE cases (those considering the VSW), five different values are selected to broad the analysis results on this morphing-related parameter that stands as the main differentiating variable in relation to conventional wing mass studies. By increasing the levels in $\bar{l}_{var}$, more DoE data points are required, which come at a computational cost, whereas the decision lays in the desire to better comprehend the impact of this morphing related parameter on the wing mass. The first three values of $\bar{l}_{var}$ are considered fixed and settled as 5%, 10% and 20% of the wing semi-span, the fourth value is equal to the arithmetic mean between the third and the fifth, and the last fifth value is equal to the maximum geometrically achievable semi-span variation for each wing parameters' set. A full-factorial 3-level design for the response surface is used, which corresponds to n^3 experiments for each DoE. In these lines, the first DoE case (for the FW) has three DoE variables with three levels and one DoE variable with two levels ($\bar{c}_{flap}$),

which totals 54 DoE data points; the second and third DoE cases have one extra DoE variable ($\bar{l}_{var}$) with five levels, which totals 270 DoE data points for each of them.

The VSW design previously presented in Chapters 3 and 4 is used as baseline wing for the current parametric studies. Since the beginning of this work, the VSW acronym has been used to refer to the wing that has been previously designed. Nevertheless, all wings in the parametric studies are variable-span wings as well, differently sized though. To avoid confusion, the previously designed VSW is hereinafter referred to as baseline wing. Therefore, previous FEM analysis, optimisation results and mesh convergence study are applicable to the present parametric studies. Accordingly, the three levels of the DoE variables are selected based on Olharapo III wing dimensions, which are used as the design reference values (intermediate values). Both minimum and maximum values are then set by a correlating percentage of these reference values.

Further wing parameters are computed using geometrical correlations from equations 3.1 to 3.10. Some variables that were previously considered constant in the baseline design, are now scaled for each DoE point (each wing configuration). The baseline geometry is again used as reference, which enables to keep a similar layout between wing configurations. Tip's span and chord are defined as

$$l_{tip} = \frac{l_{tip_{ref}}}{l_{ave_{ref}}} l_{ave} = 0.1 l_{ave} \tag{5.2}$$

$$c_{tip} = \frac{c_{tip_{ref}}}{c_{IFW_{ref}}} c_{IFW} = 0.578 c_{IFW} \tag{5.3}$$

with all parameters using ref in subscript, sized with baseline dimensions hereinafter. l_{IFW} and l_{OMW} are defined by knowing b, l_{tip} and l_{var}. c_{OMW} is found by subtracting an offset to c_{IFW} (the DoE variable c). A reference chord ratio is established with the baseline chords ($c_{OMW_{ref}}/c_{IFW_{ref}}$). For each DoE wing configuration, c_{OMW} is defined by multiplying this chord ratio by c. For lower and higher DoE levels for c, a correction factor is established to account for the observed geometrical variations of the chord on the TE. Therefore, a correction factor lower than unity is used for the higher chord, and higher than unity for the lower chord. l_{over1} should also be scaled to account with the higher loads transferred to it from a heavier wing or vice-versa. Therefore, l_{over1} is defined as

$$l_{over1} = \frac{l_{over1_{ref}}}{S_{OMW_{ref}} d_{p_{ref}}} S_{OMW} d_p \tag{5.4}$$

with S_{OMW}, the exposed area of the OMW (including tip) and d_p, the distance between the OMW exposed panel centroid and the end of l_{over1} (see Figure 3.2). Calculations are performed for the wing extended configuration. d_p is defined as

$$d_p = \frac{l_{var}^2 \frac{c_{OMW}}{2} + l_{tip}^2 \frac{c_{tip}+c_{OMW}}{3}}{S_{OMW}} \tag{5.5}$$

and S_{OMW} is defined as

$$S_{OMW} = l_{var} c_{OMW} + \frac{l_{tip}}{2} (c_{OMW} + c_{tip}) \tag{5.6}$$

The difference between d_p or S_{OMW} and its respective ref values is that, for ref values, Eqs 5.5 and 5.6 are evaluated using the baseline dimensions. l_{fus} and l_{over2} are still considered constant and equal to the baseline values. l_{flap} is calculated by subtracting l_{fus}, l_{var} and l_{over2} from l_{IFW}. IFW and OMW aerofoils are fixed, thus curvature, aerofoil relative thickness and leading edge radius are also fixed and constant to any wing configuration. Accordingly, the aerofoil maximum thickness position is fixed and any wing-box starts at this fixed position (30% of the chord) and ends in the chord position where the flap begins, which is dictated by $\overline{c}_{flap}$.

Finally, $l_{var_{max}}$ needs to be iteratively computed as it is a function of l_{over1}, which in turn is a function of the selected l_{var} value. Firstly, l_{over1} is calculated using $l_{var_{ref}}$ from the baseline wing. Secondly, $l_{var_{max}}$ is calculated using the previously found l_{over1} value as

$$l_{var_{max}} = \frac{\frac{b}{2} - (l_{fus} + l_{over1} + l_{over2} + l_{tip})}{3} \tag{5.7}$$

A loop is run based on the previous methodology and iteratively calculates l_{over1} and $l_{var_{max}}$. The absolute error, defined as the difference between actual and last iteration $l_{var_{max}}$ values, is computed and a stopping criteria of 0.01 mm is considered. $\bar{l}_{var_{max}}$ is finally defined by dividing $l_{var_{max}}$ by $b/2$. A script is written in APDL to apply the parametric studies and obtain a FEM-based optimised solution for each experiment of the two parametric studies.

5.2.2 Optimisation

An optimisation loop is carried out for each DoE data point in the same lines as presented in Chapter 4. Identically, the optimisation objective is to reduce wing mass while ensuring that each wing supports its respective loading. The same design variables are adopted, as well as the same three constraint functions, with equal stiffness limits and failure criterion. The minimum mass optimisation procedure is built in APDL and solved in ANSYS. Each combination of wing parameter's values defines a specific wing configuration and its respective elliptic loading, which is detailed in Section 5.2.4. With the performed modifications to the CCD method and summing the two DoE databases (m_{FW} and $mVSW$), 324 experiments are required. For such a large number of experiments, the FEM-based optimisation procedure takes some days to run. Figure 5.2 summarises the performed work flow steps of the parametric design script.

As in the baseline optimisation, minimum limits for the optimisation variables are similarly considered to the spar caps' width and skins' laminate thickness, with wider limits though. In the current parametric optimisations, constraints are wider because the aim is to validate a morphing concept and the analysed wings are not intended to be manufactured, therefore industrially available minimum sizes do not need to be considered. Moreover, in the parametric models, both larger and smaller wings are analysed, so only narrower constraints would enable structural sections to be effectively optimised to minimum mass values. Spar caps' width maximum values are limited to the inside of the wing-box bounds, i.e. limited to the maximum width that avoids mutual intersection and that keeps an unfilled intermediate small space to enable some clearance. Maximum bounds of skins' laminate thickness are chosen based on the optimisation limitations when applying thin shell element derivation assumptions. These assumptions dictate that shells elements can not have a radius of curvature to thickness ratio ≤ 0.5.

Summing up, an optimisation is performed for each data set by ensuring that each wing supports

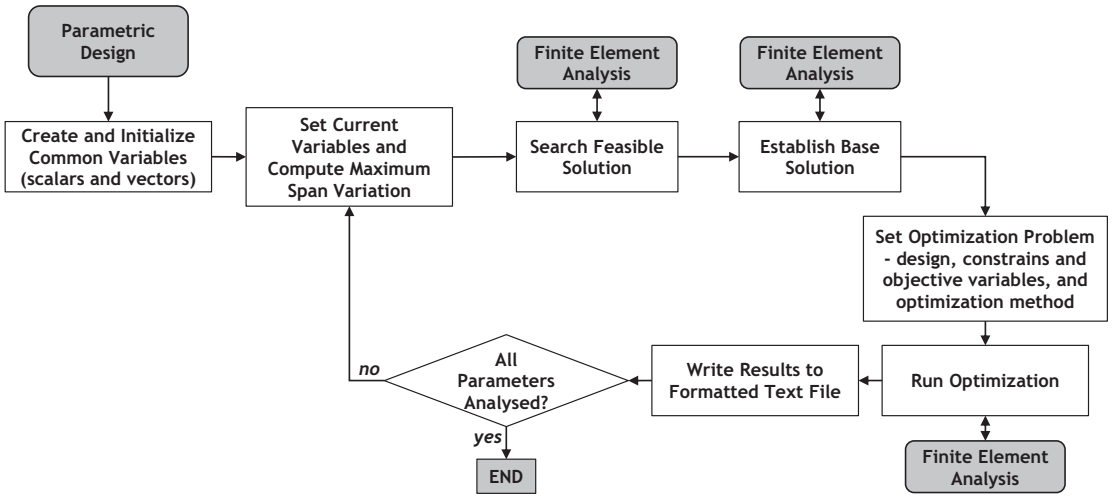

Figure 5.2: Optimisation design flowchart.

the required loading and with the main objective of reducing wing mass. For such, the FEM-based solution is established and constraints are assessed for compliance. The optimisation problem uses a feasibility tolerance of 0.01 and reaches the objective when a change between loops is less than a convergence criteria of 0.2%.

5.2.3 Finite Element Analysis

The baseline wing underwent structural optimisation and subsequent structural analysis of the optimised structure. As the same wing concept is currently applied, the functionality and correctness of the finite element model and optimisation scripts were already assessed. Accordingly, the applied APDL model's geometry, materials, boundary conditions, finite elements, contacts, constraints, errors and mesh convergence study are presented for the baseline wing in Chapter 4. Figure 5.3 summarizes the general structure of the FEM script.

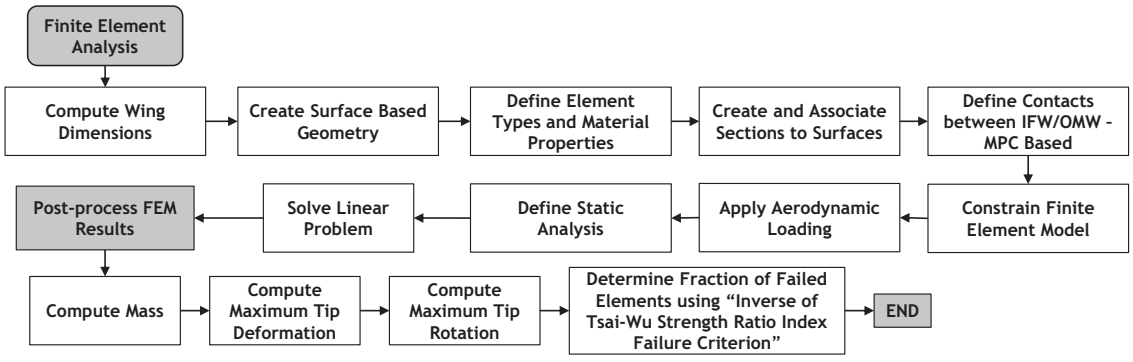

Figure 5.3: Finite element model flowchart.

The differentiating aspect of the current FEA lays in the need to compute wing dimensions for each DoE wing configuration. Moreover, the mesh refinement approach is also modified once to perform a mesh study for each DoE data point is not practical.

It is possible to conclude from the baseline wing mesh convergence study that the solution stabilized for a grid with about 10000 elements, where both tip deflection and rotation varied below 1% with small mesh modifications. Notwithstanding, it should be noted that, due to the

nature of parametric studies, wing geometric changes may force the mesh to be updated. In order to avoid the need of performing a mesh convergence study for each geometry, the grid relative sizing is kept unaltered, i.e. the relative spacing between elements is kept constant across all FEM analysis from the two parametric studies.

5.2.4 Wing Loading

A loading model that assumes a spanwise elliptic lift distribution is implemented. Furthermore, spanwise uniform drag and pitching momentum are assumed in this model. This methodology suits better the parametric studies than scaling the baseline evaluated wing loading for each DoE wing configuration, which is explained by the aerodynamic loading distribution being significantly different at each wing, specially in the DoE cases where the wing has maximum b and minimum c values or vice-versa, hence completely different AR values. The elliptic lift theory is therefore a simple and convenient approach to approximate the lift distribution for each DoE wing. Notwithstanding, reference aerodynamic coefficients from the baseline wing design are still used for simplicity and applicability to the current parametric models.

The applied concept follows the methodology described in Anderson [181] that uses a distributed circulation ($\Gamma(y)$) which varies elliptically with the distance y along the span and considers a constant, uniform downwash and induced angle-of-attack over the span. An elliptical lift distribution is an approximation that has been proved to predict the real wing lift distribution with a good accuracy, where the error is based on overestimating e as equal to unity. Accordingly, a lift distribution is here assumed to have an elliptic shape along the wing span by means of a vertical force (V) perpendicular to the wing chord, a horizontal force (H) parallel to the wing chord and the pitching moment (M). These loads are applied in the wing structure by loading-equivalent forces, as seen in Figure 5.4.

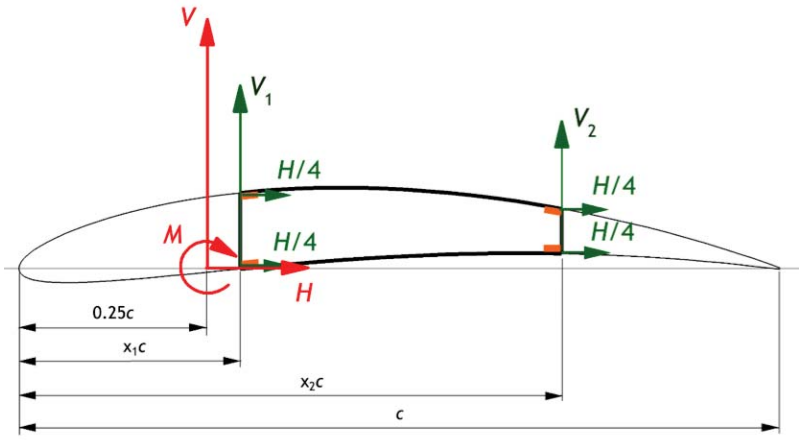

Figure 5.4: Equivalent system of forces at wing cross-section for an elliptic lift distribution.

V, H and M are applied at the aerofoil quarter chord position. V is divided into two smaller vertical forces (V_1 and V_2) that are applied in the main and secondary spars, respectively. V_1 and V_2 are scaled as a function of V and M and are inversely proportional to their positions relative to the aerofoil chord ($x_1 c$ and $x_2 c$). H is applied in the structure by being equally divided into four components, each applied in one spar cap. The sum of all vertical force components applied in the structure multiplied by its distance to the quarter chord position, must match the value of M. Inertial loads from the wing structure are already included in the script. Moreover,

as the maximum design load factor is not constant, as seen in V-n diagrams represented in Figures 3.23 to 3.25, n and its respective velocity are computed within the APDL script for each wing configuration. This is implemented in accordance with CS-VLA and using the same methodology previously presented in Chapter 3. Table 5.1 presents some wing parameters and aerodynamic variables from the baseline aerodynamic study, which values are used as reference values in the parametric study.

Table 5.1: Baseline wing parameters used in the loading adaptation for each wing configuration.

V_{ref} [m/s]	ρ_{ref} [kg/m^3]	AR_{ref}	c_{ref} [m]	n_{ref}	W_{ref} [N]	$C_{M_{ref}}$	L/D_{ref}	α [°]
43.03276	1.225	13.83	0.268	3	150	-0.1404	32.5931	-2.92

L/D_{ref} is the wing's lift-to-drag ratio (not the full aircraft's). DoE design variables and ISA conditions are used. With these parameters, L and D are computed for both the baseline and each DoE wing configurations as

$$L(y) = \frac{2nW}{\pi\, b/2}\sqrt{1-\left(\frac{2y}{b}\right)^2} \tag{5.8}$$

$$D = L/\left(\frac{L}{D}_{ref}\frac{AR}{AR_{ref}})\right) \tag{5.9}$$

Thereafter, V and H are found for each wing section by neglecting α effect, thus $V = L$ and $H = D$.Wing pitching moment is dependent on each wing design velocity. H is divided by four and each component is applied in a spar cap. V_1 and V_2 forces are computed as

$$V_1 = V - V_2 \tag{5.10}$$

$$V_2 = \frac{M - 0.25cV + x_1cV}{c(x_1 - x_2)} \tag{5.11}$$

with x_1, the non-dimensional position of front spar; x_2, the non-dimensional position of aft spar and M, the pitching moment defined as

$$M = \frac{1}{2}\rho * V^2 ScC_M \tag{5.12}$$

5.2.5 Wing Structural Mass Function

As soon as the FEM-optimised mass results were generated, the three DoE databases are collected and a proper morphing wing mass function may be fitted by means of regression analysis. A mass function regression is duly derived to enable further understanding of the effects and interactions between wing parameters on wing mass. A mathematical data fitting procedure is therefore required to set a mass predicting function with proper approximation accuracy. Accordingly, this data fitting procedure is performed for each DoE case study ($\overline{m}_{FW}$, $\overline{m}_{VSW}$ and $\overline{m}_{VSW}/\overline{m}_{FW}$) as a function of the design variables for its large number of combinations. The desired functions are of the form

$$\begin{aligned} \overline{m}_{FW} &= f(b, c, W, \overline{c}_{flap}) \\ \overline{m}_{VSW} &= f(b, c, \overline{l}_{var}, W, \overline{c}_{flap}) \\ \overline{m}_{FW}/\overline{m}_{VSW} &= f(b, c, \overline{l}_{var}, W, \overline{c}_{flap}) \end{aligned} \tag{5.13}$$

Eq. 5.13 denotes the parameters considered in this study. It is considered that all selected parameters have significant influence in the wing mass, thus the selection of such parameters. In Section 5.3, the computation of the wing mass equation includes a screening of the significance of each of the selected parameters to consolidate this statement. The mass function is produced by fitting a multivariable high order polynomial to the obtained data. The resulting polynomial is multivariable because each of the five (four for the FW case) wing parameters is an independent variable that is preponderant for an adequate modelling of the wing mass results. A high order polynomial is also considered, as the user may choose to model it as a second or third order polynomial to fit the data for maximum accuracy. One must be aware of the behavioural complications inherent to high order polynomials though. Regression modelled high order polynomials suffer from severe ringing between each data value and tend to diverge wildly outside the data points. The desired polynomial should be, for the VSW case, in the following form

$$\overline{m}_{VSW}\left(\{X\}\right) = a_0 + \sum_{i=1}^{n} a_i X_i + \sum_{i=1}^{n}\sum_{j=1}^{n} a_{ij} X_i X_j + \sum_{i=1}^{n}\sum_{j=1}^{n}\sum_{k=1}^{n} a_{ijk} X_i X_j X_k \tag{5.14}$$

with $\{X\}$, the parameters' array and $\{a\}$, the array of unknown coefficients. For the current study, the respective polynomial is defined as

$$\begin{aligned}\overline{m}_{VSW} = a_0 + a_1 b + a_2 c + a_3 \bar{l}_{var} + a_4 W + a_5 \bar{c}_{flap} + \\ + a_6 b^2 + a_7 bc + a_8 b\bar{l}_{var} + (\ldots)\end{aligned} \tag{5.15}$$

with a_0, the constant term; a_1 to a_5, the coefficients of the linear terms and a_6 forward, the coefficients of the higher order terms. From such polynomial, besides the possibility to study the effect in the wing mass produced by each individual parameter, also two or three level interactions between parameters will be possible to investigate when analysing a second or third order polynomial, respectively.

5.2.6 Regression Model

The method presented here provides an approach to fit an empirical function from the obtained physics-based FEM-optimised mass database of a morphing wing's primary structure. In order to use this approach, research on suitable data fitting regression methods and particularly, response surface based methods, is conducted.

To define the fitted polynomial, the main purpose of each regression model is to find the unknown polynomial coefficients. The number of coefficients is equal to the number of polynomial terms and coefficients are calculated by using combinations with repetitions of the independent variables number (n) plus one with the polynomial order (${}^{n+1}C_{order}$). With five independent variables, a second order polynomial would have 21 terms and a third order polynomial would have 56 terms. For the FW DoE case, four variables are used and a second order polynomial would have 15 terms and a third order polynomial would have 35 terms. To fit quadratic or cubic response surfaces we need at least that many experiments (DoE points), and at least three or four levels for each design variable, respectively.

Model's system equations are composed by all combinations of a scope of wing parameters'

values, thus the dataset will be in the order of thousands and so, there are surely more equations than unknowns. A full-factorial 3-level design for the quadratic response surface is used, which corresponds to n^3 experiments for each DoE case. For $n \geq 2$ this number of experiments is higher than the minimum number of required data points to fit quadratic response surfaces, which validates the method for both four and five wing parameters. Accordingly, our model is an overdetermined system. Furthermore, the wing mass dataset (dependent variable) does not have constant variance. The standard approach in regression analysis for estimating the solution of such systems is using an iterative weighted least squared method. The residual, in our case, is the difference between m_w calculated in the parametric study and corresponding estimated wing mass values ($\overline{m}_w$), predicted from the fitted polynomial under development.

To understand the effects of the wing parameters as predictor variables in the wing mass response, both linear and nonlinear regression models are employed. Fitting parameters are estimated using the least-square method, followed by an analysis of the regression results for each method to allow a selection of the more adequate model on estimating the best fitting curve to the dataset. The matrix of the current regression model is close to singular and ill-conditioned which means it cannot be inverted. The two different linear methods that are implemented have that in account, one using a left matrix divide operation with QR decomposition (decomposition of a matrix into a product of an orthogonal matrix Q and an upper triangular matrix R) and the other using a Moore-Penrose pseudo-inverse (a generalization of the inverse matrix). Each method uses a different approach to fit the data, so they may possibly return very different results and proper evaluation of whether the results are acceptable for our data should be assessed. Moore-Penrose pseudo-inverse is more adequate for singular, ill-conditioned systems because its computation is based on singular value decomposition (SVD) and any singular values less than a settled tolerance are treated as zero.

Although linear regression models are easier to fit and the statistical properties of the resulting estimators are easier to determine, also a nonlinear regression method that uses successive approximations to fit the data is employed in the present work. Nonlinear regression provides the most flexible curve-fitting functionality and its applicability relies in the possibility of the predicting wing mass to relate nonlinearly to the polynomial coefficients. The nonlinear model applied is a proposed extension for causality nonparametric detection methods that comprises an orthogonal least squares algorithm, uses a nonlinear system identification to screen significant terms and performs an error reduction ratio-causality (ERR-causality) test for what it is called. ERR-causality test, developed by Zhao, can be used to “detect and track causal relationships between two signals” and is fully explained in Zhao et al. [150] and [151]. The author explains that a major advantage of the ERR test, is that it may be applied to linear or nonlinear dynamic systems.

A script is developed using MATLAB® (MATrix LABoratory), a multi-paradigm numerical computing environment and fourth-generation programming language. The script is structured to compute the previous regression models from the existing DoE databases, as displayed in flowchart 5.5. The input file is a matrix defined by six vectors, one for the wing mass values m_w extracted from the results of the APDL structural analysis and the other five for each selected wing parameter by varying its levels. Accordingly, the vectors for the independent variables (*indepvar*) are constructed in a DoE approach, i.e. fulfilling all possible combinations for the scope of selected wing parameters’ values by using sequential repetition of such levels. The user also

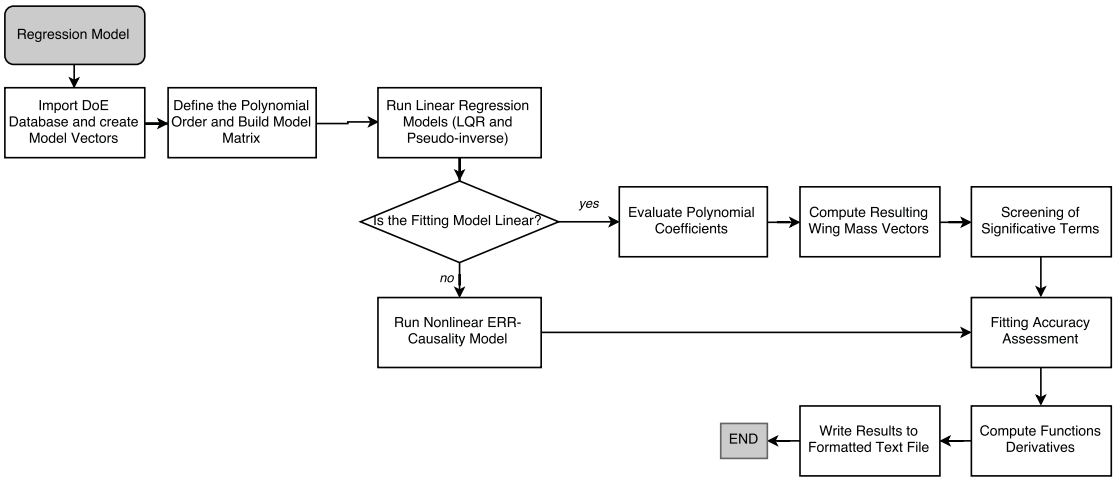

Figure 5.5: Multivariable high order polynomial regression model.

defines a list with the dependent variables' names (*varnames*), the type of regression method to use and the desired polynomial order. *indepvar* design matrix (*I*) is scaled to unit variance and a model matrix (*M*) is created. The selected fitting method is computed and the polynomial coefficients are obtained. Soon after, the scaling is recovered, the resulting polynomial coefficients (*coef*) are determined and $\overline{m}_w$ values are calculated as $\overline{m}_w = coef * indepvar$.

Afterwards, a screening is made to the significant terms and a goodness-of-fit assessment is computed by displaying the error parameters' values. The obtained coefficients are integrated in a polynomial by converting the terms into a symbolic form and using variable precision arithmetic to easier visualization of the equation and also, to solve possible numerical problems of the coefficients, with the disadvantages of a higher computational cost. One should consider that for the ERR-causality nonlinear method, the fitting coefficients are evaluated using the algorithm explained in Zhao et al. [150] and only after are imported for the MATLAB script, for polynomial analysis.

Besides analysing the calculated parameter error estimates it is also crucial to visually validate regression results by plotting the resulting polynomials. With five independent variables, the fitted polynomials describe a hypersurface and a five-dimension representation would be needed. As this is not possible to plot in a 3D graph, the regression polynomials are reduced in several polynomials by fixing three of the five independent variables. Such equations enable 3D plotting for visualisation of interactions between parameters. With these plots it is easier to take final considerations on the effects of each parameter in the observational wing mass data.

5.2.7 Sensitivity Analysis Formulation

The selection between the three regression methods is made by the evaluation of some goodness-of-fit parameters as the R-Square, the adjusted R-Square, p-value and the fitting corresponding maximum relative error, maximum absolute error, maximum residual and root mean squared error (RMSE). A detailed explanation of error analysis for the study of uncertainties in physical calculations is presented by Taylor [182]. To obtain the final polynomials, further considerations to the significance of the polynomial terms are made by screening it and selecting the less significant terms that have less influence in the response function and delete them. The minimum

number of significant terms that would fit adequately the dataset is evaluated by calculating the Pearson's correction coefficient, which should be approximately equal to one for a suitable fitting accuracy [183]. Moreover, partial derivatives of each mass polynomial are computed within the script and analysed for a selected design wing configuration. Partial derivatives of mass with respect to each wing parameter provide a measure of the model sensitivity to each parameter. In addition, partial derivatives for each parameter at the nominal value of a wing configuration are normalized to a selected parameter's variation. Such normalized results describe mass variation with respect to each parameter and may be used to assess the relative sensitivity of mass across model parameters.

5.2.8 Full VSW Mass Function

Although analysis and optimisation of wing primary structures based on aerodynamic loading is accounted in the current parametric study, the author recognizes that mass for wing secondary components, inertial relief and non-optimum effects are not included in the parametric study and so, not yet covered in the predicting polynomials. To cover these influences in the wing mass breakdown, further polynomials and correction factors are added to an overall VSW mass polynomial. Mass estimation for secondary structures commonly include leading and trailing edge structures, high-lift devices, control surfaces or lift-reducers. For the VSW concept, flaps are the unique secondary component to add to our analysis. A huge information dispersion on flap's mass exists in the literature, which does not enable an unique applicable mass prediction for the current design. Flap's structural mass is assumed based on the skin's surface area covered by flaps and considering a sandwich-structured skin identical to the one considered in the baseline design. The following equations are defined in SI units and are derived from semi-empirical relationships. Flap's structural mass is defined as

$$\overline{m}_{flap,struct} = k_{flap}\frac{S_{flap}}{S}\overline{m}_{VSW} \tag{5.16}$$

with k_{flap}, a correcting factor that is equal to unity for simple flap concepts and higher than unity if an adaptive flap is used. S_{flap} is the planform area of the flap which is calculated by

$$S_{flap} = 2c_{IFW}\overline{c}_{flap}l_{flap} \tag{5.17}$$

Flap's actuation system has also a mass penalty that may be estimated as

$$\overline{m}_{flap,sys} = \phi_{flap,sys}S_{flap} \tag{5.18}$$

with $\phi_{flap,sys}$, the mass per unit area considered for the the actuation system of the flap. A value of 2kg/m^2 which accounts for servos, links and cables for flap's actuation system is considered. To account for the mass increment in the wing primary structure due to the required structural reinforcement of the secondary spar and increased wing aerodynamic loading due to implementation of a flap, a correction increment (k_1) is considered by multiplying a selected correction factor by $\overline{m}_{VSW}$.

Wing structural self-weight is already considered in FEM analysis, therefore inertial relief components that could be here considered are already accounted in the structural mass function.

Morphing actuation system provide mass increase in the wing centre and its mass is determined by adding servomotors, spur gears, potentiometers, rack spurs and other miscellaneous (misc) components' empirical mass functions. The mass of two servomotors for wings with sizes comprised by the bounds of the current parametric study, may be approximated by

$$\overline{m}_{servomotor} = 2\left(0.05 + 0.01 + 0.02k_{act,type}\right) \tag{5.19}$$

with $k_{act,type}$, a boolean variable that is zero if the telescopic wing is only aimed for performance purposes (symmetric actuation) and equals unity if the wing is also aimed for control (asymmetric actuation). For the latter, the actuation system must perform span change ten times faster (100 mm/s) to achieve an effective rolling control. Higher torque values are thus required to reach higher motion acceleration by counteracting the aerodynamic drag and IFW-OMW skins' friction that is a function of the IFW mass and exposed area. By consulting the Pololu® catalogue, gearmotors with higher torque values belong to a different class (37D instead of 25D), which are heavier. The remaining equation terms account with gearmotor's mass (first term) and spur gear's mass (second term). Also, for wings with increased b and $\bar{l}_{var}$, rack spurs' length increases and its required stiffness increases, which results in an heavier component. A second equation is thus created to predict the contributing component of systems' mass variation due to the rack spur mass, as

$$\overline{m}_{rack} = 1.05 \times 0.102b\left(0.8 - 2\bar{l}_{var}\right)\left(1 + 0.1\frac{b}{3.55} + 0.25k_{act,type}\right) \tag{5.20}$$

The first term is the rack spur length fraction that is required to keep a safety margin so that it does not eventually disengage from the spur gear; the second is the mass of the rack per unit of length, for which a cross-section of 6×15 mm is considered; the third term is the rack span sized as a function of b and $\bar{l}_{var}$; the fourth groups two correction factors. One respects to a potential structural instability for such a small cross-section beam, therefore for extreme b values, it accounts with an extra mass for higher b values and vice-versa. The last correction factor considers that if the actuation system is also for control purposes, selected by varying the same boolean variable, loads in the rack will be higher and a larger cross-section is required. Mass for other components is estimated as

$$\overline{m}_{misc} = 0.1 + 0.03b(1 - \bar{l}_{var}) \tag{5.21}$$

with the first term meant to predict the total mass of several remaining actuation system's components (mounting hubs, brackets, curbs, PTFE film tape, etc.) and the second term, an empirical mass contribution that considers actuation system cabling. Finally, flaps' mass and actuation system's mass functions are defined, as

$$\overline{m}_{flap} = \overline{m}_{flap,struct} + \overline{m}_{flap,sys} \tag{5.22}$$

$$\overline{m}_{sys} = \overline{m}_{servomotor} + \overline{m}_{rack} + \overline{m}_{misc} \tag{5.23}$$

Mass due to non-optimum effects are determined by Torenbeek equations [101] which complement the structural predicted mass by adding the effects of non-ideal design parts or small

components as joints, attachments, connections and mountings as well as structurally non-ideal sections as large cut-outs and material thickness variations. To account with such increase in the structure mass, a correction increment (k_2) is considered by multiplying a selected correction factor by $\overline{m}_{VSW,full}$.
$\overline{m}_{VSW,full}$, the final VSW mass predicting function defined in Eq. 5.1, results from adding the mass contributions of Eqs. 5.22 and 5.23, to the VSW structural mass predicting function $\overline{m}_{VSW}$ and the correction increments k_1 and k_2.

5.3 Mass Functions Results

5.3.1 Parametric Study Results and Boundary Conditions

A grid of DoE data is generated. This data grid defines the range of values used along all parametric study and therefore, the solution interval where it is valid i.e. the range of values for which the predicting functions' error is admissible for estimating wing mass in early design phases. Using the selected DoE methodology, five factors are selected as the main wing design parameters to conduct the parametric study for the VSW mass and VSW/FW mass ratio, whereas four are selected for the FW mass. The chosen factors and levels, for each DoE design variable, are presented in the following table:

Table 5.2: Selected DoE variables' factors and levels as a modification to the CCD type.

Variables	0	1	2	3	4
b	-	2.665	3.553	4.442	-
c	-	(1^*)	0.257	0.321	0.386
$\bar{l}_{var}$	0.05	0.1	0.2	(2^*)	$L_{var_{max}}$
$W \times 10^{-2}$	-	1.2	1.5	1.8	-
$\overline{c}_{flap}$	-	-	0.3	0.4	-

(1^*) Lower chord DoE level unconsidered in the study.
(2^*) $\bar{l}_{var}$ value computed by Eq. 5.24.

In the current parametric model, DoE levels are chosen using Olharapo III wing's dimensions as design reference values, i.e. the DoE intermediate level (column two of Table 5.2) values are defined by the baseline wing dimensions. Remaining DoE levels are calculated from the intermediate values by a factor of 0.75 and 1.25 for the lower and upper levels (columns one and three), respectively. The CCD type of DoE would use a grid of design parameters with only these three central columns, as highlighted in Table 5.2. Due to the modifications performed, it may be seen that $\bar{l}_{var}$ parameter is extended for five levels and $\overline{c}_{flap}$ is reduced for two levels (eliminating the lower level).

Besides, if keeping the DoE intermediate level, the first from three c values (1^*) would be equal to 0.19275 m, notwithstanding preliminary results showed that by using such low wing chord, wings obtained for high b values would present too high AR values. Sizing results for such high AR wings were not satisfactory as optimisation variables were being limited by the imposed structural constrains and the optimisation did not converged. Accordingly, higher wing chords are required and a third c value is scaled with a factor of 1.5. W is hereinafter scaled to $W \times 10^{-2}$ so that it presents an order-of-magnitude similar to the remaining parameters. The

fourth $\bar{l}_{var}$ value (2^*) is selected as the intermediate value between the baseline $\bar{l}_{var}$ value and the geometrical maximum achievable $\bar{l}_{var}$ value, therefore it is found as follows:

$$(2^*) = \frac{0.2 + L_{var_{max}}}{2} \tag{5.24}$$

Parametric studies are employed for DoE data acquisition and FEM-based optimised mass results for the 324 (54+270) experiments are obtained approximately after 75 hours of continuous computational runtime. Output files are computed for the two FW and VSW cases. For each data point, this two DoE databases include all levels' combinations of the DoE variables and the resulting m_w, $t_{lam,IFW}$, $t_{lam,OMW}$, $w_{cap,IFW}$, $w_{cap,OMW}$, $w_{tip_{max}}$, $\theta_{y,tip}$ and $\overline{FE}_{ITWSR}$. Soon after VSW/FW data points are calculated as the quotient of the previous results to form the third DoE database.

5.3.2 Multivariable High Order Polynomials Fitting

Firstly, the two linear regression methods are computed. The method using a left matrix divide with QR decomposition is firstly applied. The model's matrix is evaluated based on statistical variables, which show that the determinant is close to zero and the conditional number tend for a too high value thus, the system matrix is close to singular and ill-conditioned. For such reason, the second implemented linear method, using a Moore-Penrose pseudo-inverse, which is more adequate for singular, ill-conditioned systems is computed. The tolerance selected for our case is 11.6465 x10^{-6} that is settled as a function of the size and norm of the system matrix.

Linear regressions are computed for the three DoE databases. Even though most of the data is well fitted, divergent results are found in certain regions of the dataset and while mean error parameters registered a satisfactory accuracy of the data, the maximum errors and residuals were far greater than desired for an accurate model. As an example, for the second DoE database and applying the first and second linear regression methods, the maximum relative error is equal to 0.587 and 0.3459 and the maximum residual is equal to 1.226 and 0.710, respectively. Such results were far too high to consider these methods adequate. Before submitting the data to a more complex nonlinear model, a p-value test is performed to assure that the linear models were not suitable. P-value is as a tool to decide whether to accept or reject the null hypothesis, i.e. if the p-value is lower than the significance level of the test, usually 5%, the result is said to be statistically significant and between the three implemented methods the one achieving lower p-value would give a superior fit for our problem [184]. The p-test value for the first linear method is 0.18 and for the second is 0.10. As expected, the pseudo-inverse method shows a better fitting but both methods are inadequate to fit our problem as the p-value is greater than 0.05. ERR-Causality method is subsequently applied. As both linear and nonlinear regressions are possible to implement by this method, also a linear approach is attempted and again results prove a nonlinear relation between coefficients and so, requiring a nonlinear regression method.

Terms of the resulting polynomials from the ERR-Causality method are already organized from higher to lower order of significance. After selecting the number of polynomial terms to be generated from the regression, this method also returns the sum of the error reduction ration (SERR) with respect to each term, i.e. a type of Pearson correction coefficient (PCC) that is defined as a percentage and accounts for the contribution of all ERR values in relation to

a polynomial with that selected number of terms. A SERR value equal to 100% would stand for an ideal regression polynomial, where a perfect match between calculated and predicted data would exist in the regression range of values. Although higher fitting precision would be expected for higher number of terms, a shorter number of terms may be advantageous as the objective of the current study is to create concise equations, proper for wing mass predictions in the conceptual design, and such equations should be short and simple to apply. In these lines, a balance between this two opposing concepts is searched by a parametric study, which is performed to minimise the number of significant terms to be used while achieving an acceptable data fitting accuracy.

Firstly, nonlinear regressions are computed for 2^{nd} and 3^{rd} order polynomials, followed by an iterative determination of SERR values for different number of polynomial terms. With 5 independent variables, a full 2^{nd} order polynomial would have 21 terms and a full 3^{rd} order polynomial would have 56 terms. Results in terms of fitting accuracy are similar when considering polynomials with the same number of terms, with SERR results for 3^{rd} order polynomials slightly better than for 2^{nd} order polynomials. Therefore, 2^{nd} order polynomials are selected for a higher simplicity of parameters' interaction. Secondly, SERR increment ($SERR_i$) values are determined as the quotient of the increment of SERR of that term with the SERR value of the previous term. Finally, a study is conducted on the adequate number of significant terms for each polynomial by selecting the minimum number of terms that would correspond to a $SERR_i$ value with a convergence stopping criteria of 0.1%. Results of such parametric studies for 2^{nd} order polynomials may be seen in Table 5.3 where the selected number of terms is highlighted for each function. A comparative study is performed not only to select the number of significant terms for each polynomial, but also to compare polynomials fitting of different DoE cases.

Table 5.3: Polynomial significance levels measured for different DoE cases and number of terms.

$\overline{m}_{FW}$ Function

N. of terms	6	7	8	9	10	11	12	13
ERR	1.611%	0.3417%	0.282%	0.254%	0.508%	0.159%	0.0391%	0.019%
$SERR$	98.13%	98.48%	98.76%	99.01%	99.52%	99.68%	99.72%	99.74%
$SERR_i$	1.669%	0.348%	0.287%	0.257%	0.513%	0.160%	0.039%	0.019%

$\overline{m}_{VSW}$ Function

N. of terms	7	8	9	10	11	12	13	14
ERR	0.345%	0.342%	0.683%	0.365%	0.268%	0.227%	0.077%	0.064%
$SERR$	97.45%	97.79%	98.47%	98.84%	99.11%	99.33%	99.41%	99.47%
$SERR_i$	0.355%	0.350%	0.698%	0.371%	0.271%	0.229%	0.078%	0.064%

$\overline{m}_{VSW}/\overline{m}_{FW}$ Function

N. of terms	10	11	12	13	14	15	16	17
ERR	1.657%	0.660%	0.572%	0.585%	0.520%	0.467%	0.068%	0.026%
$SERR$	94.54%	95.20%	95.77%	96.36%	96.88%	97.34%	97.41%	97.44%
$SERR_i$	1.784%	0.698%	0.601%	0.611%	0.539%	0.482%	0.070%	0.027%

As expected, when the number of terms increases in Table 5.3, SERR increases thus fitting accuracy increases. Nevertheless, it is seen that most of the times (but not always), $SERR_i$

is reduced when the number of terms increases. An extra term is thus evaluated to verify if $SERR_i$ does not increase again after reaching convergence for the selected number of terms. The parametric study shows that a number of significant terms equal to 12, 13 and 16, is respectively selected for each function, with the convergence stopping criteria of 0.1% in $SERR_i$. On one hand, a lower number of terms than the range of values selected for this parametric study would disregard terms with significant ERR values. On the other hand, considering a higher number of terms would result on a larger, more complex polynomial with only few added significance as last terms present very low ERR values (in a magnitude order of 10^{-5}). This conclusion may be clarified by the difference in SERR between the higher considered number of terms and the respective full polynomials where for $\overline{m}_{FW}$, SERR is 99.737% or 99.741% for 12 or full terms (15), respectively; for $\overline{m}_{VSW}$, SERR is 99.475% or 99.578% for 14 or full terms (21), respectively and for $\overline{m}_{VSW}/\overline{m}_{FW}$, SERR is 97.438% or 97.464% for 17 or full terms (21), respectively.

For the selected numbers of polynomial significant terms, resulting SERR values (99.72%, 99.41% and 97.412%) are close to unity, which indicates that the matching strength between variables is very high and the method is adequate to fit all data. Comparing the three data fittings, $\overline{m}_{FW}$ presents higher SERR hence the highest fitting accuracy and converges for a polynomial with lower number of terms hence simpler. It is closely followed by $\overline{m}_{VSW}$ with a similar SERR value and converging for a polynomial with only one extra term. $\overline{m}_{VSW}/\overline{m}_{VSW}$ presents the lowest fitting accuracy. Nevertheless, it still presents a good fitting with SERR above 95%, requiring more five terms to achieve convergence though. Considering previous polynomials with the selected number of terms, an additional comparison between polynomial fittings is assessed by the analysis of error statistical parameters shown in the following tables:

Table 5.4: Nonlinear ERR-Causality 2^{nd} order method errors and goodness-of-fit parameters.

Function	η_{max}	ε_{max}	Max residual	RMSE	R^2	Adj. R^2	Terms	SERR
$\overline{m}_{FW}$	0.0184	0.0463	0.0463	0.0148	0.9995	0.9994	12	0.99718
$\overline{m}_{VSW}$	0.0069	0.0935	0.0935	0.0191	0.9994	0.9993	13	0.9941
$\overline{m}_{VSW}/\overline{m}_{FW}$	0.0084	0.0491	0.0491	0.0147	0.9998	0.9998	16	0.9741

The lowest value of the maximum percent relative error (η_{max}) is presented for $\overline{m}_{VSW}$ and its highest value, presented for $\overline{m}_{FW}$, is more than twice the lowest. Contrariwise, the lowest value of the maximum absolute error (ε_{max}) is presented for $\overline{m}_{FW}$, being the highest value, for $\overline{m}_{VSW}$, more than twice the lowest. $\overline{m}_{VSW}/\overline{m}_{FW}$ also presents low values of ε_{max} although in this case, ε_{max} does not seemingly represent a comparable goodness-of-fit, as $\overline{m}_{VSW}/\overline{m}_{FW}$ is a mass ratio hence absolute errors are not related to mass but to mass ratio. Maximum residuals are in our case, equal to ε_{max} values. RMSE is lower for $\overline{m}_{FW}$ and $\overline{m}_{VSW}/\overline{m}_{FW}$. Overall, and as seen by the close to unit values of both R-Squared and adjusted R-Squared parameters, a high goodness-of-fit is accomplished for the three polynomials with the selected number of terms.

5.3.3 Sensitivity Study

While numerical error analysis and magnitudes of polynomials' significance have been presented along the selection of the data fitting procedure, a sensibility study may be performed to clearly understand how similarly predicted data (from the polynomial formulation) expounds calculated data (from FEM-based optimisation). Two plots for each polynomial are represented and anal-

ysed. Firstly, polynomials are used to generate a vector of predicting data for the same DoE design variables as the calculated data. Secondly, these vectors are plotted for an even comparison. Plots on the left side of Figures 5.6 to 5.8 show mass results for each DoE data point, while plots on the right side enable a proper comparison between calculated and predicted data with respective fitting errors. In addition, data variability is illustrated in the right side of these figures.

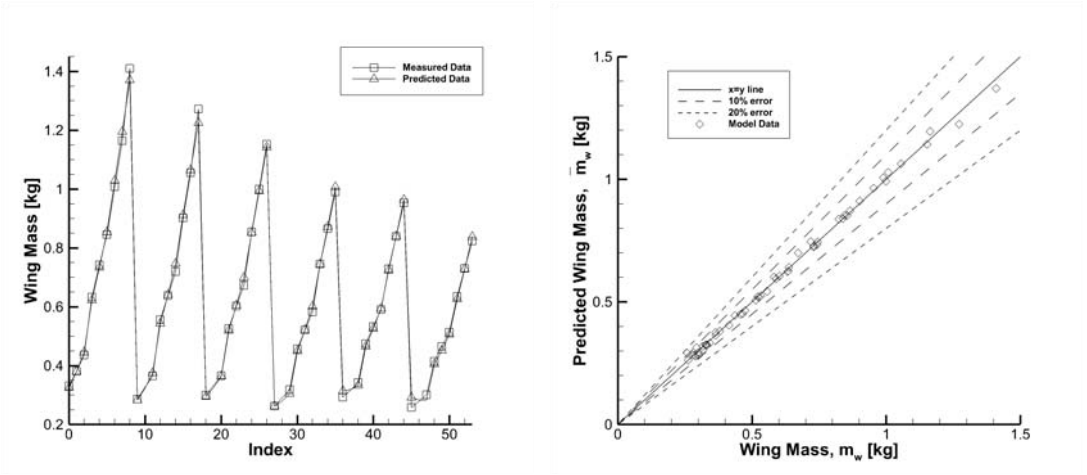

(a) Wing mass results per experiment. (b) Measured vs predicted wing mass datasets.

Figure 5.6: Data fitting accuracy for the FW mass case.

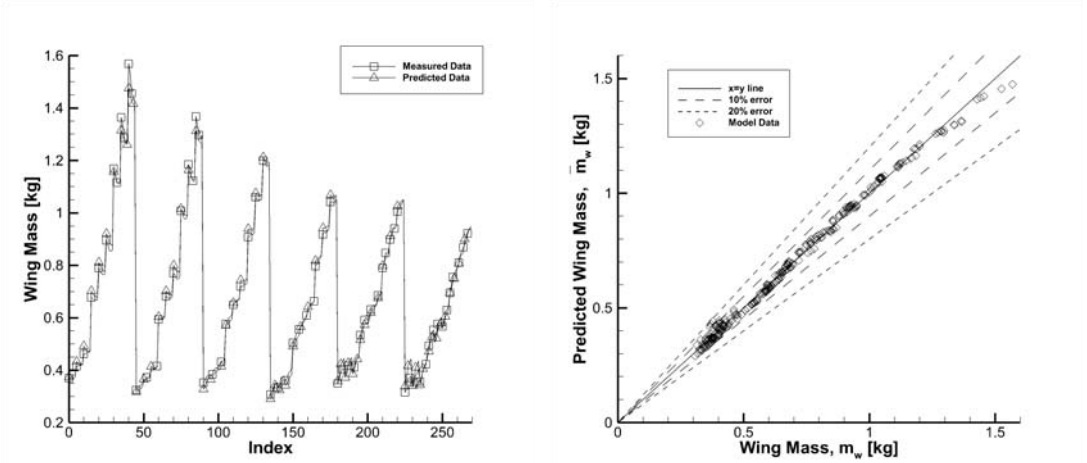

(a) Wing mass results per experiment. (b) Measured vs predicted wing mass datasets.

Figure 5.7: Data fitting accuracy for the VSW mass case.

A first analysis of fitting accuracy may be observed from the plots located in the left hand side, where predicted data lines overlap quite accurately measured by visualizing the design points for which the fitting polynomial is incapable of an adequate representation, mainly the outermost and innermost data points (lowest and highest mass values). From the right hand side plots, it is noticeable that most points are in the neighbourhood of the $x = y$ line, thus validating visually the suitability of the method employed. No data points surpass the 20% error line and only few surpass the 10% error line, which means that mass functions generally approximate the discrete data with acceptable accuracy. The fitting error under analysis in these plots is

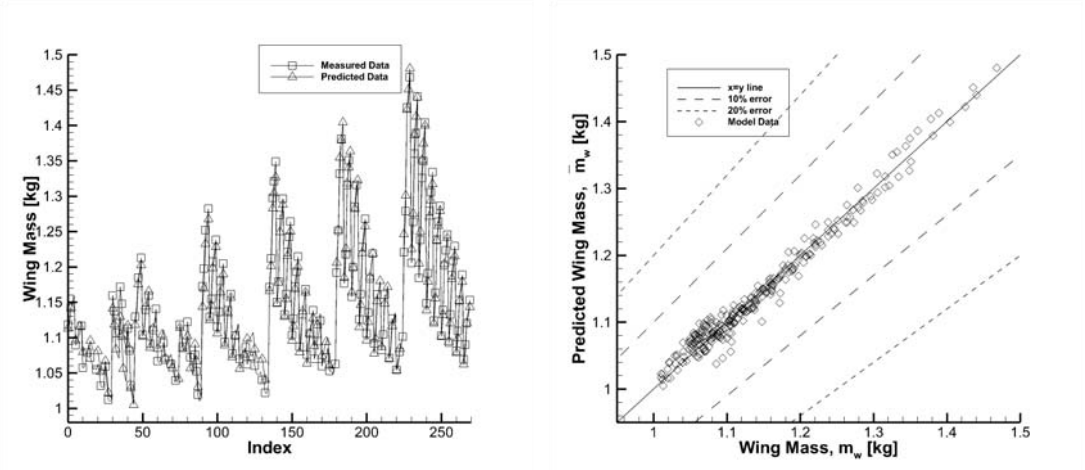

(a) Wing mass results per experiment. (b) Measured vs predicted wing mass datasets.

Figure 5.8: Data fitting accuracy for the VSW/FW mass ratio case.

a percent absolute error, the reason why errors are lower for the VSW/FW mass ratio case, as seen in Figure 5.8.

5.3.4 Wing Structural Mass Functions

Finally, resulting polynomials are computed for the selected data-fitting approach and are represented with the converged number of terms in descending order of significance. To simplify equations, $W \times 10^{-2}$ is expressed as W' hereinafter. The $\overline{m}_{FW}$ function obtained by using the nonlinear ERR-Causality regression method, resulted in a multivariable 2^{nd} order polynomial with 12 significant terms and is represented by the following equation

$$\begin{aligned}\overline{m}_{FW} = {} & 0.121763673b + 0.656478979c - 0.009130511W' - 1.28929bc \\ & +16.29543874\bar{c}_{flap} + 0.2076bW' - 1.32205cW' - 0.42563b\bar{c}_{flap} \\ & +0.06819b^2 - 22.00708\bar{c}^2_{flap} + 5.95774c^2 - 0.4691W'\bar{c}_{flap}\end{aligned} \tag{5.25}$$

$\overline{m}_{VSW}$ function resulted in a 2^{nd} order polynomial with 13 terms, defined as

$$\begin{aligned}\overline{m}_{VSW} = {} & 0.181526365b - 1.631693335c + 0.112782703W' \\ & -1.49982bc + 19.97699743\bar{c}_{flap} + 0.18747bW' - 0.47517b\bar{c}_{flap} + 0.07991b^2 \\ & -28.00155\bar{c}^2_{flap} + 9.18231c^2 - 1.18482cW' + 3.56318c\bar{l}_{var} - 0.804634309\bar{l}_{var}\end{aligned} \tag{5.26}$$

Finally, $\overline{m}_{VSW}/\overline{m}_{FW}$ function resulted in a 2^{nd} order polynomial with 16 terms, defined as

$$\begin{aligned}\overline{m}_{VSW}/\overline{m}_{FW} = {} & -0.040366559b - 1.008071842c - 0.64679bc - 0.851742757\bar{l}_{var} \\ & +6.17159c\bar{l}_{var} - 0.038854783W' - 0.32748b\bar{l}_{var} - 0.26330917c_{flap} \\ & +0.03999b^2 - 0.03561 + 3.85975c^2 + 1.86028\bar{l}_{var}c_{flap} + 2.69658cc_{flap} \\ & -0.1838bc_{flap} - 0.33888\bar{l}_{var}W' + 0.73159\bar{l}^2_{var}\end{aligned} \tag{5.27}$$

The full functions, with all terms and respective ERR parameters represented, are enclosed in Table E.1, in Appendix E. The presented functions accurately describe the dependent variables of interest taking into account that terms are arranged in a significance decreasing order and

first terms of the polynomial parameters' arrangement were selected. It may be observed that b, c and W' are the main players in the wing mass functions (first and second DoE cases), with presence in the first four more significant terms and similarly, b and c with presence in four equation terms. For example, in the $\overline{m}_{VSW}$ polynomial, only the first term b itself, represents 80.72% of the entire solution, reflecting the critical effect of b in the wing mass.

The high influence of b, W' and c in the wing mass is already well known. A higher aspect ratio (higher b and/or lower c) would have a distributed aerodynamic loading further from the fuselage and again demanding extra structural rigidity to comply with tip deflection and rotation requirements, thus the great impact of both b and c to the resulting wing mass. W' has direct influence in the wing loading and also presents large effect in the wing mass. Remaining parameters are still relevant for the fitting and are included in the resulting nine more significant terms of the equation, with less significance in the overall wing mass though. It may be understood that $\bar{l}_{var}$ has no representative influence on the wing mass when compared with other wing parameters as it only occupies the last terms positions.

For the third DoE case, it is not the wing mass of a specific concept that is under evaluation, but the mass ratio between a VSW concept and a FW concept. This function already describes the considerable increment in the wing structural mass that morphing technologies are formerly known to have. In this case, significance orders are better distributed with b representing 29.81% (instead of 80%) and c representing 29.03% (instead of 5%) of the function significance. $\bar{l}_{var}$ finally manifests a slightly higher significance relative to other parameters, as it is present in the fourth and fifth terms, with a representation of 6.86% of the function significance for the fourth term. Such results are comprehensible and lay inside the expectations of the present work, as only the third DoE case clearly describes the mass penalty associated with the implementation of a morphing concept in relation to a conventional one. Notwithstanding, b and c parameters still keep the highest significance on the wing mass ratio function. More detailed conclusions may be taken from ensuing partial derivatives and 3D plots analysis.

5.3.5 Wing Structural Mass Partial Derivatives

Partial derivatives are used to sample variables independence and its marginal effect on wing mass. The same in-house developed script that is used to compute the post-processing of the regression model (polynomial significance, data fitting accuracy, plots and derivatives), is used. Firstly, partial derivative equations are computed from each of the three DoE cases with the selected number of terms. Wing parameters independence is proved from the complete functions as all selected wing parameters are required to define each mass partial derivative. The reduced partial derivative functions for the developed FW, VSW and VSW/FW mass predicting functions (Eqs. 5.25 to 5.27) are presented in Appendix D. Equations from Appendix D should only be considered valid in the wing parameters' range of values defined in Table 5.2. Partial derivative results, coupled with the previous ERR analysis, assemble a screening of the selected parameters' significance which consolidates the selection of such parameters as it proves that all selected parameters have significant influence in the wing mass. As observed in the partial derivative functions from Appendix D, terms with c parameter quite frequently present the highest coefficients' values, thus the marginal effect on mass with respect to each wing parameter is significantly influenced by c. Eqs. D.4, D.9 and D.13 are exceptions to this trend, in which $\overline{c}_{flap}$ parameter shows a surprisingly high influence on the marginal effect on mass with

respect to $\overline{c}_{flap}$ and $\overline{l}_{var}$ parameter with respect to W'. Moreover, functions that define the marginal effect on mass and mass ratio with respect to $\overline{l}_{var}$ and W' present less terms as these parameters have less significant terms in mass equations.

Secondly, partial derivatives are evaluated for a case study. The baseline wing (b=3.554m, c=0.257m, $\overline{l}_{var_{max}}$=0.254, W=150N (W'=1.5 hN), $\overline{c}_{flap}$=0.3) is used in the application of the case study and results may be seen in Table 5.5. As partial derivative results for each wing parameter are related to the magnitude of such parameter, the actual influence on mass of each wing parameter may be only compared by computing mass variation for a certain variation on the baseline parameters' values, i.e by multiplying partial derivatives with respect to each parameter by the baseline wing value of such parameter and a variation factor. Thirdly and last, and following the previous lines, mass variability is assessed. A 10% variation of each baseline wing parameter is selected, thus the variation factor is 0.1.

Table 5.5: Partial derivatives evaluated for the baseline wing.

DoE case	$\frac{\partial \overline{m}_w}{\partial b}$	$\frac{\partial \overline{m}_w}{\partial c}$	$\frac{\partial \overline{m}_w}{\partial \overline{l}_{var}}$	$\frac{\partial \overline{m}_w}{\partial W'}$	$\frac{\partial \overline{m}_w}{\partial \overline{c}_{flap}}$
$\overline{m}_{FW}$	0.4587	-2.8458	0	0.2481	0.8751
$\overline{m}_{VSW}$	0.5027	-3.1138	0.1111	0.4745	4.8646
$\overline{m}_{VSW}/\overline{m}_{FW}$	-0.0607	1.0540	-0.0079	-0.1249	0.2491

Table 5.6: Mass variability for a 10% variation on baseline wing parameters.

DoE case	$\Delta\,\overline{m}_{w_b}$	$\Delta\,\overline{m}_{w_c}$	$\Delta\,\overline{m}_{w_{\overline{l}_{var}}}$	$\Delta\,\overline{m}_{w_{W'}}$	$\Delta\,\overline{m}_{w_{\overline{c}_{flap}}}$
$\overline{m}_{FW}$	0.1630	-0.0731	0	0.0372	0.0263
$\overline{m}_{VSW}$	0.1786	-0.0800	0.0028	0.0712	0.1459
$\overline{m}_{VSW}/\overline{m}_{FW}$	-0.0216	0.0271	-0.0002	-0.0187	0.0075

In Table 5.5, partial derivatives present the highest absolute values with respect to c and $\overline{c}_{flap}$. Model sensitivity is thus higher to these wing parameters for each respective mass function evaluated for the baseline configuration, i.e. c and $\overline{c}_{flap}$ design parameters have a predominant effect in the presented functions. In Table 5.6, the actual influence of each design parameter on mass may be compared by the normalized values that describe mass variability. The marginal effect on mass variation is predominant for a variation of b and on mass ratio variation for a variation of c, followed by b.

As a first conclusion, b is the design parameter that mostly influence wing structural mass of both FW and VSW concepts. It presents at least twice the influence on mass variability relative to other design parameters, as seen in the first two lines of Table 5.6. While a predominant marginal effect of b on wing mass was already expected and brings no breaking-through conclusions for the current study, the marginal effect on wing mass is quite similar for a variation of the remaining design parameters, being $\overline{l}_{var}$ the exception. On one hand, c and W' have higher influence in mass variability for the FW concept. On the other hand, $\Delta\,\overline{m}_{w_{\overline{c}_{flap}}}$ is higher for $\overline{m}_{VSW}$ than for $\overline{m}_{FW}$, which means that $\overline{c}_{flap}$ has higher preponderance in wing mass increase for the VSW concept. It is interesting to notice the significant marginal effect of $\overline{c}_{flap}$ on VSW mass, with almost twice the mass variability than c and W'. The early assumption that flaps' position relative to chord would be less significant to wing mass, the reason why only two DoE

levels for $\overline{c}_{flap}$ were used in the parametric study, is therefore not validated by results. As a second conclusion, further $\overline{c}_{flap}$ levels should have been applied so that more than its linear behaviour (achieved with two levels) could be investigated.

Moreover, $\Delta\,\overline{m}_{w_{\overline{c}_{flap}}}$ is positive in both FW and VSW cases, thus this representative effect points on increasing wing mass for a positive variation on $\overline{c}_{flap}$. When $\overline{c}_{flap}$ increases, wing outer skin perimeter reduces, but the aft spar web is moved forward hence its height increases. While the skin perimeter reduction is only applied in the flap area, the aft spar web is moved forward in a higher span fraction of the IFW and in the entire OMW span. This explains why net results increase in overall wing perimeter and therefore, why wing mass increases with increasing $\overline{c}_{flap}$. Notwithstanding, wing stiffness is decreased with increasing $\overline{c}_{flap}$ due to the torsion-box area reduction. If the skin thickness does not increase to accommodate a possible reduction in torsion stiffness, then the increase in wing mass is due to the above reason.

Wing c has the most significant marginal effect in telescopic wing mass penalties, as seen in the third line of Table 5.6. As a third conclusion, c is therefore, the most important parameter to consider in wing design for predicting wing structural mass penalties related to telescopic concepts. Soon after c, b and W' design parameters also present a significant effect in mass penalties. W' and b effects on mass penalties due to telescopic concepts was already commented. Regarding c parameter, wing mass is increased by reducing c, but this effect is quite more noticeable for FW concepts than VSW concepts, as it may be observed from mass variability results. Therefore, telescopic wing designs with small chords grant low mass penalties.

In the current study, $\bar{l}_{var}$ is the variable that enables selecting between a conventional fixed wing design, when zero valued, and a morphing telescopic design with different telescopic moving fractions, when $\bar{l}_{var}$ is higher than zero. Accordingly, considering that morphing concepts have an inherent cost on wing mass due to its increased complexity, a crucial effect in wing mass penalties was expected from $\bar{l}_{var}$. Notwithstanding, the marginal effect on VSW mass and on $\overline{m}_{VSW}/\overline{m}_{FW}$, for a variation of $\bar{l}_{var}$, is quite negligible in relation to the remaining design parameters under analysis. Fourth and last conclusion, $\bar{l}_{var}$ is therefore not a significant design parameter in predicting wing mass of telescopic concepts and the early assumption that this morphing-related parameter is paramount to understand how mass increases due to telescopic wing concepts is now disproved. While current results are uniquely indicative in the neighbourhood of the baseline wing sizing, further analysis are conducted based on 3D plots to better understand the trends of such neutral effect of $\bar{l}_{var}$ on VSW structural mass.

In sum, the most relevant conclusion to obtain a low structural mass in a wing design point of view (both FW and VSW concepts) is to reach a wing sizing with over and above small b, and secondly large c, low W and $\overline{c}_{flap}$ values. When comparing VSW and FW concepts with the baseline size, low c and also, high b values, are the most effective design options to decrease structural mass penalties on telescopic wing designs over conventional concepts. Therefore the application of telescopic wing concepts is worthier when design requirements limit wing mean chord to a low value or even better, if wing AR is limited to a maximum low value. $\bar{l}_{var}$ variations have no significant effect on telescopic wing mass penalties (when evaluated to the wing baseline dimensions) hence in a design point of view this wing parameter should be maximized to increase wing morphing skills with a negligible cost on wing mass.

5.3.6 Effect of Design Parameters on Wing Structural Mass - 3D Plots

Further plots are produced to a visual validation of polynomials as well as to analyse how design parameters perform and interact between each other. Scatter plots exhibit 'real' structural mass data points with regard to the database generated from the FEM-based optimisation procedure. Contour plots illustrate the developed wing structural mass estimative functions and are generated by computing a discrete range of estimated mass data points from these functions, for a selected grid of wing parameters within the boundaries of the DoE levels. The number of data point is selected, between 27 and 40, depending on the DoE variable and so that resulting grids are smooth and contour plots clearly represent parameters variability. Estimated mass values are obtained from the predicting polynomials of each respective DoE case, either related to the non-morphing fixed wing, the telescopic wing or the wing mass ratio.

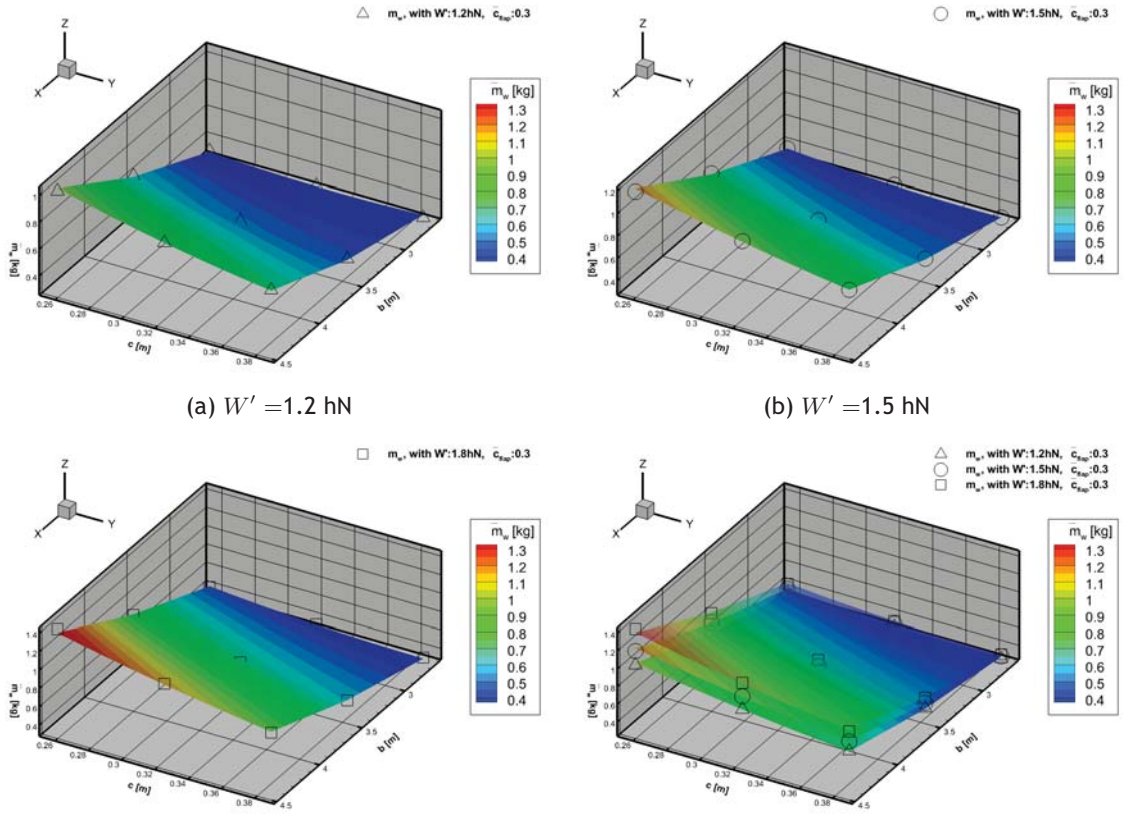

(a) W' =1.2 hN (b) W' =1.5 hN

(c) W' =1.8 hN (d) All W' values for comparison.

Figure 5.9: FW mass estimation as a function of c and b for different W' values.

In Figure 5.9, FW mass is plotted as a function of c and b for different W' values, with constant $\overline{c}_{flap}$. It may be seen that FW mass increases with increasing b and decreasing c. The former happens as for a fixed chord, surface area increases with increasing b hence resulting in a heavier wing. Moreover, for a given lift, root bending moments increase with span, thus wing sizing converges for thicker components. The latter occurs as the wing-box is smaller for a lower c hence the wing cross-section is less stiff, which results in a higher tip rotation and displacement that are optimisation constrains. Therefore, less bending and torsion inertia due to structural height require more material to compensate hence resulting in a heavier wing.

AR increases with increasing b and decreasing c, so the lift loading is further distributed for the tip and increased bending moments are spanwise applied. By comparing the contour plots for different values of W', a positive vertical translation occurs for higher b and lower c values. This means that the effect of W' on wing mass is increased for increasing b and decreasing c values. Therefore, W' presents a more considerable effect on FW mass for higher AR wing designs, whereas for lower AR wings, FW mass is little or not affected at all by W'.

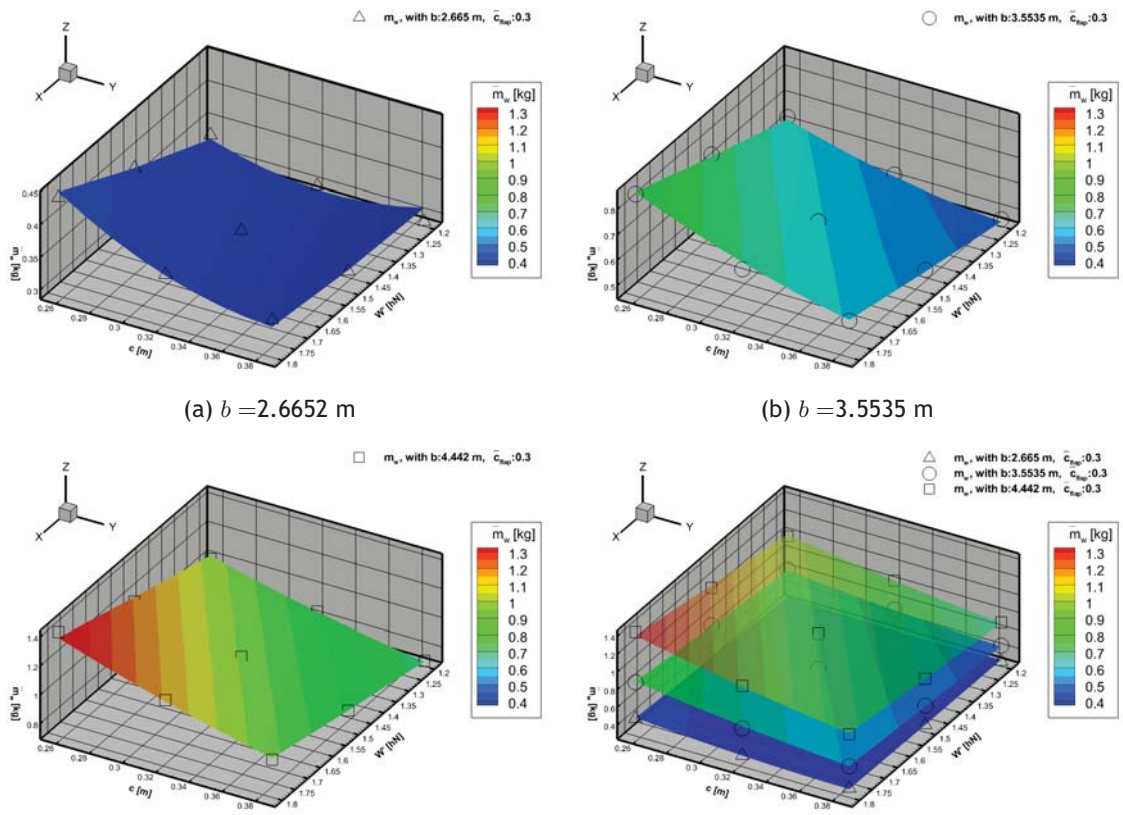

(a) b =2.6652 m

(b) b =3.5535 m

(c) b =4.4420 m

(d) All b values for comparison.

Figure 5.10: FW mass estimation as a function of c and W' for different b values.

In Figure 5.10, FW mass is plotted as a function of c and W' for different b values, with constant $\bar{c}_{flap}$. It may be seen that as a general trend, FW mass increases with increasing W' and decreasing c. Mass increases with W' as expected, once wing loading increases for a heavier aircraft. By comparing contour plots for different values of b, a vertical positive translation is presented for increasing b values, therefore wing mass is again clearly affected by b.

Contours overall slope slightly increase for increasing b, but for the lowest b plot a concavity opens upward near the $x = y$ line with higher wing mass values for higher W' and lower c values. In this plot, with b =2.665 m, wing mass is nearly constant for maximum c and varying W' values, whereas for the lowest c value, wing mass increases more significantly for increasing W' values. This means that in a FW design point of view, if c is large, the aircraft may be as heavier as desired (considering the DoE parameters range) without a significant wing mass penalty. This trend is more significant for lower b values. For plots (b) and (c), with higher b values, the concavity is not presented but a near constant slope, which means that wing mass increases more linearly with increasing W' and decreasing c values.

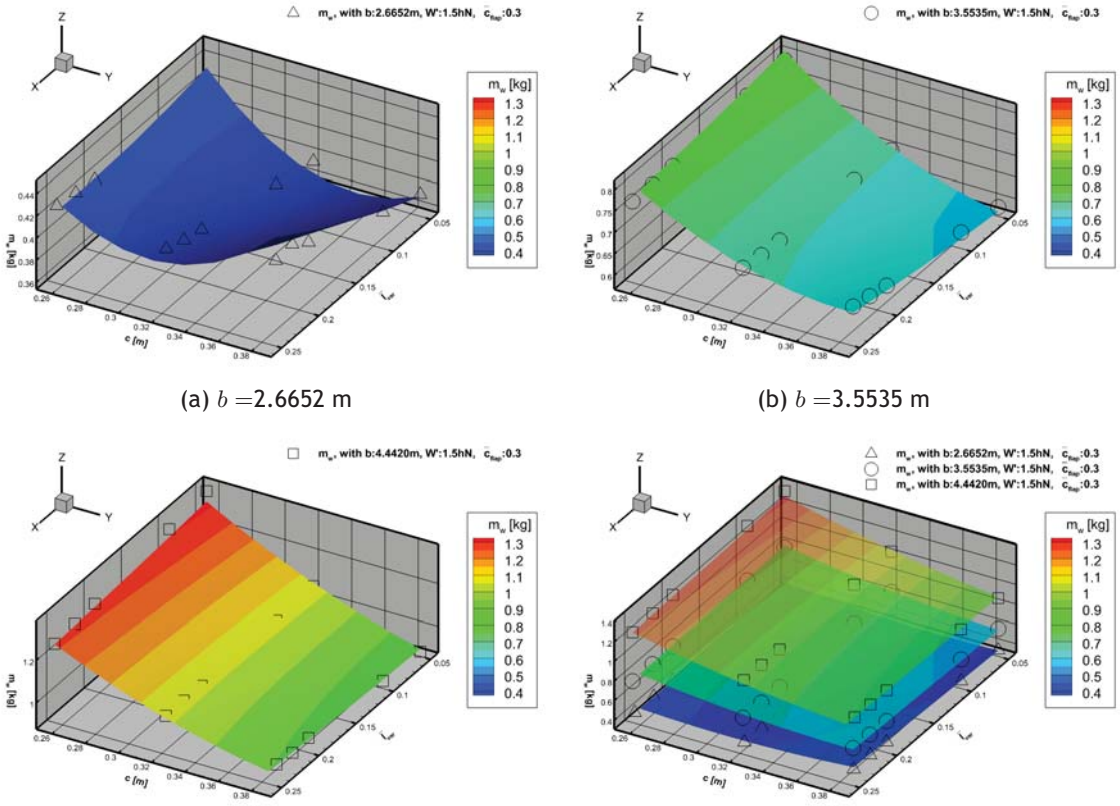

(a) b =2.6652 m

(b) b =3.5535 m

(c) b =4.4420 m

(d) All b values for comparison.

Figure 5.11: VSW mass estimation as a function of c and $\bar{l}_{var}$ for different b values.

In Figure 5.11, VSW mass is plotted as a function of c and $\bar{l}_{var}$ for different b values, keeping $\bar{c}_{flap}$ and W' constants. VSW mass increases with increasing b values and increases with decreasing c values. From comparing contour plots, VSW mass is not significantly affected by c for a wing with low b values, whereas for higher b values, wing mass slightly increases with decreasing c values. In a VSW design point of view, for low wingspans, c or $\bar{l}_{var}$ may be aerodynamically optimised without the risk of even slight mass variations. Furthermore, from comparing plots, for different values of b, a positive vertical translation occurs for increasing b values, which shows mass increase trend when increasing b. Notwithstanding, the contour plot with the lowest b value exhibits a different behaviour. It has a positive concavity that opens upward with the minimum line for an approximately mean c value. This result may be conceptually explained by the two conditions that present a mass increase. A wing with a smaller c is less stiff to resist torsion moments as an effect of the wing cross-section being smaller, thus mass increases.

For a larger c, the wing is stiffer to resist torsion moments but not necessarily stiffer in bending, for which spar caps have a more central role. Nevertheless, the aerofoil is thicker for a larger c hence spar caps are more spaced and so, the vertical moment of inertia is increased and the wing is stiffer in bending. This fact also dictates that VSW mass increases with decreasing c. The opposite happens for high c and low b values, for which the cross-section structure in the overlapping area has material in excess that is not transferring loads to the IFW, therefore VSW mass increases with increasing c as seen in Figure 5.11 (a). This structural behaviour is not presented in plots with larger b because an increase in the wingspan generates a higher bending moment in the interface and the overlapping structure has to react to such higher loads.

VSW mass due to $\bar{l}_{var}$, is again clearly close to constant in plots with medium and higher b values, being contour plot with the lowest b value the exception, even so presenting only slight variations on VSW mass. In this plot (a), wing mass increases with increasing $\bar{l}_{var}$ for high c values and slightly decreases with increasing $\bar{l}_{var}$ for low c values. Overall, VSW mass is again negligibly affected by $\bar{l}_{var}$, which leads to the conclusion that in a VSW design point of view, the designer should maximise the wing variable-span length that is permitted by geometrical constrains. Consequently, higher $\bar{l}_{var}$ values enable higher morphing actuation capabilities without perceptible VSW mass costs, which stretches the flight envelope, enhances aircraft performance, energy efficiency and extends manoeuvrability.

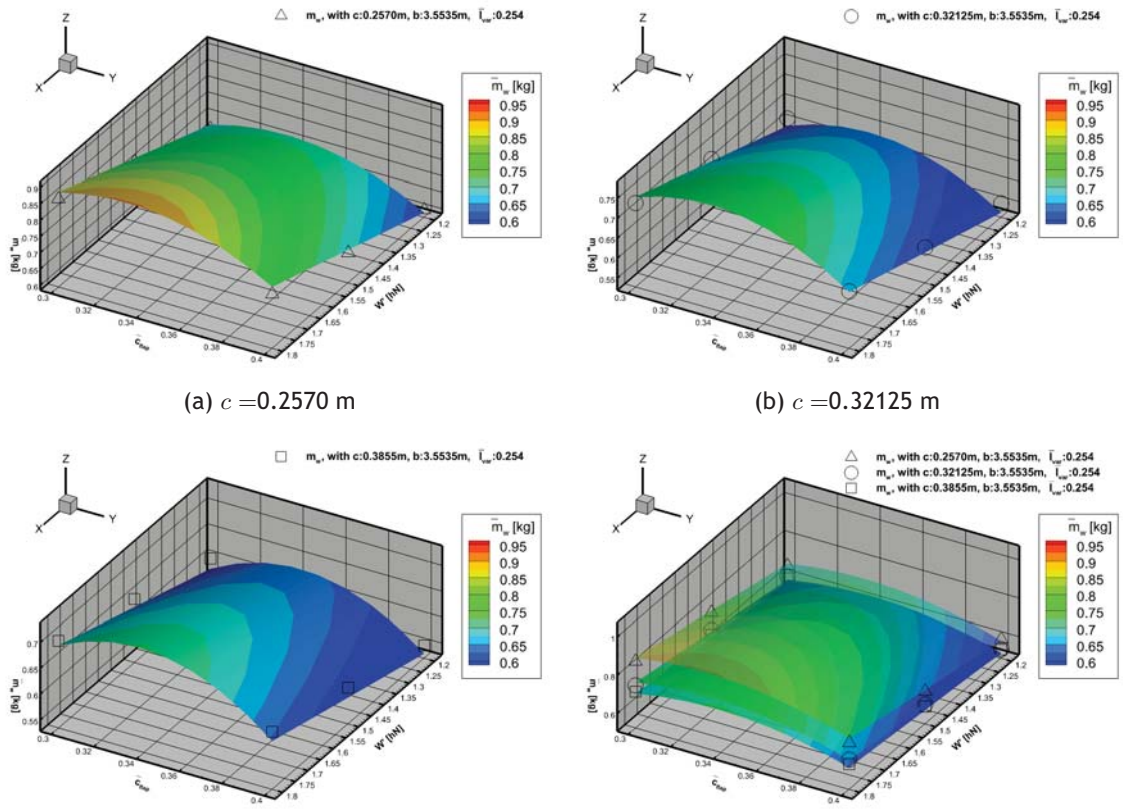

(a) c =0.2570 m

(b) c =0.32125 m

(c) c =0.3855 m

(d) All c values for comparison.

Figure 5.12: VSW mass estimation as a function of $\bar{c}_{flap}$ and W' for different c values.

In Figure 5.12, VSW mass is plotted as a function of $\bar{c}_{flap}$ and W' for different c values, keeping b and $\bar{l}_{var}$ constants. From comparing plots, it is once again explicit the VSW mass increase with decreasing c. Contour plots exhibit a negative concavity that opens inward with the maximum line for an approximately mean $\bar{c}_{flap}$ value. As a general trend, VSW mass increases with increasing W' values. This was expected as wing loading increases with increasing W' hence wing needs to be sized accordingly. VSW mass also increases with increasing $\bar{c}_{flap}$ for low $\bar{c}_{flap}$, which is in consonance with baseline partial derivatives' results. On the other hand, VSW mass decreases with increasing $\bar{c}_{flap}$ for high $\bar{c}_{flap}$ values. Overall, between the two DoE levels of $\bar{c}_{flap}$, which only define a linear behavior, VSW mass decreases with increasing $\bar{c}_{flap}$.

In Figure 5.13, VSW mass is plotted as a function of c and b for two $\bar{l}_{var}$ values, the minimum and maximum values used in the parametric study, keeping $\bar{c}_{flap}$ and W' constants. Comparing both

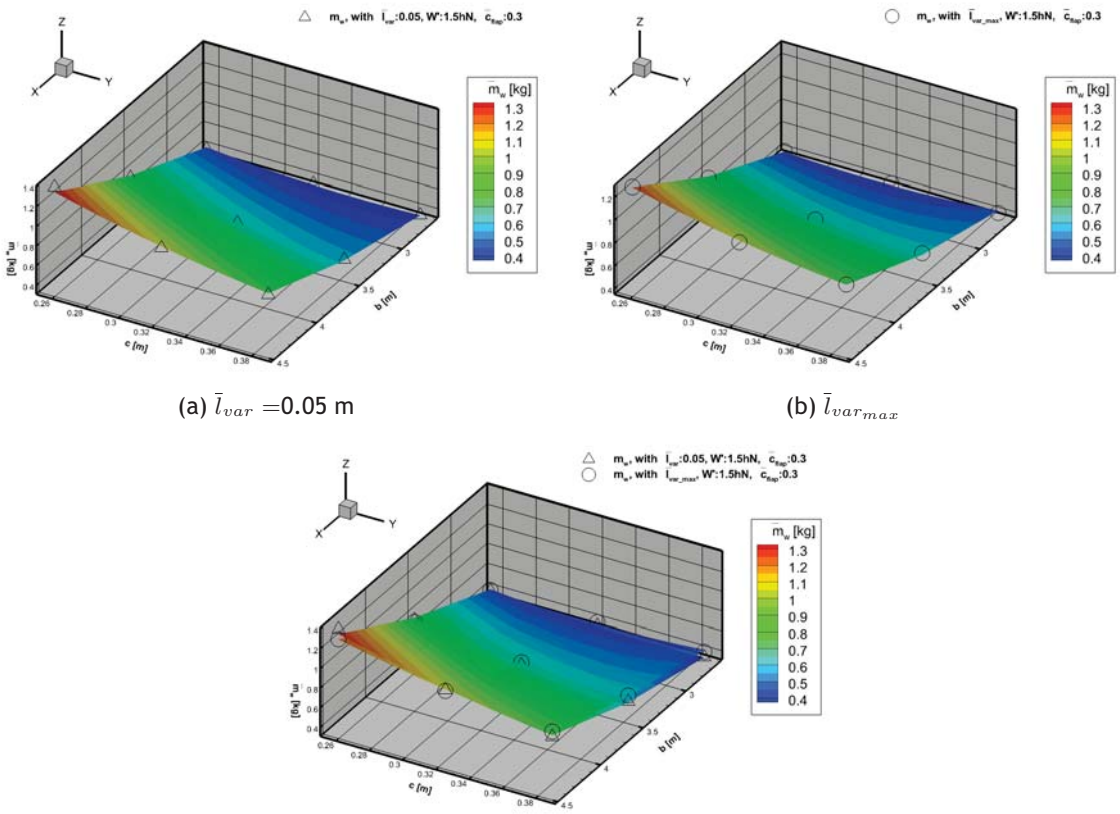

(a) $\bar{l}_{var}$ =0.05 m

(b) $\bar{l}_{var_{max}}$

(c) $\bar{l}_{var}$ minimum and maximum considered values for comparison.

Figure 5.13: VSW mass estimation as a function of c and b for different $\bar{l}_{var}$ values.

plots, a slight negative rotation in the $x = y$ line is visible, with wing mass to be maximum for the contour plot with $\bar{l}_{var}$ =0.05 and minimum for the plot with $\bar{l}_{var_{max}}$. Once again, evidence shows that $\bar{l}_{var}$ has no preponderance in VSW mass and the reason for such may be seen conceptually, for two different geometrical and structural reasons, both with two main contributing factors that have opposite reactions in the wing mass variation. Firstly, from the geometrical characteristics of the VSW concept, l_{IFW} decreases considerably less than what l_{OMW} increases for higher $\bar{l}_{var}$ values. As the IFW panel is naturally heavier than the OMW panel, for higher $\bar{l}_{var}$ values, a small l_{IFW} decrease is balanced in volume/weight by a higher l_{OMW} increase.

Secondly, wing mass neutrality to $\bar{l}_{var}$ variation may be also explained due to VSW loading characteristics. The structural optimisation most critical load in the VSW sizing is the wing root bending moment, which is constant for a fixed b value with same loading and wing cross-section. Therefore, skin and spar caps of the IFW panel are equally sized for a fixed b, no matter which $\bar{l}_{var}$ value is considered. Moreover, OMW panel mass is also kept approximately constant for different $\bar{l}_{var}$ values. On one hand, the loading acting in the OMW panel is higher for a higher $\bar{l}_{var}$ value, as a higher OMW area relatively to wingspan is exposed to the airstream hence a stronger, more rigid wing structure is required. On the other hand, this loading is transferred for the IFW through a higher overlapping area and placed closer to the root hence loading is better distributed between panels. As the overlapping area is the structural most critical region when sizing the OMW, even if loads are higher for a higher $\bar{l}_{var}$, panels applied pressure is lower for a higher overlapping area and therefore, for a fixed b also the OMW is sized for approximately

equal spar caps widths and skin thicknesses, no matter which $\bar{l}_{var}$ value is considered.

Similarly to Figure 5.11, it is shown that b and c parameters present considerably higher magnitudes than $\bar{l}_{var}$, hence it is difficult to duly evaluate effects in wing mass due to the implementation of the morphing wing concept. In these lines, the third DoE case, $\overline{m}_{VSW}/\overline{m}_{FW}$, is performed with the aim to understand mass penalties of the VSW concept with respect to a FW concept.

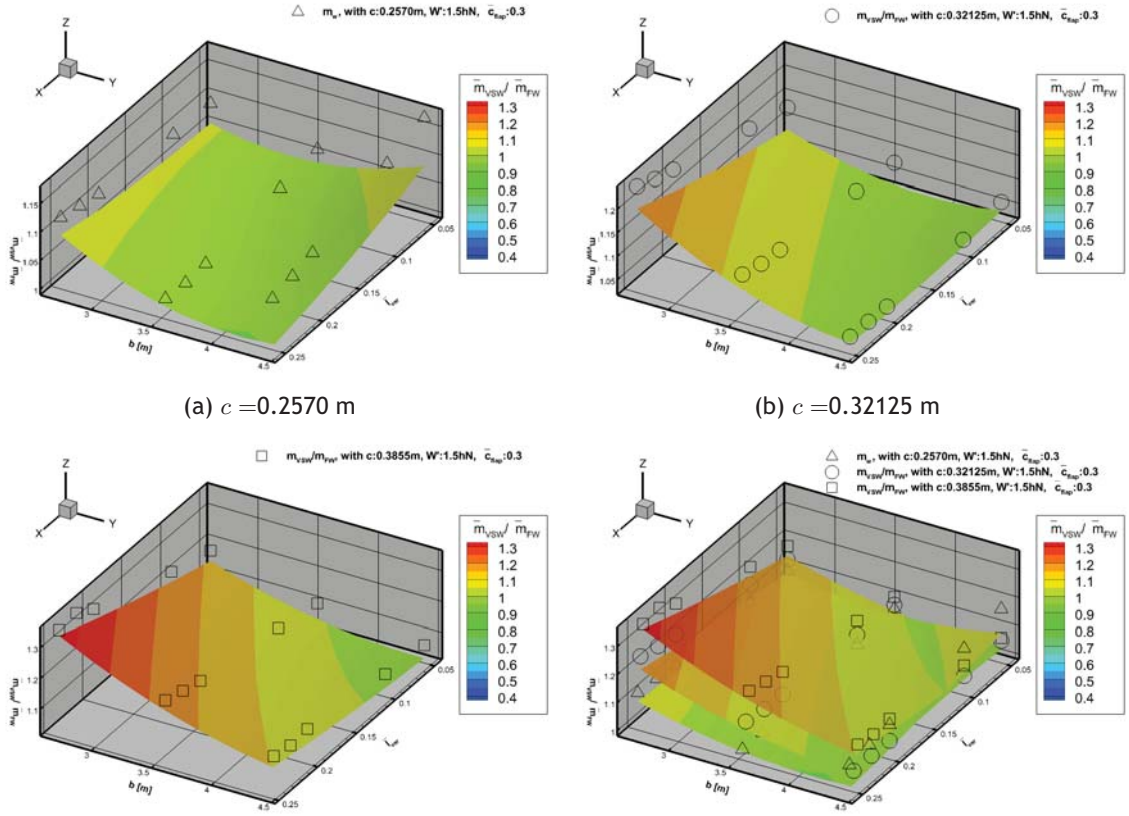

(a) c =0.2570 m

(b) c =0.32125 m

(c) c =0.3855 m

(d) All c values for comparison.

Figure 5.14: VSW/FW mass estimation as a function of b and $\bar{l}_{var}$ for different c values.

In Figure 5.14, VSW/FW mass ratio is plotted as a function of b and $\bar{l}_{var}$ for different c values, keeping $\bar{c}_{flap}$ and W' constants. First and foremost, it may be seen that all VSW/FW results are above unity hence the VSW concept is clearly heavier than the FW concept for all studied wing configurations. Secondly, mass penalty in plot (a) is closer to unit hence conditions in this plot (small wing chord) enhance VSW benefits. Moreover, mass penalties generally increase with decreasing b and increasing c, i.e the wing configuration that carries less mass penalty is the one with the highest AR. This is consistent with partial derivatives results and may be seen by comparing contour plots, where a positive vertical translation is exhibited for increasing c values coupled with a negative rotation near the $x = y$ line for higher c values. In opposition to such rotation, an exception to the presented trend is found for average to minimum $\bar{l}_{var}$ values in plot (a), in which mass penalties increase with increasing b. Therefore, for small c values, and if $\bar{l}_{var}$ is reduced due to design constrains, b should be decreased for a mean DoE level value to minimise mass penalties.

As the effect on VSW mass due to wing parameters is now scaled by a conventional wing mass, the effect of $\bar{l}_{var}$ is hereinafter more seemingly represented. Mass penalties due to $\bar{l}_{var}$ are now more perceptible in Figure 5.14, in particular for low b values in plots (b) and (c). In such plots, for average and high c values, VSW mass penalties increase more significantly with increasing $\bar{l}_{var}$ values. This trend occurs more significantly for higher c and lower b values hence for decreasing AR. Notwithstanding, for low c value, $\bar{l}_{var}$ contribution on mass is negligible, with even a slight decrease in mass penalties when increasing $\bar{l}_{var}$ (as evaluated by partial derivatives case study). It is interesting to point out that the design point of the baseline wing is located in plot (a) for mean b and maximum $\bar{l}_{var}$ values, which corresponds to one of the design points that lead to lower mass penalties. Although lower c values were not evaluated for structural feasibility reasons, this results shows that baseline wing dimensions were well selected to maximise VSW benefits relatively to the FW, on Olharapo III performance comparative study.

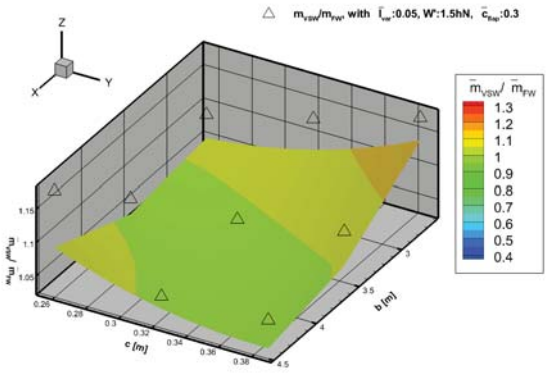

(a) $\bar{l}_{var}$ =0.05 m

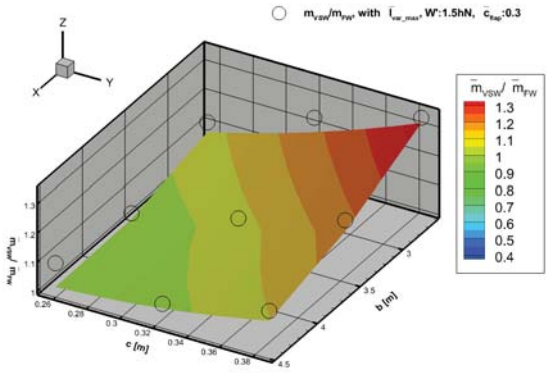

(b) $\bar{l}_{var_{max}}$

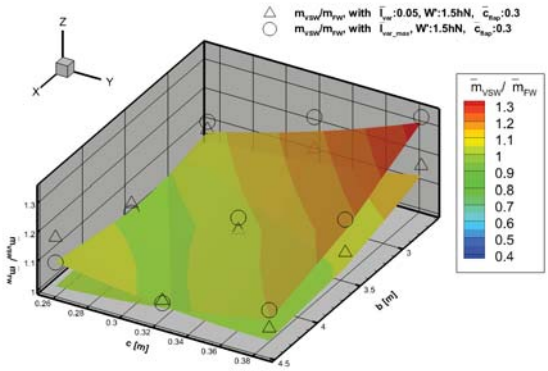

(c) $\bar{l}_{var}$ minimum and maximum considered values for comparison.

Figure 5.15: VSW/FW mass estimation as a function of c and b for different $\bar{l}_{var}$ values.

In Figure 5.15, VSW/FW mass ratio is plotted as a function of c and b for two $\bar{l}_{var}$ values, the minimum and maximum values used in the parametric study, keeping $\bar{c}_{flap}$ and W' constants. Mass ratio increases for increasing c and decreasing b values, with exception for high b values of the minimum $\bar{l}_{var}$ plot, in which mass ratio increases for decreasing c values. As a general trend, plots shows that mass penalties are kept constant if the AR is fixed and decrease for increasing AR. By comparing plots, it may be seen a rotation in a parallel axis to the $x = y$ line, with a slope increase to increasing $\bar{l}_{var}$ values. Accordingly, mass ratio increases for increasing $\bar{l}_{var}$ values if the AR is lower than 13.5, approximately; and decreases for increasing $\bar{l}_{var}$ values

if the AR is lower than this value. On one hand, if a wing is designed with a low AR, then it is best to choose a design point with lower $\bar{l}_{var}$ value or not to employ a telescopic concept at all. On the other hand, if the wing under design has a high AR, then using $\bar{l}_{var_{max}}$ is highly beneficial both in performance and to significantly reduce VSW mass penalties when compared to a non-morphing concept.

In sum, mass ratio results show that VSW concepts are worthier in a wing design point of view where a high b and low c values are design requirements and $\bar{l}_{var}$ is maximised. For small c values, and if $\bar{l}_{var}$ is necessarily reduced due to design constrains, b should be decreased for a mean DoE level value to minimise mass penalties. With increasing c values, $\bar{l}_{var}$ presents a more preponderant effect on wing mass penalties and should be decreased to minimise mass penalties. By decreasing $\bar{l}_{var}$, morphing capabilities are being reduced, which is not ideal. In these lines, as mass penalties reduce flight performance, the designer should consider a VSW over a FW first and foremost, if design requirements or optimisation results point towards a small wing chord and secondly, if the wing AR is high or may be increased in following design iterations. If the design points towards a low AR wing, the option on applying a VSW concept carries increased mass penalties and its benefits over a FW should be decided with an overall assessment of aircraft performance, depending on the magnitude of mass increase and the level of desired operational multi-task flexibility.

5.3.7 Full VSW Mass Function

The methodology detailed in Section 5.2.8 to define a preliminary full VSW mass predicting function is applied. $\overline{m}_{VSW,full}$ is defined in Eq. 5.1 and results from adding the predicting functions for flap's mass (Eq. 5.22), for actuation system's mass (Eq. 5.23) and for VSW structural mass (Eq. 5.26) as well as the correction increments k_1 and k_2. While $\overline{m}_{VSW}$ is already described by a single polynomial function, $\overline{m}_{flap}$ and $\overline{m}_{sys}$ need to be arranged so that the full function may be presented in an overall numeric table. For the $\overline{m}_{flap}$ function, auxiliary calculations are made by considering the wing planform area S equal to $b\bar{c}$ and l_{flap} defined as

$$\begin{aligned} l_{flap} &= b/2 - l_{fus} - 2l_{var} - l_{over2} - l_{tip} \\ &= 0.4564b - \bar{l}_{var}b - 0.145 \end{aligned} \tag{5.28}$$

Moreover, there is a dependency relation on $\overline{m}_{VSW}$ to compute $\overline{m}_{flap,struct}$, as seen in Eq. 5.16, hence for each wing sizing an iterative study should be employed. This is not possible to implement when defining a general single VSW full mass function. Therefore, an approximation is assumed by considering $\overline{m}_{VSW} = 0.181526b$ as this first function term represents 80.72% of the entire solution for the wing structural mass, as previously explained. Another approximation is employed to simplify the resulting function by considering the model's already in use c parameter, instead of $\bar{c}$.

Correcting factors may be preliminary defined to a more particular application, as $\phi_{flap,sys}$ and k_{flap}, in $\overline{m}_{flap}$ function and $k_{act,type}$, in $\overline{m}_{sys}$ function. For $\phi_{flap,sys}$ a value of 2kg/m^2, which accounts for servos, links and cables for the flaps' actuation system, is considered. k_{flap} is a correcting factor that is equal to unity for simple flap concepts and higher than unity if an adaptive flap is used. A simple flap is considered, therefore an unitary k_{flap} is applied. $k_{act,type}$

is a boolean variable and in the current application, it is considered equal to unity because the following VSW case study is aimed for both performance and control purposes.

Correction increments k_1 and k_2 considered in the current study use correction factors of 5% and so, are equal to 1.05$\overline{m}_{VSW}$ and 1.05$\overline{m}_{VSW,full}$, respectively. The former estimates a 5% increase on wing structural mass due to the increase structural loads applied due to flaps actuation and the latter estimates a 5% increase on the full wing mass for non-optimum effects, as it is assumed in a class II-1/2 method presented by Torenbeek for commercial aircraft [101]. Both correction factors are overestimated as they are empirical values derived from manned aircraft studies and RPAS commonly present less critical mass penalties hence resulting $\overline{m}_{VSW,full}$ should be conservative.

Table 5.7: Full VSW mass predicting function.

Term No.	$\overline{m}_{VSW,full}$	
	Coef	Vars
1	1.33343	b
2	-1.88461	c
3	0.13026	W'
4	-1.73229	bc
5	23.07343	$\overline{c}_{flap}$
6	0.21653	bW'
7	-0.54882	$b\overline{c}_{flap}$
8	0.09622	b^2
9	-32.34179	$\overline{c}^2_{flap}$
10	10.60557	c^2
11	-1.36847	cW'
12	4.11547	$c\bar{l}_{var}$
13	-0.92935	$\bar{l}_{var}$
14	3.29014	$c\overline{c}_{flap}$
15	-2.33886	$b\bar{l}_{var}$
16	-0.43026	$W'\overline{c}_{flap}$
17	1.05044	$\bar{l}_{var}\overline{c}_{flap}$
18	-0.20903	$\bar{l}_{var}W'$
19	0.53034	$\bar{l}^2_{var}$
20	0.00441	W'^2
20	0.17154	b/c
20	-0.38120	$b\bar{l}_{var}/c$
20	-0.04574	$1/c$
20	-0.00393	$b^2\bar{l}_{var}$
21	-3.38531	(constant)

The resulting full VSW mass breakdown, presented in Table 5.7, may provide estimates for overall mass properties of telescopic wings' future designs. This new mass function is again a multivariable high order polynomial that uses the same design variables has previous mass functions, although with some new terms, including now even few 4^{rd} order terms.

To validate this preliminary function, a case study should be employed in the follow-up of the current research. Such case study should have been built under similar methods and materials, should have similar geometrical characteristics to the VSW concept considered to generate the $\overline{m}_{VSW,full}$ function and should be subject to a design including a minimum-mass optimisation

procedure, so that it is not oversized in relation to the current study. At the present day, without the existence of a manufactured telescopic wing, with a documented mass breakdown and a structurally optimised design, suitable case study wings for validation purposes could not be found. Even though $\overline{m}_{VSW,full}$ function is not currently validated by a built VSW wing, its results within the DoE levels' limits seem to be reasonable and may be seen as a stepping stone into solving the literature gap on mass functions for telescopic wing morphing concepts.

Chapter 6

Conclusions and Future Research

In this final chapter, conclusions from the resulting VSW design and sizing, as well as from the developed mass functions and design parameters' effect on wing mass, are presented along with future work proposals.

6.1 Concluding Remarks

Overall, some achievements have been made along this work. The conceptual and preliminary design of a telescopic wing to suit a RPAS was developed and documented. Effects of design parameters on wing structural mass were acknowledged and discussed, and a literature gap concerning wing mass predicting functions for morphing applications was assessed by presenting a solution for telescopic wings.

6.1.1 Telescopic Wing Design

A variable-span wing of the telescopic type was designed as an improvement of previous versions for the new Olharapo III RPAS. An integrated and iterative design seems mandatory to drive innovative solutions on being applicable and competitive over conventional designs and overcome the penalties associated with low TRL solutions, as current telescopic wings. In the current work, this integrated approach required multi-disciplinary thinking from early design phases of the VSW development, which associated with the increased parameters interactions inherent to morphing concepts, significantly increased the overall design complexity. While most telescopic concepts have a TRL that is still very low, Olharapo RPAS suited with the VSW, has been upgraded along each version, with proven in-flight performance till version II, being flight proven and still operational. Further improved capabilities were conducted in the conceptual and preliminary design phases of a new third VSW version to suit Olharapo III. Inspired in previous versions, it is a high mounted, straight telescopic wing, without using ailerons as rolling moments are controlled by asymmetrical wing deployment. The differentiating factors of the current version is that, besides the increased dimensions to enable higher payloads, its design makes use of aerodynamically optimized aerofoils and winglets, a minimum-mass optimised structure and actuation system and also, it comprises the possibility of adding morphing high-lift surfaces.

VSW geometry is based on a telescopic wing concept and the wing layout was defined by understanding VSW technology constraints and geometric correlations. The devised structural design and materials' selection was paramount to achieve a lightweight morphing-capable solution that withstands the prescribed loads and has realistic applications. VSW actuation system was designed and sized to enable a simple, lightweight and energy efficient telescopic capability. The resulting VSW actuation mechanism has a mass of 0.325 kg, which represents 2.3% of the aeroplane design MTOM. The application of a continuous flap was selected to extend VSW morphing capabilities and force application requirements for flap's deflection were briefly investigated.

VSW mission profile has multiple operating conditions and its design was performed so that Olharapo III RPAS operates in the range of speeds from about the stall speed of 11m/s to 40m/s. A methodology for developing offset aerofoils given any existing aerofoil, including corrections for the leading edge and trailing edge geometries of the resulting aerofoils, was presented. The outcome of aerodynamic studies gave some hints on the geometry and performance trends expected from the development of geometric offset aerofoil designs intended to slide inside one another and helped design a set of compatible aerofoils suitable to be applied to the VSW design. Both aerofoil and type of offset were selected to achieve an aerodynamic performance that best fits VSW requirements and flight envelope.

Based on the LE correction and TE extension studies, a better aerodynamic performance was achieved with the double-elliptic LE, with x_{LE} =0.64%, for the inward offset aerofoils and the second degree polynomial TE for the outward offsets. Moreover, a small inward offset value was concluded to be favourable to suit the OMW, as it decreases θ, although also decreases $C_l(\alpha)$. UBI-03-012 aerofoils' set (original+inward offset) presented the highest $(L/D)_{max}$ value for the the current design C_l range and overall performance measured, UBI-03-012 was selected between the analysed aerofoils. UBI-03-012 was used as the IFW aerofoil and a inward offset modified version of UBI-03-012 was used as the OMW and tip panel's aerofoil. A winglet with a l_{tip} of 155 mm, a Γ of 31.6°, a sweep angle (Λ) of 19.1° and no ε was added to the OMW geometry to increase aerodynamic efficiency as well as to meet the wing's stability requirements. An in-house developed MDO procedure was employed to obtain wing's final mission-optimised dimensions. VSW overall characteristics, final layout and aerofoils data were documented. A 3D CAD representation of the VSW was developed in *CATIA V5*, renders were computed in different views and 2D technical drawings were produced. V-n combined diagrams were developed for each wing configuration. The aerodynamic loading applied to the wing structure was analyzed for the three wing configurations.

In sum, both conceptual and preliminary designs were detailed and wing characteristics documented. The resulting morphing wing has a $\bar{c}$ of 0.257 m, a $\bar{c}_{flap}$ of 0.3, a b_{max} of 3.554 m in the full extended configuration and a b_{min} of 3.104 m in the full retracted configuration. Accordingly, l_{var} is approximately 0.45 m for the full extended configuration.

6.1.2 Wing Structural Sizing

FEM-based structural analysis and optimisation was employed to reach an optimal sizing of some key VSW structural components. For such, it was developed a minimum mass-objective optimisation, constrained by structural strength and stiffness limits. A surface-based geometry was created using VSW characteristics and its fully extended configuration as this is the design most structurally demanding configuration. Contact elements' behaviour was chosen to be bonded, also to reduce computation cost of each analysis. However, an increase in the local stiffness was foreseen hence underestimating wing tip's displacement and rotation. Another model's simplification example was to merely select the lower surface of the l_{over1} area and the upper surface of the l_{over2} to apply the bounded contact.

ANSYS®Mechanical APDL optimisation facilities were used to carry out the optimisation using the APDL internal language. The APDL optimisation method employed was the first order method, which is the most accurate and robust method available within this software. FEA design vari-

ables adopted were skin's laminate CRFP thicknesses and spar cap's pultruded profiles widths, which were subjected to geometrical limits. Besides user errors, the model presents errors introduced due to assumptions and simplifications as considering a linear structure, small displacements, thin shell element derivation assumptions and boundary conditions approximations. Moreover, loads and material properties are not accurately known and derived from already approximated data. Accordingly, adequate correcting factors were considered for material properties. A mesh convergence study was carried out to assess the sensitivity of maximum tip displacement and rotation values as a function of the element number in the mesh. The refinement of the grid was achieved by changing the global element size and using line size refinements in ANSYS. A FEM with 10000 elements was selected as the solution stabilized for a grid with this number of elements, where both the tip deflection and rotation presented variations well below 1%. Mesh element sizes of 0.024 m were employed in the overall geometry, whereas a refinement was applied in more critical parts.

From the numerical results obtained in the course of the optimisation procedure, VSW skin converged for an overall thickness of 2.24 mm, with t_{lam} =0.12. IFW and OMW spar caps were sized to a width of 21.7 mm and 0.8 mm, respectively. For this condition, the VSW was sized to a minimum mass of 1.0 kg with a convergence of w_{tip} to 0.088 m, of $\theta_{y,tip}$ to -0.36 and of $\overline{FE}_{ITWSR}$ to 0.0113. Strength is not critical and $\overline{FE}_{ITWSR}$ was far from the constraint value of 0.1%. Both tip deflection and rotation results satisfy the imposed optimisation constraints. Tip deflection reached the optimisation bound limits, but torsion was far from its maximum values. Torsion is dominated by the skin, which means that the minimum value selected for the skin fabric, due to its market availability, was too high. If thinner fabrics were available, the optimisation could probably reach a lighter wing solution. Notwithstanding, the obtained VSW mass is already highly satisfactory when compared with previous VSW versions.

Post-processed results were assessed with graphical displays of wing vertical displacement and ITWSR failure criterion. They showed that constraint variables were kept within the desired boundaries. Wing maximum displacement was 0.88 m, in the first quarter chord of the wing tip. Maximum twist also appeared at the wing tip, with a value of 0.45°. Most of the wing presented considerably lower values of ITWSR (up to ten times lower) than the maximum felt in a particular point of the structure. Between the three layers, the one that presented higher ITWSR is the inner layer, closely followed by the outer layer. The maximum value of ITWRS is located in the wing root, near the LE region of the inner and core layers of the VSW skin. Transversal reinforcements increase structure strength in the overlapping area. A variation on ITWSR occurs in the spar regions, where material changes. Interpretation of these results was pivotal to identify structural areas of potential concern (wing-root, although with very low probability of failure) and areas of material waste (panels' outer parts). Due to the bounded contact type, both IFW and OMW were analysed together as a unique piece. Accordingly, after the overlapping area a thickness reduction occurs and ITWSR values are slightly higher in such region of the OMW panel.

Summing up, the performed wing structural sizing, coupled with the selected materials and structural layout lead to a functional design, in terms of span actuation, and to a lightweight structure, with adequate strength and stiffness characteristics.

6.1.3 Wing Mass Function

Morphing wing technologies are still recent and lack adequate maturity, morphing concepts typically present actuation challenges and an undesired mass increase due to their inherent complexity both in the load carrying structure and in the systems that perform morphing. Simple yet suitably accurate mass prediction methods to aid design RPAS telescopic wings at early design phases, as well as to assess the benefits that a VSW can offer over a FW, are non-existent in the scientific community. A parametric study is conducted by using the designed VSW as a baseline wing. $\bar{l}_{var}$, b, c, W' and $\bar{c}_{flap}$ were the selected geometrical and inertial design parameters to supply the model. Three DoE databases were created (m_{FW}, m_{VSW} and m_{VSW}/m_{FW}) with the combination grid of selected DoE levels for these design parameters and respective FEM-based measured structural mass.

A physics-based structural sizing, which enclosed a minimum-mass optimisation loop performing FEA in a similar way as the baseline sizing, was computed for 324 DoE data points. The remaining 270 data points, from the third DoE case, are computed by the quotient of the firsts DoE cases. A wing loading model that assumes a spanwise elliptic lift distribution and is flexible to wing configurations is implemented. FEM-based solution is established and constraints are assessed for compliance. The optimisation problem uses a feasibility tolerance of 0.01 and reaches the objective when a change between loops is less than a convergence criteria of 0.2%. Due to the nature of parametric studies, wing geometric changes may force the mesh to be updated. In order to avoid the need of performing a mesh convergence study for each geometry, the grid relative sizing is kept unaltered. Mass results for each wing structure are found and added to the DoE databases.

These databases fed data fitting regression models to create a wing structural mass predicting function for each DoE case. A MATLAB® script was developed to compute the regression models, obtain the resulting polynomial coefficients and perform post-processing calculations. A screening to the significant terms and a goodness-of-fit assessment were made by both analysis of the error parameters' values and data fitting accuracy plots. Both linear and nonlinear regression models were employed. Results proved a nonlinear relation between coefficients and so, a nonlinear method was selected. Multivariable 2^{nd} order polynomials were fitted by the nonlinear ERR-Causality regression method. Polynomial terms are arranged in a significance decreasing order and a number of significant terms equal to 12, 13 and 16 for $\overline{m}_{FW}$, $\overline{m}_{VSW}$ and $\overline{m}_{VSW}/\overline{m}_{FW}$ functions was respectively selected, for a convergence stopping criteria of 0.1% in SERR$_i$. η_{max}, ε_{max} and RMSE presented reasonable low errors and Adj. R^2 and SERR parameters presented close to unit values. Accordingly, from the analysis of error statistical parameters, a high goodness-of-fit was accomplished for the three polynomials with the selected number of terms. A sensitivity study evidenced that no fitted data points surpassed the 20% error line and only few surpassed the 10% error line, which proves that mass functions approximate the discrete data with acceptable accuracy.

b, c and W' were by this order, the most significant design parameters in the wing mass functions (first and second DoE cases). For example, in the $\overline{m}_{VSW}$ polynomial, only the first term b itself, represents 80.72% of the entire solution, reflecting the critical effect of b in the wing mass. $\bar{l}_{var}$ has in these DoE cases no representative influence on wing mass, when compared with other wing parameters. Mass penalties associated with the implementation of the telescopic

concept were only described by the third DoE case as it is the mass ratio between a VSW and a FW. In this case, significance orders were better distributed, with b describing 29.81% (instead of 80%) and c describing 29.03% (instead of 5%) of the results. $\bar{l}_{var}$ finally manifested a slightly higher significance relatively to other parameters, with a representation of 6.86% of the function significance in the fourth term.

More detailed conclusions on the effects of each design parameter on wing structural mass were taken from ensuing partial derivatives and 3D plots analysis. Partial derivative functions were evaluated for a case study using the baseline wing and mass variability is assessed for a 10% variation of each baseline wing parameter. Most relevant conclusion to obtain a low structural mass in a wing design point of view (both FW and VSW concepts) is to reach a wing sizing with over and above small b, and secondly large c, low W and $\bar{c}_{flap}$ values. When comparing VSW and FW concepts with the baseline size, low c and also, high b values, are the most effective design options to decrease structural mass penalties on telescopic wing designs over conventional concepts. Therefore the application of telescopic wing concepts is worthier when design requirements limit wing mean chord to a low value or even better, if wing AR is limited to a maximum low value. $\bar{l}_{var}$ variations have no significant effect on telescopic wing mass penalties hence in a design point of view this wing parameter should be maximized to increase wing morphing skills with a negligible cost on wing mass.

3D plots enabled a more general comprehension on the structural mass effects of design parameters and data fitting errors were illustrated by comparing contour and scatter plots. It was concluded that FW mass increases with increasing b, increasing W' and decreasing c. W' presents a more considerable effect on FW mass for higher AR wing designs, whereas for lower AR wings, FW mass is little or not affected at all by W'. In a FW design point of view, if c is large, the aircraft may be as heavier as desired (considering the DoE parameters range) without a significant wing mass penalty. This trend is more significant for lower b values. On the contrary, for higher b values, wing mass increases more linearly with increasing W' and decreasing c values. VSW structural mass increases almost linearly with increasing b values and increases with decreasing $\bar{l}_{var}$, although being not much influenced by it. VSW mass commonly increases with decreasing c values. Nevertheless, for high c and low b values the cross-section structure in the overlapping area has material in excess that is not transferring loads to the IFW, therefore VSW mass increases with increasing c. In a VSW design point of view, for small wingspans, c and $\bar{l}_{var}$ may be aerodynamically optimised without the risk of perceivable mass variations.

Differently to what was expected in this study, $\bar{l}_{var}$ has no preponderance in VSW structural mass. Furthermore, instead of representing a mass penalty, VSW mass normally decreases with increasing $\bar{l}_{var}$ values, although slightly. The exception is for small b and large c values, for which VSW mass increases with increasing $\bar{l}_{var}$, with even a sightliest impact. The reason why $\bar{l}_{var}$ is no significant for VSW mass was carefully explained along the discussion of results. Overall, VSW mass is negligibly affected by $\bar{l}_{var}$, which leads to the conclusion that in a VSW design point of view, the designer should size l_{var} till the maximum permitted by geometrical constrains. Consequently, higher $\bar{l}_{var}$ values enable higher morphing actuation capabilities without perceptible VSW mass costs, which stretches the flight envelope, enhances aircraft performance, energy efficiency and extends manoeuvrability. Although $\bar{l}_{var}$ parameter itself represents no significant mass penalty for VSW concepts, it does not mean that telescopic wing are lighter than FW, as the mass effect of the remaining parameters is increased. As a matter of fact, from

$\overline{m}_{VSW}/\overline{m}_{FW}$ function plots, it was concluded that for equal wing dimensions, VSW concepts were always heavier than FW concepts. The design point of the baseline wing corresponds to one of the design points that lead to lower mass penalties, as observed in mass ratio plots for mean b, small c and maximum $\bar{l}_{var}$ values. Although lower c values were not evaluated for structural feasibility reasons, this results showed that baseline wing dimensions were well selected to maximise VSW benefits when comparing the performance of Olharapo III fitted with it and fitted with the FW.

Mass ratio results showed that VSW concepts are worthier in a wing design point of view where a high b and low c values are design requirements and $\bar{l}_{var}$ is maximised. The wing configuration that carries less mass penalty is the one with the highest AR. For small c values, and if $\bar{l}_{var}$ is necessarily reduced due to design constrains, b should be decreased for a mean DoE level value to minimise mass penalties. With increasing c values, $\bar{l}_{var}$ presents a more preponderant effect on wing mass penalties and should be decreased to minimise mass penalties. By decreasing $\bar{l}_{var}$, morphing capabilities are being reduced, which is not ideal. In these lines, as mass penalties reduce flight performance, the designer should consider a VSW over a FW first and foremost, if design requirements or optimisation results point towards a small wing chord and secondly, if the wing AR is high or may be increased in following design iterations. If the design points towards a low AR wing, the option on applying a VSW concept carries increased mass penalties and its benefits over a FW should be decided with an overall assessment of aircraft performance, depending on the magnitude of mass increase and the level of desired operational multi-task flexibility.

$\overline{m}_{VSW,full}$, a new VSW full mass predicting function, resulted from adding the mass contributions of the developed $\overline{m}_{sys}$ and $\overline{m}_{flap}$ functions, to the VSW structural mass predicting function $\overline{m}_{VSW}$ and two correction factors. This function is meant to be a compact and feasible solution to access the mass properties of telescopic wings' upcoming designs. It may be seen as a stepping stone into solving the literature gap on mass models for early design phases of such wing morphing concepts. $\overline{m}_{VSW,full}$ resulted in a multivariable 4^{rd} order polynomial that uses same design variables has previous mass functions. To validate this preliminary function, a benchmarking case study should be employed in the follow-up of the current research.

In short, it is general belief that morphing is an interesting and justified research that deserves best attention. Goals of the current thesis were accomplished. A detailed guide on a morphing wing design was presented, effects of design parameters on wing structural mass were investigated and a VSW full wing mass predicting function was developed so that any student or engineer could easily and in a short period of time apply on future telescopic wing designs.

6.2 Prospects for Future Developments

Based on the acquired knowledge during the current work, it is believed that the follow-up of this research should cross the following investigation lines:

- As a suite of technologies, much work is still required on current and following versions of Olharapo RPAS for its potential be truly realised. These may be focused on maturing component and material technologies, actuators/mechanisms (coupled actuator-structure

design, i.e to use the actuation system as an integrating part of the load carrying structure) and control theory (both primary flight and actuation);

- Multi-task capability is one of the main drivers of the current design requirements. However, only loiter and fast cruise flight conditions were considered. The impact on considering further flight conditions in a span morphing design could be considered in future work;
- To extend the VSW design by characterising its aeroelastic behaviour, further mass properties as components positioning and wing CG as well as fatigue and stress effects due the repeated actuation of the morphing moving surfaces. Not only mass penalties in the VSW design should be considered, but also a complete life cycle assessment, including physical degradation of materials, maintenance requirements, manufacturing techniques, economic and environmental factors, should be held to prove their advantages over conventional fixed wings;
- As stated throughout this work, simplifications, assumptions and empirical approximations are extensively considered. Such considerations have associated errors which decrease results accuracy. Future designs and methodology improvements may focus on excelling models' accuracy;
- Further research on the applicability of a morphing flap in the VSW design should be performed. Although experimental results were obtained, further FEM and CFD studies should consider a dynamic load response when deflecting the flap. A structural analysis the secondary spar thickness increase to support flaps actuation should also be addressed.
- The bounded contact between the IFW and the OMW is an approximation considered in the FEM model that increases wing stiffness, which contributes for a lower $\overline{m}_w$ value and increases model errors. To implement a more suitable type of contact, through more CPU cost, is of paramount importance to quantify the impact of this simplification in the developed mass function;
- A larger range of DoE levels should be implemented, thus considering further wing dimensions and achieving mass functions with wider applications. In particular, further $\overline{c}_{flap}$ levels should have been applied so that more than its linear behaviour (achieved with two levels) could be investigated.
- The parametric study used a limited set of design parameters to generate wing mass functions. Further design parameters could be added to validate the assumption that the select parameters are the most significant as well as to broaden the analysis of their effects on wing mass.
- Besides the full quadratic approximation, different regression equation types, as conventional wing weight equations, radial basis functions or interpolating models, could have been implemented to assess the most suitable to fit our data.
- Future work should also focus in the effort to finalize the construction of Olharapo III RPAS and in the new VSW version. A mass breakdown should be documented to validate the $\overline{m}_{VSW,full}$ function, by comparing VSW mass estimative results to the actual wing mass.
- Whereas the $\overline{m}_{VSW,full}$ function is not applicable beyond the bounds of the parametric design variables, $\overline{m}_{VSW}/\overline{m}_{FW}$ function already is. To use the latter function to predict

VSW mass outside DoE levels limits, it needs to be coupled with an existing mass model. $\overline{m}_{VSW}/\overline{m}_{FW}$ should be multiplied by a mass ratio to account with secondary structural mass and non-structural mass of a VSW concept over a FW concept and then multiplied by a full conventional wing mass equation from an existing mass model.

- As wing morphing concepts are tremendously different from each other in terms of geometrical characteristics and design constrains, to develop a single general wing mass for all morphing concepts would be virtually impossible. Notwithstanding, by employing same developed methodology, further equations for different singular types of morphing concepts could be developed. In the end, a list of wing mass predicting functions could be gathered, with a particular function for each type of morphing wing and even for mixed concepts.

6.3 Author's note

While aviation market increasingly demands flight operations to be performed in a environmentally friendly manner, variable-span wing designs may not be a quick solution for increasing performance on manned aircraft applications. Telescopic wing concepts are being successfully designed and flight proven in RPAS, although still with a very low TRL. Nevertheless, the fact remains that morphing presents a promising and practicable solution for future multi-task missions involving RPAS, and with more research than that is already being held, it may be possible to overcome morphing inherent disadvantages and suit RPAS for a wider variety of applications. Once these disadvantages are overcome, the world takes one step closer in the run to mimic birds flight and achieve higher performance levels. The developed full VSW mass function will hopefully be a stepping stone into solving the literature gap on mass models for early design phases of telescopic wing concepts.

This entire project, thesis and published articles proved to be challenging and very satisfying to accomplish and all of these could never be performed without the assistance of both my supervisor, Pedro Gamboa, and my friend, Eng. Pedro Santos, to whom I never tire of thanking, being forever grateful for everything we have accomplished together.

Bibliography

[1] CHANGE FP7 project website. (Accessed on 04.04.2017). [Online]. Available: http://change.tekever.com/

[2] S. Joshi, Z. Tidwell, W. Crossley, and S. Ramakrishnan, "Comparison of morphing wing stategies based upon aircraft performance impacts," in *45th AIAA/ASME/ASCE/AHS/ASC Structures, Structural Dynamics, Materials Conference*. American Institute of Aeronautics and Astronautics, apr 2004.

[3] A. Rodriguez, "Morphing aircraft technology survey," in *45th AIAA Aerospace Sciences Meeting and Exhibit*. American Institute of Aeronautics and Astronautics, jan 2007.

[4] A. Tabor (Editor) and K. Cheung (Image credits). Go, go, green wing! mighty morphing materials in aircraft design. MADCAT, NASA's Ames Research Center, 2016. [Online]. Available: https://www.nasa.gov/ames/feature/go-go-green-wing-mighty-morphing-materials-in-aircraft-design

[5] T. A. Weisshaar, "Morphing aircraft technology - new shapes for aircraft design," NATO RTO-MP-AVT-154, Purdue University, Tech. Rep., 2006.

[6] T. A. Weisshaar, "New aircraft systems concepts - towards new horizons in aeroelasticity," NATO RTO-MP-AVT-154, Purdue University, Tech. Rep., 2006.

[7] ANSYS, Inc. *Mechanical* APDL *Element Reference, Version 15.0,* ANSYS® *Release*, 2013.

[8] M. Amador and V. Kulkarni, "Morphing wing design for uavs: A proposed concept," Master's thesis, BSc Thesis, Department of Mechanical and Industrial Engineering, University of Toronto, 2009.

[9] Z. Tidwell, S. Joshi, W. Crossley, and S. Ramakrishnan, "Comparison of morphing wing strategies based upon aircraft performance impacts," in *AIAA Paper 2004-1722, 45th AIAA/ASME/ASCE/AHS/ASC Structures, Structural Dynamics and Materials Conference, Palm Springs, California*, 19-22 apr 2004.

[10] J. Valasek, Ed., *Morphing Aerospace Vehicles and Structures*. Wiley-Blackwell, mar 2012.

[11] L. R. Jenkinson and P. S. Jenkinson, *Civil Jet Aircraft Design*. Elsevier Ltd, 1999.

[12] P. Gamboa, J. Vale, F. J. P. Lau, and A. Suleman, "Optimization of a morphing wing based on coupled aerodynamic and structural constraints," *AIAA Journal*, vol. 47, no. 9, pp. 2087–2104, sep 2009.

[13] J. Mestrinho, P. Gamboa, and P. Santos, "Design optimization of a variable-span morphing wing for a small UAV," in *52nd AIAA/ASME/ASCE/AHS/ASC Structures, Structural Dynamics and Materials Conference*. American Institute of Aeronautics and Astronautics (AIAA), apr 2011.

[14] J. Felício, P. Santos, P. Gamboa, and M. Silvestre, "Evaluation of a variable-span morphing wing for a small UAV," in *52nd AIAA/ASME/ASCE/AHS/ASC Structures, Structural Dynamics and Materials Conference*. American Institute of Aeronautics and Astronautics (AIAA), apr 2011.

[15] P. V. Gamboa and P. D. Santos, "Telescopic wing-box for a morphing wing," in *24th AIAA/AHS Adaptive Structures Conference*. American Institute of Aeronautics and Astronautics (AIAA), jan 2016.

[16] P. Santos, J. Sousa, and P. Gamboa, "Variable-span wing development for improved flight performance," *Journal of Intelligent Material Systems and Structures*, jul 2015.

[17] B. W. McCormick, *Aerodynamics, Aeronautics, and Flight Mechanics*. JOHN WILEY & SONS INC, 1995.

[18] E. Leylek and M. Costello, "Benefits of autonomous morphing aircraft in loiter and attack missions," in *AIAA Atmospheric Flight Mechanics Conference*. American Institute of Aeronautics and Astronautics (AIAA), aug 2010.

[19] A. R. McGowan, D. D. Vicroy, R. C. Busan, and A. S. Hahn, "Perspectives on highly adaptable of morphing aircraft," in *RTO Applied Vehicle Technology Panel (AVT) Symposium, RTO-MP-AVT-168 AC/323(AVT-168)TP/268, Evora, Portugal*, 2009.

[20] T. Seigler, "Dynamics and control of morphing aircraf," Ph.D. dissertation, Virginia Polytechnic Institute and State Universit, 2005.

[21] M. I. Friswell, "Morphing aircraft: An improbable dream?" in *Volume 1: Development and Characterization of Multifunctional Materials*. ASME Conference on Smart Materials, Adaptive Structures and Intelligent Systems, SMASIS2014, sep 2014.

[22] O. Lilienthal, *Birdflight As the Basis of Aviation: A Contribution Towards a System of Aviation*. Markowski International Publishers, 2000.

[23] P. Marks. The next 100 years of flight - part one & two. News service, 2003. http://www.NewScientist.com.

[24] J. May, "Les obsèquies de clément ader," *l'Aérophile*, vol. 33, pp. 130–131, may 1925.

[25] , "The annals of the polymorph: A short history of V-G," *Air International*, pp. 134–140, mar 1975.

[26] J. Flanagan, R. Strutzenberg, and R. M. abd J.E. Rodrian, "Development and flight testing of a morphing aircraft, the nextgen mfx-1," in *AIAA Paper 2007-1707, 48th AIAA/ASME/ASCE/AHS/ASC Structures, Structural Dynamics and Materials Conference, Honolulu, Hawaii*, 23-26 apr 2007.

[27] I. Boyd Perry, S. R. Cole, and G. D. Miller, "Summary of an active flexible wing program," *Journal of Aircraft*, vol. 32, no. 1, pp. 10–15, jan 1995.

[28] A. R. McGowan, D. E. Cox, B. S. Lazos, M. R. Waszak, D. L. Raney, E. J. Siochi, and S. P. Pao, "Biologically inspired technologies in NASA's morphing project," in *Smart Structures and Materials 2003: Electroactive Polymer Actuators and Devices (EAPAD)*, Y. Bar-Cohen, Ed. SPIE-Intl Soc Optical Eng, jul 2003.

[29] T. A. Weisshaar, "Morphing aircraft systems: Historical perspectives and future challenges," *Journal of Aircraft*, vol. 50, no. 2, pp. 337–353, mar 2013.

[30] J. Bowman, B. Sanders, B. Cannon, J. Kudva, S. Joshi, and T. Weisshaar, "Development of next generation morphing aircraft structures," in *48th AIAA/ASME/ASCE/ AHS/ASC Structures, Structural Dynamics & Materials Conference, 23-26 apr Honalulu, Hawai*, 2007.

[31] G. Ivanco, C. Scott, H. Love, Z. Scott, and T. Weisshaar, "Validation of the lockheed martin morphing concept with wind tunnel testing," in *48th AIAA/ASME/ASCE/ AHS/ASC Structures, Structural Dynamics, and Materials Conference, Honalulu, Hawai*, 23-26 apr 2007.

[32] T. Johnson, M. Frecker, M. Abdalla, Z. Gurdal, and D. Lindner, "Nonlinear analysis and optimization of diamond cell morphing wings," *Journal of Intelligent Material Systems and Structures*, vol. 20, no. 7, pp. 815–824, nov 2009.

[33] A. K. Jha and J. N. Kudva, "Morphing aircraft concepts, classifications, and challenges," in *Smart Structures and Materials 2004: Industrial and Commercial Applications of Smart Structures Technologies*, E. H. Anderson, Ed., NextGen Aeronautics, Inc. SPIE, jul 2004.

[34] S. Barbarino, O. Bilgen, R. M. Ajaj, M. I. Friswell, and D. J. Inman, "A review of morphing aircraft," *Journal of Intelligent Material Systems and Structures*, vol. 22, no. 9, pp. 823–877, jun 2011.

[35] D. Moorhouse, B. Sanders, M. von Spakovsky, and J. Butt, "Benefits and design challenges of adaptive structures for morphing aircraft," *The Aeronautical Journal*, vol. 110, no. 1105, pp. 157–162, mar 2006.

[36] E. Pendleton, P. Flick, D. Paul, D. Voracek, E. Reichenbach, and K. Griffin, "The X-53 - a summary of the active aeroelastic wing flight research program," in *48th AIAA/ASME/ASCE/AHS/ASC Structures, Structural Dynamics, and Materials Conference*. American Institute of Aeronautics and Astronautics, apr 2007.

[37] H. Rodrigue, W. Wang, B. Bhandari, M.-W. Han, and S.-H. Ahn, "Cross-shaped twisting structure using sma-based smart soft composite," *International Journal of Precision Engineering and Manufacturing-Green Technology*, vol. 1, no. 2, p. 153, Apr. 2014.

[38] M. Mistry, F. Gandhi, M. Nagelsmit, and Z. Gurdal, "Actuation requirements of a warp-induced variable twist rotor blade," *Journal of Intelligent Material Systems and Structures*, vol. 22, no. 9, pp. 919–933, may 2011.

[39] J. Manzo, "Analysis and design of a Hyper-Elliptical cambered span morphing aircraft wing," Master's thesis, Cornell University, Ithaca, NY, 2006.

[40] V. P. Galantai, A. Y. N. Sofla, S. A. Meguid, K. T. Tan, and W. K. Yeo, "Bio-inspired wing morphing for unmanned aerial vehicles using intelligent materials," *International Journal of Mechanics and Materials in Design*, vol. 8, no. 1, p. 71, Mar. 2012.

[41] J. Anderson, *Introduction to Flight*. McGraw-Hill Education, 2011.

[42] G. George and H. Roland, "Aircraft," US Patent Patent 2,670,910, Mar. 2, 1954.

[43] D. Perkins, J. Reed, and E. Havens, "Morphing wing structures for loitering air vehicles," in *45th AIAA/ASME/ASCE/AHS/ASC Structures, Structural Dynamics, Materials Conference*. American Institute of Aeronautics and Astronautics (AIAA), apr 2004.

[44] H. Parker, "The parker variable camber wing," *NACA Technical Report 77*, 1920.

[45] A. D. Gaspari and S. Ricci, "A two-level approach for the optimal design of morphing wings based on compliant structures," *Journal of Intelligent Material Systems and Structures*, vol. 22, no. 10, pp. 1091–1111, jul 2011.

[46] M. Marques, P. Gamboa, and E. Andrade, "Design and testing of a variable camber flap for improved efficiency," in *The Applied Vehicle Technology Panel Symposium (AVT-168), Évora, Portugal*, 20-23 apr 2009.

[47] J. K. Strelec, D. Lagoudas, M. Khan, and J. Yen, "Design and implementation of a shape memory alloy actuated reconfigurable airfoil," *Journal of Intelligent Materials Systems and Structures*, vol. 14, no. 4, pp. 257–273, apr 2003.

[48] J. Fincham and M. Friswell, "Aerodynamic optimisation of a camber morphing aerofoil," *Aerospace Science and Technology*, vol. 43, pp. 245–255, jun 2015.

[49] C. Bovais and P. Davidson, "Flight testing the flying radar target (FLYRT)," in *Biennial Flight Test Conference*. American Institute of Aeronautics and Astronautics, jun 1994.

[50] J. McMasters, "Advanced concepts in variable geometry sailplanes," *Soaring*, pp. 26–29, 1980.

[51] P. Lert, "The fs-29, a telescoping wing sailplane," *Soaring*, pp. 21–27, 1976.

[52] F. Thomas, *Fundamentals of Sailplane Design*. College Park Press, 1999.

[53] Gevers Aircraft Inc., "Multi-purpose aircraft," U.S. Patent 5,645,250, 1997.

[54] L. Arrison, k. Birocco, C. Gaylord, B. Herndon, K. Manion, and M. Metheny, "2002-2003 AE/ME morphing wing design," Virginia Tech Aerospace Engineering Senior Design Project, Spring Semester Final Report, 2003.

[55] D. Neal, M. Good, C. Johnston, H. Robertsha, W. Mason, and D. Inman, "Design and wind-tunnel analysis of a fully adaptative aircraft configuration," in *AIAA Paper 2004-1727, 45th AIAA/ASME/ASCE/AHS/ASC Structures, Structural Dynamics and Materials Conference, Palm Springs, California*, 19-22 apr 2004.

[56] D. Neal, J. Farmer, and D. Inman, "Development of a morphing aircraft model for wind tunnel experimentation," in *47th AIAA/ASME/ASCE/AHS/ASC Structures, Structural Dynamics, and Materials Conference& 14th AIAA/ASME/AHS Adaptive Structures Conference*. American Institute of Aeronautics and Astronautics, may 2006.

[57] J. Blondeau, J. Richeson, and D. Pines, "Design of a morphing aspect ratio wing using an inflatable telescoping spar," in *44th AIAA/ASME/ASCE/AHS/ASC Structures, Structural Dynamics, and Materials Conference*. American Institute of Aeronautics and Astronautics, apr 2003.

[58] J. Blondeau and D. Pines, "Pneumatic morphing aspect ratio wing," in *45th AIAA/ASME/ASCE/AHS/ASC Structures, Structural Dynamics & Materials Conference*. American Institute of Aeronautics and Astronautics, apr 2004.

[59] J. Blondeau and D. J. Pines, "Design and testing of a pneumatic telescopic wing for unmanned aerial vehicles," *Journal of Aircraft*, vol. 44, no. 4, pp. 1088–1099, jul 2007.

[60] J.-S. Bae, T. M. Seigler, D. J. Inman, and I. Lee, "Aerodynamic and aeroelastic considerations of a variable-span morphing wing," *AIAA Paper*, vol. 1726, p. 2004, 2004.

[61] Y. Heryawan, H. C. Park, N. S. Goo, K. J. Yoon, and Y. H. Byun, "Design and demonstration of a small expandable morphing wing," in *Smart Structures and Materials 2005: Smart Structures and Integrated Systems*, A. B. Flatau, Ed. SPIE, may 2005.

[62] A. H. Supekar, "Design, analysis and development of a morphable wing structure for unmanned aerial vehicle performance augmentation," Master's thesis, University of Texas at Arlington, 2007.

[63] C. Han, S. Lee, and K. Ruy, "Experimental study of a telescopic morphing aspect ratio wing inside a channel," *Journal of Aircraft*, vol. 44, no. 3, pp. 1029–1030, may 2007.

[64] J. Vale, F. Lau, A. Suleman, and P. Gamboa, "Multidisciplinary design optimization of a morphing wing for an experimental UAV," in *11th AIAA/ISSMO Multidisciplinary Analysis and Optimization Conference*. American Institute of Aeronautics and Astronautics (AIAA), sep 2006.

[65] J. Vale, "Designing, building and wind tunnel testing of a morphing wing for drag reduction," Master's thesis, IST, Lisbon Technical University, Portugal, 2007.

[66] P. Gamboa, P. Aleixo, J. Vale, F. Lau, and A. Suleman, "Design and testing of a morphing wing for an experimental uav," in *Proceedings of Platform Innovations and System Integration for Unmanned Air, Land and Sea Vehicles (AVT-SCI Joint Symposium), 14-18 May, Florence , Italy, RTO-MP-AVT-146*, no. Paper 17, 2007.

[67] M. Secanell, A. Suleman, and P. Gamboa, "Design of a morphing airfoil using aerodynamic shape optimization," *AIAA Journal*, vol. 44, no. 7, pp. 1550–1562, jul 2006.

[68] J. Vale, A. Leite, F. Lau, and A. Suleman, "Aero-structural optimization and performance evaluation of a morphing wing with variable span and camber," *Journal of Intelligent Material Systems and Structures*, vol. 22, no. 10, pp. 1057–1073, jul 2011.

[69] J. Vale, F. Lau, and A. Suleman, "Energy efficiency studies of a morphing unmanned aircraft," *Journal of Aeronautics & Aerospace Engineering*, vol. 02, no. 05, 2013.

[70] D. A. Vicente, P. V. Gamboa, and M. A. R. Silvestre, "Parameterization formulations for aerofoil shape optimization," *Engineering Optimization*, pp. 279–284, 2014.

[71] P. Albuquerque, P. Gamboa, and M. Silvestre, "Parametric aircraft design optimisation study using span and mean chord as main design drivers," *Advanced Materials Research 1016*, 2014.

[72] P. F. Albuquerque, P. V. Gamboa, and M. S. Silvestre, "Multidisciplinary and multilevel aircraft design methodology using enhanced collaborative optimization," in *16th AIAA/ISSMO Multidisciplinary Analysis and Optimization Conference*. American Institute of Aeronautics and Astronautics (AIAA), jun 2015.

[73] A. Leite, J. Vale, F. Lau, and A. Suleman, "Development of morphing strategies for a flight demonstrator remotely piloted vehicle," in *50th AIAA/ASME/ASCE/AHS/ASC Structures, Structural Dynamics, and Materials Conference*. American Institute of Aeronautics and Astronautics (AIAA), may 2009.

[74] R. M. Ajaj, M. I. Friswell, and E. I. Saavedra-Flores, "Span morphing: a conceptual design study," in *20th AIAA/ASME/AHS adaptive structures conference, Honolulu, HI, paper no. 2012-1510*, 23–26 apr 2012.

[75] R. M. Ajaj, M. I. Friswell, W. G. Dettmer, G. Allegri, and A. T. Isikveren, "Dynamic modelling and actuation of the adaptive torsion wing," *Journal of Intelligent Material Systems and Structures*, vol. 24, no. 16, pp. 2045–2057, jul 2012a.

[76] R. M. Ajaj, M. I. Friswell, E. I. S. Flores, A. Keane, A. T. Isikveren, G. Allegri, and S. Adhikari, "An integrated conceptual design study using span morphing technology," *Journal of Intelligent Material Systems and Structures*, vol. 25, no. 8, pp. 989–1008, sep 2013.

[77] M. Love, P. Zink, R. Stroud, D. Bye, S. Rizk, and D. White, "Demonstration of morphing technology through ground and wind tunnel tests," in *48th AIAA/ASME/ ASCE/AHS/ASC Structures, Structural Dynamics & Materials Conference, Honalulu, Hawai*, 23-26 apr 2007.

[78] D. Bye and P. McClure, "Design of a morphing vehicle," in *48th AIAA Structures, Structural Dynamics, and Materials Conference, Honolulu, HI, Paper No. AIAA 2007-1728*, 23-26 apr 2007.

[79] N. M. Wereley and F. Gandhi, "Flexible skins for morphing aircraft," *Journal of Intelligent Material Systems and Structures*, vol. 21, no. 17, pp. 1697–1698, nov 2010.

[80] E. A. Bubert, B. K. S. Woods, K. Lee, C. S. Kothera, and N. M. Wereley, "Design and fabrication of a passive 1d morphing aircraft skin," *Journal of Intelligent Material Systems and Structures*, vol. 21, no. 17, pp. 1699–1717, sep 2010.

[81] R. D. Vocke, C. S. Kothera, B. K. S. Woods, and N. M. Wereley, "Development and testing of a span-extending morphing wing," *Journal of Intelligent Material Systems and Structures*, vol. 22, no. 9, pp. 879–890, jun 2011.

[82] M. T. Kikuta, "Mechanical properties of candidate materials for morphing wing," Master's thesis, Department of Mechanical Engineering, Virginia Polytechnic Institute and State University, 2003.

[83] C. Thill, J. Etches, I. Bond, K. Potter, and P. Weaver, "Morphing skins," *The Aeronautical Journal*, vol. 112, no. 1129, pp. 117–139, mar 2008.

[84] A. Tarabi, S. Ghasemloo, and M. Mani, "Experimental investigation of a variable-span morphing wing model for an unmanned aerial vehicle," *Journal of the Brazilian Society of Mechanical Sciences and Engineering*, vol. 38, no. 7, p. 1833, Oct. 2016.

[85] A. Elham and M. J. L. van tooren, "Effect of wing-box structure on the optimum wing outer shape," *The Aeronautical Journal*, vol. 118, no. 1199, pp. 1–30, jan 2014.

[86] Z. You and J. Crabtree, "Mechanisms for large shape change in morphing aircraft," in *RTO-NATO Morphing Vehicles Symposium, Évora, Portugal.*, 20-24 apr 2009.

[87] S. Kota, R. Osborn, G. Ervin, D. Maric, P. Flick, and D. Paul, "Mission adaptive compliant wing - design, fabrication and flight test," in *RTO Applied Vehicle Technology Panel (AVT) Symposium*, 2009.

[88] P. Skalski, "Morphing structure with a magnetorheological material – preliminary approach," in *Mechatronics 2013*. Springer, Jan. 2014.

[89] L. Grigorie, R. M. Botez, and A. V. Popov, "Self-adaptive morphing wing model, smart actuated and controlled by using a multiloop controller based on a laminar flow real time optimizer," in *24th AIAA/AHS Adaptive Structures Conference*. American Institute of Aeronautics and Astronautics (AIAA), jan 2016.

[90] L. da Rocha-Schmidt andLeri S. Datashvili and H. Baier, "A multistep morphing structures design approach applied to different types of applications in aerospace," in *24th AIAA/AHS Adaptive Structures Conference*. American Institute of Aeronautics and Astronautics (AIAA), jan 2016.

[91] W. Su, S. S.-M. Swei, and G. G. Zhu, "Optimum wing shape of highly flexible morphing aircraft for improved flight performance," *Journal of Aircraft*, vol. 53, no. 5, pp. 1305–1316, 2017/01/13 2016.

[92] G. Molinari, A. F. Arrieta, M. Guillaume, and P. Ermanni, "Aerostructural performance of distributed compliance morphing wings: Wind tunnel and flight testing," *AIAA Journal*, vol. 54, no. 12, pp. 3859–3871, dec 2016.

[93] M. T. Debiasi, W. L. Chan, and S. Jadhav, "Measurements of a symmetric wing morphed by macro fiber composite actuators," in *54th AIAA Aerospace Sciences Meeting*. American Institute of Aeronautics and Astronautics (AIAA), jan 2016.

[94] A. Falken, S. Steeger, O. Heintze, and R. D. Breuker, "From development of multi-material skins to morphing flight hardware production," in *24th AIAA/AHS Adaptive Structures Conference*. American Institute of Aeronautics and Astronautics (AIAA), jan 2016.

[95] R. J. H. Wanhill and B. Ashok, "Shape memory alloys (smas) for aerospace applications," in *Aerospace Materials and Material Technologies*. Springer, Jan. 2017.

[96] A. C. Henry, G. Molinari, and A. F. Arrieta, "Smart morphing wing: Optimization of distributed piezoelectric actuation," in *25th AIAA/AHS Adaptive Structures Conference*. American Institute of Aeronautics and Astronautics (AIAA), jan 2017.

[97] Q. Ai and P. Weaver, "A novel span-wise morphing trailing edge concept," in *25th AIAA/AHS Adaptive Structures Conference*. American Institute of Aeronautics and Astronautics (AIAA), jan 2017.

[98] J. M. Martinez, D. Scopelliti, C. Bil, R. Carrese, and P. Marzocca, "Design, analysis and experimental testing of a morphing wing," in *25th AIAA/AHS Adaptive Structures Conference*. American Institute of Aeronautics and Astronautics (AIAA), jan 2017.

[99] M. Ardema, M. C. Chambers, A. P. Patron, A. S. Hahn, H. Miura, and M. D. Moore, "Analytical fuselage and wing weight estimation of transport aircraft," NASA Technical Memorandum 110392, Tech. Rep., 1996.

[100] P. York and R. Labell, "Aircraft wing weight build-up methodology with modification for materials and construction techniques," NASA, Ames Research Center, Tech. Rep. Contract No. NAS2-9805, 1980.

[101] E. Torenbeek, "Development and application of a comprehensive, design-sensitive weight prediction method for wing structures of transport category aircraft," Delft University of Technology, Tech. Rep., 1992.

[102] J. Roskam, *Airplane Design Part V - Component Weight Estimation*. Design, Analysis and Research Corporation (DARcorporation), 1985.

[103] E. Torenbeek, *Advanced Aircraft Design*. John Wiley & Sons, 2013.

[104] D. P. Raymer, *Aircraft Design: A Conceptual Approach*. AIAA, 2013.

[105] E. Torenbeek, *Synthesis of Subsonic Airplane Design*. Delft University Press, 1982.

[106] D. Howe, *Aircraft Conceptual Design Synthesis*. JOHN WILEY & SONS INC, 2005.

[107] A. Elham, G. L. Rocca, and M. van Tooren, "Development and implementation of an advanced, design-sensitive method for wing weight estimation," *Aerospace Science and Technology*, vol. 29, no. 1, pp. 100 – 113, 2013.

[108] M. Burt, "Weight prediction for wings of box construction, report 186," *RAE*, 1955.

[109] S. Macci, *Semi-analytical method for predicting wing structural mass*. Society of Allied Weight Engineers Incorporated, 1995.

[110] R. Kelm, M. Läpple, and M. Grabietz, "Wing primary structure weight estimation of transport aircrafts in the pre-development phase," in *54th Annual Conference of Society of Allied Weight Engineers, Inc., SAWE Paper*, no. 2283, 1995.

[111] R. M. Ajaj, M. I. Friswell, D. Smith, and A. T. Isikveren, "A conceptual wing-box weight estimation model for transport aircraft," *The Aeronautical Journal*, vol. 117, no. 1191, pp. 533–551, may 2013.

[112] J. Petermeier, G. Radtke, M. Stohr, A. Woodland, T. Takahashi, S. Donovan, and M. Shubert, "Enhanced conceptual wing weight estimation through structural optimization and simulation," in *13th AIAA/ISSMO Multidisciplinary Analysis Optimization Conference*. American Institute of Aeronautics and Astronautics (AIAA), sep 2010.

[113] A. Elham, G. L. Rocca, and R. Vos, "Refined preliminary weight estimation tool for airplane wing and tail," in *SAE Technical Paper Series*. SAE International, oct 2011.

[114] A. Elham and M. J. van Tooren, "Tool for preliminary structural sizing, weight estimation, and aeroelastic optimization of lifting surfaces," *Proceedings of the Institution of Mechanical Engineers, Part G: Journal of Aerospace Engineering*, vol. 230, no. 2, pp. 280–295, jun 2015.

[115] M. Droegkamp, "Finite element model weight estimation," *SAWE Paper*, no. 2089, 1992.

[116] M. Sensmeier, B. Stewart, and J. Samareh, "Rapid generation and assessment of aircraft structural topologies for multidisciplinary optimization and weight estimation," in *Collection of Technical Papers*. AIAA/ASME/ASCE/AHS/ASC structures, structural dynamics and materials conference, vol. 7, pp.4722–4733, 2006.

[117] G. Bindolino, G. Ghiringhelli, S. Ricci, and M. Terraneo, "Multilevel structural optimization for preliminary wing-box weight estimation," *Journal of Aircraft*, vol. 47, no. 2, pp. 475–489, mar 2010.

[118] G. K. W. Kenway and J. R. R. A. Martins, "Multipoint high-fidelity aerostructural optimization of a transport aircraft configuration," *Journal of Aircraft*, vol. 51, no. 1, pp. 144–160, jan 2014.

[119] R. P. Liem, C. A. Mader, E. Lee, and J. Martins, "Aerostructural design optimization of a 100-passenger regional jet with surrogate-based mission analysis," in *2013 Aviation Technology, Integration, and Operations Conference*. American Institute of Aeronautics and Astronautics (AIAA), aug 2013.

[120] T. Winter, J. Marquez, and B. Scheneman, "Development of a physics-based weight (PB-Weight) prediction tool for conceptual design," in *AIAA Modeling and Simulation Technologies Conference*. American Institute of Aeronautics and Astronautics (AIAA), jun 2016.

[121] F. Hürlimann, R. Kelm, M. Dugas, K. Oltmann, and G. Kress, "Mass estimation of transport aircraft wingbox structures with a CAD/CAE-based multidisciplinary process," *Aerospace Science and Technology*, vol. 15, no. 4, pp. 323–333, jun 2011.

[122] H. Miura and A. Shyu, "Weight estimation of unconventional structures by structural optimization," in *SAWE, Annual Conference, 45th, Williamsburg, VA*, N. A. R. Center, Ed., 12-14 may 1986.

[123] P. Hajela and J. L. Chen, "Preliminary weight estimation of conventional and joined wings using equivalent beam models," *Journal of Aircraft*, vol. 25, no. 6, pp. 574–576, jun 1988.

[124] M. Kaufman, V. Balabanov, A. A. Giunta, B. Grossman, W. H. Mason, S. L. Burgee, R. T. Haftka, and L. T. Watson, "Variable-complexity response surface approximations for wing structural weight in HSCT design," *Computational Mechanics*, vol. 18, no. 2, pp. 112–126, mar 1996.

[125] S. A. Andrews, R. E. Perez, and D. Wowk, "Wing weight model for conceptual design of nonplanar configurations," *Aerospace Science and Technology*, vol. 43, pp. 51–62, jun 2015.

[126] G. Ghiringhelli, A. Frediani, and M. Terraneo, "Weight prediction of the lifting system for an unconventional aircraft configuration," *Aerotecnica Missili & Spazio*, vol. 94, no. 1, May 2016.

[127] J. Gundlach, *Designing Unmanned Aircraft Systems: A Comprehensive Approach*. AIAA, 2014.

[128] L. F. Campanile, "Initial thoughts on weight penalty effects in shape-adaptable systems," *Journal of Intelligent Material Systems and Structures*, vol. 16, no. 1, pp. 47–56, jan 2005.

[129] M. Skillen and W. Crossley, "Developing response surface based wing weight equations for conceptual morphing aircraft sizing," in *46th AIAA/ASME/ASCE/AHS/ASC Structures, Structural Dynamics and Materials Conference*. American Institute of Aeronautics and Astronautics (AIAA), apr 2005.

[130] R. Cunha, "Structural analysis of a variable-span wing-box," Master's thesis, University of Beira Interior, 2014.

[131] V. Balabanov, M. Kaufman, A. Giunta, B. Grossman, W. Mason, L. Watson, and R. Haftka, "Developing customized weight function by structural optimization on parallel computers," in *37th Structure, Structural Dynamics and Materials Conference*. American Institute of Aeronautics and Astronautics, apr 1996.

[132] C. W. E. J. N. Kettaneh-Wold, *Design of Experiments, Principles and Applications*. Umetrics Academy, 2000.

[133] M. Ledvij, "Curve fitting made easy." *Industrial Physicist*, vol. 9, no. 2, pp. 24–27, 2003.

[134] O. Bretscher, *Linear Algebra with Applications*. Addison Wesley Pub Co Inc, 2012.

[135] H. Rocha, "Model parameter tuning by cross validation and global optimization: application to the wing weight fitting problem," *Structural and Multidisciplinary Optimization*, vol. 37, no. 2, pp. 197–202, apr 2008.

[136] R. H. Myers, D. C. Montgomery, and C. M. Anderson-Cook, *Response Surface Methodology*. John Wiley & Sons Inc, 2016.

[137] S. M. Stigler, "Gauss and the invention of least squares," *The Annals of Statistics*, vol. 9, no. 3, pp. 465–474, may 1981.

[138] S. Weisberg, *Applied Linear Regression*. Wiley, 2005.

[139] G. A. F. Seber and C. J. Wild, *Nonlinear Regression*. John Wiley & Sons Inc, 2003.

[140] B. Parlett, "The QR algorithm," *Computing in Science & Engineering*, vol. 2, no. 1, pp. 38–42, 2000.

[141] A. Ben-Israel and T. N. E. Greville, *Generalized Inverses - Theory and Applications*, C. M. Society, Ed. Springer, 2003.

[142] E. H. Moore, "On the reciprocal of the general algebraic matrix," *Bulletin of the American Mathematical Society, Vol. 26*, pp. 394–395, 1920.

[143] M. A. Rakha, "On the moore-penrose generalized inverse matrix," *Applied Mathematics and Computation*, vol. 158, no. 1, pp. 185–200, oct 2004.

[144] W. H. Press, B. P. Flannery, S. A. Teukolsky, and W. T. Vetterling, *Numerical Recipes in C: The Art of Scientific Computing, Second Edition*. Cambridge University Press, 1992.

[145] C. W. J. Granger, "Investigating causal relations by econometric models and cross-spectral methods," *Econometrica*, vol. 37, no. 3, p. 424, aug 1969.

[146] C. Granger, "Testing for causality," *Journal of Economic Dynamics and Control*, vol. 2, pp. 329–352, jan 1980.

[147] C. W. Granger, "Some recent development in a concept of causality," *Journal of Econometrics*, vol. 39, no. 1-2, pp. 199–211, sep 1988.

[148] C. Berzuini, P. Dawid, and L. Bernardinelli, "An overview of statistical causality," in *Causality, Front Matter*. Wiley-Blackwell, jun 2012, pp. i–xxv.

[149] M. Eichler, "Causal inference in time series analysis," in *Causality*. Wiley-Blackwell, jun 2012, pp. 327–354.

[150] Y. Zhao, S. A. Billings, H. Wei, and P. G. Sarrigiannis, "Tracking time-varying causality and directionality of information flow using an error reduction ratio test with applications to electroencephalography data," *Physical Review E*, vol. 86, no. 5, nov 2012.

[151] Y. Zhao, S. A. Billings, H.-L. Wei, and P. G. Sarrigiannis, "A parametric method to measure time-varying linear and nonlinear causality with applications to EEG data," *IEEE Transactions on Biomedical Engineering*, vol. 60, no. 11, pp. 3141–3148, nov 2013.

[152] EASA, "CS-VLA / amendment 1, certification specifications for very light aeroplanes," March 2009, (Accessed on 22.02.2017). [Online]. Available: https://www.easa.europa.eu/document-library/certification-specifications/cs-vla-amendment-1

[153] T. H. G. Megson, *Aircraft Structures for Engineering Students*, E. A. Engineering, Ed. Butterworth Heinemann, 2012.

[154] H. Monner and S. Opitz, "DLR's morphing activities within the european network," in *RTO-NATO Morphing Vehicles Symposium, Évora, Portugal*, 20-24 apr 2009.

[155] H. P. Monner, H. Hanselka, and E. J. Breitbach, "Development and design of flexible fowler flaps for an adaptive wing," in *5th Annual International Symposium on Smart Structures and Materials*. International Society for Optics and Photonics, 1998, pp. 60–70.

[156] Q. Ai, P. Weaver, and M. Azarpeyvand, "Design optimization of a morphing flap device using variable stiffness materials," in *24th AIAA/AHS Adaptive Structures Conference*. American Institute of Aeronautics and Astronautics (AIAA), jan 2016.

[157] Bms-210dmh metal gear coreless digital nano servo - specifications. (Accessed on 22.06.2017). [Online]. Available: http://www.blue-bird-model.com/en/servos/bms-210dmh.html

[158] D-mg16 metal gear digital servo. (Accessed on 22.06.2017). [Online]. Available: http://hobbyking.com/pt_pt/d-mg16-digital-metal-gear-2-9kg-0-08sec-18-8g.html

[159] M. Drela, "XFoil 6.94 user guide," *Massachusetts Institute of Technology & Astro Harold Youngren Aerocraft, Inc., USA*, vol. 10, 10 dec 2001.

[160] M. Selig, "Low reynolds number airfoil design lecture notes," VKI Lect. Ser, 24-28, Tech. Rep., 2003.

[161] J. Morgado, R. Vizinho, M. Silvestre, and J. Páscoa, "XFoil vs CFD performance predictions for high lift low reynolds number airfoils," *Aerospace Science and Technology, 52, 207-214*, 2016.

[162] Equivalent dihedral angle calculator. (Accessed on 20.06.2017). [Online]. Available: http://www.charlesriverrc.org/articles/design/eda1.xls

[163] A. Deperrois, "About XFLR5 calculations and experimental measurements," 2009.

[164] A. Deperrois, "XFLR5 Guidelines - Analysis of foils and wings operating at low reynolds numbers," February 2013, (Accessed on 08.02.2017). [Online]. Available: http://www.xflr5.com/

[165] B. Maskew, "Program VSAERO theory document: A computer program for calculating nonlinear aerodynamic characteristics of arbitrary configurations," NASA-CR-4023, NAS 1.26:4023, AMI-8416, Tech. Rep., Sep 01, 1987.

[166] C. Soutis, "Fibre reinforced composites in aircraft construction," *Progress in Aerospace Sciences*, vol. 41, no. 2, pp. 143 – 151, 2005.

[167] M. Kutz, *Handbook of materials selection*. John Wiley & Sons, 2002.

[168] Detailed product information on the dpp standard profiles with technical specifications. vDijk Pultrusion Products (DPP BV). (Accessed on 11.03.2017). [Online]. Available: http://www.dpp-pultrusion.com/en/the-product-micro-pultrusion-products/standard-pultrusion-sections-in-carbon-epoxy/rectangular-rods/

[169] 47:1 metal gearmotor 25dx52l mm hp 12v with 48 cpr encoder, specifications. Pololu®. (Accessed on 14.03.2017). [Online]. Available: https://www.pololu.com/product/3217/specs

[170] Pololu jrk 12v12 usb motor controller with feedback, specifications. Pololu®. (Accessed on 14.03.2017). [Online]. Available: https://www.pololu.com/product/1393/specs

[171] M. C. Niu, "Airframe stress analysis and sizing," *3rd ed. AD Adaso/Adastra Engineering LLC*, 1997.

[172] ANSYS, Inc. *Mechanical* APDL *Theory Reference, Version 15.0,* ANSYS® *Release*, 2013.

[173] P. Gamboa, "Apontamentos de projecto de aeronaves, capítulo 12 - estruturas e cargas," 2017.

[174] F. Dorbath, B. Nagel, and V. Gollnick, "Comparison of beam and shell theory for mass estimation in preliminary wing design," in *RAeS 2nd aircraft structural design conference, London, UK*, 26–28 October, 2010.

[175] E. Reissner, "The effect of transverse shear deformation on the bending of elastic plates," *Journal of Applied Mechanics (American Society of Mechanical Engineers: ASME)*, 1945.

[176] R. Mindlin, "Influence of rotary inertia and shear on flexural motions of isotropic elastic plates," *Journal of Applied Mechanics (American Society of Mechanical Engineers: ASME)*, 1951.

[177] S. W. Tsai, "Strength characteristics of composite materials," NASA, CR-224, 1965.

[178] S. Tsai and H. Hahn, *Introduction to Composite Materials*. Technomic Pub. Co., 1980, vol. 302, no. 6.

[179] ANSYS, Inc. *Mechanical* APDL *Modeling and Meshing Guide, Version 13.0,* ANSYS® *Release*, 2010.

[180] ANSYS, Inc. *Mechanical* APDL *ANSYS Mechanical APDL Command Reference, Version 15.0,* ANSYS® *Release*, 2013.

[181] J. D. Anderson Jr, *Fundamentals of aerodynamics*. Tata McGraw-Hill Education, 2010.

[182] J. R. Taylor, *Introduction to Error Analysis: The Study of Uncertainties in Physical Measurements*. Univ Science Books, University of Colorado, 1997.

[183] P. Bevington and D. K. Robinson, *Data Reduction and Error Analysis for the Physical Sciences*. Mcgraw Hill Book Co, 2002.

[184] R. Nuzzo, "Scientific method: Statistical errors," *Nature*, vol. 506, no. 7487, pp. 150–152, feb 2014.

Appendices

Appendix A

VSW Specifications and Olharapo III Performance Indicators

Table A.1: VSW-related results of the multidisciplinary and multilevel design optimisation.

Parameter	Value	Unit
$\bar{c}$	0.257	m
c_{IFW}	0.268	m
c_{OMW}	0.233	m
c_{tip}	0.180	m
b_{ave}	3.100	m
b_{max}	3.553	m
AR_{max}	13.83	-
l_{over1}	0.125	m
l_{over2}	0.025	m
l_{fus}	0.120	m
$l_{var_{ave}}$	0.225	m
$l_{var_{max}}$	0.45	m
k_{tip}	0.1	-
l_{tip}	0.155	m
$l_{flapmax}$	0.575	m
l_{IFW}	1.170	m
l_{OMW}	1.205	m
l_{ext}, $b_{max}/2$	1.775	m
l_{ave}	1.550	m
l_{retr}	1.325	m
Γ	4.651	deg
θ	2.396	deg
Λ	19.1	deg
$MTOW$	150	N
m/S	16,745	kg/m^2
Performance Variable	**Value**	**Unit**
RoC	3.3	m/s
V_{stall}	13.646	m/s
V_l	18.000	m/s
V_c	30.000	m/s
V_D	51.123	m/s
V_{TO}	15.491	m/s
d_{TO}	56.968	m

Mission phase	Energy required [J]	Thrust setting	Time [s]
Take-off	9019.6 (0.5%)	1.000	6.1
Climb$_1$	105058.6 (5.6%)	0.905	90.9
Loiter	965834.9 (51.2%)	0.508	3600.0
Descend$_1$	2248.4 (0.1%)	0.000	112.4
Climb$_2$	175008.5 (9.3%)	0.910	151.5
Fast cruise	623726.3 (33.0%)	0.825	833.3
Descend$_2$	6673.8 (0.35%)	0.000	333.7
Total	1887570.1 (100%)	-	5128.0

Appendix B

VSW Aerofoils Data

Table B.1: IFW aerofoil coordinates (201 points).

UBI-03-012 Original							
x	y	x	y	x	y	x	y
1	0.0018	0.5	0.08126	0	0	0.5	-0.00774
0.999753	0.001887	0.484295	0.08187	0.000247	-0.00217	0.515705	-0.00676
0.999013	0.002149	0.468605	0.082365	0.000987	-0.0038	0.531395	-0.00579
0.997781	0.002585	0.452946	0.082748	0.002219	-0.00521	0.547054	-0.00483
0.996057	0.003193	0.437333	0.083019	0.003943	-0.00652	0.562667	-0.00388
0.993844	0.003967	0.421783	0.083179	0.006156	-0.00781	0.578217	-0.00295
0.991144	0.0049	0.406309	0.08323	0.008856	-0.0091	0.593691	-0.00205
0.987958	0.00598	0.390928	0.083172	0.012042	-0.0104	0.609072	-0.00116
0.984292	0.007189	0.375655	0.083007	0.015708	-0.01169	0.624345	-0.00031
0.980147	0.008513	0.360504	0.082734	0.019853	-0.01295	0.639496	0.000522
0.975528	0.009935	0.345492	0.082356	0.024472	-0.01417	0.654508	0.001319
0.97044	0.011445	0.330631	0.081872	0.02956	-0.01533	0.669369	0.002085
0.964888	0.013034	0.315938	0.081284	0.035112	-0.01643	0.684062	0.002816
0.958877	0.014697	0.301426	0.080591	0.041123	-0.01746	0.698574	0.003513
0.952414	0.016429	0.28711	0.079793	0.047586	-0.01841	0.71289	0.004173
0.945503	0.018228	0.273005	0.078891	0.054497	-0.01928	0.726995	0.004794
0.938153	0.020092	0.259123	0.077885	0.061847	-0.02007	0.740877	0.005375
0.930371	0.022015	0.245479	0.076777	0.069629	-0.02076	0.754521	0.005915
0.922164	0.02399	0.232087	0.07557	0.077836	-0.02137	0.767913	0.006411
0.91354	0.02601	0.218958	0.074269	0.08646	-0.0219	0.781042	0.006862
0.904508	0.028067	0.206107	0.072878	0.095492	-0.02236	0.793893	0.007266
0.895078	0.030156	0.193546	0.071402	0.104922	-0.02274	0.806454	0.00762
0.885257	0.032271	0.181288	0.069845	0.114743	-0.02305	0.818712	0.007922
0.875056	0.034405	0.169344	0.06821	0.124944	-0.02329	0.830656	0.008169
0.864484	0.036555	0.157726	0.066503	0.135516	-0.02345	0.842274	0.008359
0.853553	0.038714	0.146447	0.064725	0.146447	-0.02355	0.853553	0.008488
0.842274	0.040877	0.135516	0.062882	0.157726	-0.02358	0.864484	0.008551
0.830656	0.043041	0.124944	0.060975	0.169344	-0.02353	0.875056	0.008543
0.818712	0.045199	0.114743	0.059006	0.181288	-0.02342	0.885257	0.008458
0.806454	0.04735	0.104922	0.056978	0.193546	-0.02324	0.895078	0.00829
0.793893	0.049488	0.095492	0.05489	0.206107	-0.02298	0.904508	0.008039
0.781042	0.051609	0.08646	0.052742	0.218958	-0.02265	0.91354	0.007706
0.767913	0.053709	0.077836	0.05053	0.232087	-0.02226	0.922164	0.007294
0.754521	0.055781	0.069629	0.048248	0.245479	-0.0218	0.930371	0.006806
0.740877	0.057822	0.061847	0.045887	0.259123	-0.02128	0.938153	0.00625
0.726995	0.059824	0.054497	0.043446	0.273005	-0.02071	0.945503	0.005634
0.71289	0.061783	0.047586	0.040923	0.28711	-0.02008	0.952414	0.004967
0.698574	0.063692	0.041123	0.038318	0.301426	-0.0194	0.958877	0.004265
0.684062	0.065546	0.035112	0.035629	0.315938	-0.01868	0.964888	0.003542
0.669369	0.067339	0.02956	0.032857	0.330631	-0.01791	0.97044	0.002814
0.654508	0.069064	0.024472	0.030001	0.345492	-0.01711	0.975528	0.0021
0.639496	0.070715	0.019853	0.027061	0.360504	-0.01627	0.980147	0.001415
0.624345	0.072287	0.015708	0.024042	0.375655	-0.0154	0.984292	0.000774
0.609072	0.073773	0.012042	0.02096	0.390928	-0.0145	0.987958	0.00019
0.593691	0.075166	0.008856	0.017854	0.406309	-0.01358	0.991144	-0.00033
0.578217	0.076461	0.006156	0.014827	0.421783	-0.01263	0.993844	-0.00077
0.562667	0.077651	0.003943	0.01198	0.437333	-0.01167	0.996057	-0.00114
0.547054	0.07873	0.002219	0.0093	0.452946	-0.01069	0.997781	-0.00143
0.531395	0.079691	0.000987	0.006743	0.468605	-0.00971	0.999013	-0.00163
0.515705	0.080534	0.000247	0.004195	0.484295	-0.00873	0.999753	-0.00176
						1	-0.0018

Table B.2: OMW aerofoil coordinates (202 points).

UBI-03-012 Modif.*							
x	y	x	y	x	y	x	y
1	0.021105	0.435566	0.080205	0	0	0.45947	-0.00774
0.995431	0.022082	0.424203	0.080114	2.01E-05	-0.00123	0.471024	-0.00703
0.986946	0.023863	0.412851	0.079973	0.000413	-0.0024	0.482588	-0.00631
0.977133	0.025876	0.401498	0.079782	0.001248	-0.00345	0.494152	-0.0056
0.966535	0.028	0.390155	0.079541	0.002375	-0.00441	0.505717	-0.00487
0.955575	0.030133	0.378812	0.079239	0.003754	-0.0053	0.517291	-0.00415
0.944484	0.032247	0.367479	0.078876	0.005395	-0.00619	0.528875	-0.00341
0.933322	0.03432	0.356146	0.078464	0.007367	-0.00708	0.54045	-0.00269
0.92214	0.036353	0.344834	0.078001	0.009732	-0.008	0.552024	-0.00196
0.910938	0.038326	0.333521	0.077467	0.012621	-0.00899	0.563598	-0.00124
0.899716	0.040269	0.322229	0.076884	0.016184	-0.01008	0.575163	-0.00051
0.888474	0.042161	0.310936	0.076229	0.020552	-0.01116	0.586727	0.000201
0.877222	0.044013	0.299674	0.075515	0.026249	-0.01221	0.598291	0.000916
0.86597	0.045824	0.288412	0.07474	0.033435	-0.0134	0.609845	0.00162
0.854697	0.047596	0.277169	0.073884	0.04198	-0.01457	0.621399	0.002325
0.843425	0.049317	0.265947	0.072968	0.051551	-0.01567	0.632954	0.003019
0.832142	0.050997	0.254725	0.071982	0.061746	-0.01662	0.644498	0.003704
0.82086	0.052648	0.243523	0.070915	0.072314	-0.01741	0.656052	0.004378
0.809567	0.054238	0.232342	0.069778	0.083134	-0.01807	0.667596	0.005052
0.798275	0.055798	0.22118	0.06857	0.094094	-0.0186	0.67913	0.005717
0.786972	0.057318	0.210028	0.067272	0.105165	-0.01903	0.690674	0.006371
0.77566	0.058787	0.198907	0.065903	0.116307	-0.01936	0.702208	0.007005
0.764347	0.060217	0.187806	0.064454	0.127509	-0.01961	0.713742	0.007639
0.753034	0.061606	0.176745	0.062924	0.138751	-0.01978	0.725276	0.008253
0.741722	0.062944	0.165714	0.061294	0.150033	-0.01988	0.73681	0.008857
0.730399	0.064242	0.154723	0.059583	0.161336	-0.01991	0.748334	0.009451
0.719087	0.06549	0.143783	0.057771	0.172658	-0.01989	0.759858	0.010034
0.707764	0.066698	0.132903	0.055859	0.184001	-0.0198	0.771382	0.010598
0.696431	0.067856	0.122094	0.053846	0.195364	-0.01966	0.782906	0.011152
0.685108	0.068963	0.111365	0.051712	0.206727	-0.01948	0.79443	0.011685
0.673786	0.07002	0.100747	0.049458	0.21811	-0.01923	0.805944	0.012198
0.662463	0.071036	0.09027	0.047072	0.229513	-0.01895	0.817458	0.012702
0.65113	0.071992	0.079973	0.044546	0.240927	-0.01863	0.828962	0.013185
0.639808	0.072908	0.069929	0.041879	0.25236	-0.01827	0.840466	0.013648
0.628485	0.073764	0.060186	0.039041	0.263804	-0.01786	0.85197	0.01409
0.617162	0.074569	0.050846	0.036041	0.275247	-0.01743	0.863453	0.014513
0.605839	0.075324	0.04203	0.032901	0.286711	-0.01698	0.874937	0.014916
0.594517	0.076018	0.033948	0.029681	0.298184	-0.01649	0.886411	0.015278
0.583184	0.076652	0.026822	0.02648	0.309668	-0.01597	0.897874	0.01563
0.571851	0.077236	0.020834	0.023461	0.321162	-0.01544	0.909328	0.015942
0.560508	0.077769	0.015952	0.020713	0.332656	-0.01489	0.920761	0.016224
0.549166	0.078252	0.012198	0.018147	0.34416	-0.0143	0.932175	0.016466
0.537813	0.078675	0.009219	0.015661	0.355663	-0.01371	0.943548	0.016667
0.52646	0.079047	0.006834	0.013366	0.367177	-0.01309	0.95486	0.016818
0.515097	0.07937	0.004942	0.011252	0.378701	-0.01247	0.966012	0.016919
0.503744	0.079641	0.003472	0.00929	0.390225	-0.01183	0.976791	0.016969
0.492381	0.079863	0.002325	0.007458	0.401759	-0.01117	0.986735	0.016949
0.481018	0.080034	0.001459	0.005747	0.413293	-0.01051	0.99533	0.016898
0.469655	0.080155	0.000835	0.004157	0.424827	-0.00982	1	0.016828
0.458292	0.080225	0.000403	0.002667	0.436372	-0.00914		
0.446929	0.080235	0.000141	0.001278	0.447916	-0.00844		

(*) Modification consisting on an inward offset of the aerofoil,
a modified elliptic LE and a TE cut-off (see Section 3.2).

Appendix C

VSW CAD and Technical Drawings

Isometric view

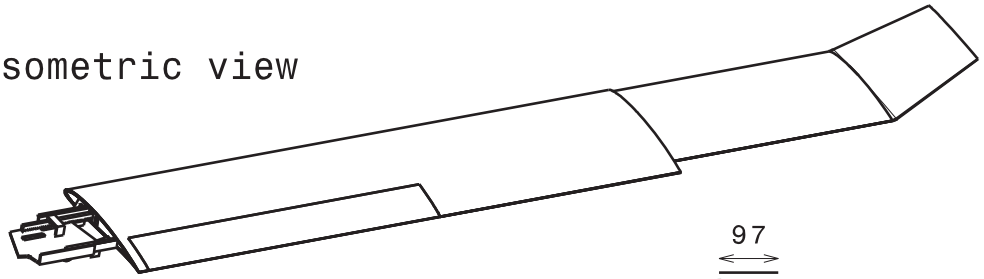

Right view

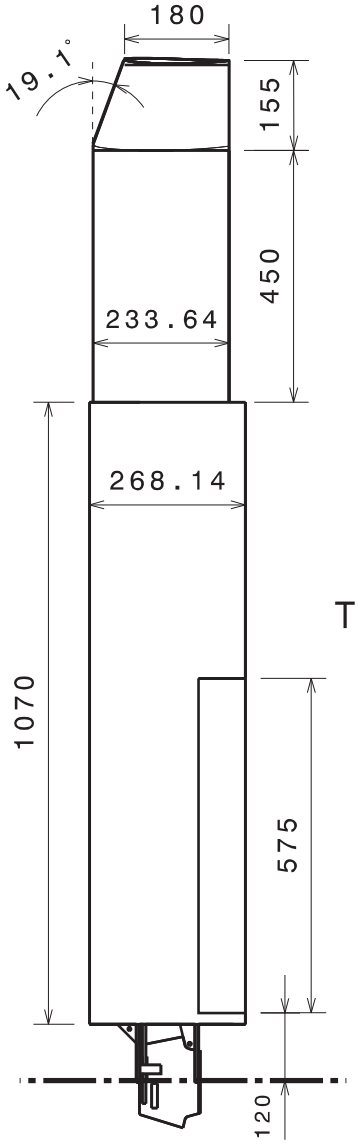

Top view

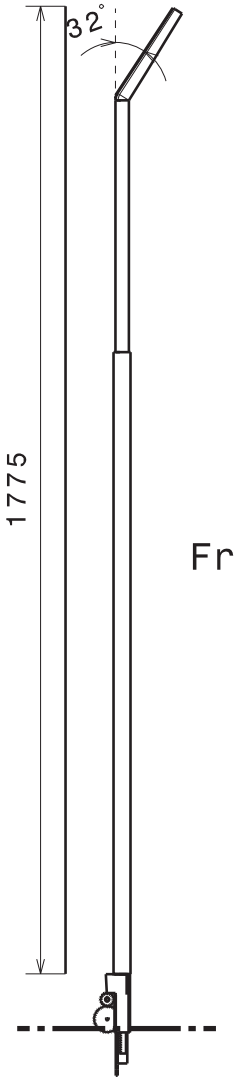

Front view

DESIGNED BY: Diogo Sousa DATE: 05-04-2017		Designed in CATIA V5/R21
SIZE A4	Object under design	Olharapo III's morphing wing, VSW concept
	Main dimentions	Wingspan, b=3.5535m; mean chord, c=0.257m
SCALE 1:13 / WEIGHT (kg) 0.766	Materials	Carbon-epoxy composite, PVC foam, plywood
	Units	millimeters, degrees

(a) VSW semi-span perspective view.

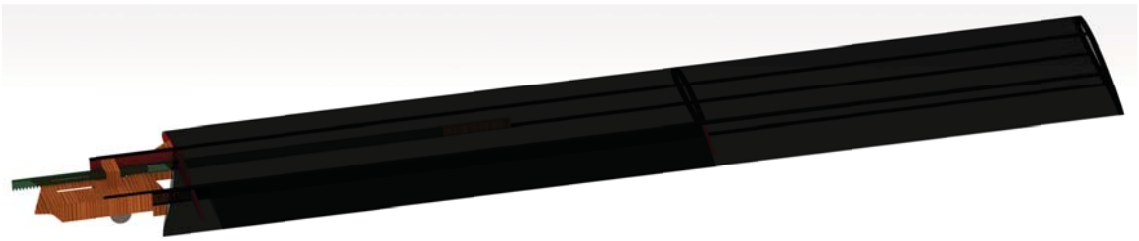

(b) IFW inner structure.

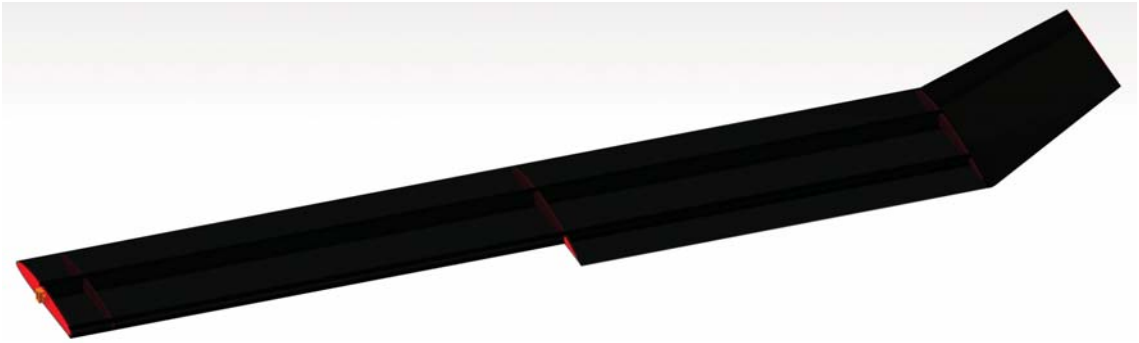

(c) OMW inner structure.

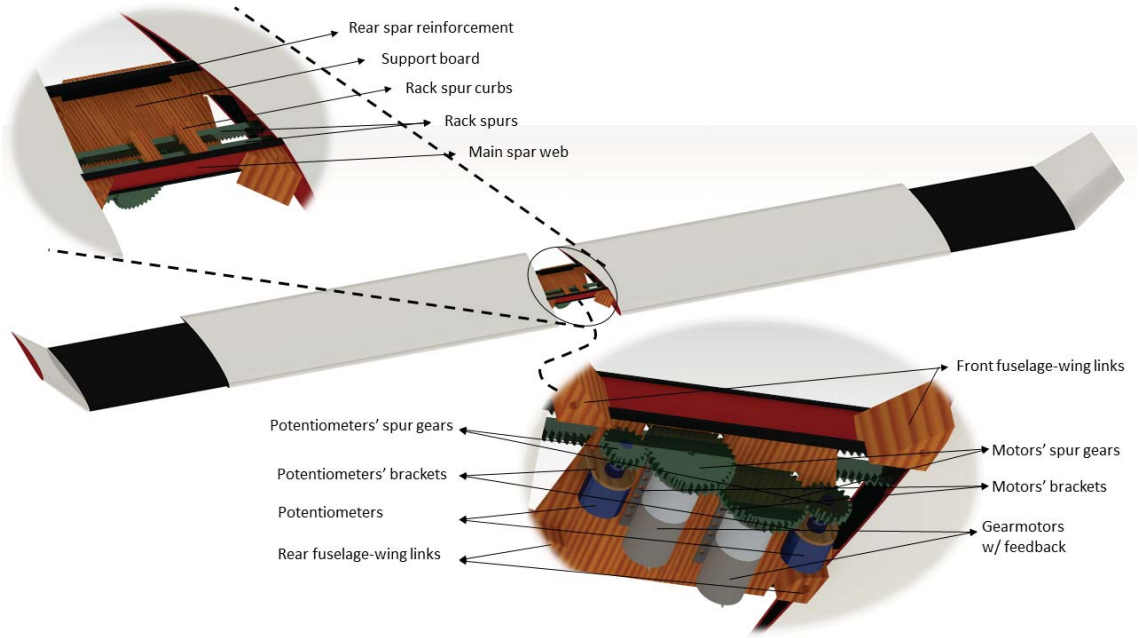

(d) VSW actuation system.

Figure C.1: VSW structural details and actuation system CAD views.

(a) Olharapo III fitted with the VSW.

(b) VSW without actuation systems cover.

Figure C.2: Olharapo III and VSW CAD views.

Appendix D

Partial derivative functions

Partial derivative functions for the FW mass predicting function are:

$$\frac{\partial \overline{m}_{FW}}{\partial b} = 0.2076W' + 0.13638b - 1.28929c - 0.42563\overline{c}_{flap} + 0.12176 \tag{D.1}$$

$$\frac{\partial \overline{m}_{FW}}{\partial c} = 11.91548c - 1.28929b - 1.32205W' + 0.65648 \tag{D.2}$$

$$\frac{\partial \overline{m}_{FW}}{\partial W'} = 0.2076b - 1.32205c - 0.4691\overline{c}_{flap} - 0.00913 \tag{D.3}$$

$$\frac{\partial \overline{m}_{FW}}{\partial \overline{c}_{flap}} = -0.42563b - 0.4691W' - 44.01416\overline{c}_{flap} + 16.29544 \tag{D.4}$$

Partial derivative functions for the VSW mass predicting function are:

$$\frac{\partial \overline{m}_{VSW}}{\partial b} = 0.18747W' + 0.15982b - 1.49982c - 0.47517\overline{c}_{flap} + 0.18153 \tag{D.5}$$

$$\frac{\partial \overline{m}_{VSW}}{\partial c} = 18.36462c - 1.49982b - 1.18482W' + 3.56318\overline{l}_{var} - 1.63169 \tag{D.6}$$

$$\frac{\partial \overline{m}_{VSW}}{\partial \overline{l}_{var}} = 3.56318c - 0.80463 \tag{D.7}$$

$$\frac{\partial \overline{m}_{VSW}}{\partial W'} = 0.18747b - 1.18482c + 0.11278 \tag{D.8}$$

$$\frac{\partial \overline{m}_{VSW}}{\partial \overline{c}_{flap}} = -0.47517b - 56.0031\overline{c}_{flap} + 19.97700 \tag{D.9}$$

Partial derivative functions for the VSW/FW mass ratio predicting function are:

$$\frac{\partial \overline{m}_{VSW/FW}}{\partial b} = 0.07998b - 0.64679c - 0.1838\overline{c}_{flap} - 0.32748\overline{l}_{var} - 0.04037 \tag{D.10}$$

$$\frac{\partial \overline{m}_{VSW/FW}}{\partial c} = 7.7195c - 0.64679b + 2.69658\overline{c}_{flap} + 6.17159\overline{l}_{var} - 1.00807 \tag{D.11}$$

$$\frac{\partial \overline{m}_{VSW/FW}}{\partial \overline{l}_{var}} = 6.17159c - 0.32748b - 0.33888W' + 1.86028\overline{c}_{flap} + 1.46318\overline{l}_{var} - 0.85174 \tag{D.12}$$

$$\frac{\partial \overline{m}_{VSW/FW}}{\partial W'} = -0.33888\overline{l}_{var} - 0.03885 \tag{D.13}$$

$$\frac{\partial \overline{m}_{VSW/FW}}{\partial \overline{c}_{flap}} = -0.1838b + 2.69658c + 1.86028\overline{l}_{var} - 0.26331 \tag{D.14}$$

Appendix E

Regression Mass Results with Full Polynomial's Terms

Table E.1: Mass predicting functions with full number of terms.

No.	$\overline{m}_{FW}$			
	Coef*	Vars	ERR	SERR
1	0.1217637	b	78.36%	78.36%
2	0.656479	c	7.80%	86.16%
3	-0.009131	W'	5.44%	91.60%
4	-1.28929	bc	2.85%	94.45%
5	16.295439	$\overline{c}_{flap}$	2.07%	96.52%
6	0.2076	bW'	1.61%	98.13%
7	-1.32205	cW'	0.34%	98.48%
8	-0.42563	$b\overline{c}_{flap}$	0.28%	98.76%
9	0.06819	b^2	0.25%	99.01%
10	-22.00708	$\overline{c}^2_{flap}$	0.51%	99.52%
11	5.95774	c^2	0.16%	99.68%
12	-0.4691	$W'\overline{c}_{flap}$	0.04%	99.72%
13	1.52479	$c\overline{c}_{flap}$	0.02%	99.74%
14	0.04571	W'^2	0.00%	99.74%
15	-2.99106	(constant)	0.00%	99.74%

No.	$\overline{m}_{VSW}$				$\overline{m}_{VSW}/\overline{m}_{FW}$			
	Coef*	Vars	ERR	SERR	Coef*	Vars	ERR	SERR
1	0.181526	b	80.72%	80.72%	-0.04037	b	29.81%	29.81%
2	-1.63169	c	5.07%	85.80%	-1.00807	c	29.03%	58.84%
3	0.112783	W'	4.35%	90.15%	-0.64679	bc	6.96%	65.81%
4	-1.49982	bc	3.78%	93.92%	-0.85174	$\overline{l}_{var}$	6.86%	72.66%
5	19.977	$\overline{c}_{flap}$	1.89%	95.81%	6.17159	$c\overline{l}_{var}$	7.05%	79.72%
6	0.18747	bW'	1.29%	97.10%	-0.03885	W'	6.12%	85.83%
7	-0.47517	$b\overline{c}_{flap}$	0.35%	97.45%	-0.32748	$b\overline{l}_{var}$	3.82%	89.65%
8	0.07991	b^2	0.34%	97.79%	-0.26331	$\overline{c}_{flap}$	2.31%	91.96%
9	-28.0016	$\overline{c}^2_{flap}$	0.68%	98.47%	0.03999	b^2	0.92%	92.88%
10	9.18231	c^2	0.37%	98.84%	1.411713	(constant)	1.66%	94.54%
11	-1.18482	cW'	0.27%	99.11%	3.85975	c^2	0.66%	95.20%
12	3.56318	$c\overline{l}_{var}$	0.23%	99.33%	1.86028	$\overline{l}_{var}\overline{c}_{flap}$	0.57%	95.77%
13	-0.80463	$\overline{l}_{var}$	0.08%	99.41%	2.69658	$c\overline{c}_{flap}$	0.58%	96.36%
14	2.84861	$c\overline{c}_{flap}$	0.06%	99.47%	-0.1838	$b\overline{c}_{flap}$	0.52%	96.88%
15	-0.11724	$b\overline{l}_{var}$	0.05%	99.52%	-0.33888	$\overline{l}_{var}W'$	0.47%	97.34%
16	-0.37252	$W'\overline{c}_{flap}$	0.02%	99.55%	0.73159	$\overline{l}^2_{var}$	0.07%	97.41%
17	0.90947	$\overline{l}_{var}\overline{c}_{flap}$	0.01%	99.56%	-0.11614	cW'	0.03%	97.44%
18	-0.18098	$\overline{l}_{var}W'$	0.01%	99.57%	0.00834	bW'	0.03%	97.46%
19	0.45917	$\overline{l}^2_{var}$	0.00%	99.58%	0.01668	$W'\overline{l}_{var}$	0.00%	97.46%
20	0.00382	W'^2	0.00%	99.58%	0.00103	W'^2	0.00%	97.46%
21	-3.38531	(constant)	0.00%	0.00%	0	$\overline{c}^2_{flap}$	0.00%	0.00%

Appendix F

Scientific Articles (first pages)

Aerodynamic Performance of Aerofoils Obtained from a Geometric Offset Applied to a Given Initial Aerofoil

1. Introduction

Morphing wing technologies for flight regime adaptation have received great attention recently and may become important for aircraft's operations in near-optimal overall flight efficiency point. Advances in these technologies enable new design approaches and improvements in multi-task flexibility, by considering wing geometric transformations. A thorough review of morphing concepts that thrived to be functional in flight is presented by Barbarino [1] showing the huge effort of researchers to develop efficient and reliable morphing aircraft systems.

From an aerodynamics perspective, the overall shape of the wing (including cross-section) is the most important design aspect for an aircraft so that there is usually an ideal single configuration of the aircraft suitable for each specific type of mission [2]. Therefore a non-morphing aircraft is highly efficient in some design flight conditions while it becomes less suitable in others. Furthermore, morphing wing technologies contribute for efficient performance during distinct mission roles, or enable new multi-role missions that are not possible with a fixed geometry aircraft, as demonstrated by Tidwell et al [3].

Many projects have focused on aircraft morphing concepts with the ultimate goal of enhancing performance and increasing energy efficiency of aircraft [4]. As these technologies are still recent and lack adequate maturity, their progress is an iterative process between design and experiment. Also, a large number of projects have produced extensive work on aerodynamic shape optimization of aerofoils and multidisciplinary design optimization of wing systems [5-9]. Methods of aerofoil and wing morphing can include thickness and camber change [10], variable twist, variable chord, sweep change, and variable span [5]. Moreover, unmanned aerial vehicles (UAVs) have great potential for testing morphing technologies due to their flexibility, simple operation, low production and operation costs and the absence of direct risk to the crew. All in all, due to their characteristics, UAV concepts usually minimize the disadvantages and maximize the advantages of several research assignments.

The motivation behind the present work lies in the desire to improve a variable-span wing (VSW) design of the telescopic type previously developed at the Aerospace Sciences Department of University of Beira Interior [8, 9, 11]. This new VSW design will make use of purposely optimized aerofoil sections and will also include aerofoil camber changes. The variable span capability allows the wing to be fully extended for take-off and landing, in a configuration of high lift where the lift-to-drag ratio is improved, and provide reduced take-off and landing distances. The fully extended span configuration is also suitable for low speed loiters. On the other hand, with the outboard panel retracted, while in cruise or at high speeds, the wing planform area and aspect ratio are reduced, decreasing parasite drag for improved range and cruise efficiency [11]. In this manner, the layout of the VSW concept is based on a hollow inboard fixed wing (IFW) that is fixed to the fuselage inside of which slides an outboard moving wing (OMW) slides actuated by an electromechanical mechanism.

The shape and size of the VSW is obtained through an in-house computational constrained aerodynamic shape optimization code, aimed at determining the wing mean chord and span values that minimize its drag for a specified mission profile. A detailed description of the aerodynamic optimization procedure is given by Albuquerque et al [12]. As inputs to this optimization procedure, two aerofoils' data points must be provided. For such task, it is mandatory to design two geometrically compatible aerofoils, with the chord length of the IFW larger than that of the OMW, in order for the outboard wing panel to slide inside the inboard wing panel. Accordingly, both IFW and OMW wing panels have the design constraint of keeping chord and aerofoil geometry constants along each panel's span, enabling proper

Research Article **Open Access**

Diogo Sousa, Pedro Gamboa*, and David Melo

Aerodynamic performance of aerofoils obtained from a geometric offset applied to a given initial aerofoil

DOI 10.1515/eng-2016-0098
Received March 16, 2016; accepted August 11, 2016

Abstract: Many studies concerning morphing aircraft concepts in which enhanced performance and increased energy efficiency are two of the main goals have been recently conducted. Some of those concepts deal with wing span changes. In line with those, in a variable-span wing of the telescopic type, the cross-sections of the sliding panels, whether be two, three or more, must be made geometrically compatible among them. This requirement serves two purposes: to minimize the aerofoils' geometric discontinuity which negatively affects wing drag and lift; and to provide a simple structural support between any two sliding panels. This paper describes the methodology employed to develop geometrically compatible aerofoils obtained from a constant geometric offset applied to a given initial aerofoil. This methodology is used to create inward offset aerofoils and outward offset aerofoils. The geometric and aerodynamic characteristics of the resulting offset aerofoils are compared with those of the original aerofoils. From the analysis of six different original aerofoils, strong trends in the geometric changes and in the aerodynamic characteristics of the resulting inward and outward offset aerofoils are observed. Ultimately, this study can help a telescopic wing designer decide whether an inward or an outward offset aerofoil is more appropriate for the specific design at hand.

Keywords: aerofoil offset; aerofoil geometry; aerodynamic analysis; morphing technologies; variable-span wing; XFOIL

***Corresponding Author: Pedro Gamboa:** Department of Aerospace Sciences, University of Beira Interior, Covilhã, 6201-001, Portugal, E-mail: pgamboa@ubi.pt
Diogo Sousa, David Melo: Department of Aerospace Sciences, University of Beira Interior, Covilhã, 6201-001, Portugal

1 Introduction

Morphing wing technologies for flight regime adaptation have received great attention in recent years and may become important for aircraft's operations allowing near-optimal overall flight efficiency over different design points. Advances in these technologies enable new design approaches and improvements in multi-task flexibility, by considering wing geometric transformations. A thorough review of morphing concepts which thrived to be functional in flight is presented by Barbarino et al. [1] showing the huge effort that researchers have committed to developing efficient and reliable morphing aircraft systems.

From an aerodynamics perspective, the overall shape of the wing (including cross-section) is the most important design aspect for an aircraft so that there is usually an ideal single configuration of the aircraft suitable for each specific type of mission [2]. Therefore a non-morphing aircraft is highly efficient at some design flight condition while it becomes less suitable in others. Furthermore, morphing wing technologies contribute to efficient performance during distinct mission roles, or enable new multi-role missions that are not possible with a fixed geometry aircraft, as demonstrated by Tidwell et al. [3].

Many recent developments have focused on aircraft morphing concepts with the ultimate goal of enhancing performance and increasing energy efficiency of aircraft [4]. As these technologies are still recent and lack adequate maturity, their progress is an iterative process between design and experiment. Also, a large number of projects have produced extensive work on aerodynamic shape optimization of aerofoils and multidisciplinary design optimization of wing systems [5–8]. Methods of aerofoil and wing morphing can include thickness and camber change [9], variable twist, variable chord, sweep change, and variable span [5].

The motivation behind the present work lies in the desire to improve a variable-span wing (VSW) design of the telescopic type previously developed at the Aerospace Sciences Department of University of Beira Interior [8, 10,